

**Addressing Electrode-Specific Degradation in the Production and
Performance of Electrochemical Energy Storage Systems**

by

Kavian Khosravinia

A thesis submitted to the
School of Graduate and Postdoctoral Studies in partial
fulfillment of the requirements for the degree of

Doctor of Philosophy in Mechanical Engineering

Department of Automotive, Mechanical, and Manufacturing Engineering

Faculty of Engineering and Applied Science

University of Ontario Institute of Technology (Ontario Tech University)

Oshawa, Ontario, Canada

August 2023

© Kavian Khosravinia, 2023

THESIS EXAMINATION INFORMATION

Submitted by: **Kavian Khosravinia**

PhD in Mechanical Engineering

Thesis title: Addressing Electrode-Specific Degradation in the Production and Performance of Electrochemical Energy Storage Systems

An oral defense of this thesis took place on August 2, 2023, in front of the following examining committee:

Examining Committee:

Chair of Examining Committee	Dr. Martin Agelin-Chaab
Research Supervisor	Dr. Amirkianoosh Kiani
Research Co-supervisor	Dr. Xianke Lin
Examining Committee Member	Dr. Yuping He
Examining Committee Member	Dr. Ghaus Rizvi
University Examiner	Dr. Sheldon Williamson
External Examiner	Dr. Amir Gandomi, Hofstra University

The above committee determined that the thesis is acceptable in form and content and that a satisfactory knowledge of the field covered by the thesis was demonstrated by the candidate during an oral examination. A signed copy of the Certificate of Approval is available from the School of Graduate and Postdoctoral Studies.

ABSTRACT

This thesis addresses the pressing issue of sustainable development and climate change by examining the life cycle (degradation) of electrochemical energy storage devices. Specifically, it investigates a green synthesis technique for high-performance pseudocapacitor electrodes and uses machine learning algorithms to predict and prevent degradation mechanisms in lithium-ion batteries. The research demonstrates the effectiveness of the laser irradiation technique, called ultra-short laser pulses for in situ nanostructure generation (ULPING) for fabricating a metal oxide layer on a titanium sheet under ambient conditions, as well as the potential of machine learning algorithms as a tool for constructing mathematical models to forecast the electrochemical behavior of pseudocapacitors. The thesis also highlights the importance of utilizing data-driven approaches in electrode design procedures and promoting sustainable habits in all aspects of life. In addition, the study provides insight into the modeling and prediction of the electrochemical behavior performance of pseudocapacitors, which could facilitate the development of optimal electrodes. Moreover, the research examines one of the most detrimental degradation mechanisms that occur during the fast-charging process, known as the deposition of metallic lithium or lithium plating, in lithium-ion batteries. The proposed machine learning approach based on ensemble selection accurately predicts the anode potential under various charging conditions and achieves high accuracy in preventing lithium plating. Overall, this research offers promising methods for employing ultra-short laser pulses for in situ nanostructure generation to fabricate nanostructures on transition metals that have the potential to be used in pseudocapacitor electrodes and highlights the

importance of utilizing machine learning techniques in predicting and preventing degradation mechanisms in electrochemical energy storage devices.

Keywords: Lithium-ion batteries; Machine Learning; Simulated Annealing; Nanotechnology; Supercapacitor

AUTHOR'S DECLARATION

I hereby declare that this thesis consists of original work of which I have authored. This is a true copy of the thesis, including any required final revisions, as accepted by my examiners.

I authorize the University of Ontario Institute of Technology (Ontario Tech University) to lend this thesis to other institutions or individuals for the purpose of scholarly research. I further authorize University of Ontario Institute of Technology (Ontario Tech University) to reproduce this thesis by photocopying or by other means, in total or in part, at the request of other institutions or individuals for the purpose of scholarly research. I understand that my thesis will be made electronically available to the public.

Kavian Khosravinia

Kavian Khosravinia

STATEMENT OF CONTRIBUTIONS

Parts of this thesis have been published or submitted for publication in the following:

Journal Articles

***(1) Kavian Khosravinia, A. Kiani.** "Optimizing the Ultrashort Laser Pulses for In Situ Nanostructure Generation Technique for High-Performance Supercapacitor Electrodes Using Artificial Neural Networks and Simulated Annealing Algorithms", American Chemical Society ACS Omega, <https://doi.org/10.1021/acsomega.3c01676>.

***(2) Kavian Khosravinia, A. Kiani.** "Unlocking Pseudocapacitors prolonged electrode fabrication via ultrashort laser pulses and machine learning", Cell Press, <https://doi.org/10.1016/j.isci.2023.106438>.

***(3) S. Mahala, Kavian Khosravinia, and A. Kiani.** "Unwanted Degradation in Pseudocapacitors: Challenges and Opportunities", *Journal of The Energy Storage*, <https://doi.org/10.1016/j.est.2023.107558>.

***(4) Kavian Khosravinia, A. Kiani.** " Protocol for fabricating Pseudocapacitor electrodes using ultra-short laser pulses for in situ nanostructure generation", *Star Protocols - Cell Press*, <https://doi.org/10.1016/j.xpro.2023.102469>.

* The research papers presented in this thesis were conducted under the supervision of **Dr. Amirkianoosh Kiani**.

** The research papers presented in this thesis were conducted under the supervision of **Dr. Xianke Lin**.

** (5) X. Lin, **Kavian Khosravinia**, X. Hu, Ju. Li, and W. Lu. "Lithium Plating Mechanism, Detection, and Mitigation in Lithium-Ion Batteries", *Progress in Energy and Combustion Science*, <https://doi.org/10.1016/j.pecs.2021.100953>. (Published)

** (6) **Kavian Khosravinia**, X. Lin. "Toward Enhanced Anode Potential Prediction of Lithium-ion Batteries: Using Optimized Ensemble Selection Approach for Lithium Plating Mitigation", *Journal of The Electrochemical Society*, (Accepted with Minor Revisions).

Conference Proceedings

* (7) **Kavian Khosravinia**, A. Kiani. "Cracking the Code to Electrode-Specific Degradation: Insights from Data-Driven Approaches in ULPING Fabricated Pseudocapacitor", *7th International Conference of Theoretical and Applied Nanoscience and Nanotechnology (TANN 2023)*, [https:// DOI: 10.11159/tann23.156](https://doi.org/10.11159/tann23.156).

* (8) **Kavian Khosravinia**, A. Kiani "AI-Driven Laser Parameter Optimization for Enhanced Pseudocapacitor Electrodes", 2023 14th International Symposium on Modern Optics and Its Applications, (Accepted for Presentation).

** (9) **Kavian Khosravinia**, X. Lin. "Data-Driven Anode Potential Prediction in Lithium-ion Batteries for Lithium Plating Prevention Based on Gaussian Process Regression", *13th International Green Energy Conference in Tianjin, China (IGEC-XIII-2021)*, (Published).

* The research papers presented in this thesis were conducted under the supervision of **Dr. Amirkianoosh Kiani**.

** The research papers presented in this thesis were conducted under the supervision of **Dr. Xianke Lin**.

DEDICATION

To the true teachers of my life:

My beloved mother for endless love and sincere generosity.

My dear father for lifelong investigation, pure poetry, and diligent publications.

ACKNOWLEDGEMENTS

A debt of gratitude goes to my supervisor, Associate Professor Dr. Amirkianoosh Kiani, for his precious guidance throughout this research. Without his supervision and constant help, this thesis would not have been possible. I am also thankful to my supervisory committee, Professor Ghaus Rizvi, and Professor Yuping He, for their valuable observations and comments. A special thank you to all the people who made the development of this work possible in their own particular way. I extend my heartfelt appreciation to my parents for their everlasting support. Additionally, I am grateful to Peji, Toufi, Ami, Pooyi, and Javad for their boundless friendship and generous and constant help during this long journey. My thanks also go to my colleagues at Silicon Hall laboratory for their assistance at all times.

TABLE OF CONTENTS

THESIS EXAMINATION INFORMATION	ii
ABSTRACT.....	iii
AUTHOR’S DECLARATION	v
STATEMENT OF CONTRIBUTIONS.....	vi
DEDICATION.....	viii
ACKNOWLEDGEMENTS	ix
TABLE OF CONTENTS	x
LIST OF TABLES	xiv
LIST OF FIGURES	xvi
LIST OF ABBREVIATIONS	xxviii
Chapter 1 : Introduction	1
1.1 Problem statement and Motivations.....	3
1.2 Scope of Research	4
1.3 Objectives.....	6
1.4 Work Novelties	6
1.4.1 Manufacturing phase.....	6
1.4.2 Operational Phase.....	7
1.5 Thesis Outline	8
Chapter 2 : Literature Reviews	9
2.1 Manufacturing Phase: Unwanted Degradation in Pseudocapacitors.....	9
2.1.1 Introduction	9
2.1.2 Background	10
2.1.3 Degradation mechanisms of pseudocapacitors	17

2.1.4	Degradation mechanism in pseudocapacitors at the microstructure level	24
2.1.5	Degradation mechanism through electrochemical and kinetic analysis	29
2.1.6	Degradation characterization approaches	32
2.1.7	Optimizing and controlling the rate of degradation	44
2.1.8	Manufacturing Phase Summary	62
2.2	Operational Phase: Unwanted Degradation in Lithium-ion Batteries	63
2.2.1	Introduction	63
2.2.2	Lithium Plating Reactions	72
2.2.3	Main Factors Affecting Lithium Plating	75
2.2.4	Lithium Plating Detection Approaches	82
2.2.5	Recent Non-Destructive Approaches for Detecting Lithium Plating	106
2.2.6	Model-Based Investigation of Lithium Plating	111
2.2.7	Operational Phase Summary	116
Chapter 3 : Methodologies		117
3.1	Manufacturing Phase: Method Details	117
3.1.1	Section Overview (Pseudocapacitors Electrode Fabrication via ULPING)	117
3.1.2	Experimental Phase	123
3.1.3	Computational Phase	130
3.1.4	Optimization of Pseudocapacitors Electrode Fabrication Strategy	145
3.2	Operational Phase: Method Details	151

3.2.1	Section Overview (Anode Potential Prediction for Lithium Plating Mitigation)	151
3.2.2	Experimental Setup for Anode Potential Prediction	157
3.2.3	Anode Potential Dataset Preparation for Machine Learning Algorithms	165
3.2.4	Machine Learning for Anode Potential Prediction	171
3.2.5	Optimized Ensemble Selection for Anode Potential Prediction	176
	Chapter 4 : Results and Discussion (Manufacturing Phase)	182
4.1	Results of Fabricated Pseudocapacitor Electrodes via ULPING	182
4.1.1	Morphology and Structural Properties of Selected Electrodes	182
4.1.2	Electrochemical Performance of Selected Electrodes.....	186
4.1.3	Electrochemical Performance of All 496 Coin Cells	195
4.2	Electrochemical Behavior Prediction of Pseudocapacitor Electrodes via Machine Learning Algorithms.....	197
4.2.1	Specific Capacitance and Impedance Prediction Based on Test Dataset	197
4.2.2	Specific Capacitance and Impedance Prediction Based on Cross Validation	199
4.3	Discussion and Summary	200
4.4	Optimization for Enhancing Electrochemical Behavior of Pseudocapacitors Electrode	202
4.4.1	Morphology and Structural Properties of Optimized Electrodes	202
4.4.2	Electrochemical Properties of Optimized electrodes	209
4.5	Discussion and Summary	214
	Chapter 5 : Results and Discussion (Operational Phase).....	215

5.1 Evaluation Performance of Machine Learning Algorithms for Anode Potential Prediction.....	215
5.2 valuation Performance of Optimized Ensemble Selection for Anode Potential Prediction.....	217
5.3 Discussion and Summary	219
Chapter 6 : Conclusions	225
6.1 Limitations of study	227
Bibliography	229
Appendix A	284
Appendix B – Copyright Permission.....	289

LIST OF TABLES

CHAPTER 2

Table 2-1. The relation of the three main factors of a pseudocapacitor.	14
Table 2-2. Common advantages and disadvantages of all types of pseudocapacitors.....	17
Table 2-3. Individual techniques (with examples) for the characterization of the materials used in pseudocapacitors.....	37
Table 2-4. Mass loss surface characterization techniques with examples of the materials used in pseudocapacitor.	38
Table 2-5. Different electrochemical analysis techniques were used to predict their operational properties.....	42
Table 2-6. Summary of different electrodes used for minimizing the rate of degradation in pseudocapacitors.	60
Table 2-7. Electrodes, electrolyte, preparation method, and their operational results.....	61
Table 2-8. Factors causing lithium plating.	82
Table 2-9. Advantages and disadvantages physical characterization of surface morphologies for lithium plating detection.....	103
Table 2-10. Advantages and disadvantages physical characterization of surface chemistry for lithium plating.	104
Table 2-11. Advantages and disadvantages of on-line electrochemical lithium plating detection techniques.....	109

CHAPTER 3

Table 3-1. Comparison of conventional synthetic methods and ULPING.	119
Table 3-2. Laser variables for different samples	125
Table 3-3. SA parameters for optimal electrode design.	149
Table 3-4. SA optimal laser fabrication parameters for electrode design.....	150

Table 3-5. Battery model parameters.....	159
Table 3-6. Pearson correlation coefficient between the input variables vs output variables.	168
Table 3-7. The pseudocode of the forward selection method.....	178
Table 3-8. Summary of model configurations used in this study.....	181

CHAPTER 4

Table 4-1. Summary of the specific areal capacitance, porosity, energy density, and power density of the selected samples.....	195
Table 4-2. Performance comparison of ML algorithms on the test dataset.....	199
Table 4-3. Performance comparison of ML algorithms based on cross-validation.....	199
Table 4-4. Summary of the specific areal capacitance, porosity, energy density, and power density of the selected samples.....	214

CHAPTER 5

Table 5-1. Performance comparison of different learning algorithms on the training dataset.	216
Table 5-2. Performance comparison of different learning algorithms and the developed ES model on the test dataset.....	219
Table 5-3. Average training and testing time of the proposed method and different learning algorithms.....	221

LIST OF FIGURES

CHAPTER 1

Figure 1-1: The relation between material life cycle and sustainable development [1]. 2

CHAPTER 2

Figure 2-1: (a) Sketch of Ragone plot to compare different types of energy storage devices
(b) A typical diagram of a pseudocapacitor. 12

Figure 2-2: Pseudocapacitor working principles. (a) Underpotential pseudocapacitor where lead (Pb) is deposited on the gold (Au) electrode, forming an adsorbed monolayer. The working principle is electrosorption, which is potentially induced adsorption on the surface of the active electrode material [35], [36]. (b) Redox pseudocapacitor where ions from the electrolyte are electrochemically adsorbed onto the surface or near the surface of RuO₂ accompanied by Faradaic charge transfer. The principle is a redox transfer mechanism in which a chemical reaction takes place between an oxidizing substance/substrate and a reducing substance/substrate. (c) Intercalation pseudocapacitance where ions like lithium are intercalated or inserted into the layers of the electrode material. The working principle is the intercalation of ions of molecules into layers of a material or a substrate [37], [38]. 16

Figure 2-3: Main findings or observations for degradation mechanisms at several levels ranging from microstructure to electrode, the electrode to the device, and device to applications in various sectors/industries. 19

Figure 2-4: Degradation occurs due to many factors that take place in the electrolyte and electrode, and to external factors such as kinetics, potential, and temperature. All of these factors lead to different degradation mechanisms through which we can identify the deterioration of the device happening in real time during the experiment. 20

Figure 2-5: (a) Degradation mechanism of the NiO film, which is used as a redox pseudocapacitive electrode. Reprinted with permission from [47]. (b) P-MnO₂ and Sn-doped MnO₂ discharge capacity vs. cycle number at C/15 rate in the voltage range 1.5-4.0

V vs. Li^+/Li^0 . The electrolyte used for this pseudocapacitor is 1 mol L^{-1} LiPF_6 in ethylene carbonate-dimethyl carbonate (1:2), which is an organic electrolyte. Reprinted with permission from [56].....	23
Figure 2-6: Cracks in the microstructure because of irreversible reduction and chemical products formed during cycling. Low ion-transfer kinetics are caused by dissimilar interlayer spacing and non-uniform morphology. No intercalation or redox transfer occurs because of the formation of pore blockages and obstruction of the ion/electron transfer pathway (post-precipitation).	25
Figure 2-7: Morphology of the CuO electrodes synthesized from a $\text{Cu}:\text{HMT}$ complexing agent after 5000 cycles in 1 M Na_2SO_4 electrolyte. (a) SEM image of the electrode, showing cracks. (b) TEM image of the electrode, showing uniform morphology with good porosity. Reprinted with permission from [71].....	26
Figure 2-8: SEM images of (a) A fibrous Millipore JVWP separator. (b) a monolithic/defined GE Osmotics K50CP01300 separator. Reprinted with permission from [85].....	29
Figure 2-9: Flow chart for operating conditions that influence the rate of degradation or deterioration of the device, including potential range or potential window, current density, number of cycles (charge and discharge cycles).....	31
Figure 2-10: ^1H NMR spectrum of (a) The quinoxaline-based amine compound (dpqa). (b) quinoxaline-based benzoxazine (BA-dpqa). Reprinted from [113].	36
Figure 2-11: The schematic detailed diagram for the fabrication process of the MoS_2 nanosheets and the tubular (hollow) $\text{V}_2\text{O}_3@/\text{MoS}_2$ composites. Reprinted with permission from [133].	46
Figure 2-12: (a) CV curve for the symmetric pseudocapacitor $\text{V}_2\text{O}_3@/\text{MoS}_2/\text{V}_2\text{O}_3@/\text{MoS}_2$. (b) CV curve for the asymmetric pseudocapacitor $\text{V}_2\text{O}_3@/\text{MoS}_2/\text{AC}$. (c) & (d) TiO_2 nanosheets (hollow nanofibers) manufactured by electrospinning method. (e) Graph for capacity retention against the number of cycles for the MSO and MnO_2 electrodes. The	

inset in the graph shows the solution after cycling tests. Reprinted with permission from [51], [133], [145].....	48
Figure 2-13: Synthesis route of NFA/NCO/CS. Reprinted with permission from [151].	49
Figure 2-14: (a) CV curve for composite electrode for pseudocapacitors, using NFA/NCO NWs/CS or NFA/NCO NFsCS at a scan rate of 10 mV s^{-1} . (b) GCD curve of the NFA/NCO NWs/CS composite electrode at different current densities. Reprinted with permission from [151].	50
Figure 2-15: Schematic diagram of the processing of hierarchical Co-NTC@Co ₃ S ₄ . Reprinted with permission from [160].....	52
Figure 2-16: (a) Specific capacitance vs. the number of cycles of NiO and NiO/G. The cycling performance is carried out at a current density of 5 Ag^{-1} . (b) Nyquist plots of the NiO and NiO/G electrodes. (c) CV curve of Co-NTC@Co ₃ S ₄ and AC at a scan rate of 10 mV s^{-1} . (d) Cycling performance/stability of Co-NTC@Co ₃ S ₄ /AC at a current density of 10 Ag^{-1} . Reprinted with permission from [154], [160].....	53
Figure 2-17: (a) SEM image of the NG/Co (OH) ₂ composite electrode. (b) Capacity retention vs. cycles for the NG/Co (OH) ₂ composite electrode material at a current density of 1 Ag^{-1} over 2000 cycles. Reprinted with permission from [166].	55
Figure 2-18: (a) & (b) SEM images before and after cycling test of 10,000 cycles for PANi@C-2h and PPy@C-2h respectively. (c) & (d) Capacity retention vs. the number of cycles for PANi and PANi@C electrodes, and for PPy and PPy@C electrodes. The cycling performance is analyzed at a scan rate of 100 mV s^{-1} . Reprinted with permission from [174].	56
Figure 2-19: (a) Schematic diagram of the manufacturing of the PANi-g-rGO/AgCl ternary nanocomposites. (b) SEM images of (i) GO, (ii) rGO/Ag, (iii) rGO/AgCl, and (iv) PANi-g-rGO/AgCl ternary nanocomposites used in the electrodes of the supercapacitor. Reprinted with permission from [178].....	57

Figure 2-20: (a) The curve of specific capacitance of PANi-g-rGO/AgCl, PANi-g-rGO, and PANi NFs at different current densities. (b) Cyclic performance of the PANi-g-rGO/AgCl, PANi-g-rGO, and PANi NFs. Reprinted with permission from [178]. 58

Figure 2-21: (a) The fabrication of WO₃ nanotubes and the PEDOT: PSS layer is depicted schematically. The electrospun WO₃ nanotube is coated with a thin layer of PEDOT: PSS before being drop-coated onto an Ag nanowire-embedded PDMS substrate. (b) CV test of all (transparent stretchable electrochromic supercapacitor (TSES) electrodes at a scan rate of 1 mV s⁻¹. The curve clearly shows that, with the addition of WO₃ nanotubes and the PEDOT: PSS, the capacity increases dramatically. Reprinted with permission from [182]. 59

Figure 2-22: Lithium Plating Phenomena at Different Research Levels. 64

Figure 2-23: Schematic of a Battery Cell During Charging Process and Lithium Plating Behavior under Different Operational Conditions. (A) In the intercalation/de-intercalation process, Li-ions intercalate into or de-intercalate from the active material between the two electrodes in a reversible manner. (B) Schematic of lithium plating-stripping on the graphite anode electrode. The primary SEI layer (yellow color) is formed at the anode surface during the first charge of the cell to protect the electrode against corrosion. Because the primary SEI layer prevents electrons from making direct contact with the electrolyte, metallic lithium (red color) is deposited between the primary SEI layer and graphite particles. Mossy and dendritic deposition are two well-known morphologies of deposited lithium. When deposited lithium reacts with electrolyte solutions, the secondary SEI layer (green color) forms. (C) Under ideal conditions, the charge-transfer process consists of three steps: 1. de-solvation of solvated Li⁺ ions, 2. Li⁺ shuttle through the SEI, and 3. solid-state lithium diffusion into graphite particles. (D) At low temperature, Li⁺ ions move slowly in graphite due to the low diffusivities of lithium ions and the sluggish charge transfer kinetics which leading to lithium plating. (E) At high charging C-rate, Li⁺ ions move fast and a large amount of Li⁺ accumulate at the electrode interface because the lithium solid diffusion is lower Li⁺ diffusion in the electrolyte, then saturate concentration

happens on the lithium ions, and lithium plating happens. (F) Under the high SOC condition, Li⁺ ions move slowly in graphite under high SOC conditions. 68

Figure 2-24: Degradation Modes, Ageing Mechanisms, and the Affected Components in Lithium-ion Batteries. There are many different ageing mechanisms, and they are generally divided into three different degradation modes (DMs): loss of lithium inventory (LLI), loss of active material (LAM) and loss of electrolyte. There is a general relationship between battery working conditions and the affected components with the corresponding ageing mechanisms. Charging at a high C-rate, a high state of charge (SOC), or at a low temperature are all critical operating conditions that accelerate battery degradation [220]. 70

Figure 2-25: One-set Lithium Plating C-rates/ Temperature Summary. (A) Analyzing the existing literature on lithium plating based on two common testing conditions: temperature and C-rate. Larger dots represent a greater number of publications that used that C-rate at that temperature. (B) Cells from the literature that had been evaluated for lithium plating were compared. The data sources are listed in the supplementary file..... 71

Figure 2-26: Overview of Post-Mortem Analysis for Lithium-Ion Cells. A) Cell is required to be deep discharged before any further steps. B) Cell is moved to the safe or controlled environment for the opening procedure, where the controlled environment is chosen based on the study goals. Cell casing is removed. C) Cell components are separated and washed, and they are ready to be sent to the testing facilities. D) Cell components are subjected to further analysis to investigate lithium plating..... 85

Figure 2-27: In-situ Cell Design and Results of Optical Microscopy and Ex-situ SEM for Lithium Plating Morphology Characterization. (A) Schematic of the custom-made optical in-situ cell with a quartz glass window. (B) In-situ optical microscopy at a current density of 1 mA/cm² ($t = 0\text{ s} - t = 600\text{ s}$), the gap between lithium metal and separator helps in the observation of the dendrite growth until it reaches the separator. (C) In-situ optical microscopy at a current density of 1 mA/cm² ($t = 0\text{ s} - t = 795\text{ s}$), there is no gap between the separator and the lithium electrode, penetration started at ($t = 595\text{ s}$) and quickly changed to the bush like structure (Reprinted from Liu et al. [282] with permission of

American Chemical Society Publications). (D) The color of graphite is affected by the concentration of lithium X in Li_xC_6 (data adapted from Ref.[450], the random occupation of all superlattices defined as 'liquid-like' or L stage). (E) Side-view schematic of a custom-made coin-type half-cell for in-situ optical microscopy (Reprinted from Thomas-Alyea et al. [286] with permission of Electrochemical Society). (F) The MCMB electrode surface inside an in-situ optical half-cell, three different graphite colors (stages) were observed over 3 hours. Lithium Plating on an MCMB electrode was observed when a voltage (+2 mV) is applied to the current collector, although according to bulk thermodynamics, lithium metal plating should not occur unless the voltage becomes negative. The image (G) is taken 8 h before (H) (Reprinted from Harris et al. [229] with permission of Elsevier). (I) and (J) Ex-situ SEM images show the morphology of an anode surface with mossy lithium plating. The anode is charged with a high current of 10 C and then instantly dismantled in less than 5 minutes to interrupt the relaxation phase, scale bars: 20 μm and 2 μm (Reprinted from Uhlmann et al. [285] with permission of Elsevier). 92

Figure 2-28: Different Physical Characterization Approaches for Lithium Plating investigation. (A) Schematic of the in-situ SEM EC-liquid cell setup for direct observation of lithium plating, Li/Cu electrode during lithium plating for a)200 s, b)250 s, c)350 s, and d)50 s, e)270 s, f)600 s for stripping under 0.15 mA cm⁻². Scale bars: 20 μm , (Reprinted from Rong et al. [294]with permission of Advanced Materials). (B) Schematic of Li-metal nucleation on the uncoated graphite surface and coated graphite surface during high current charging, the nucleation is significantly decreased due to increased overpotential for Li-metal deposition, which was obtained by the nanoscale coating of Cu and Ni, backscatter SEM images of the deposited lithium metal on the uncoated graphite and coated graphite with Cu and Ni. Scale bar: 20 μm (Reprinted from Tallman et al. [295]with permission of American Chemical Society). (C) Schematic of in-situ TEM liquid cell for nanoscale observation of electrode-liquid electrolyte interfaces using lithium dendrite growth. Scale bars: 800 nm, (Reprinted from Zeng et al. [301]with permission of Nano Letters). (D) The stacked in-situ NMR spectroscopy for different cells at -5 °C. These spectra were measured at the fully charged state in the latest cycle. Pulse current mode: cells were cycled with pulse current (PC) mode pattern, and no lithium plating was detected. Continuous current

mode: cells were cycled with continuous current (CC) mode pattern and lithium plating observed at 265 ppm (Reprinted from Arai et al. [306] with permission of Electrochemical Society). 97

Figure 2-29: Electrochemical Methods. (A) Differential voltage over time (dV/dt) for the two discharge cases and the 5C charge relaxation event, as well as a schematic diagram of the anode's internal characteristics at the start of relaxation. During relaxation Li^+ ions that are not consumable at the separator travel and diffuse through the electric field (migration) and concentration gradient (diffusion) towards the foil, where they are intercalated into graphite (Reprinted from Yang et al. [23]4] with permission of Elsevier). (B) Differential voltage over capacity (dV/dQ) in the discharge phase because of discharge capability and a schematic diagram of the anode's internal characteristics at the start of discharge. During discharge, Li^+ ions formed by Li stripping near the separator have three destinations: they are intercalated into graphite, they travel to the cathode to deliver output current, and they move under an electrical field (migration) and a concentration gradient (diffusion) towards the foil and are intercalated along the path into graphite (Reprinted from Yang et al. [234] with permission of Elsevier). (C) Cycling data versus time extracted by a high-precision charger. A two-stage charge process is applied on pouch cells at different rates from (C/50 to 5C) at 30 °C ((a) Capacity, (b) Coulombic efficiency, (c) Coulombic inefficiency per hour) (Reprinted from Burns et al.[356] with permission of Electrochemical Society). (D) Resistance values $R_{cc} + R_{SEI}$ as a function of time for various electrolyte solutions (Reprinted from Schweikert et al. [307] with permission of Elsevier). 110

Figure 2-30: Non-Destructive Approaches for Detecting Lithium Plating. 111

CHAPTER 3

Figure 3-1: Schematic diagram of the experimental setup for the formation of a TiO layer with ULPING approach. (A). Laser parameters can be adjusted using computer-aided software (Marking Mate 2.7). (B) An example of TiO properties and specimen components derived using a combination of several characterization instruments (SEM and EDS) and specified software (ImageJ). 122

Figure 3-2: ULPING method worktable. (A) Top view. (B) Front view. 124

Figure 3-3: TiO electrode preparation. (A) Cleaned Ti sheet. (B) Oxide forming (TiO after irradiation via ULPING method. (C) The irradiation samples were punched into 6 mm circle discs using a round disc cutter. (D). TiO electrode is prepared. 126

Figure 3-4: Coin cell electrochemical analysis setup. 128

Figure 3-5: 31 fabricated electrodes via ULPING. 129

Figure 3-6: Dataset generation and preparation steps. Stage 1: data were collected from the experimental setup, including laser fabrication parameters and results of electrochemical and microscopy analysis. Stage 2: the data was pre-processed, which involved cleaning and transformation to ensure the dataset was ready for use in the ML algorithm. Stage 3: feature selection was used to finalize the dataset and select the most important features for use in the ML algorithm. Stage 4: the ML algorithms were trained on the dataset to predict the electrochemical behavior of the pseudocapacitors. 131

Figure 3-7: Data generation steps from the experimental setup. A one-of-a-kind mix-and-match testing matrix is introduced where each of the 31 prepared electrodes is individually tested against itself and the other electrodes. 133

Figure 3-8: Heatmap of a correlation matrix. The threshold is set to 0.7 and the feature above the threshold is eliminated from the dataset. 137

Figure 3-9: Multi-Layer Perceptron with one hidden layer. 142

Figure 3-10: The modeling and optimization process consist of four stages. Stage 1: involves the generation of a comprehensive dataset from the experimental setup, which includes information on laser fabrication parameters and results of electrochemical and microscopy analysis. Stage 2: the generated dataset is structured and prepared for the next stage. Stage 3: ANN is built and trained on the dataset to forecast electrochemical performance measures, such as impedance and specific areal capacitance, of pseudocapacitors. Stage 4: the trained ANN is employed in a meta-heuristic optimization algorithm to identify the optimal laser fabrication parameters. 146

Figure 3-11: (a) Schematic of lithium plating on the graphite anode electrode. The primary SEI layer (yellow color) is formed at the anode surface during the first charge of the cell to

protect the electrode. Because the primary SEI layer prevents electrons from making direct contact with the electrolyte, metallic lithium (red color) is deposited between the primary SEI layer and graphite particles. (b) Charge curve of graphite anode potential, X-axis shows the state of lithiation, and the Y-axis shows the anode potential [375]. 152

Figure 3-12: Experiment setup and data generation steps based on a physics-based model. Stage 1: data acquisition from experimental setup (CCCV charging protocol was used). Stage 2: physics-based-model parameterization (CC phase was extracted and used as input for the model). Stage 3: final dataset for use in data-driven approaches. 159

Figure 3-13: Flowchart for anode potential prediction through physics-based model (COMSOL). 160

Figure 3-14: Disassembly of an 18650 cell and internal measurements. 161

Figure 3-15: (A) Voltage comparison between model prediction and experimental data. (B) Surface temperature comparison between model prediction and experimental data. 162

Figure 3-16: A Model-based Approach for Lithium Plating Detection. 164

Figure 3-17: Anode Potential Dataset Preparation for Machine Learning Algorithms (lithium plating mitigation). 166

Figure 3-18: Illustration of pairwise relationships for the dataset features, and the diagonal plots show the distribution of features in the dataset. 170

Figure 3-19: Training and Test Data Splitting. 171

CHAPTER 4

Figure 4-1: Morphological characterization using SEM images with EDX element mapping (weight %) of 12 selected samples. The EDX analysis demonstrated the presence of Ti and O species in the samples. The samples analyzed were as follows: (A-C) S1, S2, and S3 at x500 magnification (100 μm); (D-F) F2, F4, and F5 at x500 magnification (100 μm); 187

Figure 4-2: CV curves at a scan rate of 50 mVs^{-1} . (A) S1 exhibits superior redox and capacitive capabilities compared to the other samples due to its faster oxidizing rate and the presence of 3D nanoporous structures. (B) Among the samples with different

frequencies, F2 shows better charge storage capacity compared to the other samples. (C) Increasing the power in PN-2-2 leads to an improvement in the capacitive behavior of the sample. (D) PD4 with the shorter pulse duration shows better electrochemical performance compared to the other samples..... 189

Figure 4-3: GCD Curves were generated at a constant current density of 0.25 mA cm^{-2} . (A) S1 exhibits a larger charge depletion compared to S2 and S3. (B) F2 has the longest discharge duration in the frequency samples. (C) PN2-2 shows a longer charge depletion compared to other samples. (D) The discharge time of the PD4 with the shortest pulse duration is the longest. 191

Figure 4-4: EIS Analysis. (A, D, G, J) The Nyquist plot for all the selected samples. (B, E, H, K) For each sample, a basic impedance vs frequency curve was plotted. (C, F, I, L) The Bode plot (phase angle vs frequency) was plotted for all the samples. The Nyquist and impedance versus frequency plots were used to evaluate the electrode conductivity, while the Bode plot was used to investigate the capacitance behavior and diffusion properties of the samples..... 193

Figure 4-5: Ragone Plot. The energy density and power density of the selected samples is determined based on the calculated specific areal capacitance at a current density of 0.25 mA/cm^2 194

Figure 4-6: The Electrochemical Analysis for All 496 Coin cell Setups. (A) a pie chart is presented, showing the discharge time of all tested samples with a constant current density of 0.25 mA cm^{-2} . The sample set P1-PD2 displayed the longest discharge time among all tested samples, suggesting excellent electrochemical performance. (B) a pie chart showing the specific areal capacitance for all tested samples. Once again, the sample set P1-PD2 exhibited the highest specific areal capacitance of 5.7 mF/cm^2 . (C) a bar chart indicating the impedance $|Z|$ (maximum value at the lowest frequency) for all coin cell setups. The sample set P1-PD2 displayed a low impedance of 2493.2 Ohm.cm^2 , indicating a better-conducting material compared to other tested samples. 196

Figure 4-7: Comparison between experimental values for $|Z|$ and specific areal capacitance values and predictions made using the test set. (A-B) MLP. (C-D) RF. (E-F) GPR..... 198

Figure 4-8: Morphological characterization was conducted using SEM images with EDX element mapping (weight %). The EDX data demonstrates elemental composition and presence of oxygen caused during laser irradiation. The samples analyzed were: S4 at x500 magnification (100 μm) and x3000 magnification (10 μm) (a and b, respectively); S2 at x500 magnification (100 μm) and x3000 magnification (10 μm) (c and d, respectively); OPT-SYM at x500 magnification (100 μm) and x3000 magnification (10 μm) (e and f, respectively); OPT-ASY (2) at x500 magnification (100 μm) and x3000 magnification (10 μm) (g and h, respectively); OPT-ASY(1) at x500 magnification (100 μm) and x3000 magnification (10 μm) (i and j, respectively). The EDX results are presented in images (k-o). Images (b, d, f, h, and j) were taken at x3000 magnification (10 μm) to provide a closer view of the samples..... 205

Figure 4-9: XRD analysis of electrode fabricated using the ULPING technique..... 207

Figure 4-10: (a) A survey scan of the XPS spectrum demonstrates Ti and O species. (b) Ti 2p peak (c) O 1s core levels with deconvoluted two peaks. 208

Figure 4-11: (a) The CV profile of all samples at 50 mV s^{-1} scan speed. (b) The CV curve of all samples at 500 mV s^{-1} scan rates. (c) GCD Curves were generated at a constant current density of 0.25 mA cm^{-2} , OPT-ASY exhibits a larger charge depletion compared to OPT-SYM and S2-S4. (d) Nyquist Impedance analysis of all the samples. (e) OPT-ASY demonstrates the least impedance. (f) Bode plot of sample to achieve near 80° phase angle for capacitive characteristics. These results suggest that OPT-ASY is the most promising sample with superior electrochemical behavior, demonstrated by its lower impedance and larger charge depletion in GCD. The CV and GCD curves also indicate that samples with increased surface area perform better. The Nyquist and Bode plots further support this observation, with OPT-ASY showing the least impedance and closest phase angle to the ideal capacitance phase angle. Overall, these findings suggest that optimizing surface area can lead to improved electrochemical performance in the tested samples. 211

CHAPTER 5

Figure 5-1: Comparison of the anode potential predictions on the test data (EV driving current profile -Manhattan) with the initial SOCs of 65% between the physics-based model

and linear regression, gaussian process regression, support vector regression and random forests regression.	217
Figure 5-2: Anode Potential Estimation Error on the Test Data with the initial SOC of 35%, 65%, and 85% (linear regression-blue curve, GPR-orange curve, RF-green curve, SVR-purple curve).	218
Figure 5-3: Comparison of Anode Potential Predictions on the Test Data (EV Driving Current Profiles) with the Initial SOC of 65% between Physics-Based Model and Ensemble Selection.	220
Figure 5-4: Anode Potential Estimation Error for Ensemble Selection Model and RF..	221
Figure 5-5: Anode Potential Predictions on the Test Data with the Initial SOC of 35%, 65%, and 85% Using 4 Common Regression Algorithms. REF (red curve-Physics-based model), Linear regression (green curve), Gaussian process regression (blue curve), Random forests (pink curve), and Support vector regression (yellow curve).	223
Figure 5-6: Anode Potential Predictions on the Test Data with the Initial SOC of 35%, 65%, and 85% Using Ensemble Selection Algorithm and Physics-Based Model (REF).	224

LIST OF ABBREVIATIONS

ANN	Artificial Neural Network
AFM	Atomic Force Microcopy
BMS	Battery Management System
BC	Boost Charging
CAD	Computer-Aided Design
CC-CV	Constant-Current Constant-Voltage
CE	Coulombic Efficiency
CV	Cyclic Voltammetry
CVD	Chemical Vapor Deposition
DM	Degradation Mode
DMC	Dimethyl Carbonate
DV	Differential Voltage
DP	Dynamic Programming
ECM	Equivalent-Circuit Models
ESR	Equivalent Series Resistance
EESD	Electrochemical Energy Storage Devices
EV	Electric Vehicle
EDLC	Electrostatic Double-Layer Capacitors
EDX	Energy Dispersive X-ray
EIS	Electrochemical Impedance Spectroscopy
FTIR	Fourier Transform Infrared Spectroscopy
GA	Genetic Algorithm

GHG	Global Greenhouse Gas
GCD	Galvanostatic Charge/Discharge
GPR	Gaussian process regression
HEV	Hybrid Electric Vehicle
ICE	Internal Combustion Engine
IC	Incremental Capacity
LIB	Lithium-ion Battery
LFP	Lithium Iron Phosphate
LLI	Loss of Lithium Inventory
LLM	Loss of Active Materials
LSTM	Long Short-Term Memory
ML	Machine Learning
MLP	Multilayer Perceptron
MSCC	Multistage Constant Current
MPC	Model Predictive Control
NMR	Nuclear Magnetic Resonance
OCV	Open Circuit Voltage
ODE	Ordinary differential equation
P2D	Pseudo-Two-Dimensional
PC	Pulse Charging
RE	Reference Electrode
RF	Random Forest
ROM	Reduced-Order Model

RMSE	Root Mean Squares Error
SC	Supercapacitor
SEI	Solid Electrolyte Interphase
SEM	Scanning Electron Microscopy
SA	Simulated Annealing
SOC	State of Charge
TEM	Transmission Electron Microscopy
Ti	Titanium
TiO	Titanium Oxide
T3DN	Titania 3D Nanonetworks
TM	Transition Metal
ULPING	Ultra-short Laser Pulses for In-situ Nanostructure Generation
XFC	Extreme Fast Charging
XPS	X-ray Photoelectron Spectroscopy
XRD	X-ray Powder Diffraction

Chapter 1 : Introduction

Our environment and human society are both complex systems that interact in a variety of ways [1]. These interactions might be mild at times and robust at others, resulting in unforeseen effects. Regrettably, industrial society has wreaked havoc on the environment and ecosystems that sustain us, with some of the consequences lasting more than a century [1]. Though we have made steps to address some of these challenges, new ones are arising, such as the impact of human activity on the climate, which might be disastrous if we do not respond. These problems come from how we use energy and materials, and understanding the genesis, design, scale, and consequences of our present usage patterns is crucial if we are to manage them appropriately [1].

In this thesis I go beyond the conventional environmental conversation by investigating the material life cycle chain. It aims to cut through the material life cycle chain and separate the manufacturing and product/use window from material and disposal window (see Figure 1). It explains how we can improve the design, manufacturing, and usage of resources by introducing methods for controlling product operation modes. At a broader level, the goal is to achieve sustainable development by bridging renewable energies and addressing climate change while minimizing environmental impact. Sustainable development entails meeting present needs without jeopardizing future generations' ability to meet their own. Renewable energies play a crucial role in sustainable development since they can provide energy without depleting finite resources or damaging the environment. Their use can help to reduce greenhouse gas emissions and mitigate the impacts of climate change.

Renewable energy sources, such as wind, solar, hydro, geothermal, and biomass, are increasingly being utilized worldwide as they have the potential to play a significant role in mitigating climate change. However, in ideal condition where the clean energy can be

produced, storing the energy generated from these sources remains a significant challenge due to their intermittent and location-dependent nature. Electrochemical energy storage devices (EESDs) is one of the common approaches used to store energy from renewable energy sources. EESDs include several types such as lithium-ion batteries (LiB), supercapacitors (SC), fuel cells, and redox flow batteries. Each type has its specific energy and power density, with lithium-ion batteries having high energy density and supercapacitors having high power density. Fuel cells are efficient and have a high energy density, while redox flow batteries have a high energy density and are used in grid-scale energy storage and renewable energy systems. It's worth noting that the specific energy and power density of each type of electrochemical energy storage device can vary widely depending on the specific application and design. Although EESDs operate on different principles, they share a similar configuration, where two electrodes transfer charge through the electrolyte via ion kinetics in response to an applied potential. Electrochemical processes primarily occur at the electrode, making the development of advanced electrode materials a pressing task for the advancement of these electrochemical solutions.

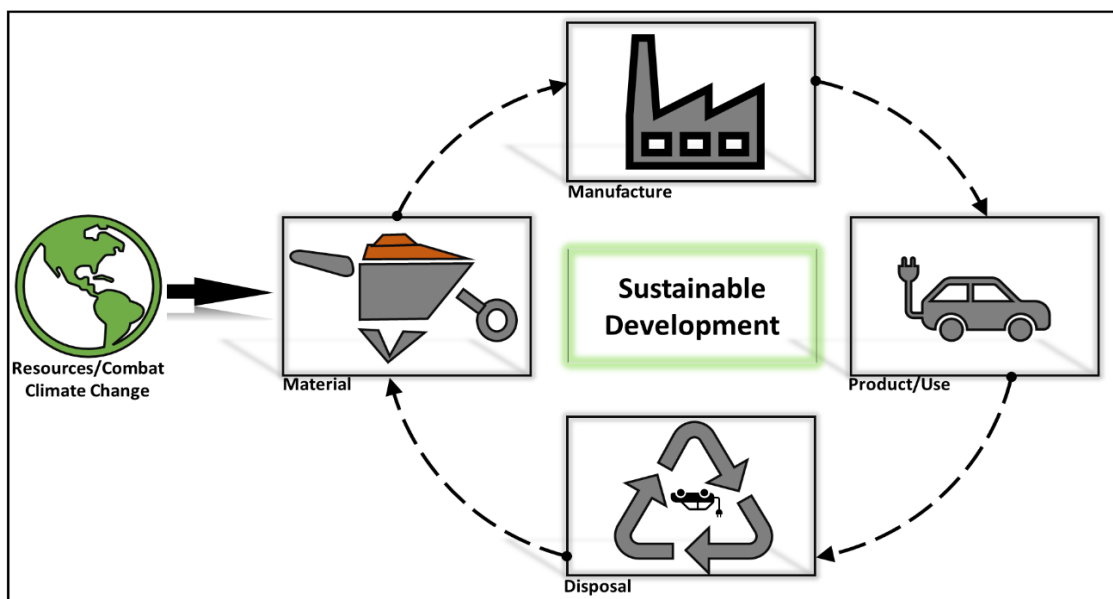


Figure 1-1: The relation between material life cycle and sustainable development [1].

1.1 Problem statement and Motivations

The development path for improved electrode materials has begun in the production of EESDs such as lithium-ion batteries and supercapacitors and centers around extending lifespan. The concept of a lifespan has its origins in biological sciences. Living organisms are born, develop, mature, age (degradation), and eventually die. EESDs, like humankind, have a finite life; we design, develop, and utilize them until they degrade and become disposal. The main distinction here is that we may design, use, or operate EESDs in a way that reduces or controls degradation and improves overall lifespan.

Indeed, degradation in EESDs can be defined as the gradual deterioration in performance over time. The degradation can be caused by various factors such as the breakdown of the electrolyte, degradation of electrode materials or damage to the device structure. The degradation mechanisms are related to the electrochemical reactions that occur during charge and discharge cycles. As the device is cycled, the reactions can lead to changes in the electrode or electrolyte materials which can result in reduced device performance such as decreased capacity, lower power output, and shorter lifespan.

Degradation management is a critical concern for EESDs since it can have a considerable impact on the device's performance and overall cost-effectiveness. When we look at the degradation issue from different perspectives, we can see several ways to mitigate degradation:

- Optimizing device design (particularly electrode),
- Using high-quality materials (transition metals (TM)),
- Improving electrolyte stability,
- Implementing effective cycling protocols,
- Monitoring and controlling degradation based on data-driven approaches.

By addressing these factors, it is possible to extend the lifespan and improve the performance of electrochemical energy storage devices.

As a result, the major motivations in this thesis can be split into two categories.

1. The primary motivation is to provide a new avenue for understanding and managing degradation in the two most common EESDs, lithium-ion batteries and supercapacitors (pseudocapacitors).
2. Another motivation for this thesis is to track the degradation of lithium-ion batteries from an operational standpoint, as well as pseudocapacitors from a manufacturing standpoint (optimal electrode design), with data-driven approaches serving as the primary tool.

1.2 Scope of Research

The degradation mechanisms in electrochemical energy storage devices can be intricate and interconnected, which poses challenges in accurately quantifying or forecasting the impact of degradation on device performance. Nevertheless, a comprehensive comprehension of these mechanisms is crucial for devising efficient approaches to alleviate degradation and prolong the lifespan of EESDs. The present research is primarily segmented into two significant parts, namely the manufacturing section and the operational section. The manufacturing section focuses on comprehending the degradation mechanism in supercapacitors, specifically pseudocapacitors, followed by the fabrication of pseudocapacitor electrodes through the ultra-short laser pulses for in-situ nanostructure generation (ULPING) technique. Subsequently, different machine learning (ML) algorithms are employed to examine the relation between laser fabrication parameters and the performance of the pseudocapacitor electrode. Finally, an optimization algorithm, simulated annealing (SA), is implemented to design an optimal pseudocapacitor electrode with improved performance and minimal degradation.

In the operational section, this research concentrates on comprehending the degradation mechanisms in lithium-ion batteries, specifically one of the most intricate degradation

mechanism, lithium plating. Subsequently, ML algorithms are implemented to forecast and manage the occurrence of lithium plating during the charging procedures. In summary, this research seeks to address the following questions for both sections,

1. How will other TMs behave as pseudocapacitor electrodes when fabricated using the ULPING method?
2. What is the impact of input laser parameters or fabrication parameters on the electrochemical behavior of the produced samples?
3. How might data-driven methodologies, notably machine learning (ML), provide insight into the relationship between fabrication parameters (structural features) and pseudocapacitor electrochemical behaviour or performance metrics?
4. How does the use of an optimization algorithm result in optimal electrode design and consequently an improvement in the electrochemical performance of the pseudocapacitor?
5. How can a data-driven anode potential estimation algorithm predict and regulate degradation (lithium plating)? Furthermore, how can it be computationally efficient and accurate enough to be suitable for online implementation?

The answers to the above questions are of utmost importance, as advanced lithium-ion batteries and supercapacitors (pseudocapacitors) are critical tools in the pursuit of sustainable development and the fight against climate change at this point in time. Therefore, understanding the behavior of transition metals as pseudocapacitor electrodes, the impact of fabrication parameters on electrochemical behavior, and the use of data-driven approaches to optimize electrode design and predict degradation are essential for developing more efficient and durable energy storage devices. Achieving these goals will facilitate the transition towards a more sustainable and environmentally conscious future.

1.3 Objectives

This research aims to achieve the following objectives:

- To understand degradation mechanisms for both lithium-ions and supercapacitors (pseudocapacitors) at electrode level.
- To generate an immense dataset for ML algorithms by fabricating numerous pseudocapacitor electrodes on Titanium sheet using ULPING.
- To theoretically bridge between the fabricated pseudocapacitors (input laser parameters) and their electrochemical performance through machine learning algorithms.
- To predict electrochemical behavior of fabricated pseudocapacitors electrode via ML.
- To design and implement an optimization algorithm to aid in identifying the optimal laser parameters for the most efficient electrode fabrication.
- To design and develop a ML algorithm based on an ensemble selection to accurately predicts the anode potential and mitigate lithium plating under various charging conditions.

1.4 Work Novelties

The research contribution for this thesis is divided into two phases, manufacturing phase and operating phase.

1.4.1 Manufacturing phase

- This thesis presents a single-step, environmentally friendly in-situ procedure for generating titanium oxide by irradiating a titanium sheet with an ultra-short pulses laser, which can be used as pseudocapacitor electrodes.

- A scalable and straightforward data generation strategy is proposed to generate a large dataset that is suitable for machine learning approaches.
- Machine learning algorithms are constructed, compared, and optimized to predict the electrochemical properties of pseudocapacitors, including impedance and specific capacitance. To the best of the authors' knowledge, this is the first time an ML approach for predicting electrochemical behavior performance has been developed and comprehensively evaluated using three distinct regression learning algorithms.
- A simulated annealing optimization algorithm is presented to maximize the objective function, which, in our case, was the specific capacitance value, and determine the most optimal laser fabrication parameters.

1.4.2 Operational Phase

- The use of an ensemble selection approach has been introduced to develop a data-driven solution for real-time anode potential estimation, with the aim of preventing lithium plating. This approach is the first of its kind to be developed for anode potential prediction.
- The proposed method relies solely on sensors to monitor battery signals such as voltage, current, and temperature, eliminating the need for an additional filter in the data generation steps. The data generation strategy is straightforward and can generate large-scale instances covering both stationary charging scenarios and EV driving profiles.
- The experimental results validate the proposed data-driven anode potential estimate model's adaptability and generalization capacity, proving its suitability for online applications with significantly improved computational efficiency.

The algorithms and methodologies developed in this thesis can be universally used for studying degradation at electrode level in lithium-ion batteries and supercapacitors (pseudocapacitors).

1.5 Thesis Outline

This thesis is structured into several chapters. Chapter 2 is divided into two sections, where the current literature about degradation in lithium-ion batteries and supercapacitors is reviewed. In chapter 3, the fabrication of pseudocapacitor electrodes using the ULPING approach is explained, followed by the use of ML algorithms to predict their electrochemical behavior performance. An optimization algorithm is then utilized to improve the performance of the pseudocapacitor electrodes while reducing degradation. The second part of chapter 3 focuses on the generation of a large dataset for predicting anode potential in LiB to mitigate lithium plating. An optimized ensemble selection method is also presented to enhance the prediction of anode potential. In chapter 4, the fabricated pseudocapacitor electrodes are analyzed and compared based on various factors such as morphological structures and electrochemical behavior performance. Chapter 5 compares the developed ensemble selection method with different ML algorithms to evaluate their performance and applicability in online applications. Finally, the last chapter provides conclusions and suggestions for future research.

Chapter 2 : Literature Reviews

2.1 Manufacturing Phase: Unwanted Degradation in Pseudocapacitors

2.1.1 Introduction

⁵For more than a century, fossil fuels — namely coal, oil, and natural gas — have been the primary source of energy, accounting for more than 80% of global energy demand [2]. However, global fossil fuel reserves are expected to become nearly inaccessible by 2050, and virtually inaccessible by the end of the twenty-first century [3]. The combustion of fossil fuels releases carbon and other greenhouse gases into the atmosphere, causing significant climate change, which is expected to continue with increased fossil fuel consumption. Nonetheless, as energy technologies advance, cleaner alternatives, such as renewable energy combined with EEDSs, offer a zero-carbon energy solution. As a result of their promising energy storage capabilities, the development of EEDSs such as batteries, electrochemical capacitors, and fuel cells has been the subject of extensive research. The primary research focus is to create the most efficient EEDSs technology capable of storing and rapidly delivering large amounts of energy. Although lithium-ion batteries have high energy densities (200 Wh Kg^{-1}), due to diffusion-limited redox reactions, they are insufficient for applications that require rapid charge and discharge within a few seconds, rather than hours. Supercapacitors are a type of electrochemical capacitor that can supplement batteries' energy storage capabilities. However, supercapacitive materials rely on the formation of electrical double layers whereby, at the material's interface with an electrolyte, an electrical double-layer capacitive material can store electrical charge in an electric double layer. This material is frequently used in energy storage

⁵ This section is based on a previously published article:

S. M, Kavian Khosravinia, and A. Kiani. "Unwanted Degradation in Pseudocapacitors: Challenges and Opportunities", (2023), Journal of The Energy Storage. The material is reproduced here with permission from the publisher, [Elsevier].

devices such as capacitors and supercapacitors. Supercapacitors ($5\text{-}30\text{ Wh Kg}^{-1}$) can store much less energy than lithium-ion batteries but charge and discharge quickly (within seconds). This begs the question of whether energy storage materials exist that can achieve both high energy density and high power density, both of which are required for practical applications. Pseudocapacitors, which provide high energy density and high power density, are a promising solution to this problem. The primary distinction between pseudocapacitors and lithium-ion batteries is that pseudocapacitive materials have charging and discharging times that range from seconds to minutes.

Pseudocapacitors have exceptional electrochemical performance, with high energy and power densities and exceptional cycle stability. The degradation of electrode materials, on the other hand, is a significant barrier to their widespread acceptance in the supercapacitor market. Several factors, including applied voltages and temperatures, initiate this degradation process, causing the electrode materials to degrade after a certain number of cycles. To address this problem, it is critical to investigate the root causes of degradation and identify practical solutions in both manufacturing and operational procedures. One promising area of study is the development of nanostructured materials with improved surface morphologies and electrode–electrolyte interactions, which can significantly improve ion-transfer kinetics and, as a result, the device's electrochemical performance and storage capacity.

2.1.2 Background

Supercapacitors are a type of electrochemical capacitor that offer high energy output while fulfilling the need for high energy and power density. There are three primary types of supercapacitors: electrostatic capacitors, pseudocapacitors, and hybrid capacitors. Electrostatic double-layer capacitors (EDLCs) rely on the interfaces between the electrodes and electrolytes to store charge electrostatically [4]. In contrast, pseudocapacitors store charge

electrochemically through the Faradaic charge mechanism, making them a potentially effective solution for energy storage with excellent performance. Pseudocapacitors bridge the gap between electrostatic capacitors, which have less energy density, and batteries, which have less power capacity and delivery. Although EDLCs lack high energy density, batteries face challenges with performance and cost, including limited lifetime, long charging times, and low charging rates [5], [6]. Pseudocapacitors offer a solution to both problems. Pseudocapacitor materials have a higher energy density than EDLCs because they have a higher capacitance due to their charge storage via surface and Faradaic mechanisms (reversible redox reactions). Faradaic processes have relatively slow kinetics and pseudocapacitive materials may have lower power density than EDLCs, but they outperform EDLCs in terms of energy storage capacity and performance. Pseudocapacitors are a promising compromise between batteries' high energy density and supercapacitors' high power density (Figure 2-1 (a)). Figure 2-1 (b) depicts a general overview of a pseudocapacitor and its operation. A pseudocapacitor is made up of two redox-active electrode materials that are separated by an electrolyte. Electron transfer between the electrode and electrolyte via redox reactions, ion adsorption (underpotential), and intercalation processes store the charge, which is referred to as pseudocapacitance.

Pseudocapacitors are devices that utilize electrochemical active materials such as conducting polymers and transition metal oxides to store electrical energy. The transfer of electrons in these materials occurs through Faradaic reactions [6]. Pseudocapacitance, which is the transfer of ions between the electrode and the electrolyte, is the principle underlying the operation of pseudocapacitors. The adsorption of ions and the Faradaic reactions contribute to pseudocapacitance [7]. The electrochemical combination of these factors helps to store energy, as the molecules formed on the electrode surface due to electrochemically induced pseudocapacitance have potential. Since the capacitance is not constant, it is referred to as

pseudocapacitance [8]. Pseudocapacitors store electrical energy by the Faradaic charge-transfer reaction of specifically adsorbed and de-solvated ions, which results from electro-sorption, redox reactions, and intercalation occurring on the electrode surface. Although there is some contribution from static electric double-layer capacitance, it is insignificant [4], [5].

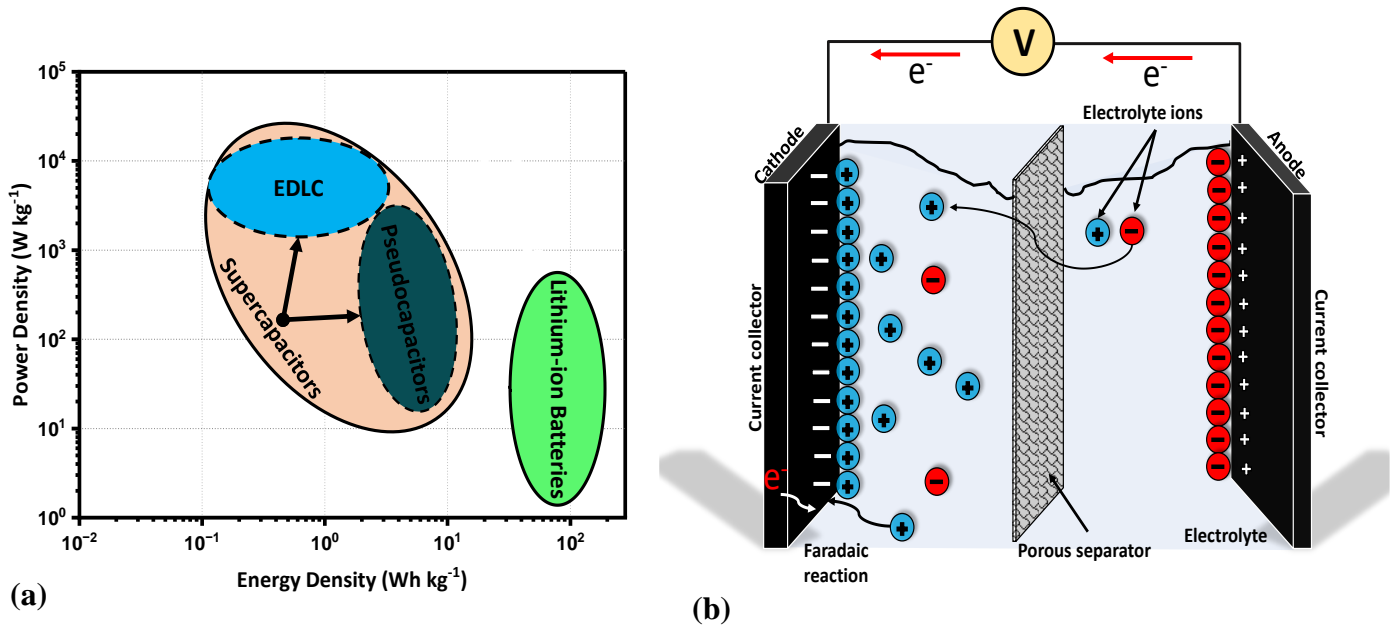


Figure 2-1: (a) Sketch of Ragone plot to compare different types of energy storage devices (b) A typical diagram of a pseudocapacitor.

In pseudocapacitors, the Faradaic reactions are rapid and reversible, and they are accompanied by reactions with Li^+ or Na^+ ions, which compensate for the lack of formation or breaking of chemical bonds during the reaction [9]. Table 2-1 shows the three main factors of the working principle of the pseudocapacitor: Faradaic charge, electrode surface area, and potential change (electrochemical potential window). The rate of ion kinetics and accessibility over a suitable range of potential is determined by these three factors. Faradaic charge pertains to the transfer of charge that transpires during a redox reaction. Such charge transfer is required for the electrochemical reaction to occur. The rate of charge transfer is influenced by several factors, including electrolyte concentration, electrode surface area, and applied potential. A larger surface area provides more sites for electrochemical reactions, increasing the rate of charge

transfer and improving overall system performance. Furthermore, potential change, or the difference in electrochemical potential between the electrode and the electrolyte, is important in determining the rate of electrochemical reactions. Changes in potential can affect the rate of charge transfer and define the potential window, which is the range of potential within which the electrochemical reaction can occur without causing unwanted side reactions.

These factors can be optimized to achieve high performance and stability in the electrochemical systems, which slow down the rate of degradation. Pseudocapacitors are classified into three types: underpotential deposition, redox, and intercalation. The adsorption of ions, specifically cations, on the surface of a metal electrode with a higher redox potential generates the pseudocapacitance of an underpotential deposition pseudocapacitor [10]. This process involves a partial charge transfer between the ions and the electrode, which is known as "electrosorption valency" in principle. Metal monolayers such as copper and gold, as well as metal oxides such as ruthenium oxide (RuO_2) [11], [12] and iridium oxide (IrO_2) [13], are examples of typical underpotential pseudocapacitive materials. To achieve advanced adsorption pseudocapacitance, two factors are critical: a high electrolyte anion surface area, which provides more active adsorption sites, and a high electrosorption valence, which leads to a greater charge transfer between the electrolyte anion and the electrode [14], [15]

In the case of a redox pseudocapacitor, the pseudocapacitance occurs near the electrode surface, where the cations and anions are adsorbed/desorbed to store energy [16]. A large proportion of pseudocapacitance is caused by surface redox reactions, in which only a thin layer of the electrode surface participates in Faradaic processes. Faradaic redox pseudocapacitance occurs only at the material's surface, and the electrolyte ions never enter the bulk of the electrode.

Table 2-1. The relation of the three main factors of a pseudocapacitor.

Factors	Relation	Reasons
Faradaic charge	Directly	If the amount of charge transferred is high between the electrode and electrolyte; it benefits the Faradaic charge transfer mechanism.
Electrode surface area	Directly	The larger the area of the electrode, the more ions can access it.
Potential change	Inversely	The less potential applied enhances the pseudocapacitance.

Rapid and reversible redox reactions between the electro-active species on the electrode surface and the electrolyte characterize these pseudocapacitive phenomena. For example, during the process of potential cycling, redox reactions involving the 2p, 3p, and 4p oxidation states in RuO₂ were observed [11], [12], [17], [18]. These reactions, combined with proton transfer, give rise to pseudocapacitance. Among the most used active materials in these electrode systems are RuO₂ [12], manganese oxide (MnO₂) [19], electrically conducting polymers such as polyaniline (PANi) [20], and oxygen- and nitrogen-containing surface functional groups [21].

In intercalation pseudocapacitors, the intercalation pseudocapacitance arises when electrolyte cations such as Na⁺, Li⁺, and H⁺ are intercalated or deintercalated into or from the layers, tunnels, or channels of the electrode materials. This process is accompanied by Faradaic charge transfer without any significant crystallographic or phase change [22]. For intercalation pseudocapacitance to occur, a crystal structure that can provide a two-dimensional (2D) ion diffusion channel that is both fast and stable must be present. This is required to avoid structural phase transitions during the ion intercalation process. Ions occupy tunnels or vacancy positions within the bulk of materials during intercalation [23], [24].

This process is extremely fast and more closely resembles the electrode reaction of a supercapacitor than that of a battery. RuO₂ [12], MnO₂ [19], titanium dioxide (B-TiO₂), and niobium oxide (Nb₂O₅) [25] are some of the most well-known intercalation pseudocapacitive electrode materials. Figure 2-2 illustrates the three types of pseudocapacitors and their respective principles. Further information on recent advances in the types of pseudocapacitors can be found in comprehensive reviews [26]–[29].

In an electrochemical capacitor, the pseudocapacitor is a crucial component that combines with the EDLC to form a supercapacitor. However, pseudocapacitive materials have a significant drawback in that they exhibit high resistance to ion/electron transfer, which results in low cyclability, low capacity, and, consequently, low power density. This is primarily due to their low conductivity and structural degradation during cycling [30]–[32]. The low conductivity of many pseudocapacitive materials increases the resistance of the electrode material and reduces the rate of charge/discharge processes, which can limit the power density of pseudocapacitor devices. Another limitation is their energy density, when compared with batteries. The relatively narrow operating voltage window of most pseudocapacitive materials limits the device's energy density. As a result, the degradation of the pseudocapacitor is the main reason for its limited applications in various sectors. Unlike other supercapacitors, the degradation of pseudocapacitors is primarily caused by chemical reactions that occur under operating conditions [33]. During cycling, irreversible components accumulate, leading to the development of cracks in the structure and the formation of an unstable solid electrolyte interphase (SEI) layer.

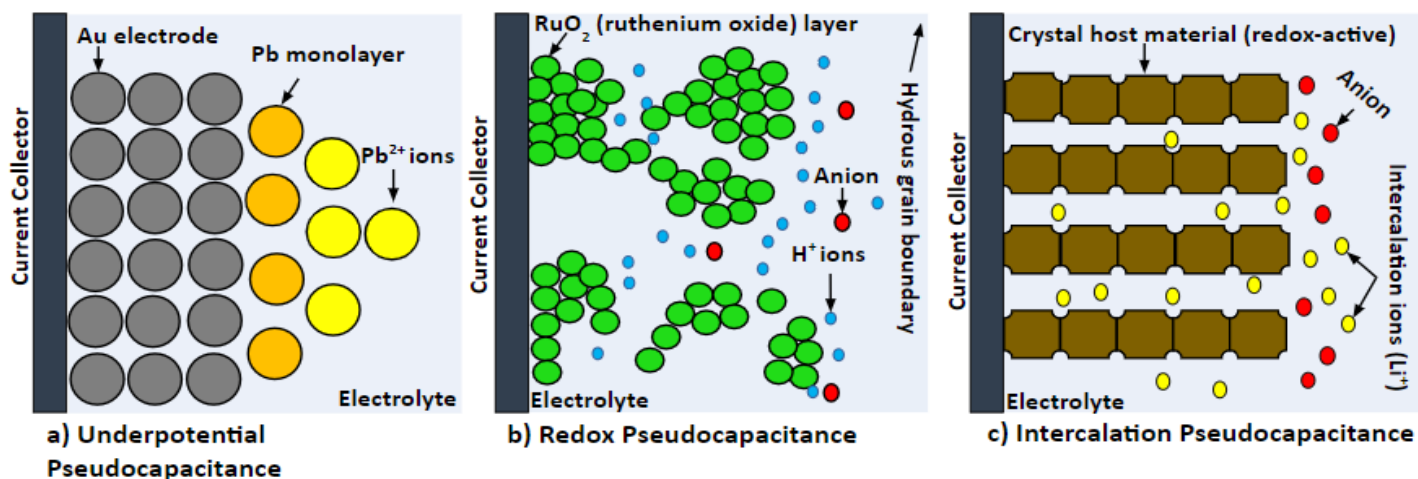


Figure 2-2: Pseudocapacitor working principles. (a) Underpotential pseudocapacitor where lead (Pb) is deposited on the gold (Au) electrode, forming an adsorbed monolayer. The working principle is electrosorption, which is potentially induced adsorption on the surface of the active electrode material [35], [36]. (b) Redox pseudocapacitor where ions from the electrolyte are electrochemically adsorbed onto the surface or near the surface of RuO₂ accompanied by Faradaic charge transfer. The principle is a redox transfer mechanism in which a chemical reaction takes place between an oxidizing substance/substrate and a reducing substance/substrate. (c) Intercalation pseudocapacitance where ions like lithium are intercalated or inserted into the layers of the electrode material. The working principle is the intercalation of ions of molecules into layers of a material or a substrate [37], [38].

The SEI layer is typically composed of a thin film of various organic and inorganic compounds formed due to electrochemical reactions that occur at the electrode surface during device charging and discharging. Overall degradation is attributed to the degradation of the electrolyte via electrolyte parasitic processes and the degradation of the electrode due to precipitate formation. Table 2-2 shows the common advantages and disadvantages of pseudocapacitors (including all three types) which helps in deciding the factors to be focused on for its applications [34]. The table concludes that improving the kinetics of redox reactions as well as optimizing the morphology and composition of pseudocapacitive materials may lead to the development of high-performance pseudocapacitive materials with high energy and power density values.

Table 2-2. Common advantages and disadvantages of all types of pseudocapacitors.

Advantages	Disadvantages
No crystallographic change (Intercalation)	Electrode materials might suffer from high resistance to ion/electron transfer
Dependence on particle size and morphology (redox and intercalation)	Specific crystalline materials with specific structures are needed for fast ion transport pathway
Ions occupy vacancy positions inside the bulk of the materials (intercalation)	Ideal electrolytes are required (e.g., potassium hydroxide [KOH])
Potentially more stable than supercapacitors and batteries	Irreversible electrode reaction leads to pseudocapacitor degradation
High-rate capability (redox and intercalation)	Transport pathways may get blocked due to degradation
High specific capacitance (underpotential and redox)	Low cyclic stability
High energy density (Intercalation)	Inferior power density

2.1.3 Degradation mechanisms of pseudocapacitors

The fundamental downside of using pseudocapacitors in real life is degradation in all forms of pseudocapacitors, including intercalation, redox, and underpotential pseudocapacitors. The ability of a capacitor to store and release energy determines its worth in industrial applications. The better they have ease of production, low cost, and slow degradation rates, the better they can perform for real-life appliances for an extended period of life. Figure 2-3 outlines all the primary factors for the degradation mechanism in a pseudocapacitor at all levels (microstructure, electrode, cell, and application), as well as the various types of degradation mechanisms that are observed or caused as a result. At the microstructural level, the irregular morphology of the microstructures and the presence of cracks makes the structure unstable. Furthermore, blocked pores result in a less effective Faradaic transfer mechanism, which may result in the decomposition of the ions present in the active electrode. Moving on to the electrode level, chemical products are formed on the surface of the electrode material due to cracks and pore blockage. A weak SEI layer results from further ion decomposition in the electrolyte and electrode degradation. The significance of SEI film in diffusion kinetics is

highly important as it acts as a protective passivation layer of high ionic conductivity and low electrical conductivity. A weak SEI layer leads to low cyclic stability as it affects the rate of intercalation of ions through it. As a direct consequence of the weak SEI layer and slow ion-transfer kinetics, at the cell level, the pseudocapacitor has limited rate capability with compromised energy density [39]–[43]. Furthermore, novel materials for the electrode are limited, which makes the manufacturing cost quite high. At the application level, aerospace (in airplanes or satellites), electronics (semiconductors and electronic devices), renewable energy devices (e.g., solar cells, wind power, thermal energy), and research and development are areas where pseudocapacitors have the potential to revolutionize. Figure 2-4 depicts a step-by-step breakdown of degradation mechanisms and effects, beginning with the microstructure and progressing to application-specific scenarios. Degradation is important in pseudocapacitors, and different factors of the degradation mechanisms (such as underpotential factors, redox factors, and intercalation factors) are showcased in the same figure. Figure 2-4 also showcases how Pseudocapacitors deteriorate via a variety of reaction pathway, including phase transformation (microstructure), surface oxidation, electrolyte decomposition, structural degradation of the electrode material, and irreversible chemical reactions. These pathways can lead to a decrease in active surface area, an increase in resistance, and a decrease in capacitance over time, resulting in decreased performance and failure of the pseudocapacitor. We have divided the degradation mechanism into three major categories in the following subsections: the electrode level (3.1), the microstructural level (3.2), and the operating conditions (3.3), with detailed subsections in between.

2.1.3.1 Degradation mechanism in pseudocapacitor at the electrode level

The degradation of the pseudocapacitor happens as a result of several events that take place during cycling (gravimetric charging/discharging) [44]. Degradation relates to the electrochemical performance of the device and electrochemical performance depends on the type of electrolyte and the physical and chemical properties of the electrode material. Generally, metal oxide electrodes are used as redox, intercalation, or hybrid-type materials (a battery-type electrode and a double-layer capacitor-type electrode are used in hybrid electrochemical supercapacitors) for pseudocapacitors [45]. These electrodes usually have low conductivity and a slow ion diffusion process, which leads to the deterioration in the rate capability and cycle stability and, thereby, degradation of the material and the device [34].

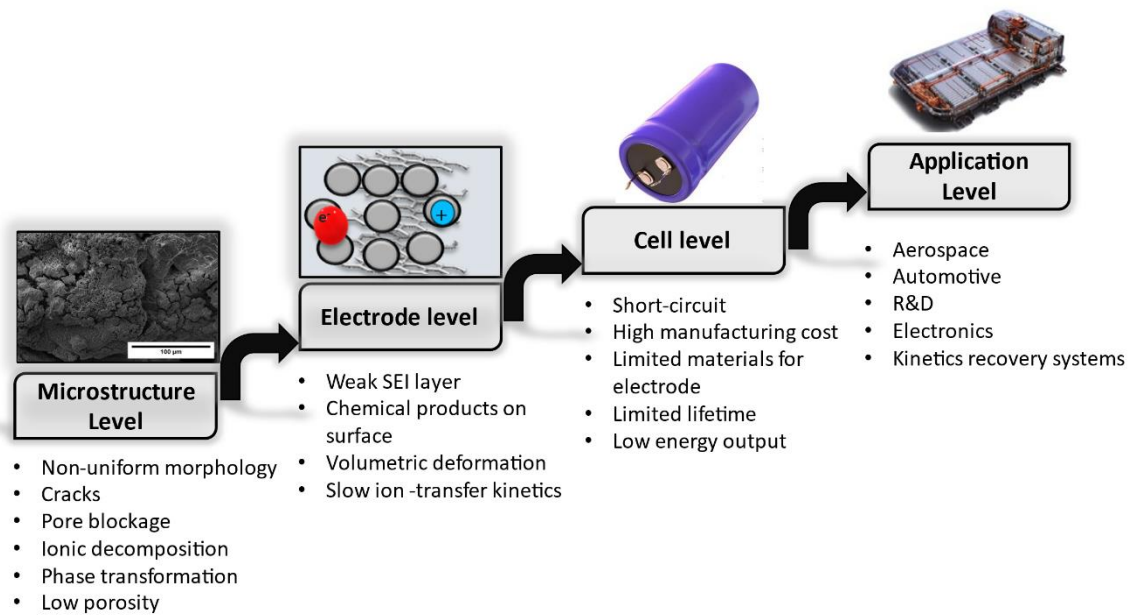


Figure 2-3: Main findings or observations for degradation mechanisms at several levels ranging from microstructure to electrode, the electrode to the device, and device to applications in various sectors/industries.

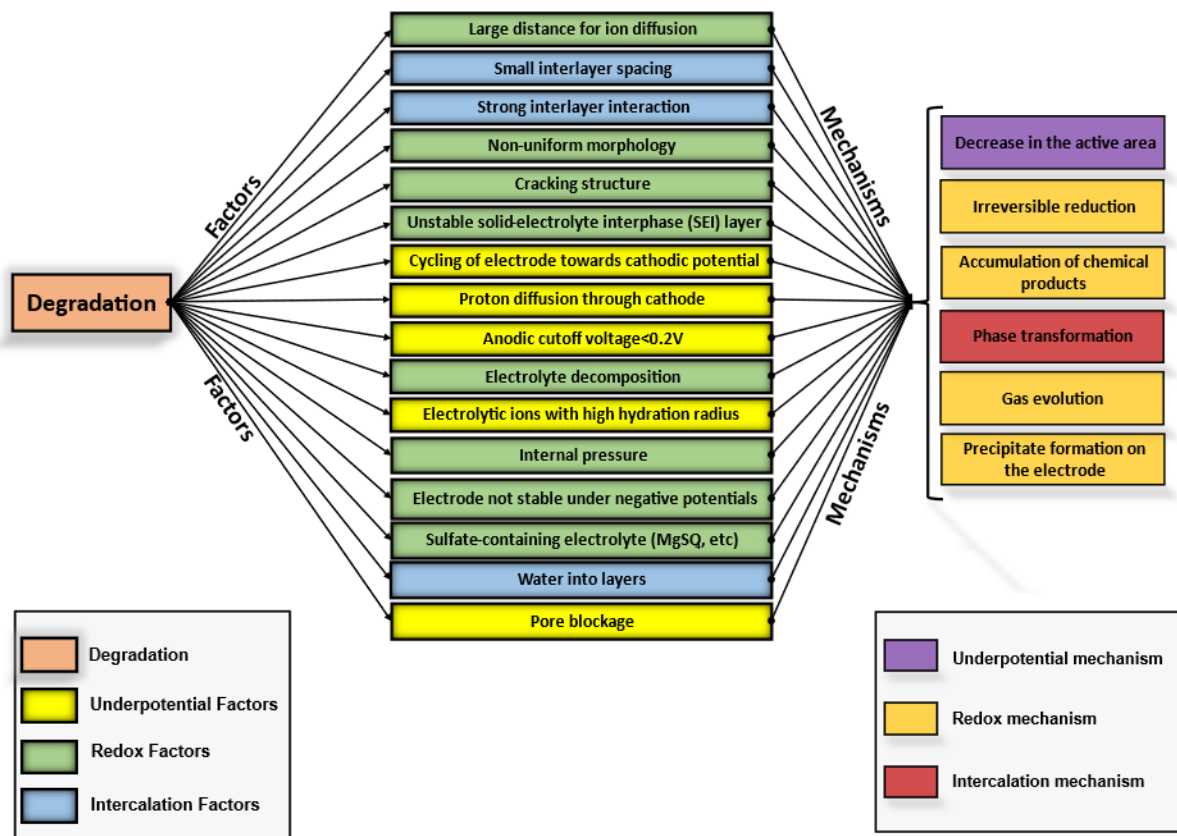


Figure 2-4: Degradation occurs due to many factors that take place in the electrolyte and electrode, and to external factors such as kinetics, potential, and temperature. All of these factors lead to different degradation mechanisms through which we can identify the deterioration of the device happening in real time during the experiment.

2.1.3.2 Electrode material degradation

The manufacturing process of the electrode material is the first and most important factor that decides the rate of degradation [46]. For instance, in the case of intercalation pseudocapacitive materials, having a small interlayer spacing and strong interlayer interaction in the electrode decreases the ion diffusion process. As a result, the charge/discharge rate is slower, and the capacitance value is lower. This is because the narrow interlayer spacing creates a higher energy barrier for ion diffusion, while the strong interlayer interaction prevents ion movement. In the case of redox pseudocapacitive materials, having a large distance for the transfer of ions/electrons through the tunnels/layer results in a decrease in the active area. The decrease in

the active area is due to the increase in the resistance of charge kinetics [34]. In redox electrode materials, ion diffusion is primarily determined by the size and morphology of the electrode particles; interlayer spacing, or interaction have no significant effect on the diffusion process. Finally, in the case of adsorption-based materials, such as activated carbon or monolayer metals, the charge is stored via reversible ion adsorption on the electrode material's surface. The pore structure and surface area of the electrode material have a large influence on the ion diffusion process. To understand electrode degradation, Wang X and colleagues identified two primary factors contributing to the breakdown of nickel oxide (NiO) electrodes, namely self-discharge, which resulted in partial dissolution of NiO, and the impact of oxygen bubbles [47]. The degradation of the pseudocapacitive performance of the Ni (II)/Ni (III) couple was found to occur gradually due to the NiO/Ni(OH)₂ Faradaic process. During cycling, oxygen evolution took place, leading to the formation of oxygen bubbles that struck the electrode film and further accelerated the rate of electrode degradation. Figure 2-5 (a) depicts the degradation process in a NiO film electrode [47]. Aside from the manufacturing process, material selection is an important factor in ion-transfer kinetics. Non-crystalline and amorphous materials, for example, do not easily support the ion transport process [48]. Because the properties of the electrode's active materials are important for the charge storage mechanism in pseudocapacitors, improving and enhancing the electrode surfaces or the current collector is required for future considerations. Binder-free electrodes and novel current collectors have recently been investigated for their effects on slowing the degradation process [34]. Another important factor could be buffer layer formation on the electrode as it helps to control the volume expansion and shrinkage of active materials during gravimetric charging and discharging, respectively [49]. Acknowledging that it may provide adequate interspace between layers of electrode active materials, the nanostructural design of the electrode surface

with strong buffer-layer compatibility may necessitate further research. As a result, the active area and ion accessibility of these surfaces increase, which improves the charge storage mechanism.

2.1.3.3 Electrolyte degradation

During cycling, over a range of potentials applied over a specific or varying temperature, it was found that the electrolyte volume shrinks and leads to the decomposition of the ions, which slows down the process of adsorption of ions from the electrolyte on the electrode surface [50]–[52]. It was previously assumed that the irreversible reduction caused by the chemical reactions was not a problem, but more recently, with the aid of sophisticated microstructural analysis techniques (characterization tools), it has been observed that the structure changes quite gradually and that many chemical products are formed [53]–[55]. Therefore, these factors/mechanisms lead to further deterioration of the electrode–electrolyte interphase and reduces the electrochemical performance of the cell. To gain a better understanding of electrolyte degradation, Hashem and colleagues investigated the electrochemical performance of nanorod-like particles composed of Sn-doped α -MnO₂ [56].

Figure 2-5 (b) shows the specific discharge capacities by cycle number for P-MnO₂ and Sn-MnO₂ electrodes. The specific capacity for the Sn-doped MnO₂ is 80 mAh g⁻¹ at the 40th cycle, compared with 65 mAh g⁻¹ at the 40th cycle for a pristine MnO₂ electrode. One of the main reasons for the electrochemical degradation of MnO₂ is the generation of Mn³⁺ during the redox process and the reduction of Mn²⁺ ions, which dissolve in the electrolyte and lead to electrolytic decomposition [56]–[58].

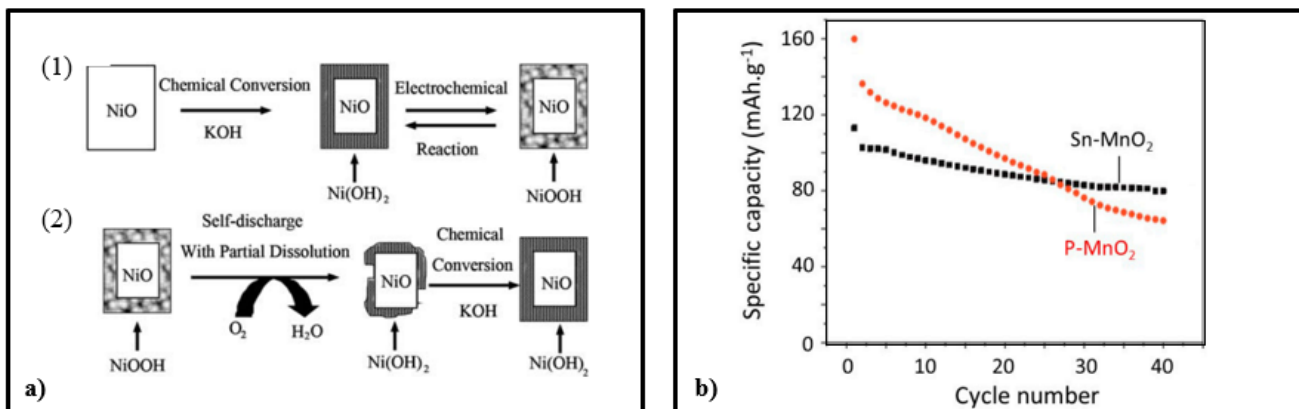


Figure 2-5: (a) Degradation mechanism of the NiO film, which is used as a redox pseudocapacitive electrode. Reprinted with permission from [47]. (b) P-MnO₂ and Sn-doped MnO₂ discharge capacity vs. cycle number at C/15 rate in the voltage range 1.5-4.0 V vs. Li⁺/Li⁰. The electrolyte used for this pseudocapacitor is 1 mol L⁻¹ LiPF₆ in ethylene carbonate-dimethyl carbonate (1:2), which is an organic electrolyte. Reprinted with permission from [56].

2.1.3.4 Separator

Although significant progress has been made in improving the performance of pseudocapacitor electrodes, research into developing properly engineered separators has been limited. Poorly designed separators can cause additional resistance within the pseudocapacitor, which can potentially lead to short circuits. The separator must be non-porous. Less capacity retention may also lead to slow ion diffusion between the electrolyte and the electrolyte. Non-conductivity, electrolyte ion permeability with minimal ionic resistance, chemical and mechanical resistance, and ease of wetting by electrolytes should all be considered when selecting appropriate separators for pseudocapacitors. In pseudocapacitor development, separators made of highly porous films or membranes — such as cellulose, polymer membranes, and glass fibers — are commonly used [4], [59]. The materials used in separators are determined by the type of electrode, working temperature, and pseudocapacitor voltage. Although cellulose separators work well in organic solvents, they may degrade in a sulfuric acid (H₂SO₄) electrolyte [59], [60]. The ionic conductivity of the electrolyte in the separator

can also influence pseudocapacitor performance by changing the internal resistance (equivalent series resistance [ESR]), especially when viscous electrolytes (e.g., ionic liquids) are used [59], [61].

2.1.4 Degradation mechanism in pseudocapacitors at the microstructure level

The chemical or side reactions during cycling in a pseudocapacitor lower the energy efficiency or may lead to an increase in the self-discharge rate [62]. An unstable electrolyte–electrode surface interaction results in microscopic cracks, chemical products on the grain boundaries, and pore blockage due to side reactions. This is mostly caused by various structures that were created because of various compositions at the microstructural level. This unstable interaction causes the electrode to degrade and results in an overall irreversible decrease (no discernible cyclic voltammogram). Therefore, to estimate the performance and cycle stability of the pseudocapacitor, the degradation mechanism at the microstructural level should be considered.

2.1.4.1 Electrode–interface degradation

Non-uniform morphology in the structure of the electrode material — such as dissimilar spacing and random spacing between layers — may lead to an overall cracking structure when cations from the electrolyte intercalate into the layers of the material of the electrode [51], [55], [63]. The cycling of the electrode toward cathodic potential, combined with proton diffusion toward the cathode, leads to the accumulation of chemical products on the electrode surface [64], [65]. This occurs because of chemical reactions occurring in real time during the process, and as a result, phase transformation occurs with microstructural changes when the sample is examined post-experiment [66], [67].

The electrode surface is covered with insulating materials, and this further prevents close contact between the electrode surface and the electrolyte. Even though ion intercalation is an effective method, it will not be able to progress due to blocked pathways and pore blockage in the microstructure of the electrode material [68]–[70]. Figure 2-6 shows the blockage of pores accompanied by blocked pathways, the formation of chemical products on or near the electrode surface, and the formation of cracks, leading to unstable SEI. This phenomenon causes the degradation rate in the pseudocapacitor to increase much faster.

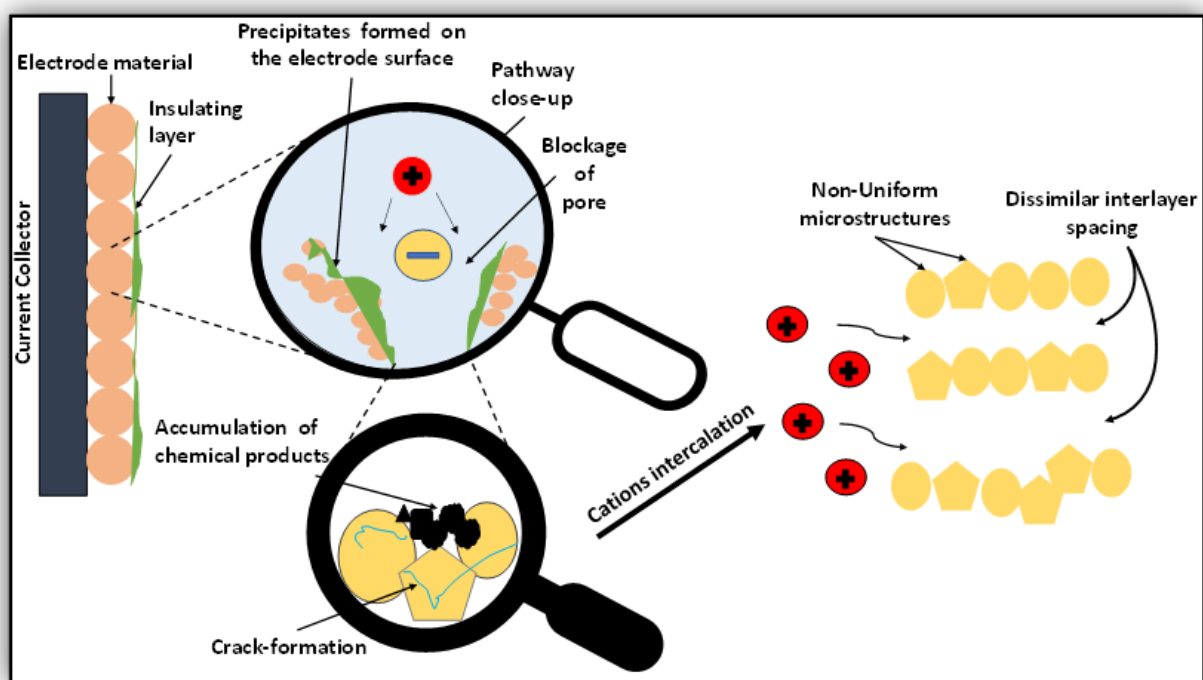


Figure 2-6: Cracks in the microstructure because of irreversible reduction and chemical products formed during cycling. Low ion-transfer kinetics are caused by dissimilar interlayer spacing and non-uniform morphology. No intercalation or redox transfer occurs because of the formation of pore blockages and obstruction of the ion/electron transfer pathway (post-precipitation).

Dubat and colleagues synthesized copper oxide (CuO) nanosheets using hexamethyltetramine (HMT) as a complexing agent, and the resulting Cu:HMT electrode was examined by scanning (SEM) and transmission (TEM) electron microscopy [71], [72]. Figure 2-7 shows the SEM and TEM images of the Cu:HMT electrode after cycling. The SEM

image (see Figure 2-7 (a)) revealed that the CuO thin films were uniformly distributed but had cracks due to the varying sizes of micro-woolens, which are related to the thickness of the Cu:HMT films. The nanosheets aggregated to form hierarchical, multilayer nanosheet clusters with a well-developed porous structure, resulting in a uniform morphology, as shown by the TEM image (see Figure 2-7 (b)).

The porous nanosheets were discovered to have a surface area of $81 \text{ m}^2 \text{ g}^{-1}$ and a pore volume of $0.20 \text{ cm}^3 \text{ g}^{-1}$ [71]. This morphology, with large pore channels (micro- and meso-pores), allowed for faster electrolyte transport and more active sites (increased surface area) for chemical reactions [71]–[76]. The interlayer and intralayer structures were found to be crucial for the porosity of the nanosheets, emphasizing the importance of the microstructure in preventing electrode deterioration and influencing the electrochemical properties of the CuO electrode [71], [77], [78].

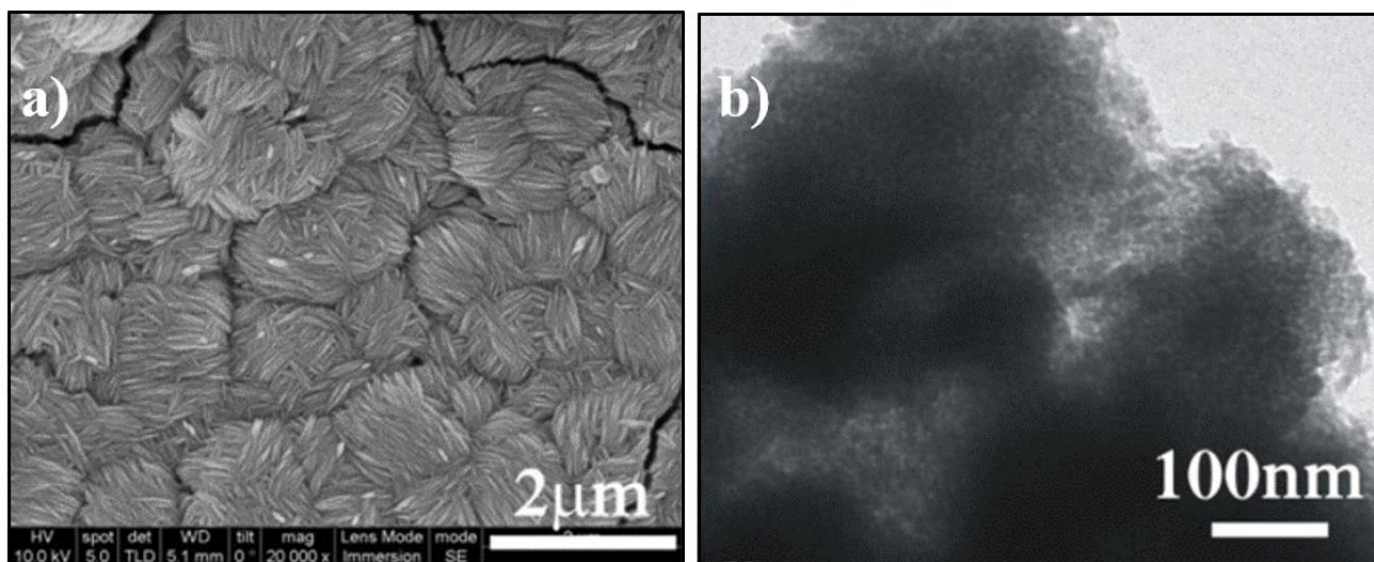


Figure 2-7: Morphology of the CuO electrodes synthesized from a Cu:HMT complexing agent after 5000 cycles in 1 M Na_2SO_4 electrolyte. (a) SEM image of the electrode, showing cracks. (b) TEM image of the electrode, showing uniform morphology with good porosity. Reprinted with permission from [71].

2.1.4.2 Electrolyte degradation and its consequences on the resulting microstructure of SEI

The degradation of electrolytes through volume shrinkage and precipitation formation on the electrode causes an unstable SEI layer. This causes the electrolytic ions to get into layers with water, and a tremendous number of gaseous products evolve during cycling as the internal pressure in the layers is increased due to the evolution of gas, which blocks the layers/tunnels for further intercalation/de-intercalation [79], [80].

Further volumetric deformation of pseudocapacitive electrode materials results in small internal stresses and cracking of the protective layer. Although volumetric deformation (swelling/expansion) is a relatively insignificant process if no energy is lost or wasted, this could result in the aggregation of such structures during long-term cycling, resulting in a large structure that annihilates the overall microstructural integrity of the active material [81].

The importance of electrolyte structure in pseudocapacitive energy storage devices was investigated by Dubal and colleagues [71]. They employed a CuO electrode with Cu:HMT in a 1 M neutral, aqueous sodium sulphate (Na_2SO_4) electrolyte. The electrode was created with interspaces between nanosheets and woolen-shaped nanostructures to let the electrolyte volume expand. The ionic resistance was reduced and electrolyte entry into the electrode matrix was facilitated by porous channels, excellent porosity, and a large ion accessible area [71], [73], [74], [76].

A high specific capacitance of 346 Fg^{-1} and increased overall stability of the supercapacitor were made possible by the ions' stability in the electrolytic microstructure. Only a small number of gaseous compounds were produced while cycling process but these were not significant to cause degradation over a large number of cycles [72]. Two mechanisms of using aqueous electrolytes can be used to explain the reduced degradation: (1) the intercalation and de-

intercalation of smaller H⁺ or alkali metal cations like Na⁺ in the electrode material's matrix during the redox reaction, and (2) the adsorption of H⁺ and Na⁺ ions on the electrode surface, as opposed to the electrode material's interior bulk. The reaction is shown as:



where A is either H⁺ or Na⁺ ions [71], [72], [82].

Overall, this study emphasizes the importance of electrolyte structure in pseudocapacitive energy storage systems and offers suggestions for enhancing their functionality and stability.

2.1.4.3 Separator

The influence of separator performance in ion kinetics in pseudocapacitors can be attributed to their low cost and high porosity (>80%) [4], [62]. Furthermore, the separator's chemical composition, thickness, pore size distribution, and surface morphology have a significant impact on performance indicators such as polarizability limits, ESR, specific capacitance, specific energy, and power densities [83]. For example, having a thick separator produces high internal resistance and stresses, and increases the manufacturing cost. Recently, polymer separators have been used extensively as they have good flexibility and high porosity, and are low cost to produce. Based on their microstructure, polymer separators are classified into two types: fibrous networks and monolithic networks with defined pores [4]. Figure 2-8 shows the types of the polymer separators. Graphene oxide (GO) films are also promising separators, as demonstrated in a study by Shulga and colleagues [4], [59], [84]. After being penetrated with an H₂SO₄ electrolyte, the separator exhibits proton conductivity.

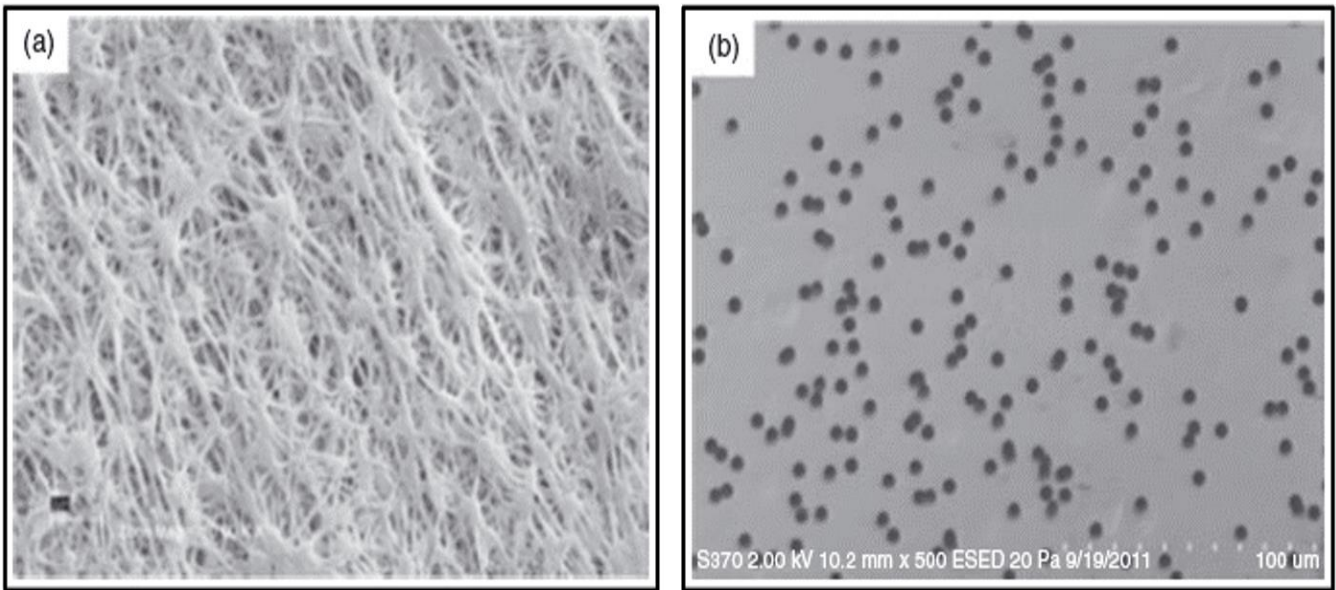


Figure 2-8: SEM images of (a) A fibrous Millipore JVWP separator. (b) a monolithic/defined GE Osmotics K50CP01300 separator. Reprinted with permission from [85].

2.1.5 Degradation mechanism through electrochemical and kinetic analysis

Capacity retention is the amount of ability of a battery or a capacitor to retain the stored energy during an extended open-circuit rest time, and depends on rest time, the temperature of the cell during the rest period/time, and the preceding history of the cell. This demonstrates how crucial capacity retention is in predicting cell electrochemical performance, and having an electrode material that works optimally is defined by the end life of the pseudocapacitor when capacity retention is less than 80% and/or the internal resistance of the cell is doubled [86]. Another aspect of this factor is Coulombic efficiency, which is the ratio of the discharge capacity and the charge capacity after a full charge over a cycle; it is also known as Faradaic efficiency, the efficiency with which the electrons (charge) are transferred in capacitors/batteries [87] A Coulombic efficiency ratio of the cathodic and anodic capacity of 100% is expected for no loss of electrons due to electrolyte parasitic reactions [50]. Pseudocapacitors have kinetic

limitations, as well as a limited potential range, depending on the type of electrode material used [88].

An increased electrochemical potential window and current density with a large number of cycles lead to a smaller number of oxygen vacancies in the active material. The number of oxygen vacancies also plays an important role in the performance of storing and releasing charges [89]. When the potential on which the device is operated exceeds the potential optimal of the electrolyte itself, the evolution of gas takes place in the form of oxygen and hydrogen gas. The gas molecules evolve on the electrode surface and get into the interlayers, blocking the further redox reaction and by doing so, degrading the electrode surface by delamination of active materials from the substrate. Delamination leads to more interspace between the layers of the active material layers and, hence, creates a pinning effect, which indicates more internal resistance. As a result, corrosion of the current collector and the electrode surface takes place [81], [90], [91] and storage capacity is limited.

2.1.5.1 Potential range or potential window

The voltage range or operating charge/discharge rate specified for cycling is an important factor that decides the mechanism of gas evolution in the form of H₂ or O₂ gas molecules. The potential range within a high potential scan rate range enhances the specific capacitance, but at the same time, impacts the reversibility of the reaction. Excess gas evolution that occurs when the potential window is increased results in a rapid degradation rate during cycling [7], [92]–[94]. As the potential window is expanded, the reversible charge and discharge rate of pseudocapacitors decreases, resulting in a decrease in capacity retention and Coulombic efficiency. This implies that the potential window must be carefully considered in the design and optimization of pseudocapacitors for various applications, as an increase in potential

window can compromise their overall performance [57], [95]. Furthermore, high temperature and kinetic constraints have a direct effect on irreversible pseudocapacitive behavior.

2.1.5.2 Current density

An increase in current density can result in a decrease in both specific capacitance and Coulombic efficiency of Pseudocapacitors [57]. This can result in a variety of changes or variations in Coulombic efficiency and specific capacitance, ultimately resulting in a decrease in storage capacity and stability of the pseudocapacitors. As a result, when designing and optimising pseudocapacitors for specific applications, it is critical to carefully consider the impact of current density.

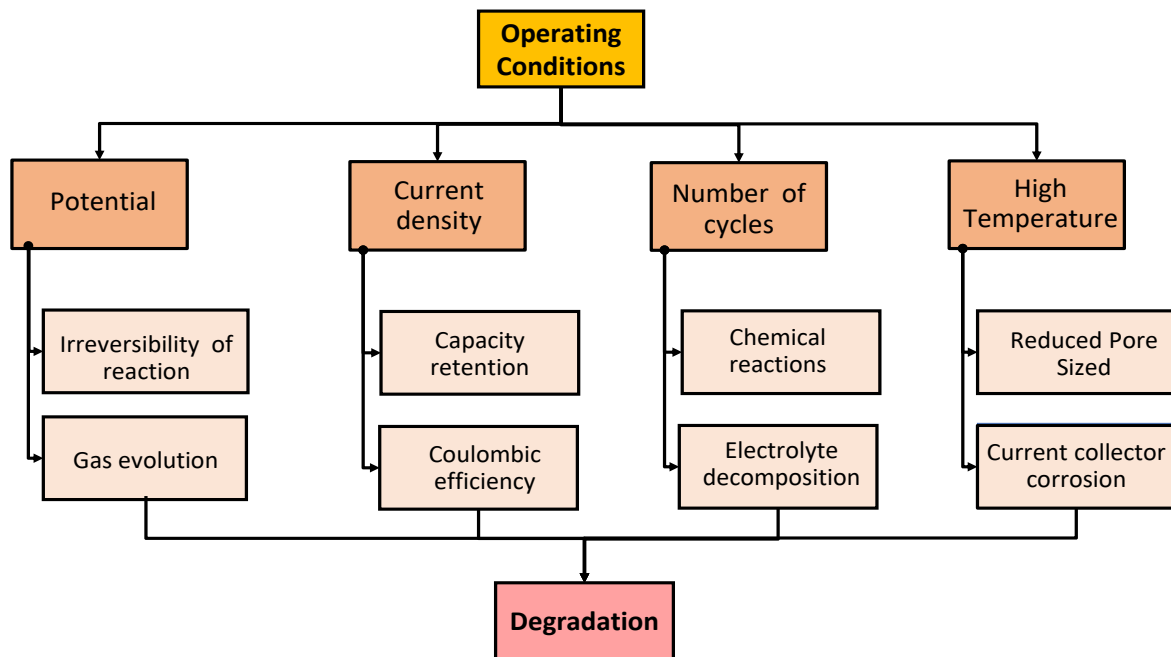


Figure 2-9: Flow chart for operating conditions that influence the rate of degradation or deterioration of the device, including potential range or potential window, current density, number of cycles (charge and discharge cycles).

2.1.5.3 Number of cycles (charge/discharge rate)

When the number of cycles is increased with increased current density, capacity retention decreases significantly lower. This shortens the charge and discharge times of the electrolytes

[66]. With a high number of cycles, the pore size is decreased due to precipitates formed by side reactions. This reduced pore size distribution may lead to less capacitance and, hence, capacitive deterioration. The ions from the electrolyte play an active role in the irreversible reduction process over a large number of cycles, causing the atomic ratio (cathodic to anodic) and the number of oxygen vacancies to decrease. This reduces electrolyte concentration, resulting in electrolyte decomposition. Figure 2-9 shows the significance of the operating conditions and how they are associated with each other to collectively increase the rate of degradation.

2.1.6 Degradation characterization approaches

In the previous section, we discussed the various types of degradation mechanisms at various levels. However, in this section, the emphasis is on detecting the degradation mechanism using various existing methods and techniques in the current literature. Characterization aids in determining the structures and properties of the materials used in the fabrication of pseudocapacitors. Characterization entails a variety of techniques and processes for further analyzing the material's properties in terms of mechanical, microscopic, and operational factors. The composition of the materials and their structural analysis are currently being studied using a variety of qualitative and quantitative techniques that are emerging or already in use.

2.1.6.1 Materials characterization

Pseudocapacitors have a high capacitance and a high output power due to reactions occurring at the surface of the electrode surface. Furthermore, the characterization of structures and electrode surface area is critical for a thorough understanding of the degradation mechanism. Materials characterization is useful when it comes to understanding certain parameters such as the surface morphology of the electrode and the electrolyte, their compositions, and various

external factors such as doping and element additions at a microscopic and nanoscopic level. All microscopic techniques are thoroughly explained in Table 2-3 along with specific examples and materials utilized. It highlights the significance of microstructural changes and how they affect the surface morphology of the microstructures and their functionality throughout cycling.

2.1.6.1.1 Surface analysis

The nanoparticle characterization of the pseudocapacitors at the microscopic level is done using various imaging techniques such as TEM, SEM, atomic force microscopy (AFM), and in-situ Raman spectroscopy. These techniques have advanced technology to detect and determine the materials at an atomic or microscopic scale [96]. They have different principles through which they operate to produce a highly magnified and high-resolution image of the sample.

a) Transmission electron microscopy

This technique is used to analyze crystal structure and has the advantage of imaging and diffractometry, which helps in providing the crystal lattice structure of the electrode material with higher resolution than SEM [97]. It determines the surface topography of the active electrode and focuses on the crystallinity of the surface.

b) Scanning electron microscopy

This method is used to determine the morphology of the microstructures of the electrode active material in the pseudocapacitor (surface morphology) [98]. SEM, accompanied by element analysis, helps to determine the existence of element and weight (mass) percentage [99], [100].

c) Atomic force microscopy

This technique is widely used to determine the thickness of the nanoparticles in a pseudocapacitor. It also detects if there is any folding or corrugation in the layer of the active electrode material [101].

d) In-situ Raman spectroscopy

Like SEM, this technique is also used to analyze the quality of the amorphous layer on the electrode material. In-situ Raman uses femtosecond laser pulses and is excellent for rapid prototyping and custom-scale manufacturing for nanofabrication of pseudocapacitors. It is also used to study and determine the crystal properties of the electrode during Faradaic charge transfer at a microstructural level through the laser irradiation technique. Although SEM is more advanced, in-situ Raman is extensively used to study the chemical composition of the electrode active material and the electrolyte in a pseudocapacitor [102].

2.1.6.1.2 Mass loss (surface/microstructure characterization)

Mass loss characterization can provide information on how much material is lost from an electrode over time because of repeated cycling, which can be indicative of degradation mechanisms in a pseudocapacitor. Researchers can determine the rate of degradation and the specific factors that contribute to degradation by measuring mass loss [103]. Identifying materials or manufacturing processes that reduce degradation can be used to improve the design and performance of the pseudocapacitor. Table 2-4 discusses different mass loss characterization techniques for pseudocapacitive materials and how they relate to degradation mechanisms or the rate at which the pseudocapacitor degrades.

a) X-ray photoelectron spectroscopy)

From the above sections, it is clear that, for a pseudocapacitor, the surface Faradaic reaction is very important and is its working principle. X-ray photoelectron spectroscopy (XPS) helps to detect different valence states of the atoms on the electrode surface [104]. For instance, Belanger observed the changes in the oxidation state of Mn for the reduced and oxidized forms of thin-film electrodes during cycling [105]. XPS detects the presence of any functional group present on the surface with the level or amount of doping of any homogeneous heteroatom. The biggest drawback of XPS is its sampling depth (50 Å) and is highly sensitive technique

to retrieve the rate of the Faradaic mechanism. As a result, it cannot be used to detect functional groups for the bulk of the surface layers [106].

b) Fourier transform infrared spectroscopy

Fourier transform infrared spectroscopy (FTIR) is used to detect and analyze the formation of the surface layer of the electrode with doping, the presence of heteroatoms, and so on. It helps to show the differences between the reference spectrum and the spectra of the oxidized, or between the oxidized, and the reduced sample [104]. This method is an alternative to XPS.

c) x-ray powder diffraction

X-ray powder diffraction (XRD) is commonly used to identify and determine the nanoparticle morphology of the resultant products formed during cycling [98], [107]. For example, having a broad peak in the XRD spectrum indicates an amorphous nature [108]. It confirms any mixed phases present in the nanocomposites of the electrode material. For example, the mixed phase of cuprous oxide (Cu_2O) and copper hydroxide ($\text{Cu}(\text{OH})_2$) was found in the XRD pattern of reduced GO (rGO)/ polypyrrole (PPy)/ Cu_2O / $\text{Cu}(\text{OH})_2$ [109], [110]. XRD is used to determine the formation of these different crystalline phases of the nanoparticles with the help of the crystalline planes [100]. It is an efficient method when it comes to estimating and calculating the spacing between the adjacent layers of the electrode material [101].

d) In-situ nuclear magnetic resonance spectroscopy

This method uses element selectivity to detect individual ionic species to study the charge storage mechanism of the pseudocapacitor. The method is used to investigate the variations at the SEI during the cycling process [111]. Grey applied in-situ nuclear magnetic resonance (NMR) spectroscopy to quantify the number of anions and cations in a pseudocapacitor and used microporous carbon as the electrode material [112]. Figure 2-10 (a) depicts the ^1H NMR spectrum of quinoxaline-based amine compound (dpqa). Aromatic protons are found between 7.1 and 7.9 ppm, while amine protons are found at 4.23 ppm. Figure 2-10 (b) depicts the peaks

at 5.49 ppm and 4.75 ppm in the ^1H NMR spectrum of quinoxaline-based benzoxazine (BA-dpqa) correspond to the O-CH₂-N- and Ar-CH₂-N- groups of the oxazine ring of BA-dpqa. Furthermore, the aliphatic protons appear at 1.63 ppm. Aromatic protons are found in concentrations ranging from 6.6 to 8.1 ppm [113]. Therefore, the NMR spectra reveal information about the materials' chemical compositions, including the presence of specific functional groups such as aromatic protons, amine protons, and aliphatic protons. If the NMR spectra show a shift or broadening of the peaks corresponding to the aromatic protons, this could indicate the formation of oxidation products or the degradation of the polymer backbone due to repeated cycling. Likewise, changes in the chemical shifts or intensities of the amine or aliphatic protons could indicate polymer structure degradation or the formation of degradation products.

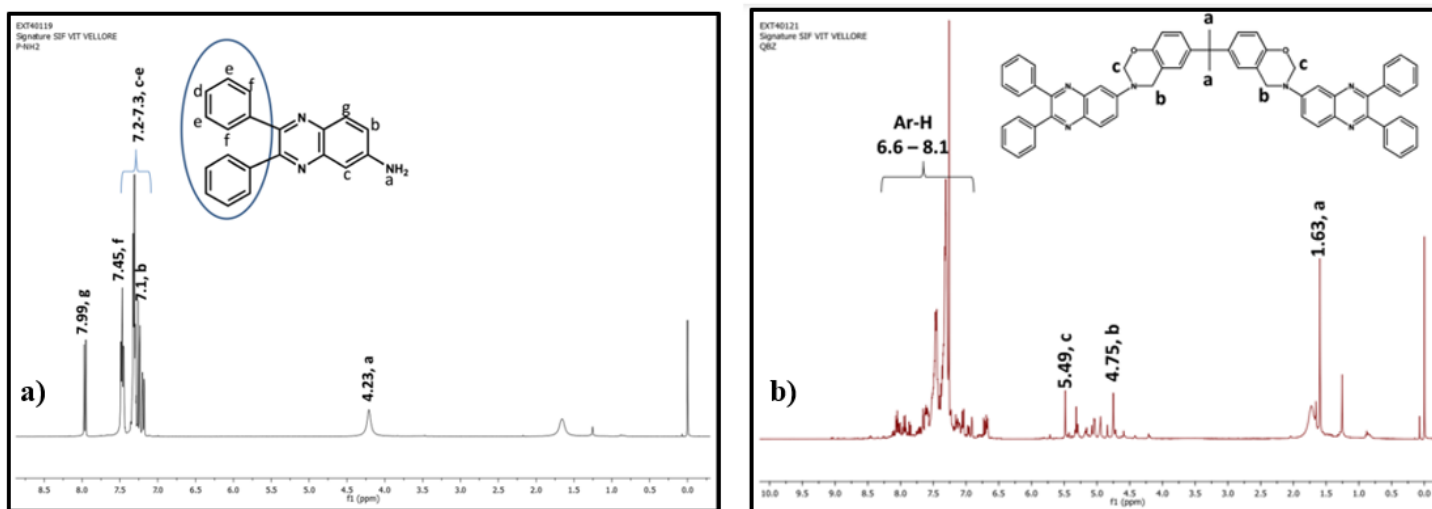
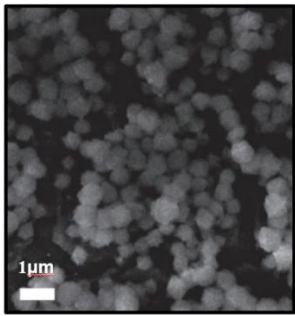
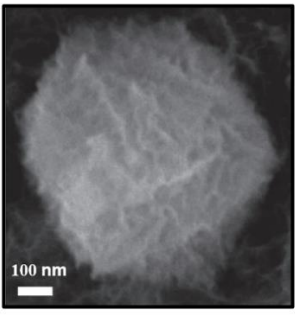
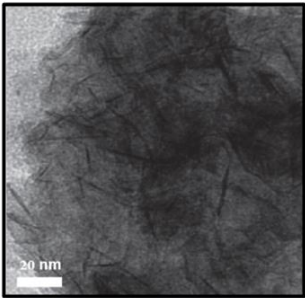
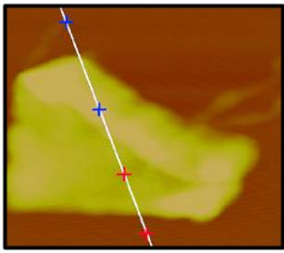
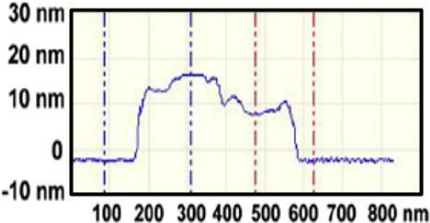


Figure 2-10: ^1H NMR spectrum of (a) The quinoxaline-based amine compound (dpqa). (b) quinoxaline-based benzoxazine (BA-dpqa). Reprinted from [113].

Table 2-3. Individual techniques (with examples) for the characterization of the materials used in pseudocapacitors.

Technique	Description	Image
SEM	<p>(a) and (b) display the SEM measurements of the amorphous Ni(OH)₂ sample that is synthesized on the graphite electrodes. SEM image at 1 μm. The amorphous nanospheres are wrinkle-like with this smaller magnification. Reprinted with permission from [114].</p> <p>SEM image at 100 nm. The well-defined nanospheres are ravine-like surfaces. Reprinted with permission from [114].</p> <p>Both (a) and (b) illustrate how the morphology is not uniform and could potentially lead to micro-cracks in the electrode material.</p>	<p>(a) </p> <p>(b) </p>
TEM	<p>(c) reveals the microscopy measurement of the amorphous Ni(OH)₂ sample. TEM image at 20 nm. The microstructure indicates wrinkled surfaces and is quite dense. The nanospheres are highly irregular and could also contribute to degradation mechanisms by generating stress and strain within the material during cycling. Reprinted with permission from [114].</p>	<p>(c) </p>
AFM	<p>AFM image of an exfoliated individual β-Ni(OH)₂/graphene hybrid nanoflake is shown in (d). It is observed from the graph that the thickness is approximately 10 nm. The graph indicates folding and corrugation, which is important for the nanofabrication of pseudocapacitors and its flexibility in applications. (e) represents the AFM measurements of the thickness of the nanoflakes before and after cycling, which can provide insight into the extent of degradation, such as changes in morphology and material loss. Reprinted with permission from [101].</p>	<p>(d) </p> <p>(e) </p>

Raman spectroscopy In-situ Raman spectra of e-PPy and c-PPy during cycling stages (f). There is no peak for c-PPy post-cycle, indicating the deterioration of the electrode material and, hence, the device. Reprinted with permission from [81].

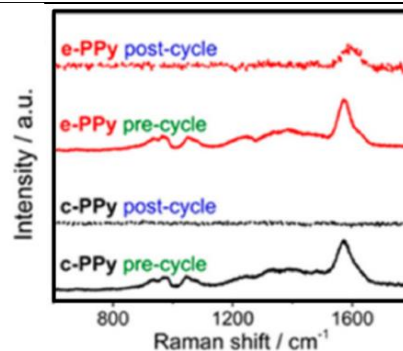


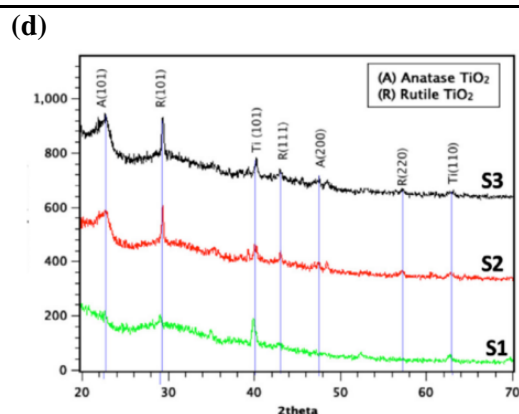
Table 2-4. Mass loss surface characterization techniques with examples of the materials used in pseudocapacitor.

Technique	Description	Image
XPS	In a study conducted by Khot and Kiani [[115], XPS was used to look for the presence of Ni species in different samples. It was observed that the Ni ³⁺ - O bonding signal increased after the discharge cycle, which is believed to be due to the presence of NiOOH on the surface, as the oxidation state of NiOOH is 3 ⁺ . (a) and (b) showcase the O 1s peaks pre-cycle and after 7000 cycles, respectively. A sharp decrease in the NiO peak is seen, which can be attributed to material degradation. Reprinted from [115].	<p>The figure contains two XPS spectra for the O 1s core level. The x-axis is 'Binding Energy (eV)' ranging from 536 to 526. The y-axis is 'Intensity (a.u.)'. <ul style="list-style-type: none"> Top plot: 'Pre cycle'. Shows three peaks: a green peak labeled 'Abs.' at ~534 eV, a blue peak labeled 'Ni³⁺' at ~532 eV, and a red peak labeled 'Ni²⁺' at ~529 eV. Bottom plot: 'Post 7000 cycles'. Shows three peaks: a green peak labeled 'Abs.' at ~534 eV, a blue peak labeled 'Ni³⁺' at ~532 eV, and a red peak labeled 'Ni²⁺' at ~529 eV. The Ni²⁺ peak is significantly smaller than in the pre-cycle plot. </p>
FTIR	(c) shows the vibration bands of an undoped, chemically synthesized polyaniline by the FTIR spectrum. There are prominent vibration bands in the spectrum at 1588, 1495, 1322, 1164, 848, and 622 cm ⁻¹ . The vibration bands at these different wavelengths are explained in detail in [116]–[120]. Changes in the intensities or positions of the vibrational bands associated with the C=C and C-N bonds, as mentioned in the paper, can indicate polyaniline	(c) <p>The figure shows an FTIR transmittance spectrum. The x-axis is 'Wavenumber (cm⁻¹)' ranging from 3850 to 350. The y-axis is 'Transmittance [%]' ranging from 0 to 80. The spectrum shows several absorption bands, with prominent ones at 1588, 1495, 1322, 1164, 848, and 622 cm⁻¹.</p>

electrode material degradation [116], [117]. This spectrum can be used to study the changes in the chemical structure and vibrational modes of the material as it degrades in a pseudocapacitor. Reprinted with permission from [116].

XRD

Using an XRD spectroscopy system, the composition, and crystallographic structures of different electrodes (untreated Ti as control sample [S1], Ti sheet treated with one-time laser irradiation [S2], and Ti sheets treated with two-time laser processing [S3]) has been studied by [121]. (d) shows the XRD results and confirms the presence of micro and nano web-like titanium oxide structures in both the S2 and S3 samples. The control sample, on the other hand, showed no oxide peaks (S1). So, increasing the number of laser treatments from one to double resulted in an increase in oxide intensity in XRD results. This increase in oxide intensity suggests that electrode degradation may be linked to titanium oxide formation during laser treatment. Reprinted with permission from [121].



2.1.6.2 Electrochemical profile evaluation (analysis)

Capacitance and energy/power density, measured at a specific current density, are commonly used to assess the electrochemical performance of a pseudocapacitor's electrode material. Table 2-5 shows the electrochemical characteristics through different types of analysis such as cyclic voltammetry (CV), galvanostatic charge/discharge test (GCD), and electrochemical impedance spectroscopy (EIS), and how they are related to operational parameters such as rate capability, structural stability, power capacity, and capacity retention.

2.1.6.2.1 Cyclic voltammetry

CV is used to measure average capacitance for the pseudocapacitive behavior with a rectangular CV curve [110], [122], [123]. The capacitance of electrode material is estimated from the rectangular CV curves:

$$C = \frac{i}{v} \quad (2-3)$$

where C is the capacitance (Fg^{-1}), i is the current density at the mean voltage (Ag^{-1}), and v is the scan rate (Vs^{-1}) [104]. The capacitance of an electrode layer can also be estimated with the following formula:

$$C_i = \left| \frac{Q}{E_2 - E_1} \right| \quad (2-4)$$

where Q is the total charge accumulated throughout the electrode layer and C_i is the capacitance; the area under the CV in both directions in the potential window from E_1 to E_2 can be used to quantify Q [122]. The main drawback of the CV method is it cannot be used to evaluate the average capacitances in the case of intercalation pseudocapacitors due to the presence of redox peaks in the CV curves.

2.1.6.2.2 Galvanostatic charge/discharge test

GCD is another efficient method to measure the capacitance of pseudocapacitors and can be estimated using the following formula:

$$C = \frac{i \times \Delta t}{m \times \Delta V} \quad (2-5)$$

where C is the capacitance (F g^{-1}), i is the current density (A g^{-1}), Δt is the charging/discharging time (s), m is the mass of the active electrode material (g) and ΔV is the working/operating potential window of the electrode [100], [104]. The method is considered efficient because it can determine the electrochemical properties of the electrode materials used in the pseudocapacitor under certain controlled current situations [124]. In this test, the pseudocapacitive behavior depends on the specified potential window (Eq 5). Through general

trends, it is observed that the specific capacitance is decreased when the current density is increased. This is because of insufficient response time for the ions in the electrolyte to reach/diffuse to/onto the electrode surface at a significant current rate [125].

Furthermore, GCD can be used to predict the rate of degradation of a pseudocapacitor through the charge/discharge curves. The more symmetrical the curves are, the more the charge/discharge process is reversible, indicating the high Coulombic efficiency of the electrode. The presence of slight plateaus in the curve also confirms the presence of a pseudocapacitor [98].

2.1.6.2.3 Electrochemical impedance spectroscopy

EIS is a technique for collecting and analyzing pseudocapacitor impedance data at the open-circuit potential with a small amplitude of interruptive potential (alternate) of ± 5 or ± 10 mV across a wide frequency range of 0.01 Hz to 100 kHz. The EIS measurement is expressed through Nyquist plots and is plotted as the imaginary part of the impedance $Z(f)''$ versus the real part of the impedance $Z(f)'$. The plot is composed of three regions. The pseudocapacitive mechanism lies in the middle region and represents the internal resistance through a high-to-medium frequency (i.e., 10 kHz to 1 Hz) [104], [110], [122], [126]–[128]. The intersection of the curve in the Nyquist plot represents the ESR, which is the sum of the intrinsic resistance of the electrode material, the electrolyte resistance, and the contact resistance at the interface between the current collector and the electrode material [116], [129], [130]. Through the EIS measurements, the relationship between the imaginary part of the impedance and the frequency is easily determined. The capacitance is calculated through the following equation:

$$C = \frac{1}{2\pi f |Z|} \quad (2-6)$$

where the capacitance is known through the Bode plot (linear part of $\log|Z|$ vs. $\log(f)$ curve).

The plot trend displays the decrease of capacitance with increasing frequency. The plot further

explains how supercapacitors perform as a pure resistance at the high-frequency region and thereby indicating the failure of ions in the electrolyte to penetrate the microstructural pores under considerable frequencies [104], [110], [122]. Therefore, EIS shows how a pseudocapacitor is an ideal mechanism in the middle region for ion kinetics transfer. The value of ion transfer resistance is determined from EIS measurements and depends on the dielectric and the insulating features at the SEI [100]. To conclude, EIS is used to study the response time of the pseudocapacitors [108].

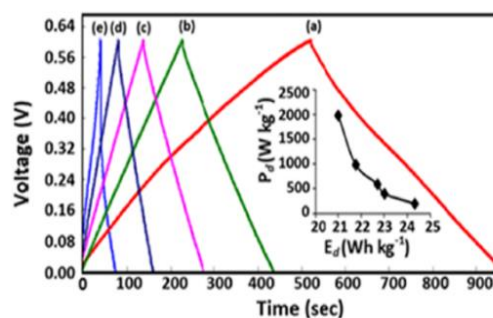
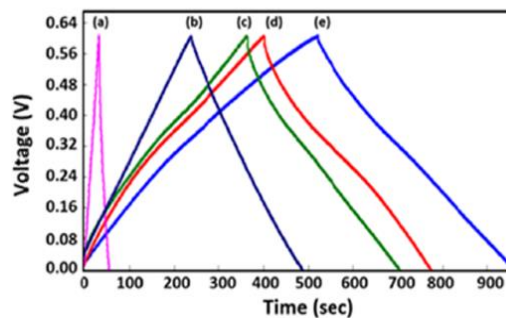
Table 2-5. Different electrochemical analysis techniques were used to predict their operational properties.

Example	Characteristics	Graph
CV	<p>(a) CV curves for graphene-carbon nanofiber/MnO₂ nanocomposite paper (GMP) at different scan rates. At low scan rates (10 mV s⁻¹), the curve is more rectangular and symmetric, indicating much faster reversible Faradaic redox reactions compared with slow diffusion at high scan rates, where the shape deviates significantly from the rectangular-like curve [109].</p> <p>(b) CV curves for MnO₂, MnO₂/rGO, GMP, PPy were used in 1M Na₂SO₄ at a specific scan rate of 50 mV s⁻¹. It is observed that GMP has the highest area under the curve, which indicates higher capacitance than other electrodes used. Reprinted with permission from [109], [131].</p>	

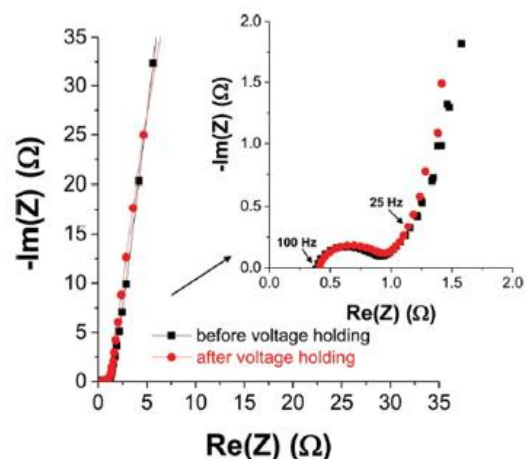
GCD

(c) GCD curves for different composites/aqueous electrodes (a) C_{SA} (sulfonated carbon), (b) Aq- PANi-SA (polyaniline-sulfate salt by aqueous polymerization pathway), (c) Int- PANi-SA• C_{SA} (polyaniline-sulfonated carbon hybrid by emulsion polymerization pathway), (d) Eml- PANi-SA• C_{SA} (polyaniline-sulfonated carbon hybrid by interfacial polymerization pathway) and (e) Aq- PANi-SA• C_{SA} (polyaniline-sulfonated carbon hybrid by aqueous polymerization pathway) respectively with a current density of 0.35 A g^{-1} . Through measurements, it is observed that the aqueous polymerized electrode (Aq-PANi-SA• C_{SA}) shows the best electrochemical performance due to high conductivity, yield, and fast ion transport process.

(d) GCD curves for (Polyaniline) Aq- PANi-SA• C_{SA} at different current densities (a) 0.35 , (b) 0.7 , (c) 1 , (d) 1.7 , and (e) 3.5 A g^{-1} respectively. The graph has an inset plot known as the Ragone plot showing the relationship between the energy storage and the power capabilities of the pseudocapacitor. Through this plot, it is concluded that the electrode has a high rate capability meaning good specific capacitance with high-capacity retention Reprinted with permission from [108], [131].



EIS (e) exhibits a Nyquist plot for the OLC/MnO₂ (onion-like carbon/manganese oxide) symmetric pseudocapacitor before and after 50-hour voltage holding experiments [132]. The low-frequency region is represented by the straight line. The inset is the expanded portion of the high frequency region, and the semicircle corresponds to the charge transfer resistance. Extrapolating the vertical portion of the plot to the real axis, considering both the ESR and the ionic resistance within the porous structure, yielded the equivalent distributed resistance for the OLC/MnO₂ nanohybrid material and OLC alone (RC semicircle). The OLC/MnO₂ nanohybrid material demonstrated an increase in ionic resistance within the porous structure, as evidenced by a slightly larger RC semicircle (1.8 Ω cm²) when compared with the OLC alone (1.2 Ω cm²). Therefore, EIS helps to determine the rate of charge and discharge and the power capability of the material, which is crucial to degradation rate. Reprinted from [132].



2.1.7 Optimizing and controlling the rate of degradation

To increase the efficiency of the pseudocapacitor, it is crucial to reduce the rate of degradation or optimize the factors affecting it. All the mechanisms mentioned in Section 2.1.3 have their consequences on the deterioration of the device and slow down the efficiency of the pseudocapacitors. It is therefore important to address this mechanism and enhance or modify the parts used in the pseudocapacitor for their prolonged lifetime with an increase in efficiency. Furthermore, we refer the reader to the supplementary information, which includes a comma-separated values file, for an exhaustive account of the various electrode and electrolyte variants

implemented in a pseudocapacitive device. This file contains information on 40 different electrode and electrolyte combinations, providing a comprehensive look at the materials used in pseudocapacitive devices. This data set's inclusion aims to facilitate further investigation and analysis of pseudocapacitive devices, contributing to the scientific community's understanding of these promising energy storage systems.

2.1.7.1 Enhancing the electrode material used at (the fabrication or structure level)

This subsection focuses on the electrode material and how different manufacturing techniques for different electrodes have been carried out to modify the structure of the electrode. In doing so, various operational parameters — such as potential window, current density, and the number of cycles — can be improved, leading to excellent electrochemical performance of the pseudocapacitor device. Changing the properties of the electrode by varying different parameters during manufacturing has enabled many desired outcomes, such as good capacity retention, cyclic stability, and rate capability. As shown in the following subsections, we have briefly explained various types of pseudocapacitive materials used in pseudocapacitors.

2.1.7.1.1 Metallic oxides

Huarong Peng conducted research on molybdenum disulfide (MoS_2)-coated vanadium trioxide (V_2O_3) composite nanosheet tubes [133]. The MoS_2 and $\text{V}_2\text{O}_3@ \text{MoS}_2$ composite tubes were created using a one-step hydrothermal reaction, as shown in Figure 2-11, and electrochemical measurements showed that the hollow tubular $\text{V}_2\text{O}_3@ \text{MoS}_2$ composite exhibited typical pseudocapacitive behaviors, including a wide operational window, high specific capacitance, and excellent cycling stability.



Figure 2-11: The schematic detailed diagram for the fabrication process of the MoS_2 nanosheets and the tubular (hollow) $\text{V}_2\text{O}_3@/\text{MoS}_2$ composites. Reprinted with permission from [133].

Figures 2-12 (a) and (b) show the CV curves of symmetric pseudocapacitors ($\text{V}_2\text{O}_3@/\text{MoS}_2/\text{V}_2\text{O}_3@/\text{MoS}_2$) and asymmetric pseudocapacitors ($\text{V}_2\text{O}_3@/\text{MoS}_2/\text{AC}$) at a scan rate of $20\text{-}100\text{ mV s}^{-1}$. The CV curves show a quasi-rectangular shape with minimal distortion. Interfacial modification in the composite, such as atomic layer deposition and molecular layer deposition, has proven to be very effective in suppressing electrochemical degradation behavior. Atomic layer deposition is a technique whereby the deposition of the thin film develops rapidly due to unique properties, including excellent uniformity, atom-scale stoichiometric deposition, and operation at low-growth temperatures [133]. The main drawbacks — such as restacking propensity and self-aggregation tendency caused by the reduction in surface energy — are avoided by either changing the structure to 3D to minimize restacking propensity or combining it with other materials to build Van der Waals heterostructures [134], [135]. This separates the layers of MoS_2 and prevents aggregation. Doing this also increases the potential window for the pseudocapacitor and allows it to function

as a cathode as well as the anode. MoS₂ has higher intrinsic ionic conductivity than metal oxides and higher theoretical specific capacity (670 mA hg⁻¹) than graphite [136], [137]. Owing to the multivalence of both Mo and V, the potential window of the composite can straddle between negative and positive potentials and offers opportunities to achieve high energy density [138], [139]. An asymmetric device made of V₂O₃@MoS₂ and activated carbon (AC) demonstrated a high energy density of 31.8Wh kg⁻¹ at the power density of 0.37kWkg⁻¹, as well as an ultra-high cycling stability, with approximately 100% capacity retention after 35000 cycles [133]. In his review paper, Chunyu Du concluded that Ti-based oxides (TiO₂) are useful for structural stability in pseudocapacitors/hybrid Pseudocapacitors [140]. Because it is used to control the thickness of 2D materials, atomic layer deposition has proven to be a powerful tool for electrode fabrication in hybrid pseudocapacitors applications [141]–[143]. Figures 2-12 (c) and (d) showcase the TiO₂ nanotubes manufactured by the electrospinning process, a process that achieves high surface area and high electron-enhanced mobility [140]. Ti-based oxides have a high operating voltage in comparison to alkali metal deposition such as Li, Na, and so on, and this ensures complete safety by preventing the formation of lithium and sodium dendrites. High working potential, on the other hand, prevents electrolyte decomposition, resulting in excellent rate capability via the unique pseudocapacitive kinetics [51]. The intrinsic poor electrical conductivity and slow ion-transfer kinetics limit its use in pseudocapacitors, but recent advances in morphological control and bulk-phase doping have demonstrated its potential for future research. When amorphous TiO₂@CNT/CFP (carbon nanotubes/carbon fiber papers) is used as an anode, structural stability and excellent rate capability is achieved.

It has a high reversible capacity of 272 mAh g⁻¹ at 0.1 Ag⁻¹ and excellent cycling performance, retaining 93% of its capacity after 10,000 cycles at 20 Ag⁻¹ [51], [144].

MnO₂ is an excellent material for use in pseudocapacitors due to its high rate and capacity performance; however, due to electrochemical instability in the aqueous electrolyte, it cannot be used at a low electrochemical potential. Yu-Ting Weng's experiment demonstrates the possibility of stabilizing the MnO₂ electrode using a silicon dioxide (SiO₂)-confined nanostructure [145]. Surprisingly, this approach achieved an exceptionally good electrochemical stability under large negative polarization in aqueous (Li₂SO₄) electrolyte between -1 V and +1 V with no Mn dissolution, which is normally unattainable for MnO₂-based electrodes. Even more intriguing, this MnO₂-SiO₂ nanostructure composite exhibits distinct mixed pseudocapacitance-battery behavior involving consecutive reversible charge transfer from Mn(IV) to Mn(II), allowing for simultaneous high-capacity and high-rate characteristics via different charge-transfer kinetic mechanisms [145]–[148]. Figure 2-12 (e) shows the cycling stability of the MSO (Mn-Si-O) electrode. It is CV scanned at 20 mV s⁻¹.

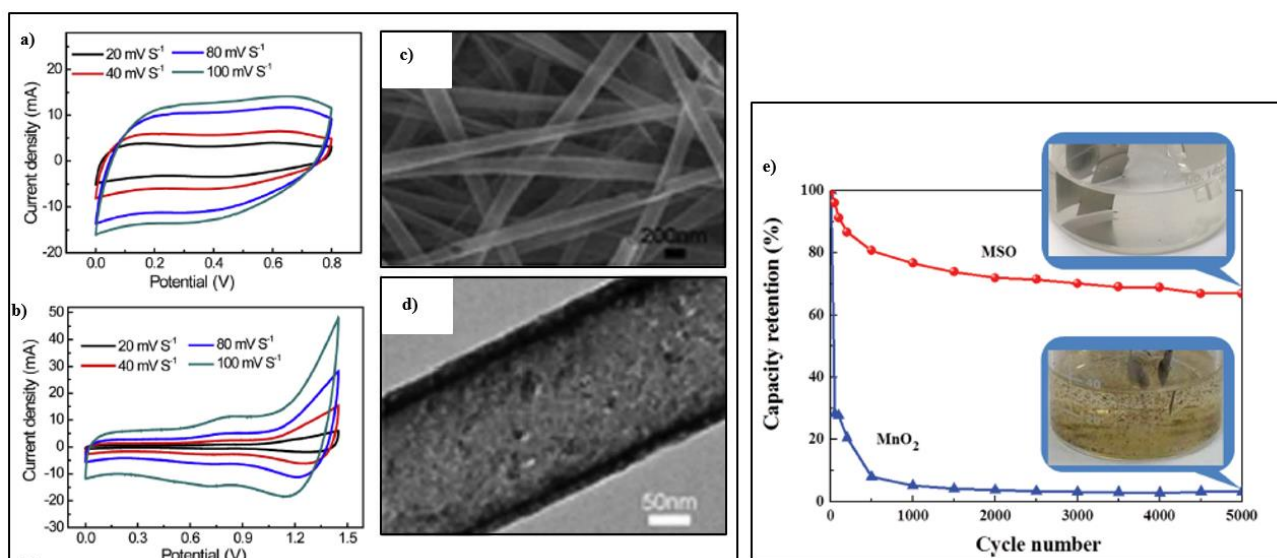


Figure 2-12: (a) CV curve for the symmetric pseudocapacitor V₂O₃@MoS₂/ V₂O₃@MoS₂. (b) CV curve for the asymmetric pseudocapacitor V₂O₃@MoS₂/AC. (c) & (d) TiO₂ nanosheets (hollow nanofibers) manufactured by electrospinning method. (e) Graph for capacity retention against the number of cycles for the MSO and MnO₂ electrodes. The inset in the graph shows the solution after cycling tests. Reprinted with permission from [51], [133], [145].

In < 500 cycles, the MnO_2 lost > 90% of its capacity and formed a brown precipitate in the electrolyte, indicating Mn^{2+} dissolution. After 5000 cycles in MSO, the electrode retained 68% of its capacity and no precipitate was formed in the electrolyte. As a result, when utilized at low potentials, the MSO electrode prevented electrode corrosion [145].

Through the manufacturing process of electrodeposition and hydrothermal method, NiCoO_2 nanowires (NCO NWs) and NiCoO_2 nanoflakes (NCO NFs) covered with CoS_2 (CS) were in-situ formed on gold-coated nickel foam (NFA). The NFA/NCO/CS electrode's manufacturing procedure is shown in Figure 2-13. The formed layered structure facilitates the rapid transmission of electrolytes and improves the mechanical stability of the electrodes [149]–[151].

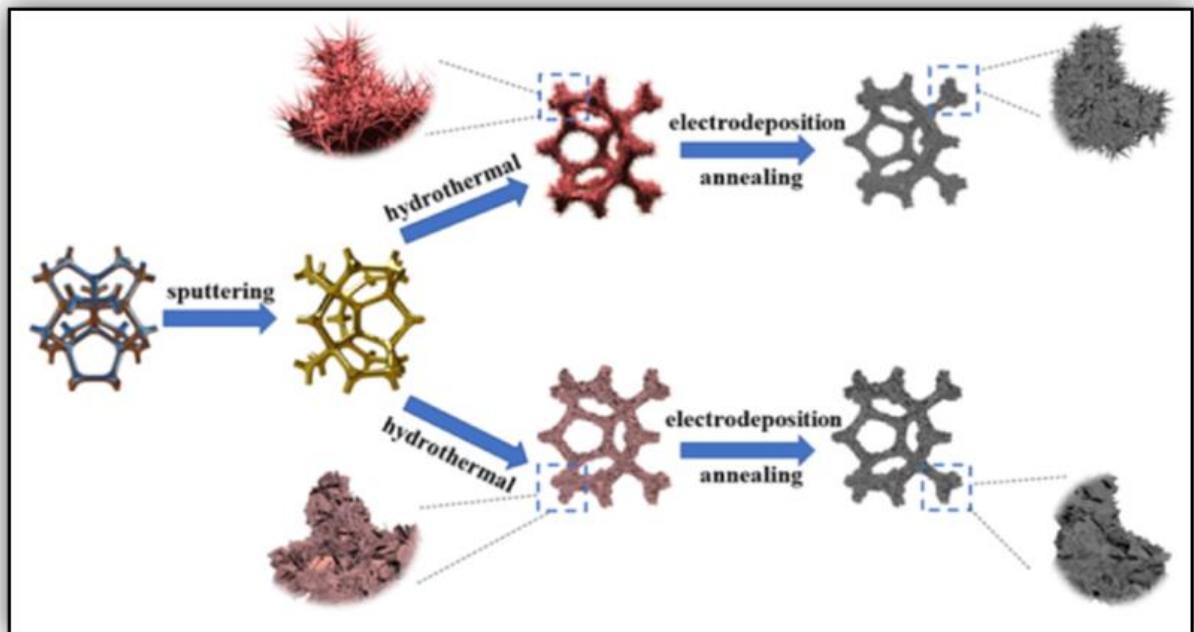


Figure 2-13: Synthesis route of NFA/NCO/CS. Reprinted with permission from [151].

Meanwhile, adding a gold layer improves conductivity and electron/ion transmission. Zhicheng Chi and his colleagues discovered experimentally that an electrode based on NiCoO₂ nanowires/CoS₂ (NFA/NCO NWs/CS) nanocomposite has an ultrahigh specific capacitance of 3.28 Fcm⁻² (2186.7 Fg⁻¹) at 2 mA cm⁻² and retains 90.4% of the initial capacitance after 4000 cycles [52], [151], [152]. In addition, Figures 2-14 (a) and (b) show that, at a scan rate of 10 mV s⁻¹, the response current of each NFA/NCO/CS electrode is extremely strong, demonstrating the CS layer's contribution to the pseudocapacitance and showing that the pseudocapacitance is primarily caused by the second stage of the charging process [150]–[153].

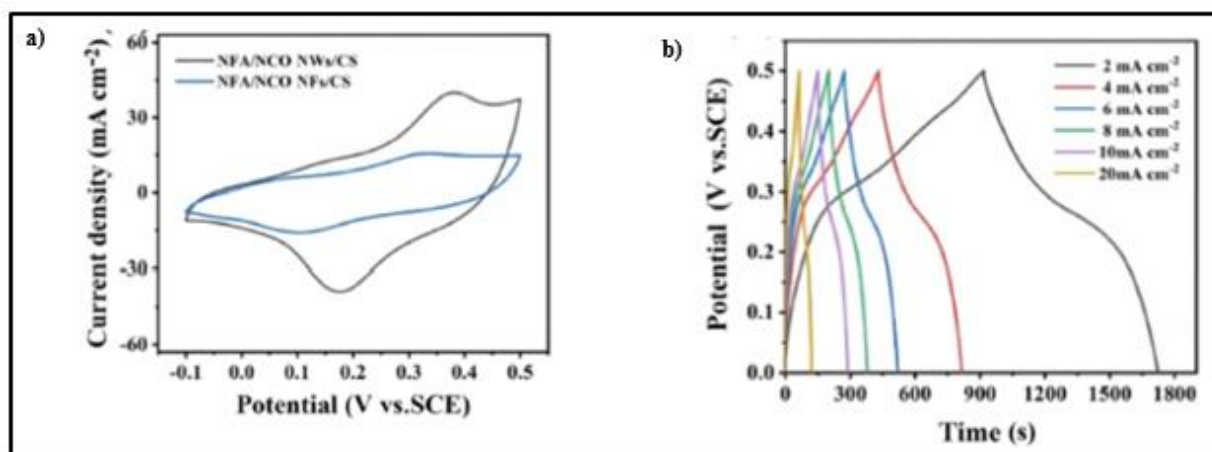


Figure 2-14: (a) CV curve for composite electrode for pseudocapacitors, using NFA/NCO NWs/CS or NFA/NCO NFsCS at a scan rate of 10 mV s⁻¹. (b) GCD curve of the NFA/NCO NWs/CS composite electrode at different current densities. Reprinted with permission from [151].

2.1.7.1.2 Carbon-based materials

In a study led by Yun-Guang-Zhu, NiO nanoflakes/graphene (NiO/G) nanocomposites were prepared using a hydrothermal method, followed by heat treatment with nitrogen (N₂) gas [154]. In this composite, NiO nanoflakes (30–80 nm in diameter) are uniformly anchored on graphene sheets layer by layer, effectively preventing aggregation and providing 2D diffusion channels for electron and ion transport. The NiO/G composite electrode outperforms bare NiO nanoflakes in terms of electrochemical properties. The specific capacitances of the NiO/G

electrode are 240 Fg^{-1} at 5 Ag^{-1} and 220 Fg^{-1} at 10 Ag^{-1} , which are significantly greater than the specific capacitances of the NiO electrode, which are 100 Fg^{-1} at 5 Ag^{-1} and 90 Fg^{-1} at 10 Ag^{-1} . NiO/G offers better channels for quick ion-transfer kinetics and aids in customizing the surface area, porosity, and pore distribution of the electrode because NiO has poor ionic conductivity and poor long-term stability due to crack formation in the electrodes. The addition of graphene boosts the ionic conductivity, as well as the energy and power density [154]–[158]. Furthermore, graphene prevents NiO nanoflakes from aggregating, and NiO nanoflakes can also impede graphene aggregation. The cycling stability of the NiO/G supercapacitor is quite high due to this hybrid structure, which exhibits a superior cycling stability of 100%–120% retention of specific capacitance after 1500 cycles at a current density of 5 Ag^{-1} between 0–0.5 V (Figure 2-16 (a)), compared with 66.7% for NiO [154]. The EIS plot of NiO and NiO/G is shown in Figure 2-16 (b). The spectra of NiO/G are very close to 90° , which is much larger than that of NiO, and the spike begins around the mid-high frequency. Therefore, this indicates that NiO/G is a much better composite than NiO, and that it can be used as an electrode material for a low-leakage supercapacitor [154], [159].

Xinjie Liu conducted an experiment whereby he used a composite structure of ZIF-67@Co-NTC that was synthesized by using ZIF-67 as a sacrificial template/precursor and rigid 1,4,5,8-naphthalene tetracarboxylic acid (NTC) as a linking ligand [160]. The composite structure was then partially vulcanized to form layer-like Co_3S_4 nanosheets to synthesize a composite heterostructure of Co-NTC@ Co_3S_4 . Figure 2-15 depicts the Co-NTC@ Co_3S_4 manufacturing process. During the charge and discharge processes, the layered structure can improve the electron transport efficiency via small diffusion electrolyte channels, while also preventing nanosheet accumulation/aggregation [160]–[162]. Also, the layered structure helps in the large specific surface areas, and it helps in the penetration of ions into the electrolyte, which improves the ion-transfer kinetics during the cycling of the electrode [160], [163]–[165].

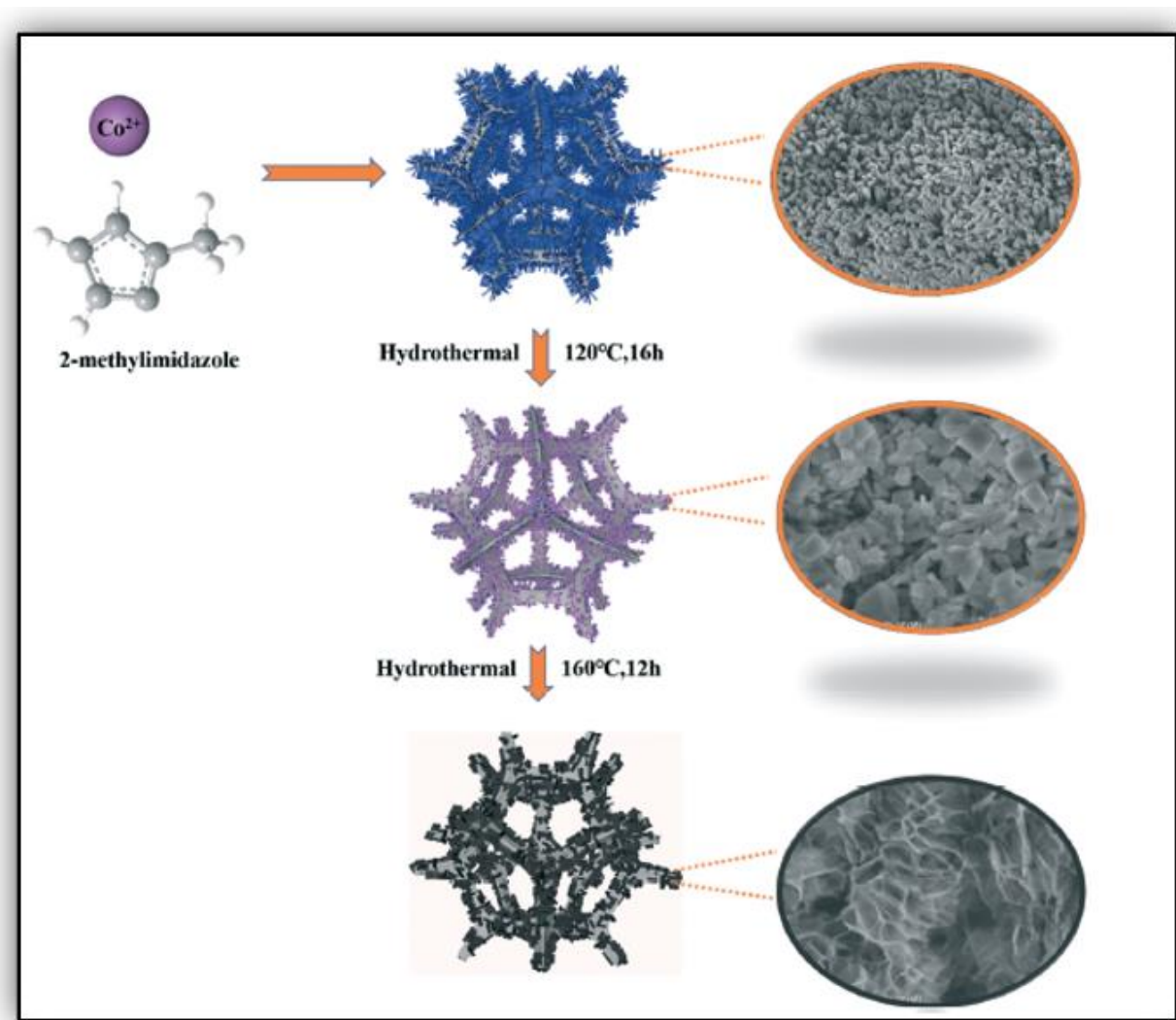


Figure 2-15: Schematic diagram of the processing of hierarchical Co-NTC@Co₃S₄. Reprinted with permission from [160].

Based on these advantages, Co-NTC@Co₃S₄ exhibits excellent electrochemical properties. It can achieve up to 3117.3 Fg⁻¹ at 1 Ag⁻¹, and the magnification capacity is about 80% at 10 Ag⁻¹; after 1000 cycles, the retention rate can reach up to 87% at the same current density. A hybrid supercapacitor (asymmetric pseudocapacitor) composed of Co-NTC@Co₃S₄ and AC exhibits ideal performance (i.e., the cyclic capability is up to 110% after 5000 cycles at a current density of 10 Ag⁻¹). This can be further seen in Figures 2-16 (c) and (d). In a 6 M KOH electrolyte, Co-NTC@Co₃S₄ is the positive electrode and AC is the negative electrode. In the mid-potential

range (i.e., the range of potentials where the electrode's pseudocapacitive behavior is most observable, typically within the potential range with the highest current density and the most rectangular CV curve), the CV curve is rectangular and exhibits pseudocapacitive behavior [160], [163].

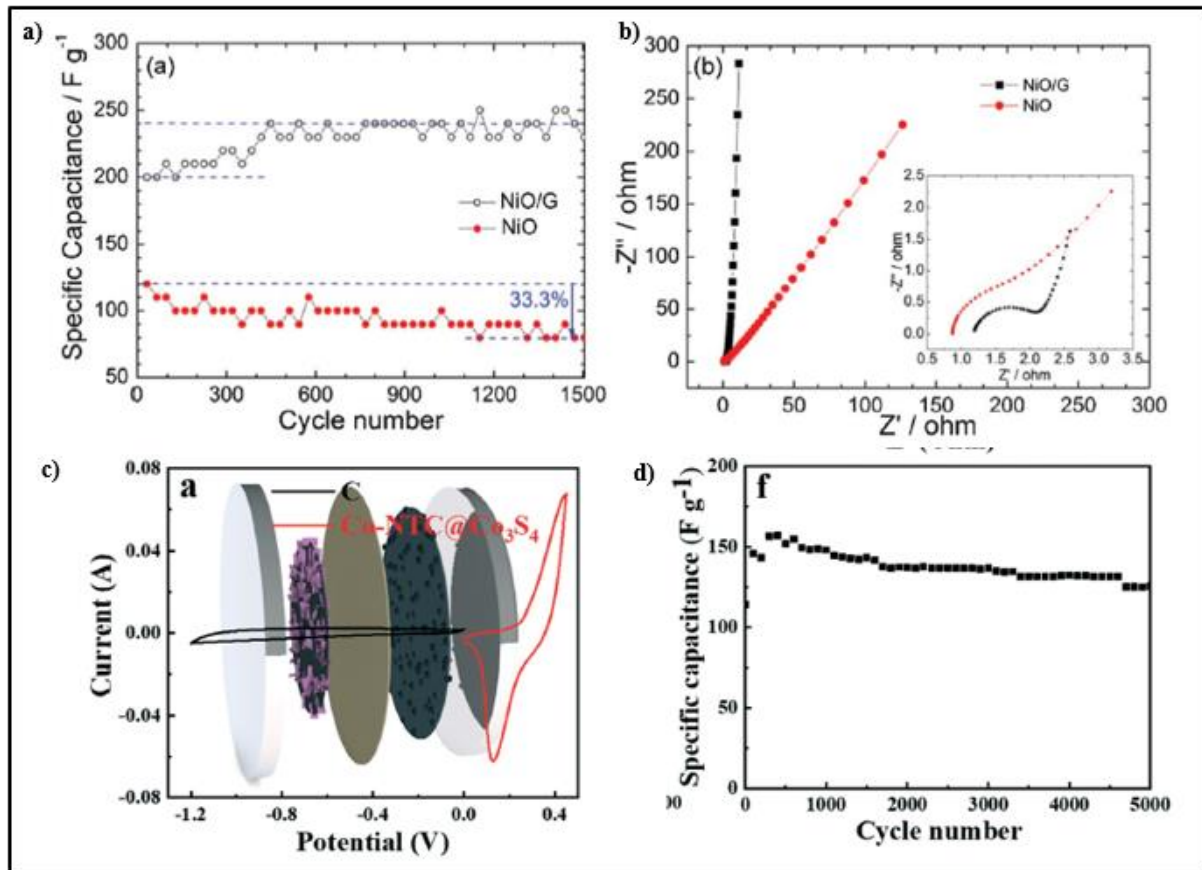


Figure 2-16: (a) Specific capacitance vs. the number of cycles of NiO and NiO/G. The cycling performance is carried out at a current density of 5 Ag⁻¹. (b) Nyquist plots of the NiO and NiO/G electrodes. (c) CV curve of Co-NTC@Co₃S₄ and AC at a scan rate of 10 mV s⁻¹. (d) Cycling performance/stability of Co-NTC@Co₃S₄/AC at a current density of 10 Ag⁻¹. Reprinted with permission from [154], [160].

Hao Xie described a simple hydrothermal synthesis of an advanced nanocomposite made of novel three-dimensional (3D) nitrogen-doped graphene (NG) networks and hexagonal cobalt hydroxide (Co (OH)₂) nanoplates that are optimized for use as electrochemical pseudocapacitor materials [166]. To achieve high porosity and capacity, parameters such as GO precursor concentration and Co (OH)₂ content are independently optimized. Inside the conductive [166],

[167]. The homogeneous distribution prevents the stacking of the nanoplates and the interconnected NG networks, single-crystalline $\text{Co}(\text{OH})_2$ plates are distributed uniformly NG. Figure 2-17 (a) shows the SEM image of the NG/ $\text{Co}(\text{OH})_2$. The 3D network is still the same approximately with no significant changes. The composite has a porous structure, with the interconnected NG. From the inset of Figure 2-17 (a), it is observed that there is no stacking, and the hexagonal morphology is retained. In this research, it was observed that the 71% $\text{Co}(\text{OH})_2$ weight content achieves a capacitance of 952 Fg^{-1} at 1.0 Ag^{-1} , more than triple that of the pure NG and nearly four times that of $\text{Co}(\text{OH})_2$ plates [168]–[170]. Furthermore, this value exceeds the recently reported values for 2D graphene/ $\text{Co}(\text{OH})_2$ composites. Capacity retention over 2000 cycles is 95%, as seen in Figure 17 (b) [166]. The improvements are primarily due to $\text{Co}(\text{OH})_2$ particles standing randomly in 3D networks rather than lying on NG nanosheets. The specific surface area is increased as a result. Furthermore, the regular morphology of $\text{Co}(\text{OH})_2$ and the 3D porosity, which prevents the stacking of the $\text{Co}(\text{OH})_2$ plates effectively in the composite, as well as the continuously connected pores and highly conductive NG networks, which facilitate electron and ion transport, are all beneficial [166], [168], [171], [172].

2.1.7.1.3 Conducting polymers

Conducting polymers, particularly PPy and PANi have a high potential for use as pseudocapacitive electrodes due to their ease of fabrication and low cost. However, the structural instability caused by volumetric swelling and shrinking (electrolyte) during the charge/discharge process is a significant barrier to their broader applications. As a result, Tianyu Liu and his colleagues' incredible work demonstrated a simple and general strategy for significantly improving the cycling stability of conductive polymer electrodes by deposition of a thin carbonaceous shell onto their surface [173]–[175].

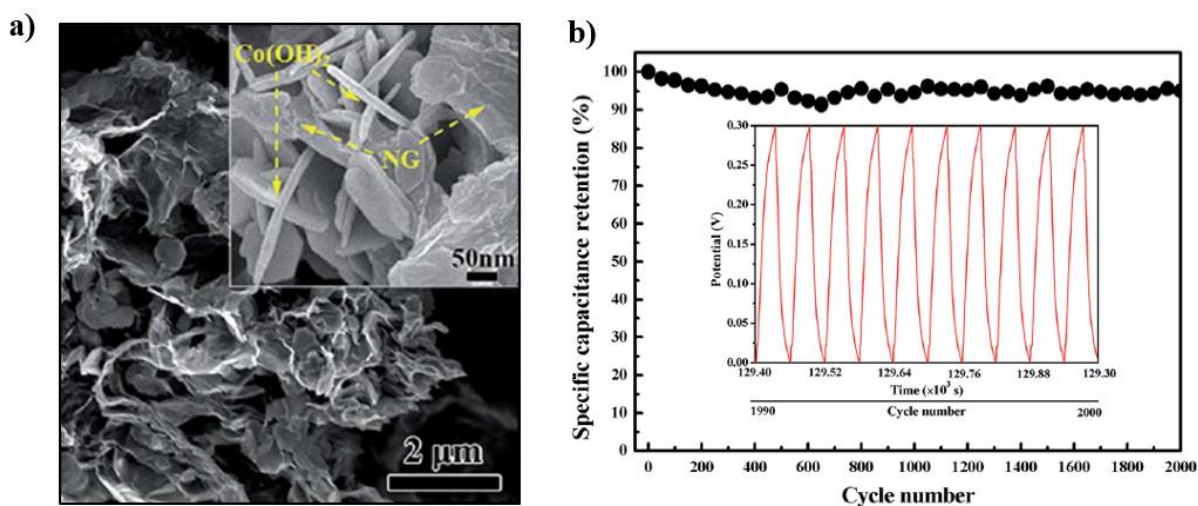


Figure 2-17: (a) SEM image of the NG/Co (OH)₂ composite electrode. (b) Capacity retention vs. cycles for the NG/Co (OH)₂ composite electrode material at a current density of 1 Ag⁻¹ over 2000 cycles. Reprinted with permission from [166].

Figures 2-18 (a) and (b) show that there are no detrimental changes in the structure after 10,000 cycles, indicating that the presence of the carbonaceous shell in the PPy and PANi has no effect [174], [176]. Furthermore, carbonaceous shell-coated PPy and PAN-electrodes achieved remarkable capacity retentions of ~85% and ~95% after 10,000 cycles, respectively, compared with 25 % and 20 % as bare electrodes. This is demonstrated in Figures 2-18 (c) and (d).

The presence of a 5-nm thick carbonaceous shell can effectively prevent the structural breakdown of polymer electrodes during the charge/discharge process, according to electron microscopy studies. Furthermore, polymer electrodes with a 5-nm thick carbonaceous shell demonstrated comparable specific capacitance and pseudocapacitive behavior to bare polymer electrodes. Moreover, the same process can be used to stabilize other similar polymer electrodes, and the ability to design and fabricate these types of electrodes has the potential to be a breakthrough in the pseudocapacitor industry [174].

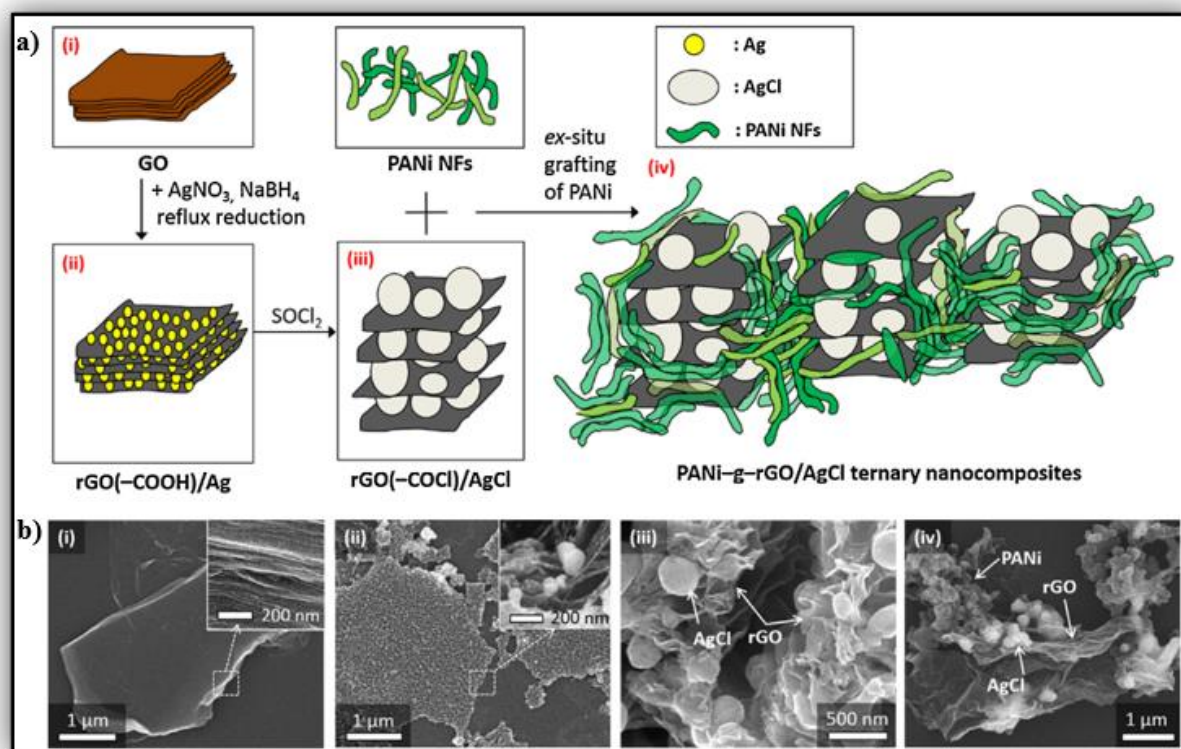


Figure 2-18: (a) & (b) SEM images before and after cycling test of 10,000 cycles for PANi@C-2h and PPy@C-2h respectively. (c) & (d) Capacity retention vs. the number of cycles for PANi and PANi@C electrodes, and for PPy and PPy@C electrodes. The cycling performance is analyzed at a scan rate of 100 mV s^{-1} . Reprinted with permission from [174].

Sungjim Im et al. showed how to improve the supercapacitive performance of a 2D nanosheet-based composite electrode. They created a hybridized electrostatic double-layer capacitor-electrochemical pseudocapacitor (EDLC-PC) electrode out of rGO-PANi nanofibers (rGO-PANi NFs). Figure 2-19 (a) showcases the fabrication of the nanocomposite supercapacitor electrode via the solution process [177], [178]. For the enhanced supercapacitive performances, insulator silver chloride nanoparticles (AgCl NPs) were intercalated into the interlayer gap of rGO. The AgCl NP intercalation exfoliated rGO layers and prevented the rGO self-restacking (which occurs through typical fabrication by the solution process) that makes it difficult to utilize the high surface-to-volume ratio of ideal mono- (or few) atomic-thick rGO layers [179]. Figure 2-19 (b) displays the SEM images with the surface morphologies of (i) GO, (ii) rGO/Ag

NPs, (iii) rGO/AgCl NPs, and (iv) PANi NFs-g-rGO/AgCl NPs nanocomposites, which can be used as a pseudocapacitor electrode.

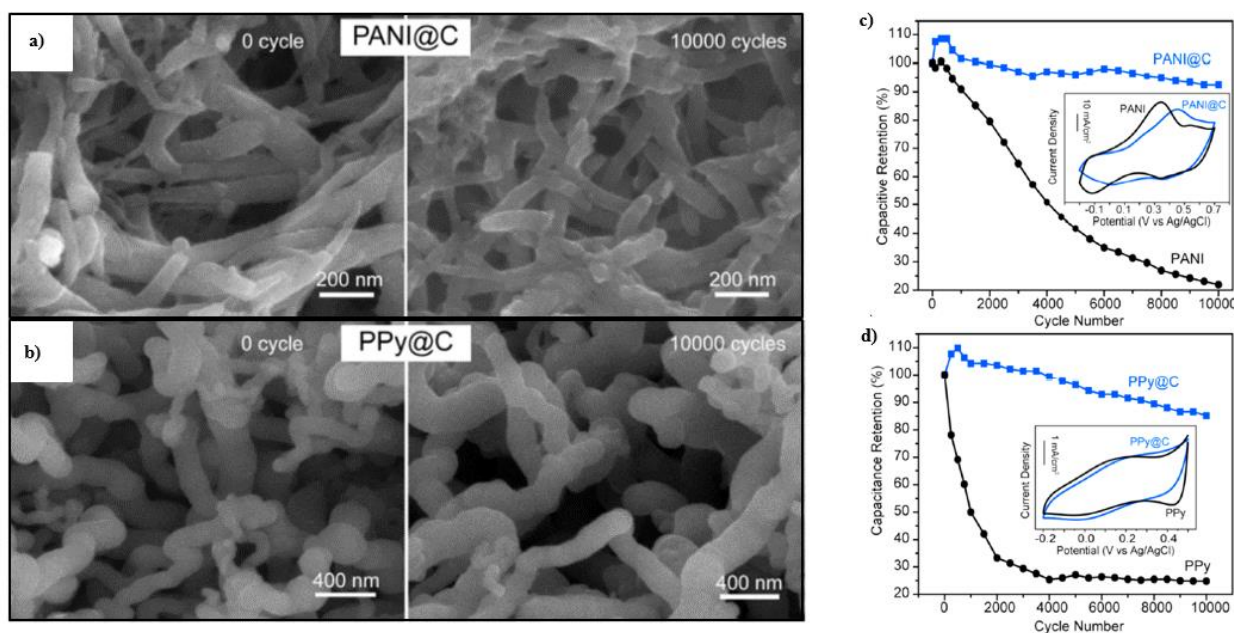
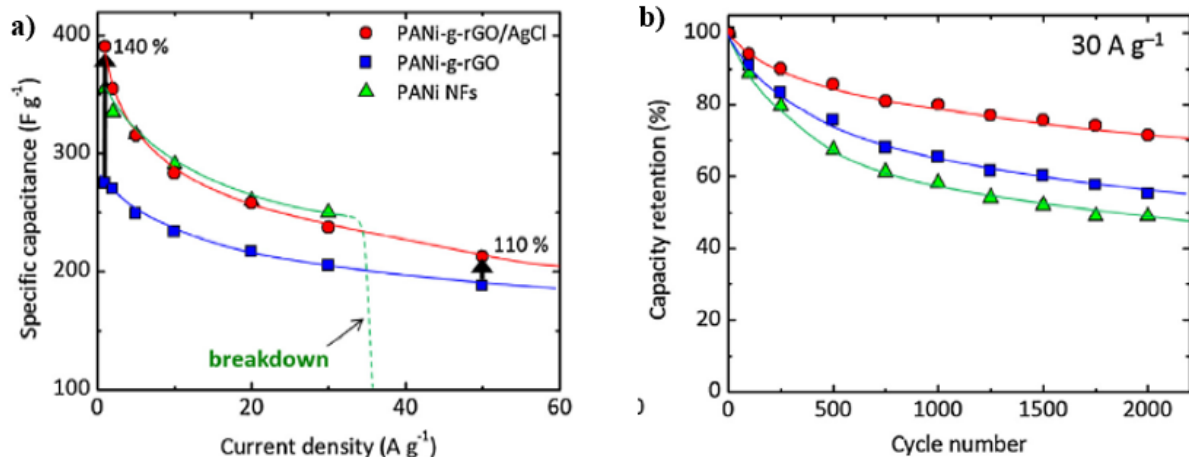


Figure 2-19: (a) Schematic diagram of the manufacturing of the PANi-g-rGO/AgCl ternary nanocomposites. (b) SEM images of (i) GO, (ii) rGO/Ag, (iii) rGO/AgCl, and (iv) PANi-g-rGO/AgCl ternary nanocomposites used in the electrodes of the supercapacitor. Reprinted with permission from [178].

As a result of this synthetic route, the specific capacitance increased by the increased specific surface area of rGO. Furthermore, the well-developed rGO edges formed by the AgCl intercalation enabled the formation of more bonds between PANi and rGO via selective grafting of PANi to the rGO edges. As a result, as conducting paths, the PANi-rGO bonds significantly reduced total electrical resistance. Increased specific capacitance, ion diffusion efficiency, and reduced electrical resistance were used to demonstrate the bi-functional roles of AgCl NP insertion in high-performance hybridized EDLC-PC electrodes [177]–[181]. Figure 2-20 (a) shows the graph of specific capacitance versus current density, the specific capacitance of ternary PANi-g-rGO/AgCl is observed to be 1.1-1.4 times higher than that of binary PANi-g-rGO at different current densities (1-50 Ag⁻¹). This is because the large

accessible surface area of rGO opened by NP intercalation makes diffusion efficient. Furthermore, Figure 2-20 (b) demonstrates that the ternary nanocomposite has higher cyclic stability (80% after 1000 cycles) than the binary composite and homogeneous PANi NFs



electrodes, which have a cyclic stability of 65% and 58%, respectively [178], [181].

Tae Guang Yun proposed an ultra-stable, stretchable electrochromic supercapacitor device made up of Au/Ag core-shell nanowire-embedded polydimethylsiloxane (PDMS), bi-stacked WO₃ nanotube/PEDOT:PSS (poly(3,4-ethylene dioxythiophene):poly(styrene sulfonate)), and a hydrogel electrolyte based on polyacrylamide (PAAm) [182]. The supercapacitor is transparent. The supercapacitor is fabricated by electrospinning the WO₃ nanotube, which is then coated with a PEDOT:PSS thin layer and drop-coated onto the Ag nanowire-embedded

Figure 2-20: (a) The curve of specific capacitance of PANi-g-rGO/AgCl, PANi-g-rGO, and PANi NFs at different current densities. (b) Cyclic performance of the PANi-g-rGO/AgCl, PANi-g-rGO, and PANi NFs. Reprinted with permission from [178].

PDMS substrate. Figure 2-21 (a) depicts the fabrication process in detail [182]. When combined with a PAAm-based hydrogel electrolyte, PDMS with an embedded Au/Ag core/shell nanowire prevents the oxidation and dehydration of silver while maintaining ionic and electrical conductivity at high voltage, even when exposed to ambient conditions. The flexible electrochemical supercapacitor is used in place of conventional supercapacitors

because it degrades less when exposed to the atmosphere and does not deform easily under tensile or compressive stress. Conventional supercapacitors degrade during cycling due to the decomposition/corrosion of the electrode and decomposition of the electrolyte [182]–[186]. Figure 2-21 (b) shows the CV curve for the different types of supercapacitors; the area under the curve is highest for WO₃NT+PL (Tungsten Trioxide Nanotubes Photoelectrochemical electrode) as the capacity increases with the incorporation of the WO₃ nanotube and the PEDOT:PSS overlayer. The achieved specific capacitance is 470 Fg⁻¹, with a capacity retention of 92.9% after 50,000 charge/discharge cycles. As a result of the dual coloration and pseudocapacitor properties of the WO₃ nanotube and PEDOT:PSS thin layer, a high coloration efficiency of 83.9 cm²C⁻¹ is observed [182]. The electrolyte choice is also critical, as PAAM has high ionic conductivity and increases the stretchability of the electrochromic pseudocapacitor by 80%. Table 2-6 shows the main factors and reasoning behind the improved electrochemical performance of the different types of pseudocapacitors.

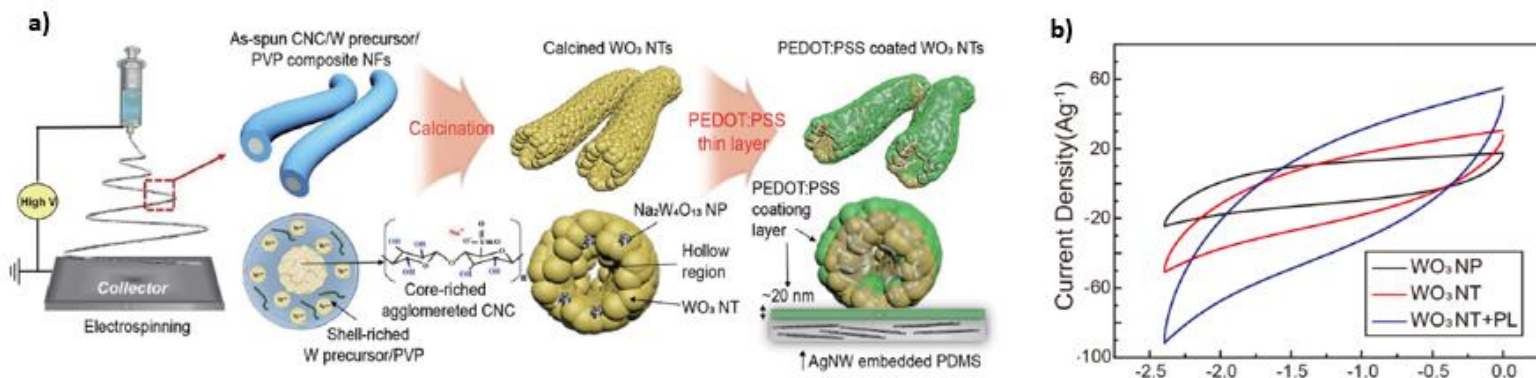


Figure 2-21: (a) The fabrication of WO₃ nanotubes and the PEDOT: PSS layer is depicted schematically. The electrospun WO₃ nanotube is coated with a thin layer of PEDOT: PSS before being drop-coated onto an Ag nanowire-embedded PDMS substrate. (b) CV test of all (transparent stretchable electrochromic supercapacitor (TSES) electrodes at a scan rate of 1 mV s⁻¹. The curve clearly shows that, with the addition of WO₃ nanotubes and the PEDOT: PSS, the capacity increases dramatically. Reprinted with permission from [182].

Table 2-7 showcases all the operational results such as capacity retention and the specific capacitance for all the electrodes used in all the cases mentioned in subsections of Section 2.1.7.1.

Table 2-6. Summary of different electrodes used for minimizing the rate of degradation in pseudocapacitors.

References	Electrode	Factors	Mechanism	Operational results
[133]	V ₂ O ₃ @MoS ₂	Atomic layer deposition, molecular layer deposition	Short ion diffusion path length, increased surface area, mass transfer, volumetric expansion	Ultra-high cycling stability
[51]	Ti-based oxides	High working potential, high operating voltage	Increased surface area, increased ion-transfer kinetics, no decomposition of the electrolyte	High voltage window, high-rate capability, good structural capability
[145]	MnO ₂ -SiO ₂	Oxidation state, negative polarization in aqueous electrolyte	No precipitate in the electrolyte (no dissolution)	High-rate capacity
[151]	NiCoO ₂ /CoS ₂	Layered structure due to the selection of nickel foam	Rapid transmission of the electrolyte, fast electron/ion transport	Mechanical stability of the electrodes (device)
[174]	Conducting polymers	Thin film/layer deposition	No significant microstructural changes during cycling	Good cycling stability
[154]	NiO/G	2D layer and diffusion channels, hybrid structure	High surface area and tailored pore distribution and porosity.	Superior cycling stability, high energy, and high power density
[160]	Co-NTC@Co ₃ S ₄ and asymmetric pseudocapacitor (Co-NTC@Co ₃ S ₄ //A C)	Layered nanosheets, conductive NG interconnected network, composite heterostructure, small diffusion electrolyte channel	Increased surface area, electron transport efficiency	Good rate capability
[166]	Co (OH) ₂ /NG	Doping, regular morphology, 3D porosity, the high diffusion rate	Large surface area, high porosity	High capacity, good structural capability, and stability
[178]	rGO@PANi	Intercalation into layers of rGO, 2D diffusion channels, conductive bonds of PANi-rGO	Enlarged specific surface area, low electrical resistance, ion-diffusion efficiency	High specific capacitance, good specific stability
[182]	WO ₃ nanotube/PEDO T: PSS	Thin layer nanostructures, less significant oxidation and dehydration of electrode, flexible electrode, incorporation of polymeric (PMMA) electrolyte	High ionic and electrical conductivity at high voltage applied, negligible deformation under high tensile stress	High specific capacitance, stretchability up to 80%

Table 2-7. Electrodes, electrolyte, preparation method, and their operational results.

Ref.	Electrode	Electrolyte	Preparation method	Specific capacitance (Fg ⁻¹)	Capacitance retention (cycles)
[133]	V ₂ O ₃ @MoS ₂	1 M Na ₂ SO ₄	One-step hydrothermal reaction	655 (3 Ag ⁻¹)	100% after 35,000 cycles
[51]	Ti-based oxides	1 M NaClO ₄ , 1 M NaPF ₆	Electrospinning, electrodeposition		93% after 10,000 cycles at 20 Ag ⁻¹
[145]	MnO ₂ -SiO ₂	Li ₂ SO ₄	Hydrothermal, electrodeposition	181	68% after 5000 cycles
[151]	NiCoO ₂ /CoS ₂	1 M KOH	In-situ, hydrothermal, electrodeposition	2186.7 (2 Ag ⁻¹)	90.4% after 4000 cycles
[174]	Conducting polymers	1 M H ₂ SO ₄	Electrodeposition	500-3500	85% (PPy) and 95% (PANi) after 10,000 cycles
[154]	NiO/G	6 M KOH	Hydrothermal method accompanied by thermal treatment. For graphene, by Hummer's method	220 (10 Ag ⁻¹), 240 (5 Ag ⁻¹)	100%-120% after 1500 cycles at 5 Ag ⁻¹
[160]	Co-NTC@Co ₃ S ₄ and asymmetric pseudocapacitor (Co-NTC@Co ₃ S ₄ //AC)	1 M KOH, 6 M KOH (asymmetric)	Hydrothermal (sacrificial template/precursor), vulcanization, and Hummer's method	3117.3 (1 Ag ⁻¹)	87% after 1000 cycles at 10 Ag ⁻¹ , 110% after 5000 cycles at 10 Ag ⁻¹ (for asymmetric)
[166]	Co (OH) ₂ /NG	6 M KOH	Hydrothermal, Hummer's method	952 (1 Ag ⁻¹)	95% after 2000 cycles at 10Ag ⁻¹
[178]	rGO@PANi	0.1 M HCl	Solution process	105	80% after 1000 cycles
[182]	WO ₃ nanotube/PEDOT: PSS	PAAm-based hydrogel	Electrospinning, coating treatment	471 (1 Ag ⁻¹)	92.9% after 50,000 cycles

2.1.8 Manufacturing Phase Summary

2.1.8.1 Summary

With the rapid development of energy storage devices such as solar cells, batteries, electric vehicles, and transportation systems, the pseudocapacitor has received a great deal of attention in the last decade due to its high energy density and high power density. The most advantageous aspect of the pseudocapacitor is its ability to function at high operating conditions — such as high operating voltages, high current densities, and a large number of cycles — at the same time with high energy output, while keeping safety parameters as a priority. Many challenges limit its applications in many sectors of the world due to the degradation mechanism, unclear energy storage mechanism, significant gas evolution, corrosion of the device, and so on. The degradation mechanism has been addressed and classified at various levels in this review, with the goal of finding potential solutions and reducing the rate of degradation for overall improved electrochemical performance of the device. Different solutions for enhancing the properties of a pseudocapacitor have been discussed in this review, with further potential improvements that could be researched or carried out for much broader applications in various industries for energy storage. The advanced nanotechnologies being researched enable pseudocapacitors to achieve high energy and power density, while also having a long cycle life. The development of long-cyclable pseudocapacitors with good rate performance and high capacity retention during the charge/discharge process has resulted from improvements to the electrode and the electrode–electrolyte interphase (surface area) or SEI. As a result of these advancements,

the rate of degradation in pseudocapacitors has been reduced, which could lead to large-scale applications in electric vehicles, energy storage, and research purposes.

2.2 Operational Phase: Unwanted Degradation in Lithium-ion Batteries

2.2.1 Introduction

⁶The transportation sector is one of the largest contributors to global greenhouse gas (GHG) emissions [187]–[189]. The negative effect of GHG on human life and the environment provides a strong driving force for reducing GHG emissions [190]. Transportation electrification is a promising solution to alleviate the growing concern about GHG emissions. More and more electric vehicles (EVs), hybrid electric vehicles (HEVs), and plug-in hybrid electric vehicles (PHEVs) have been developed and deployed as alternatives to traditional internal combustion engine (ICE) vehicles [190]–[192]. The success of transportation electrification depends largely on energy storage systems. As one of the most promising energy storage systems, lithium-ion batteries (LiBs) have many important properties to meet the wide range of requirements of electric mobility [193], [194]. The challenging requirements for further development of the LiB system are longer life, fast charging, low temperature charging, self-recovery capability, and safety performance. In fact, according to the literature, these requirements are related to the aging mechanisms of lithium plating and anode kinetics. Clear diagnosis, prognosis and understanding of the mechanisms and effects of lithium plating on the performance of cells and battery packs

⁶ This section is based on a previously published article:
X. Lin, Kavian Khosravinia, X. Hu, Ju. Li, and W. Lu. "Lithium Plating Mechanism, Detection, and Mitigation in Lithium-Ion Batteries", *Progress in Energy and Combustion Science*. The material is reproduced here with permission from the publisher, [Elsevier].

are critical to the safe and durable design of LiB systems. However, understanding the aging mechanisms is complex due to the intricate, nonlinear, and path-dependent nature of battery degradation [195], [196]. As a result, as shown in Figure 2-22, lithium plating has been the subject of several levels of research, ranging from understanding the mechanism of lithium plating to demonstrate why, where, when, and under what conditions this phenomenon occurs, to determining the most effective method to detect, predict, and prevent it. Therefore, the purpose of this article is to review the existing work in literature and identify some of the fundamental knowledge gaps at each of these levels.

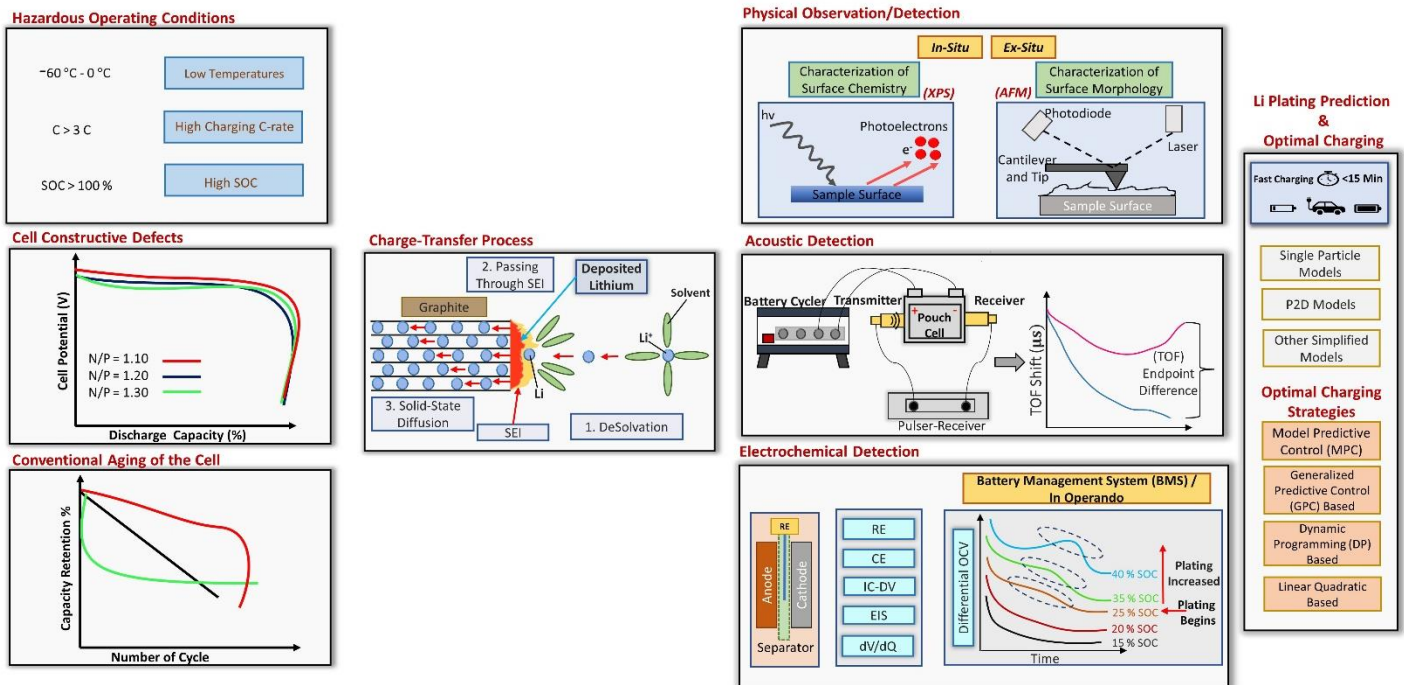


Figure 2-22: Lithium Plating Phenomena at Different Research Levels.

A typical lithium-ion battery cell, as shown in Figure 2-23 (A), comprises a composite negative electrode, separator, electrolyte, composite positive electrode, and current collectors [197], [198]. The composite negative electrode has a layered and planner crystal

structure that is placed on the copper foil, which functions as a current collector. There are three types of carbonaceous materials: graphite, graphitizable carbon, and non-graphitizable carbon (hard carbon) [199]. Graphite is frequently used as a negative electrode because of its excellent performance, low cost, and non-toxicity [200]. The composite positive electrode (cathode) is a metal-oxide with a tunneled or layered structure that is coated with aluminum foil [201]. Aluminum acts as a current collector. The Electrolyte plays a critical role in the lithium-ion diffusion process. The electrolyte allows lithium ions to move between electrodes [202]. The separator is a piece of thin microporous polymer film (10 to 30 μm) soaked in the electrolyte and sandwiched between the anode and cathode electrodes to prevent shorting of the two electrodes [197].

During the normal charging process, electrons are extracted from the cathode and moved to the anode through the external circuit by the charger. Meanwhile, Li^+ ions are de-intercalated from the cathode and moved to the anode through electrolyte [200]. During discharge, the entire procedure is reversed. The lithium-ion intercalation process (during charging) has three major steps [203]: (i) the Li^+ diffuse out of the cathode (ion movement through the solid electrode), (ii) the diffusion of solvated Li^+ ions in the electrolyte, (iii) de-solvation Li^+ ions passing through the SEI and embed into the interlayer of graphite [204]–[206]. Step (iii), generally known as the charge-transfer process, is broken into three subprocesses [207], [208]: 1) de-solvation of solvated Li^+ ions (strip off their solvation shell), 2) naked Li^+ passing through the SEI, and 3) solid-state lithium diffusion into graphite (Li^+ reaching the anode and receiving an electron, which could occur at the anode-SEI interface or the anode-electronic conductor-SEI interface [204]) (Figure 2-23 (C)).

These steps would be favored in an ideal battery working condition. Nonetheless, in real-world applications, LiBs are subjected to a variety of severe circumstances, which have a substantial impact on battery performance and longevity. Battery degradation is a complicated issue involving numerous physical and chemical processes. Degradation is dependent on a number of complex mechanisms caused by a variety of factors (e.g., intrinsic and extrinsic) [209], [210]. Intrinsic factors are classified into two categories: material properties and manufacturing procedures [211]. Extrinsic factors derive from the LiB operating conditions, such as charging at a high C-rate, high state of charge (SOC), or low temperature [209], [210]. As shown in Figure 2-24, the aging mechanisms affect not only the anode and cathode electrodes, but also other LiB components such as electrolyte, separator, binder, and current collector [211]–[213]. The most detrimental aging mechanisms impacting graphite anode electrodes are solid electrolyte interphase (SEI) film growth, binder decomposition, and lithium plating [214]–[216]. According to the literature, aging mechanisms can be divided into three main degradation modes (DMs): loss of lithium inventory (LLI), loss of active materials (LAM) [217], and loss of electrolyte [211], [218]. In LLI, lithium ions are consumed by side reactions, such as SEI film formation and decomposition, electrolyte decomposition, and irreversible plating [219]. Since these lithium ions are no longer cyclable for the intercalation process, the cell capacity is reduced (capacity fade) [220], [221]. LAM, on the other hand, is usually related with structural changes and material loss [209]. The active mass on the anode is diminished due to graphite exfoliation, binder decomposition, electrode particle cracking, or dead lithium blocking the active site pathway. Furthermore, the active mass of the cathode is reduced due to transition metal dissolution, structural disordering, and electrode particle cracking [213], [220],

[222], [223]. The other significant cause of degradation is electrolyte loss; the deposited lithium on the anode interface reacts with the electrolyte, consuming the electrolyte [202], [218]. The significant reduction in electrolyte content may result in capacity and power fading at the end of the battery's life.

Among the several aging mechanisms in LiBs, one of the most detrimental is the deposition of metallic lithium or lithium plating on the graphite anode surface. This is due to the fact that lithium plating may not only promote further degradation, but it may also have a negative impact on the safety of LiBs [224]. During charging, lithium-ions are deposited on the surface of the graphite anode rather than being intercalated into the interstitial space between the graphite anode's atomic layers [225]. In general, the deposited lithium can be reversible or irreversible. The irreversible portion can react with the electrolyte to form a secondary SEI layer, or it can form a high-impedance “dead” lithium film that is electrically isolated from the graphite anode and remains irreversible, increasing internal resistance and decreasing energy density [215], [226]. The irreversible portion causes capacity fade to be accelerated. In severe circumstances, the accumulated lithium might also form a dendrite. Dendrites can develop and pierce the separator [227]. The reversible portion describes the deposited lithium with a durable electrical contact on the anode interface, which can undergo charge transfer reaction into the electrolyte and subsequently re-intercalate into the anode, this process is known as lithium stripping. The stripping process occurs throughout the rest or discharge process following lithium plating; completely reversible lithium has no capacity retention [228], [229]. One of the major

limiting reasons for fast charging is lithium plating. As a result, one major difficulty for fast charging technologies is the reduction of lithium plating during the charging process.

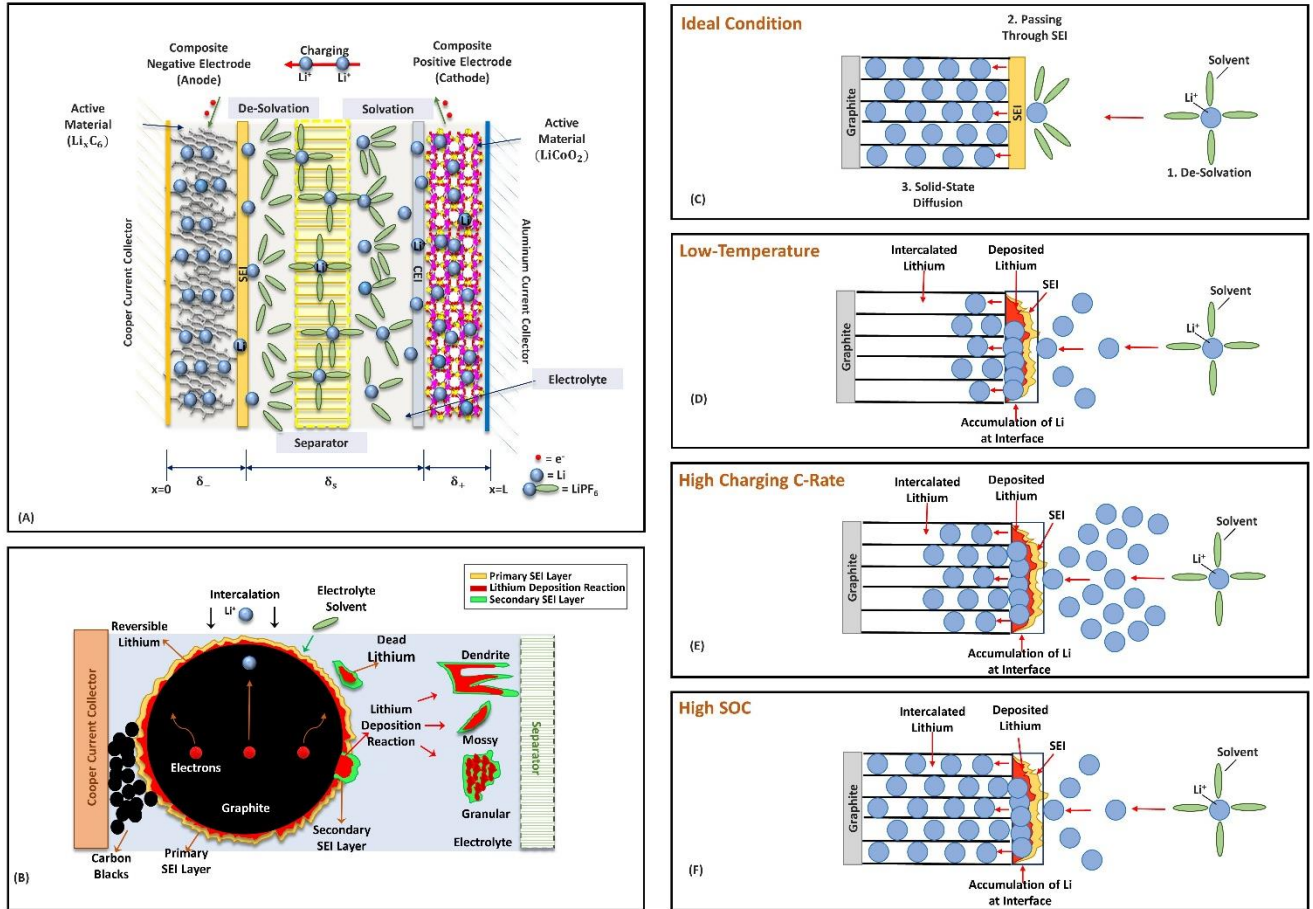


Figure 2-23: Schematic of a Battery Cell During Charging Process and Lithium Plating Behavior under Different Operational Conditions. (A) In the intercalation/de-intercalation process, Li -ions intercalate into or de-intercalate from the active material between the two electrodes in a reversible manner. (B) Schematic of lithium plating-stripping on the graphite anode electrode. The primary SEI layer (yellow color) is formed at the anode surface during the first charge of the cell to protect the electrode against corrosion. Because the primary SEI layer prevents electrons from making direct contact with the electrolyte, metallic lithium (red color) is deposited between the primary SEI layer and graphite particles. Mossy and dendritic deposition are two well-known morphologies of deposited lithium. When deposited lithium reacts with electrolyte solutions, the secondary SEI layer (green color) forms. (C) Under ideal conditions, the charge-transfer process consists of three steps: 1. de-solvation of solvated Li^+ ions, 2. Li^+ shuttle through the SEI, and 3. solid-state lithium diffusion into graphite particles. (D) At low temperature, Li^+ ions move slowly in graphite due to the low diffusivities of lithium ions and the sluggish charge transfer kinetics which leading to lithium plating. (E) At high charging C-rate, Li^+ ions move fast and a large amount of Li^+ accumulate at the electrode interface because the lithium solid diffusion is lower Li^+ diffusion in

the electrolyte, then saturate concentration happens on the lithium ions, and lithium plating happens. (F) Under the high SOC condition, Li^+ ions move slowly in graphite under high SOC conditions.

Several studies have been done, including investigations into lithium plating mechanisms at various charging conditions, the development of effective detection techniques, and the development of strategies for mitigating lithium plating. Figure 2-25 (A) and (B) outline the various charging currents (C-rates), testing temperatures, and commercial cell types used in the literature to explore one-set lithium plating. The C-rate is known as the current value that discharges a battery within 1 h from a fully charged state to a fully discharged state [230]. It is generally known in battery testing as a current value equal to a cell's rated capacity (Ah), which may not always be valid. The test temperature is the temperature at which the cell is saturated, where a climate chamber is often used to maintain a steady temperature throughout the test. The temperature of the test varies from study to study and might range from $-60\text{ }^{\circ}\text{C}$ to $80\text{ }^{\circ}\text{C}$. According to our findings, the majority of the research groups tested the cells at room temperature ($25\text{ }^{\circ}\text{C}$) at 1 C. Higher C-rates and lower temperatures also have been employed to study one-set lithium plating. Several studies, however, investigated lithium plating at lower charging rates (0.3 and 0.5 C-rate) and temperature ranges from ($-20\text{ }^{\circ}\text{C}$ to $40\text{ }^{\circ}\text{C}$). However, further research on lithium plating at lower temperatures and greater C-rates is still necessary. Furthermore, five various types of commercial cells were employed in the literature for the research of lithium plating, ranging from 18650 and 26650 types (1.5 Ah to 3.4 Ah) to large scale pouch types (9.5 Ah to 16 Ah). The most utilized cells in the literature for investigating lithium plating are cells with graphite as the anode, such as lithium nickel cobalt manganese oxide (NMC 111 (40%)), lithium iron phosphate (LFP (18%)), and lithium cobalt oxide (LCO (12%)). These

cells are particularly significant since they have been investigated by various research organizations and, as a result, with numerous complementary approaches.

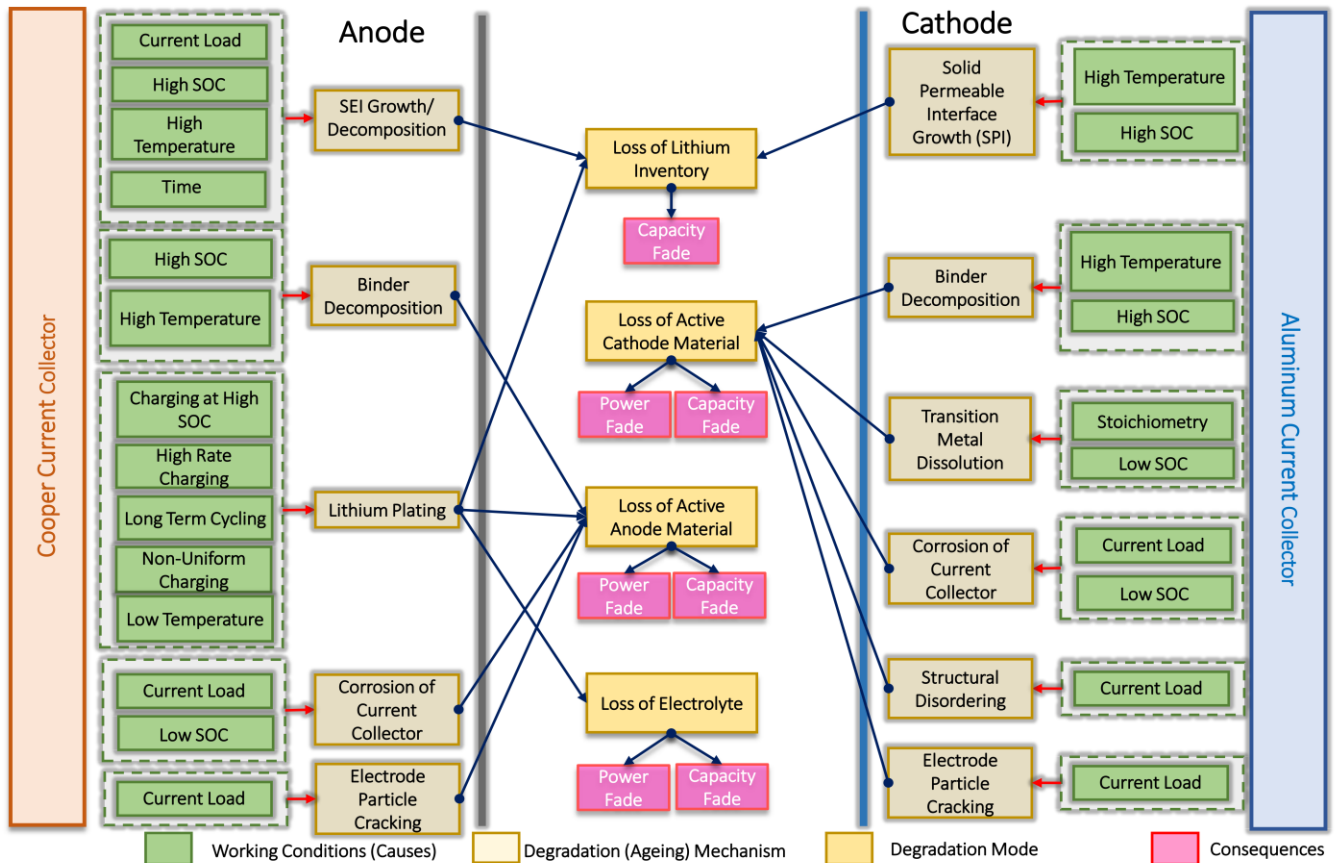


Figure 2-24: Degradation Modes, Ageing Mechanisms, and the Affected Components in Lithium-ion Batteries. There are many different ageing mechanisms, and they are generally divided into three different degradation modes (DMs): loss of lithium inventory (LLI), loss of active material (LAM) and loss of electrolyte. There is a general relationship between battery working conditions and the affected components with the corresponding ageing mechanisms. Charging at a high C-rate, a high state of charge (SOC), or at a low temperature are all critical operating conditions that accelerate battery degradation [220].

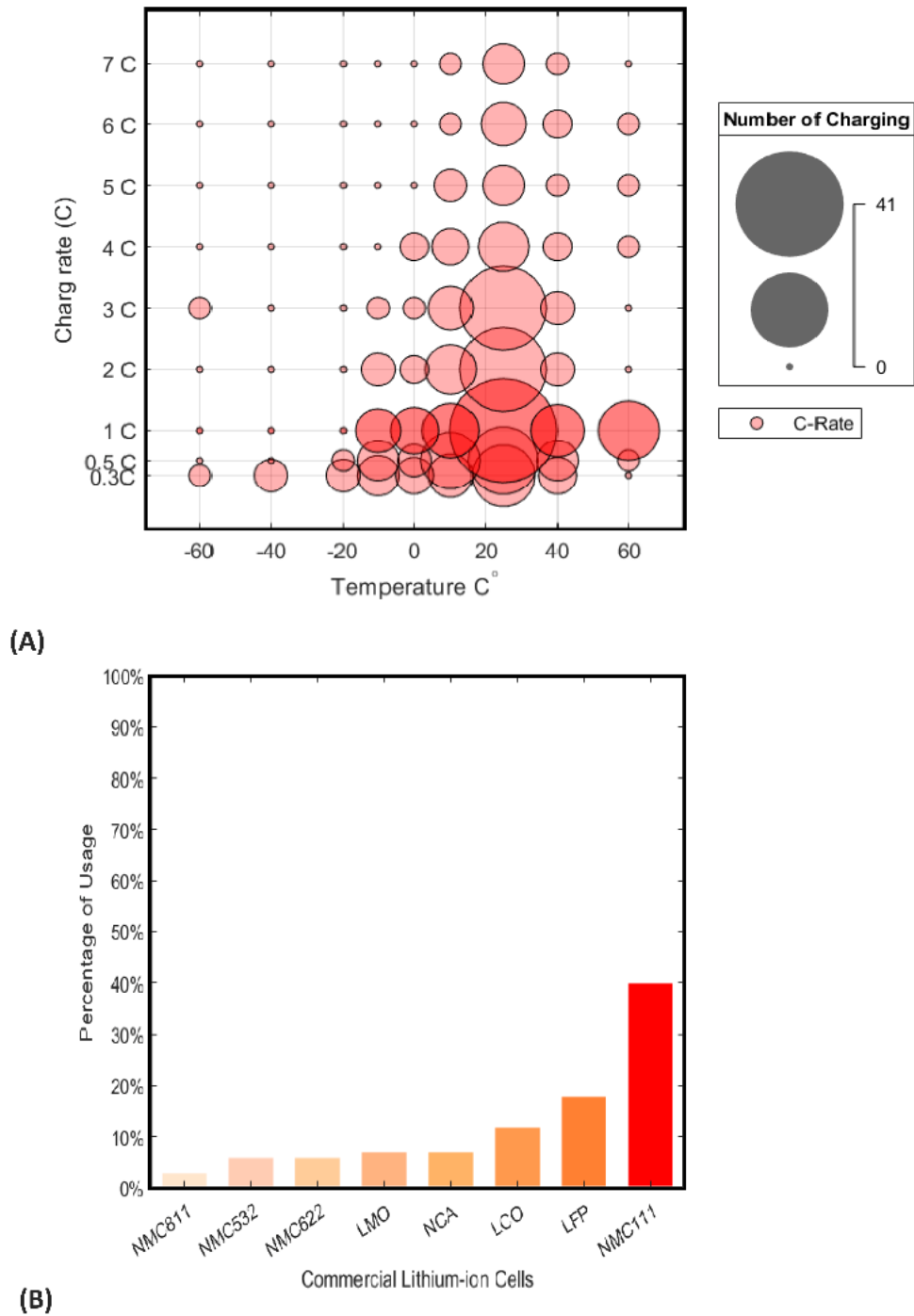
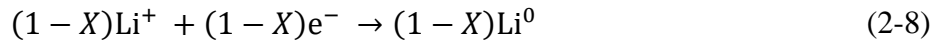


Figure 2-25: One-set Lithium Plating C-rates/ Temperature Summary. (A) Analyzing the existing literature on lithium plating based on two common testing conditions: temperature and C-rate. Larger dots represent a greater number of publications that used that C-rate at that temperature. (B) Cells from the literature that had been evaluated for lithium plating were compared. The data sources are listed in the supplementary file.

2.2.2 Lithium Plating Reactions

Lithium plating is a parasitic process that goes along with the lithium intercalation process. Equation (1) shows the complete insertion of Li^+ ions into the graphite anode electrode. Intercalation is a diffusion-limited process, meaning that a certain amount of Li^+ ions can be embedded into the interlayer of graphite per unit time at a given temperature [223]. The potential range for Li^+ ions insertion inside the graphite is 65-200 mV vs. Li^+/Li^0 and no lithium plating occurs at this level [215]. Equation (2) shows partial or full deposition of lithium on the anode surface. The charging current is divided into two parts: (i) intercalation current and (ii) lithium plating current [224]. Ideally, the charging current affects the pace at which Li^+ ions reach the anode surface. However, there is a competition between the intercalation current and the lithium plating current. As the charging process continues, the vacancy spots in the graphite layer will decrease, and therefore the intercalation current is decreased while the lithium plating current is increased [205]. When the anode potential drops below 0V, lithium plating is thermodynamically permitted because the rates of lithium deposition exceed the rates of intercalation. The main contributors to the graphite electrode overpotential are i) charge transfer, ii) electrolyte concentration (mass transfer), and iii) lithium solid-phase in the negative electrode [225]. These are the kinetics cause for lithium plating. When the local potential at the negative electrode falls below 0V (vs. Li / Li^+) due to high SOC, high charging C-rate, and low temperatures, all of which polarize the electrode, lithium plating can occur thermodynamically [193], [231]. However, because the reaction enthalpy is more positive, lithium plating is not as favorable as intercalation from a thermodynamic standpoint. Kinetic arguments alone are insufficient to address lithium plating. It must be remembered

that LiB charging is a dynamic process that is not in equilibrium, especially at high C-rates. In thermodynamic equilibrium, the cell voltage can be determined by the Nernst equation [226], [227]. The equilibrium potential difference can be used as an indicator of the thermodynamic driving force of plating vs. intercalation, as plating and intercalation compete for electrons and lithium-ions [228]. It is well-known that a redox response's equilibrium electrode potential shifts with temperature, for both lithium plating and graphite intercalation, this temperature variability leads to a heterogeneous distribution of the equilibrium potential on the anode [227]. The improvement of the Li^0/Li^+ equilibrium electrode potential enhances the thermodynamic onset for metallic lithium plating [228]. It should be noted that the plated lithium will consume more electrolytes than normal conditions and lithium plating can happen locally, due to inhomogeneity over the graphite electrode [229].



Lithium plating has three different outcomes, which are dead lithium, reversible lithium, and secondary SEI film, as shown in Figure 2-23 (B) [232]. A portion of deposited lithium that has detached and lost electrical contact with the graphite is referred to as dead lithium [206]. Dead lithium may create a tortuous pathway for lithium-ion transport, reducing the active area for intercalation [232]. The secondary SEI film is the result of a reduction of solvent electrolyte (R) by the deposited lithium (Equation (4)). Both dead lithium and SEI film are irreversible [233] and lead to removing lithium from the system and capacity loss over time [203]. Reversible lithium is reinserted into the graphite in the lithium stripping process (Equation (5)) during relaxation or resting time (Equation (3)) [234]. During

relaxation, the reinsertion continues until all the reversible lithium is inserted into the anode. The lithium stripping process is a more facile reaction than lithium deintercalation (Equation (3)). However, the reversible lithium in the lithium stripping process during discharge has two destinations, the intercalation into the graphite and transfer to the cathode to deliver output current [234].



Based on the working and charging conditions, the morphology of deposited lithium can be classified into three types, including mossy, granular (particle-like), and dendritic (needle-like deposits) [193], [233]. Morphology is determined by the current rate. Mossy and granular lithium form at low current rates, whereas dendrites form at high current rates [235]. Dendritic growth can be particularly destructive to the cell because it can penetrate the separator and reach the cathode electrode, causing an internal short-circuit and rapid heating of the cell. The generated heat may first melt dendrite and disconnect the short, and later it may trigger other aging mechanisms, such as SEI formation and electrolyte decomposition [236]. In terms of safety, the dendritic structure is considerably less safe than the mossy and granular lithium forms. Internal short circuits are classified into two types, soft shorts and hard shorts. Soft shorts normally disappear after discharge and do not cause cells to fail catastrophically. A soft short may reduce the cell's current and voltage while simultaneously raising the local temperature [237], [238]. The heat generated by the soft short can cause an exothermic reaction with the electrolyte, causing the separator to melt. Hard shorts are characterized by slightly larger short circuit currents between the

anode and the cathode due to their low resistance [237], [238]. Due to a higher increase in local temperature, hard shorts are also more likely to contribute to thermal runaway. It should be noted that lithium plating is a result of the actual operating conditions, poorly balanced cell, material properties, electrode design, and cell design [231].

2.2.3 Main Factors Affecting Lithium Plating

Many research efforts have been undertaken to understand how, where and why lithium plating occurs during both normal and fast charging conditions. However, the mechanisms of lithium plating have not been fully elucidated due to its complex nature [239]. According to numerous previous researches, lithium plating occurs as a result of three major factors, which include but are not limited to: (i) hazardous operating conditions, (ii) cell constructive defects, and (iii) conventional aging of the cell (Table 2-8) [240].

2.2.3.1 Hazardous Operating Conditions

Lithium plating occurs when batteries are subjected to harsh conditions, such as charging at high C-rates, charging at a high state of charge (SOC), and charging at low temperatures[241]–[245]. These harsh conditions can limit the charge transfer kinetics in the electrolyte and solid-state diffusion, causing anode potential to drop below the potential of lithium metal, causing lithium plating to occur [246], [247]. Because hazardous operating conditions are one of the most important factors affecting lithium plating, we will provide a comprehensive review of the main parameters that accelerate lithium plating under the aforementioned conditions in this section.

2.2.3.1.1 Low-Temperature Effects

Low temperature is generally acknowledged to be one of the critical barriers to fast charging. Charging with high charge currents frequently results in a severe capacity fade. Charging a 7.5 Ah cell at 1 C-rate at 0 °C, for example, would result in a considerable capacity loss (3.6%) [245]. Generally, the power and energy densities of LiBs are reduced at low temperatures, particularly during the charging process, due to three major factors; decreased ionic conductivity in the electrolyte, poor solid diffusivity of lithium-ion in the electrode, and charge-transfer rate[248]–[250]. According to the Arrhenius equation, at low temperatures, the cell internal resistance increases due to decreasing ionic conductivity in the electrolyte; however, decreased ionic conductivity is not the primary barrier in low temperature charging. Studies show that the poor Li^+ diffusivity within the electrodes may be one of the primary cause for lithium plating at low temperature, where lithium ions accumulate at the interface between carbon particles and electrolyte [232], [233], [245]. Indeed, lithium plating occurs when the surface concentration of lithium ions in carbon particles reaches a maximum that the particles' active ingredient can retain. The other major obstacle in low temperature charging is sluggish charge transfer kinetics. As soon as the current is applied, a large overpotential is produced, resulting in a rise in anode resistance. As anode polarization increases, the anode potential falls below 0V (vs. Li / Li^+), resulting in lithium plating, where Li^+ ions accumulate at the anode interface rather than intercalation, as shown in Figure 2-23 (D) [235], [239]. In addition, the potential drop of the interface between the composite anode and the separator is larger than that at other areas on the anode, indicating that the lithium plating begins on the separator side [232], [251], [252]. As a result, charging currents at low temperatures should be strictly

controlled. The lithium deposition at low temperatures may be suppressed by applying a pre-heating strategy prior to charging the cell or by charging the cell at low rates. Recently, Yang and coworkers developed a controllable cell structure consisting of thin nickel (Ni) foils embedded within the cell. The Ni foil acts as an internal heating material, generating immense and uniform heating in less than 10 seconds. The structured cell can be charged to 80 % SOC without lithium plating in 15 minutes with high charging currents (3.5 C-rate) at temperatures as low as -50 °C [253]. The same group recently developed an asymmetric temperature modulation (ATM) method that charging a cell by elevating the cell temperature to 60 °C during charging. They showed that lithium plating may be eliminated with a short exposure time to 60 °C (10 minutes per cycle) [254]. It should be noted that, from an EV standpoint, most modern EVs have an effective thermal management system that prevents extreme operating temperatures. In addition, at low temperatures, electricity from the grid is often used to preheat the cells.

2.2.3.1.2 High-Charging C-rate

Fast charging is becoming increasingly important for EVs and other types of applications. Fast charging, which is based on a high charging current (C-rate), has a significant impact on the battery's performance and cyclic life due to accelerated aging. The charging rate is more likely to exceed the intercalation rate during fast charging; with a higher C-rate, the amount of Li^+ ions moved from the cathode to the anode in the charge-transfer process per unit time increases. Increased charging rates are often associated with higher polarization due to transport and kinetic overpotentials, making lithium plating favorable [255], [256]. For example, to recharge a cell in 10 mins, a charge rate of 6 C is required. At this charge rate Li^+ ions start to accumulate at the anode surface (Figure 2-23 (E)), since the

Li^+ diffusivity within the electrode is substantially lower than the Li^+ diffusivity within the electrolyte. As the high-rate charging continues, the accumulated Li^+ ions result in a high concentration gradient of Li^+ ions on the graphite surface; if the concentration at the anode surface is saturated, lithium plating occurs. Furthermore, because fast charging uses a higher charge current, more heat is generated due to the quadratic dependence of the amount of irreversible heat generation rate on the current. In fact, lithium plating and temperature rise are known as major side reactions during the fast charging process [257].

2.2.3.1.3 High SOC

Each cell has an upper cutoff voltage predefined by the manufacturer. The failure of a battery management system (BMS) to stop charging beyond its upper cutoff voltage during the charging process is the main cause for overcharging (high SOC) of the cell. By definition, high SOC is a condition in which the capacity of the LiB is already full, but the electricity flow is still forced through the LiB [258]. At higher SOC, as the charging continues, it is much easier for the concentration of Li^+ ions on the anode surface to exceed the maximum allowable level and become saturated (Figure 2-23 (F)). Lithium ions start to deposit on the anode surface once the anode is saturated [205], [235]. Juarez-robles et al. [259] studied the effect of high SOC on graphite/LCO 5 Ah pouch cells at the various cut off voltages ranging from 4.2 V to 4.8 V. Cells were charged beyond 4.5 V, indicating high-rate capacity fade, lithium plating, electrolyte decomposition, and significant volume expansion. Dendrite structures are observed in cells that charged at 4.6 V, 4.7 V, and 4.8 V [259]. The dendrite structures were penetrated to the porous separator, resulting in a micro-internal short-circuit. Moreover, at the high SOC, side reactions are not only limited

to the anode electrode but also the decomposition of electrolyte occurs at the cathode electrode.

2.2.3.2 Cell Constructive Defects

The importance and effect of the cell manufacturing process and cell properties on lithium plating have been proved many times in the literature, where for example, Liu and coworkers showed that a cell with a negative to positive (N/P) ratio of 1.19 compared to a cell with an N/P ratio of 1.06 results in a lower aging rates and impedance rise [260]. The local cell defects can have an impact on lithium plating. For example, separator deformation (pore closure) which might occur during the cell manufacturing process or operation as a result of internal mechanical stress accumulation during charging or aging, would lead to lithium plating [261]. Furthermore, the kinetics on the material level can be characterized by the activation energy barrier, where the kinetics of interfacial Li^+ ion transfer in the material is one of the important factors in the charge transfer [208], [235], [262]. There is a correlation between the intercalation kinetics and the lithium plating behavior [263]. Xu et al. [207] reported that desolvation is the most energy-consuming (50 kJ mol^{-1}) step in the charge-transfer process while the overall activation energy barrier of the graphite/electrolyte is about ($60 - 70 \text{ kJ mol}^{-1}$) [264]. In another study, Yao et al. [265] found that due to the difference of the energy barrier for lithium de-solvation on the edge plane and the basal plane of graphite, the intercalation process prefers to occur at the edge plane of the graphite instead of the basal plane. We would like to note that during lithium plating, lithium-ions tend to continue deposition on the surface where lithium has been previously deposited.

2.2.3.3 Ageing of the Cell

When the cell operating conditions are safe and the defects of the cell structure are eliminated, lithium plating is still caused by the conventional aging of the cell. As stated earlier, the most common mode of degradation in the literature is LLI and LAM, where the LAM can be further divided into four types based on the affected electrode and the degree of lithiation: loss of active material on delithiated negative electrode (LAM_{deNE}), loss of active material on delithiated positive electrode (LAM_{dePE}), loss of active material on lithiated negative electrode (LAM_{liNE}), and loss of active material on lithiated positive electrode (LAM_{liPE})[217]. During cycling, lithium deposits accumulate continuously. The side reaction between the plated lithium and the electrolyte generates new SEI, resulting in capacity fading and increased impedance. Trends in these aging mechanisms can be used to study lithium plating. The analysis of capacity fade curve shapes will provide insight into the mechanism of aging and link their effects to the incidence of lithium plating. These curve shapes were classified into three types, linear capacity fade, decelerated capacity fade, and accelerated capacity fade, all of which can be a function of the number of cycles involving lithium plating. It has been proved that in the testing of commercial cells, batteries can have a two-stage capacity fade trend. The capacity fading is fairly constant in the first stage, with a degradation mode related to LLI [217]. An accelerated capacity fading is found in the second stage of degradation, usually after 500 cycles. The second stage is frequently expected to originate from LAM_{deNE} . Ansean et al. [240] showed that LAM_{deNE} occurs at a pace four times faster than LLI, resulting in cell imbalance and over-lithiation of the negative electrode, which leads to lithium plating. They found that at the turning point of sudden capacity loss (curve shape), lithium deposition becomes irreversible. The

second stage does not usually occur due to changes in cell use, but it could be the product of underlying silent degradation mechanisms from the beginning of life [266]. The type of silent degradation will be influenced by the cell's chemistry as well as its form factor (pouch and cylindrical cells). These silent degradations have an incubation duration during which, at the full-cell stage, they do not cause any capacity loss. The loss of negative electrodes is often the culprit in graphite-based cells [266]. Therefore, it is important to observe in detail the modes of degradation, particularly those that may lead to lithium plating. Aside from the ratio of LAM_{NE} to the LLI, the plating threshold ($LAM_{NE,PT}$) was postulated as a plausible predictor of an accelerated degradation stage [267]. Cell characteristics (loading ratio and starting offset), capacity loss, and the two degradation modes (LLI and LAM_{PE}), all affect this value, with values beyond this threshold resulting in lithium plating [267]. In another study, Schuster et al. [268] found a significant decrease in capacity at moderate temperatures and charging rates, where lithium plating was associated. They showed that the lithium plating was happened due to significantly decreased ionic kinetics of the graphite because of SEI growth and graphite active material loss. It should also be noted that in literature, the capacity curve is often plotted against temperature (Arrhenius plot), which is obtained from cycling experiments under various temperatures. Lithium plating leads to quicker aging at lower temperatures, although without lithium plating, it typically ages faster at rising temperatures [269].

Table 2-8. Factors causing lithium plating.

Factors Influencing Lithium Plating	Causes and Conditions
Hazardous Operating Conditions	(a) Low temperatures (b) High charging C-rates (c) High SOCs
Cell Constructive Defects	(a) Cell properties and poor balancing (negative to the positive ratio of electrodes, geometric misfits, and poor electrolyte components)
Conventional Ageing of the Cell	(a) Leading to cell unbalance (b) Kinetic degradation (Capacity fade, energy fade, CE decrease, energy efficiency fade and resistance increase)

2.2.4 Lithium Plating Detection Approaches

Detecting lithium plating in its early stages is often challenging. To understand the formation and growth of lithium plating, extensive efforts have been made in the past to characterize and observe the anode lithium plating morphology [270]. Many approaches (in-situ, ex-situ, non-destructive, and recently in-operando methods) have been presented by researchers to investigate lithium plating mechanisms in LiBs. These detection methods are classified into three main categories: (i) physical characterization of surface morphologies, (ii) physical characterization of surface chemistry, and (iii) electrochemical methods. The first and second categories are based on physical properties of the electroplated lithium films, such as morphology, chemical composition, and surface chemistry, whereas the third technique is based on electrochemical reactions between the electrolyte and metal lithium [205]. These techniques enable ex-situ and in-situ investigations. To study lithium plating using ex-situ methods, post-mortem analysis is required, in which the cell is disassembled and opened with special tools, and then the desired specimen is transferred to microscopes or spectrometers for further investigation. In-situ approaches, on the other hand, necessitate a complex and time-consuming

spectroelectrochemical cell design [271]. In the following subsections, we have systematically classified the existing lithium plating detection approaches to highlight the technological status of this ever-evolving research field and current research gaps. Furthermore, we have classified each electrochemical approach based on its ability to be used on-board in real-time automotive applications. We briefly review the post-mortem analysis steps, including cell disassembly, specimen processing, and specimen analysis, as this is the basic procedure for most of the ex-situ approaches.

2.2.4.1 Post-Mortem Analysis for Lithium Plating Study

In literature, methodologies or procedures for post-mortem analysis of lithium plating have not been clearly explained. Research groups mainly carried out the procedures based on their own expertise and experiences [272], [273]. Therefore, we provide a snapshot of the detailed steps for the disassembly process and post-mortem analysis (Figure 2-26). The first stage, as illustrated in Figure 2-26 (A), is to deep-discharge the cell (end of the discharge voltage 0 V) to reduce the potential risk of the short circuit during the cell opening process [274]–[276]. Following that, since the electrode sample surfaces are reactive to the atmospheric gases (H_2O and O_2), the cell should be transferred to the controlled environment to decrease the risk of surface contamination during the disassembly process. In general, two types of controlled environments are specified for this procedure: argon-filled glove boxes and fume hoods (Figure 2-26 (B)). The choice of either option is dependent on the cell design and the goal of the investigation [273]. Choosing an appropriately controlled environment is not only vital for safety, but it can also have an impact on the experimental outcomes [273]. The entire disassembling procedure takes

place in a controlled environment. To avoid sample contamination, the H₂O and O₂ levels in the argon-filled glove box should be between 0.1 ppm and 10 ppm [277], [278]. If the samples do not need to be protected from atmospheric gases, the disassembly procedure can be carried out in a fume hood. To avoid inhaling dangerous gases, the fume hood should evacuate the air at a rate of 60-100 feet per minute [273]. The final step of the disassembly process is cell opening. Non-conductive tools are recommended to prevent any short-circuiting between the cell terminals. The cell configuration will determine which cutting tool should be used in the disassembly process. Rotary tools, such as Dremel, are typically used for cylindrical cells; the isolated plier is used for prismatic cells; and the knife, along with a pair of scissors, can be used for pouch cells [272], [273], [279]. No heat or smoke will be produced if the disassembly procedure is successful. During the post-mortem analysis, the jelly cell is unrolled, and the cell components are separated from one another to be studied individually. The separated components are then transferred to dimethyl carbonate (DMC) solvent for washing [279]. The appropriate components are floated in the DMC liquid during the washing process to dissolve the electrolyte salt residues on the sample surface (Figure 2-26 (C)). Some authors, however, suggested two washing steps, one minute each, to remove all electrolyte salt residues [272]. It should be noted that the post-mortem analysis takes place in a controlled environment. Following that, the samples are retained in the glove box to dry and are prepared for further investigation. The cell components are now ready to be moved to the testing facility for physical characterization, and the samples must be transferred from the glove box to the testing facility in a vacuum-sealed container due to the possibility of air contamination of the cell component (Figure 2-30 (D)) [273], [280].

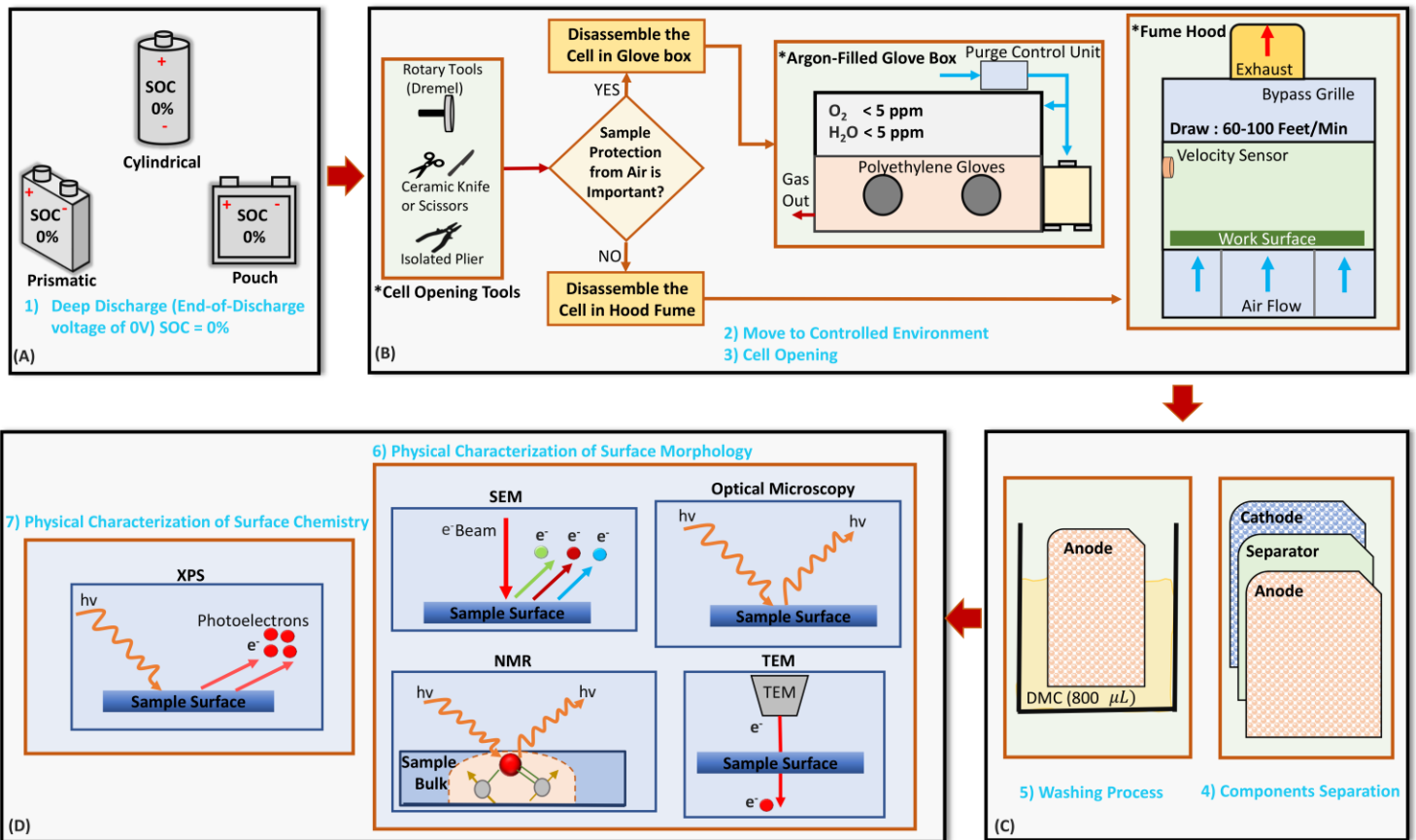


Figure 2-26: Overview of Post-Mortem Analysis for Lithium-Ion Cells. A) Cell is required to be deep discharged before any further steps. B) Cell is moved to the safe or controlled environment for the opening procedure, where the controlled environment is chosen based on the study goals. Cell casing is removed. C) Cell components are separated and washed, and they are ready to be sent to the testing facilities. D) Cell components are subjected to further analysis to investigate lithium plating.

2.2.4.2 Physical Characterization of Surface Morphologies

Several efforts have been made in recent years to study the morphology of deposited lithium using physical characterization approaches to acquire a better understanding of the lithium plating-stripping mechanism. Physical characterization approaches are commonly employed to study the structure of the deposited lithium and growth processes of the lithium dendrites on the anode surface at the laboratory scale [270]. The most prominent

approaches that use physical characterization to study lithium plating are explained. In addition, Table 2-9 summarizes the advantages and disadvantages of each approach to highlight their effectiveness.

2.2.4.2.1 Optical Microscopy

High-resolution optical microscopy can be used both in-situ and ex-situ to observe lithium plating-stripping processes during cell operation [281]. In-situ optical microscopy can be used to directly observe the plating morphology. A custom-made optical in-situ cell is designed (Figure 2-27 (A)) to study the penetration of lithium dendrite through the separator in order to find strategies to stop them (Figure 2-27 (B) and (C)) [282]. The in-situ techniques can also be used to find the position and direction of the deposited lithium on the electrode surface [283]. In Ref. [264], in-situ optical microscopy is used to study the morphology of deposited lithium. At 10 °C, mushroom-like dendrites were seen, whereas needle-like and wound-ball morphologies were observed at 5 °C and 20 °C, respectively. During the lithium stripping process, dead lithium is observed, where it grows at the tips of the lithium and eventually loses electrical contact and separates from the graphite [283]. Lithium ions are extracted from the cathode compound and intercalate into the lattice of the graphite structure; the color of the graphite changes depending on the stage of intercalation. Each stage has been associated with recognizable color, ranging from black to red to gold (as a function of lithium concentration x in Li_xC_6 (Figure 2-27 (D)) [284], [285]. As a result, the in-situ optical microscopy method based on color change can be useful for observing lithium plating. Thomas-Alyea et al. [286] designed a coin-type half-cell for in-situ optical microscopy to analyze color change at the graphite particles (Figure 2-27 (E)). Using in-situ optical microscopy, Harris et al. [229] and colleagues observed

three stages on the meso-carbon microbeads (MCMB) electrode. At first, the electrode was entirely in the blue stage (4L). The red-blue and gold-red boundaries then began at the edge of the electrode and sparsely departed from there until the voltage dropped to +2 mV (Figure 2-27 (F)). Furthermore, they observed lithium plating on the (MCMB) electrode. The MCMB electrodes became golden (stage 1) after a voltage (+2 mV) was applied to the current collector, as shown in Figure 2-27 (G) and (H). The edge of the electrode was free of lithium plating, whereas the rest of the electrode remained (stage 2) red graphite particles for many hours [229]. Moreover, they observed that lithium plating occurred when the anode potential was +0.002 V against Li/Li⁺. However, thermodynamically lithium plating should occur when the anode potential drops below 0 V against Li/Li⁺ [229]. The change in the color associated with lithium concentration is dependent on the ambient lighting condition; thus, this technique is characterized as semi-quantitative.

2.2.4.2.2 Scanning Electron Microscopy (SEM)

Since 1988, SEM has been used to investigate the surface morphology of the lithium electrode, and it has a higher resolution than optical microscopy [287]. Many studies have employed both in-situ and ex-situ SEM to investigate the lithium plating-stripping process [288], [289]. Yoshimatsu et al. [290] used ex-situ SEM observation to characterize the lithium electrode surface morphologies during an extensive cycling test on a lithium coin cell for the first time. They identified two types of lithium deposits: particulate and dendritic. During discharge, the particulate lithium structure is reinserted into the anode graphite layer. The dendritic structure, on the other hand, remained on the anode surface. Rauhala et al. [275] investigated the lithium plating on the cell that was cycled at low

temperatures using ex-situ SEM. A considerable amount of lithium plating was observed on the anode surface when the cell was cycled at $-18\text{ }^{\circ}\text{C}$. Surface contamination is always a risk during ex-situ SEM investigations, especially for highly sensitive surfaces like graphite anode electrodes [270], [283]. Using in-situ SEM to study lithium plating-stripping, on the other hand, necessitates unique cell and equipment designs. Many research groups have developed ultrahigh vacuum types of equipment to decrease the possible risk of lithium specimen contamination during the transfer process [287], [289], [291]. However, because ultra-high vacuum equipment is used in the examination process, in-situ SEM is only applicable to batteries that use solid polymer electrolytes and ionic liquids [289], [292], [293]. Uhlmann et al. [285] and coworkers applied a high charging current of up to 10 C to three different half-cells to study lithium plating. They used SEM to observe changes in the surface morphology of the deposited lithium during both the charging and relaxation phases. Figure 2-27 (I) and (J) show the surface structure of the anode sample with mossy grown lithium that is charged with a high charging current of 10 C . To avoid the relaxation period, this sample was disassembled in less than 5 minutes after charging. Another interesting approach was taken by Rong et al. [294] who developed an in-situ electrochemical scanning electron microscopy (EC-SEM) technique to observe the lithium plating-stripping process on Li/Cu electrode using liquid electrolyte LiTFSI/DOL/DME. They showed the significance and advantages of LiN_3 and Li_2S_8 as additives on lithium dendrite detention.

Figure 2-28 (A) shows the emergence of lithium dendrites with a length of $18\text{ }\mu\text{m}$ after 350 seconds. During the stripping process, however, the majority of the lithium dendrites begin

to dissolve into the electrolyte after 600 seconds, while the remainder tends to become dead lithium. Tallman et al. [295] and co-workers reduced the amount of the deposited lithium up to 50 % by increasing the deposited overpotential through surface treatment. They deposited ultrathin (10 nm) Cu and Ni film on the graphite electrode surface. Ex-situ SEM results reveal that the deposited lithium was significantly decreased on the coated graphite with Cu and Ni compared to the uncoated graphite Figure 2-28 (B).

2.2.4.2.3 Transmission Electron Microscopy (TEM)

One of the most promising observation methods for studying lithium dendrite growth at the nanoscale is transmission electron microscopy (TEM) [270]. In literature, in-situ TEM setup is divided into two major types: a liquid cell system and an open-cell system [296], [297]. In Ref. [298], a nanoscale LiB was built inside a TEM to investigate lithium plating in-operando using an ionic liquid as the electrolyte. They demonstrated how lithium ions nucleate at the anode-electrolyte interface and ultimately form fibres. The fundamental disadvantage of this approach is that volatile organic compounds (ionic liquids or solid-state electrolytes) are incompatible with the high-vacuum environment of TEM, hence it cannot be used to analyze lithium plating [299]. Mehdi et al. [300] and coworkers recently used an in-situ liquid ec-TEM cell to study the dynamic volumetric changes that happen at the electrolyte silicon nanowires interface during the charging and discharging process. They measured the thickness of the SEI layer of the anode electrode which was immersed in LiClO_4 with (EC: DMC) as electrolytes during lithium plating-stripping. They confirmed that the SEI formation kinetics is greatly reduced by electron transport. Lithium plating-stripping in a LiPF_6 -ethylene carbonate (EC)-diethyl carbonate (DEC) electrolyte was studied by Zeng et al. [301] to investigate the formation of dead lithium during cycling

Figure 2-28 (C). Overall, in-situ TEM requires further development, particularly for liquid cell constructions due to electron scattering in the liquid layer [270]. The key issue is finding a suitable electrolyte for the TEM column because the common electrolytes used in LiBs have a high vapor pressure that can be used in the TEM column [288].

2.2.4.2.4 Nuclear Magnetic Resonance Spectroscopy (NMR)

The key advantages of this technique over other approaches are its non-destructive nature and applicability to both crystalline and amorphous materials [302], [303]. Ex-situ NMR can distinguish between different chemical states of lithium in the active material of the graphite electrode. Ge et al. [243] used an ex-situ NMR to measure the quantity of plated lithium while the cell was charged from 0 % to 60 % SOC at (-25 °C), 80 % SOC (-25 °C), and 80 % SOC (-20 °C) with high currents (1.5 C). They found that the activation energy of lithium intercalation is higher than lithium plating even at low SOC, resulting in lithium plating [243]. However, the use of the ex-situ method, like the ex-situ procedures discussed above, necessitates certain additional steps before beginning the experiments, which may influence the experimental outcomes [304].

Several research groups have employed in-situ NMR to study carbon graphite electrodes, lithium metal oxide, and metal electrodes [304]–[307]. The hard carbon electrode as a negative electrode can consume more lithium during relaxation compared to the graphite electrode, Gotoh et al. [308] and co-workers constructed full LiB cells with different materials including LiCoO_2 , $\text{LiNi}_x\text{Co}_y\text{Al}_z$, and LiMn_2O_4 as the positive electrode, along with graphite and hard carbon as the negative electrodes to study relaxation effects in LiBs. They measured lithium spectra of cells at various SOC, particularly after overcharging (2 C and 3 C) at 170 % SOC. They showed that the phenomenon of the "relaxation effect"

occurs after overcharging based on the lithium metal signal measurement [308]. The lithium metal signal reduces with time as lithium atoms begin to reinsert into the graphite layer. Ota et al. [309] employed NMR spectroscopy to investigate the surface chemistry (surface film). They found that lithium cycling efficiency influences not only the morphology of deposited lithium but also the chemical components of the surface film. Arai et al. [306] studied lithium metal deposition with in-situ solid-state Li NMR on a full cell consisting of LiCoO_2 (positive electrode), graphite (negative electrode), polypropylene (separator), and an organic liquid such as electrolyte (1 M LiPF_6 , ethyl methyl carbonate 30:70 vol.%) during both continuous currents (CC) and pulses current (PC) mode operation. As shown in Figure 2-28 (D), the deposited lithium metal became visible at approximately 265 ppm at $-5\text{ }^\circ\text{C}$ temperature for different cell cycles with a CC mode pattern. Simultaneously, no lithium metal deposition was detected $-5\text{ }^\circ\text{C}$ with PC mode pattern [306]. They also computed the lithium deposition rate (k) using the slopes of the plots. The lithium deposition rate at $-5\text{ }^\circ\text{C}$ is approximately $12.4\text{ (}10^3\text{ mg mAh}^{-1}\text{)}$. Wandt et al. [310] employed electron paramagnetic resonance (EPR) spectroscopy to identify the time-resolved and quantitative beginning of lithium plating in a graphite electrode under realistic cell conditions. EPR is more sensitive than NMR, making it excellent for analyzing lithium materials in-operando [311], [312]. EPR spectroscopy, in addition to NMR, uses low-energy radiation that does not affect the chemical characteristics or morphology of the investigated species [311], [313].

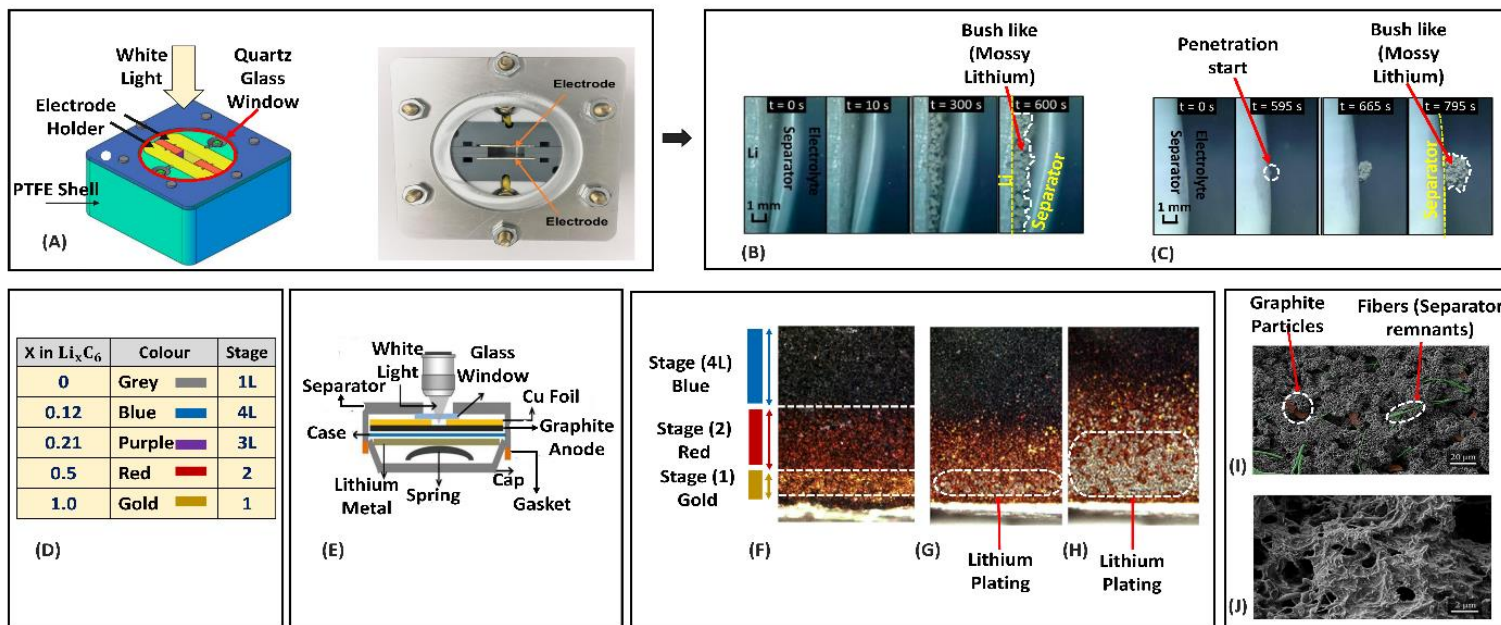


Figure 2-27: In-situ Cell Design and Results of Optical Microscopy and Ex-situ SEM for Lithium Plating Morphology Characterization. (A) Schematic of the custom-made optical in-situ cell with a quartz glass window. (B) In-situ optical microscopy at a current density of 1 mA/cm² ($t = 0\text{ s} - t = 600\text{ s}$), the gap between lithium metal and separator helps in the observation of the dendrite growth until it reaches the separator. (C) In-situ optical microscopy at a current density of 1 mA/cm² ($t = 0\text{ s} - t = 795\text{ s}$), there is no gap between the separator and the lithium electrode, penetration started at ($t = 595\text{ s}$) and quickly changed to the bush like structure (Reprinted from Liu et al. [282] with permission of American Chemical Society Publications). (D) The color of graphite is affected by the concentration of lithium X in Li_xC₆ (data adapted from Ref.[450], the random occupation of all superlattices defined as 'liquid-like' or L stage). (E) Side-view schematic of a custom-made coin-type half-cell for in-situ optical microscopy (Reprinted from Thomas-Alyea et al. [286] with permission of Electrochemical Society). (F) The MCMB electrode surface inside an in-situ optical half-cell, three different graphite colors (stages) were observed over 3 hours. Lithium Plating on an MCMB electrode was observed when a voltage (+2 mV) is applied to the current collector, although according to bulk thermodynamics, lithium metal plating should not occur unless the voltage becomes negative. The image (G) is taken 8 h before (H) (Reprinted from Harris et al. [229] with permission of Elsevier). (I) and (J) Ex-situ SEM images show the morphology of an anode surface with mossy lithium plating. The anode is charged with a high current of 10 C and then instantly dismantled in less than 5 minutes to interrupt the relaxation phase, scale bars: 20 μm and 2 μm (Reprinted from Uhlmann et al. [285] with permission of Elsevier).

2.2.4.2.5 Atomic Force Microscopy (AFM)

AFM is one of the most effective tools for analyzing the surface morphology of electrodes at the nanoscale scale [314], [315]. AFM scans the surface of a sample with a cantilever and a sharp probe. In comparison to SEM or optical microscopy, it can also provide

significantly higher morphological resolution in three-dimensional (3D) format [270]. In-situ AFM was utilized by Mogi et al. [316] to investigate the surface morphology of deposited lithium on the Nickel substrate at elevated temperatures. At 40 °C, they discovered inhomogeneous and massive deposits of lithium underneath the substrate's surface film, whereas, at 60 °C and 80 °C, they discovered a homogenous and thick surface film. The results, however, were inaccurate since the AFM observation was done in contact mode. During the investigation, the AFM probe (tip) scrapes the sample's surface in contact mode [316]. The image resolution is low in non-contact mode due to the large distance between the probe and the sample. The structure of the lithium surface, as shown by in-situ AFM in Ref. [316], includes grain boundaries, ridge-lines, and flat areas. These lines were found to be critical in controlling the morphology of the deposited lithium. Aurbach et al. [317] and co-workers studied lithium deposition on the copper electrode in a nonaqueous electrolyte system by using in-situ AFM measurements. They found that although lithium metal is soft, utilizing AFM as a detection tool does not modify the surface morphology. In another approach, Shen et al. [318], used in-situ electrochemical atomic force microscopy (EC-AFM) to study lithium dendrite growth on a graphite electrode cycled in 1 M LiPF₆-EC-DMC and 1 M LiPF₆-FEC-DMC electrolytes. They confirmed the importance and advantages of FEC-based electrolytes on lithium dendrite detention, as the formed SEI are harder and denser compared to the SEI formed in the EC-based electrolyte. Overall, AFM is an accurate and powerful technique to study the morphology and topography changes of the real-time mechanical properties in LiBs [319]. However, it is not recommended to use AFM for inspection of the dendrite formation as it has some limitations in the tip dimension and the usual vertical scanning range of instruments [320].

2.2.4.3 Physical Characterization of Surface Chemistry

One of the most common approaches in the field of LiBs is to analyze the chemical composition of the surface films on electrodes in non-aqueous solutions. The chemical composition of deposited lithium as well as the oxidation states of the elements can be examined using surface chemistry analysis techniques [321], [322]. In the following part, the methodologies used to characterize the surface chemistry of the deposited lithium on the anode surface will be introduced. In addition, for a more in-depth understanding of the existing techniques, the advantages and disadvantages of each are listed in Table 2-10.

2.2.4.3.1 X-ray Photoelectron Spectroscopy (XPS)

X-ray photoelectron spectroscopy has been widely used for surface chemistry analysis (element analysis and oxidation state of elements) of lithium electrodes due to the relative simplicity in use and data interpretation [323]. Castro et al. [322] used XPS to investigate the aging mechanism of a $\text{LiFePO}_4/\text{graphite}$ cell after 200 cycles at ambient temperature. They found that cyclable lithium can be consumed at each cycle due to the deposited lithium on the anode surface and the instability of the SEI (LAM). XPS may be a destructive method due to the usage of an argon ion sputter gun and an X-ray beam on the sample during the investigation. However, Aurbach et al. [323] found that by functioning at low emission and balancing the quality of the spectra based on the shorter measurement duration, it is possible to collect reliable and reproducible findings with minimum damage to the material when using the XPS technique. The XPS method, like most other spectroscopic methods, requires a vacuum system and there is always the potential of surface contamination in highly sensitive electrodes. As a result, a special transfer arrangement is required [324], [325]. X-ray tomography can provide a better understanding

of the structure and material composition of the electrodes, as well as morphological changes [326]–[329]. X-ray beams with energy ranging from 10-100 keV may easily penetrate the plastic and metallic cell casing and directly visualize the inner LiB components in 3D [326], [330]. Eastwood et al. [331] applied a synchrotron-based X-ray phase-contrast tomography technique to investigate the microstructures of the electrodeposited lithium, which is necessary for understanding the dendrite formation. Harry et al. [332] used synchrotron hard X-ray microtomography to investigate the lithium dendrite in a lithium/polymer/lithium cell. They discovered that the subsurface structure of the electrode is critical in facilitating dendritic formation in the polymer electrolyte.

2.2.4.3.2 Fourier Transform Infrared Spectroscopy (FTIR)

FTIR is a non-destructive method for analyzing the chemistry of the lithium surface [271]. Many researchers have used FTIR to investigate the surface chemistry of lithium in organic electrolytes [333]–[335]. To quantitatively describe liquid electrolyte solutions, Ellis et al. [336] coupled FTIR spectra with machine learning (ML) techniques. The electrolyte concentration was reported to be reduced by 10–20% (Vol) in cells after 200 cycles at 55 °C. This is a significant amount of salt loss, and it is most certainly a contributing factor to cell failure. Morigaki [334] analyzed the impact of EC⁺ dimethyl carbonate (DMC) solution on lithium surface based on the locations and strengths of the peaks in DMFTIR spectra. They found a new reduction product of the solvent on lithium after 1 and 15 hours immersion with DMFTIR. In another approach, FTIR was used by Kramer et al. [335], who studied lithium plating in pristine cells of two different forms (cylindrical and pouch). The impacts of electrolyte solvent such as propylene carbonate (PC), ethylene carbonate (EC), dimethyl carbonate (DMC), and a set of salts (LiAsF₆, LiBF₄, LiPF₆) on the lithium

surface were investigated with FTIR in [323]. The in-situ FTIR technique uses attenuated total reflectance (ATR) for examining the lithium sample in the nonaqueous system [337]. Therefore, using ATR crystal for each experiment would be prohibitively expensive due to damage to the crystal surface during the investigation.

2.2.4.1 Electrochemical Methods

Electrochemical in-situ, ex-situ, and in-operando are the most effective methods for monitoring unsafe battery behavior, such as lithium plating. Voltage plateau after charging, anode potential, electrochemical impedance spectroscopy (EIS), differential voltage (DV), and incremental capacity (IC) can be used in in-situ or in-operando electrochemical methods [230]. These methods are based on electrochemical signals, which are available in any LiB. Using electrochemical techniques is convenient because they are simple to implement into BMS [205]. The most common electrochemical approaches for detecting lithium plating in the context of possible BMS deployment are described briefly. Table 2-11 summarizes the benefits and drawbacks of each strategy for a more thorough comparison.

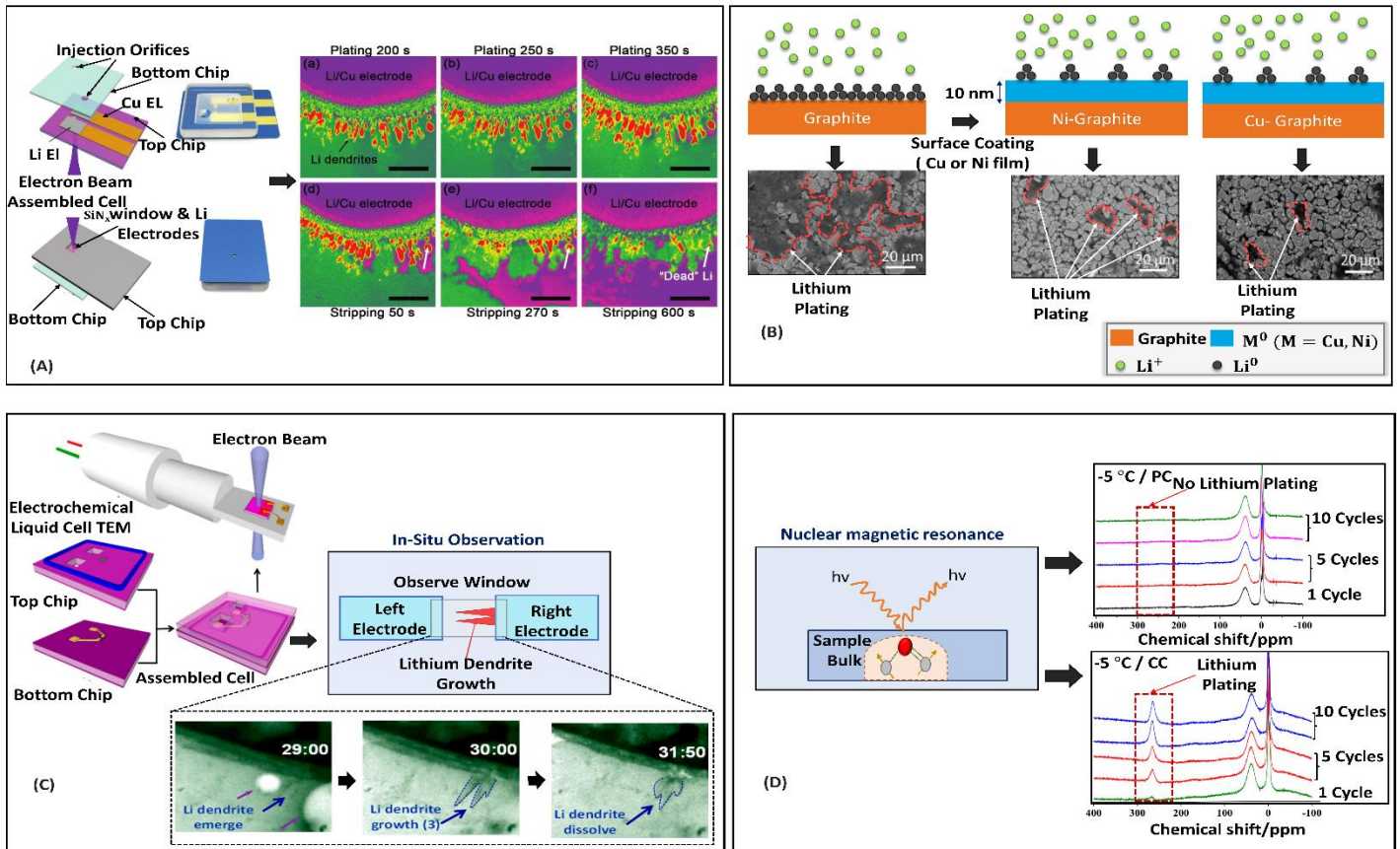


Figure 2-28: Different Physical Characterization Approaches for Lithium Plating investigation. (A) Schematic of the in-situ SEM EC-liquid cell setup for direct observation of lithium plating, Li/Cu electrode during lithium plating for a)200 s, b)250 s, c)350 s, and d)50 s, e)270 s, f)600 s for stripping under 0.15 mA cm^{-2} . Scale bars: $20 \mu\text{m}$, (Reprinted from Rong et al. [294] with permission of Advanced Materials). (B) Schematic of Li-metal nucleation on the uncoated graphite surface and coated graphite surface during high current charging, the nucleation is significantly decreased due to increased overpotential for Li-metal deposition, which was obtained by the nanoscale coating of Cu and Ni, backscatter SEM images of the deposited lithium metal on the uncoated graphite and coated graphite with Cu and Ni. Scale bar: $20 \mu\text{m}$ (Reprinted from Tallman et al. [295] with permission of American Chemical Society). (C) Schematic of in-situ TEM liquid cell for nanoscale observation of electrode-liquid electrolyte interfaces using lithium dendrite growth. Scale bars: 800 nm , (Reprinted from Zeng et al. [301] with permission of Nano Letters). (D) The stacked in-situ NMR spectroscopy for different cells at $-5 \text{ }^\circ\text{C}$. These spectra were measured at the fully charged state in the latest cycle. Pulse current mode: cells were cycled with pulse current (PC) mode pattern, and no lithium plating was detected. Continuous current mode: cells were cycled with continuous current (CC) mode pattern and lithium plating observed at 265 ppm (Reprinted from Arai et al. [306] with permission of Electrochemical Society).

2.2.4.1.1 Voltage Plateau After Charging

Voltage plateau is a non-destructive and indirect method that has the potential to be used as an online tool for lithium plating detection in automotive applications [234]. Reversible lithium is reinserted into the graphite during the relaxation or discharge time. This process affects the voltage plateau signal due to variations in the overall potential of the anode electrode during relaxation and discharging after a charging step [234], [245], [338]. Therefore, the presence and changes in the voltage plateau could provide evidence of lithium plating [339], [340]. Zinth et al. [341] mixed the voltage plateau method with in situ neutron diffraction measurements to study lithium plating at $-20\text{ }^{\circ}\text{C}$, where the degree of graphite lithiation can be used to estimate the amount of lithium plating. A quantitative detection method for lithium plating based on plotting the derivative of voltage over capacity (dV/dQ plot) was presented by Petzl et al. [339], who found that the voltage plateau appeared at the beginning of discharge. They proposed that the discharge capacity at the dV/dQ peak contributes to the total reversible part of the deposited lithium during charging. Recently, it has been reported by Campbell et al. [245] that the cell self-heating and concentration gradients during fast charging can increase the voltage plateau curve, which could be wrongly detected as lithium plating. Also, they showed that the unavailability of stripping plateau does not confirm that no lithium plating has taken place in the cell. However, a recent study showed that the relaxation process is much faster at a higher temperature and the voltage plateau is less visible as the temperature is increased [342]. Therefore, the voltage plateau detection technique works better at lower temperatures ($-20\text{ }^{\circ}\text{C}$) since the relaxation process is slower at subzero temperatures [343]. In another approach, Uhlmann et al. [285] detected a kink in the voltage curve during relaxation after

the charging process rather than during discharging. They found that for the detection of lithium plating, flattening the voltage curve can be used. This technique was later expanded by plotting the derivative voltage over time (dV/dt), where the same dV/dt peak curve for lithium stripping is seen [340]. Yang et al. [234] studied the voltage plateau during relaxation and during discharge to find out the parameters affecting the voltage curves during lithium stripping. In this study, they used a 9.5 Ah pouch cell for a plug-in hybrid EV application. The dV/dt curve is plotted and shown in Figure 2-29 (A), where it is shown that the dV/dt peaks appear sooner with a higher discharge rate compared to the dV/dQ analysis. They showed that the rate of lithium stripping is limited by the rate capability of intercalating Li^+ ions into graphite, and that the duration of the voltage plateau is highly dependent on the rate of lithium stripping. Intercalation kinetics, graphite solid-state diffusivity, and cell temperature can all have an effect on the voltage curves. Another interesting finding is represented in the schematic above Figure 2-29 (A). Near the separator, lithium metal is deposited. The high degree of graphite lithiation limits the rate of Li^+ ions insertion. Since the Li^+ ions can not be inserted into the anode near the separator, they begin moving to the other part of the anode near the foil and are intercalated into the graphite along the path [234]. At the beginning of discharge, a dV/dQ peak occurs, which corresponds with the findings in the literature. Nevertheless, in the case of C/3 discharge, the dV/dQ peak seems earlier than that of 1 C Figure 2-29 (B). Li^+ ions intercalation still takes place in the anode in the discharge phase after charging, as long as the Li stripping reaction can support the discharge current. As such, the discharge capacity would underestimate the actual amount of plated Li at the dV/dQ .

2.2.4.1.2 Third Lithium Reference Electrode (RE)

As previously stated, lithium plating takes place when the anode potential drops below 0 V (vs. Li/Li⁺). To directly measure the anode potential, a third reference electrode (RE) must be used as a measurement tool [235]. Nonetheless, because commercial cells lack a third reference electrode, measuring the anode potential directly is not currently practicable. Anode potential may, however, be measured in the laboratory using a specific setup in which the RE is inserted into the cell (machinery). The RE materials (e.g., metallic Li, FePO₄/LiFePO₄, Li-Sn, Li-Al) and cell configurations are important factors in the insertion process. The location of the RE is chosen based on these factors [235], [344], [345]. Several studies have been conducted to demonstrate how to develop and implement the RE into LiBs, as well as where the ideal position for the RE is to reduce the ohmic drop while maximizing measurement accuracy [346]–[349]. An interesting approach was taken by Waldmann et al. [235], who positioned the RE near the current collecting tab of the anode as this area has a higher current density. Due to the low diffusivity of lithium-ions in graphite at low temperatures and high SOC, they discovered that lithium-ions begin to accumulate at the anode interface. Rangarajan et al. [256] used a lithium titanate (LTO) electrode as a reference electrode in a pouch cell with a stable voltage over a range of SOC to detect and quantify lithium plating. To quantify the amount of lithium plating at each rate, the plating period, plating power, and plating energy were defined. They dubbed lithium plating a non-linear process since it does not increase monotonically under varied working conditions. Low cost and reliable RE insertion methods have been introduced in Ref. [349], which require less equipment than existing procedures for commercial 18650 cells. Non-polarizability, reliability, and reproducibility are the key characteristics in the

RE material selection process [350]. Lithium metal is the most common material for RE, but it cannot provide all these characteristics due to unstable potential (reliability) [351]. The potential of RE may vary due to mechanical treatment, the nature of the electrolyte, and the formation of the SEI layer [205], [350]. Moreover, lithium metal is not a proper choice for high-temperature applications due to its low melting point (i.e. 180 °C). The accuracy of the RE method with alternative materials such as $\text{Li}_4\text{Ti}_5\text{O}_{12}$ and LiFePO_4 has been studied by Mantia et al. [350]. They showed that these materials may be the most promising materials for RE since they exhibit a constant potential for $\text{Li}_4\text{Ti}_5\text{O}_{12}$ (1.567 ± 0.0025 V) and LiFePO_4 (3.428 ± 0.0005 V) vs. Li/Li^+ . These materials can also provide low polarizability under high current rates during the two-phase reactions. Overall, RE insertion may cause surface film modification and degradation by interfering with the battery's electrochemical process. Furthermore, due to safety concerns, RE has yet to be deployed in any commercial cells or real-time LiB applications for measuring electrochemical characteristics.

2.2.4.1.3 Incremental Capacity (IC) and Differential Voltage (DV)

IC-DV techniques are based on the rate of changes in the electrochemical equilibrium phase (EEP) [352]. The EEP changes are determined by the intercalation and de-intercalation processes that occur between the anode and cathode materials. The IC-DV curves are obtained by a constant battery charge curve, and the IC curve is mathematically estimated as the gradient of Q with respect to V ($dQ/dV = f(V)$) [352]. The DV curve is obtained by inversely computing the IC curve ($dV/dQ = f(Q)$). The researchers use prognostic/mechanistic models to directly clarify the aging mechanism by identifying model parameters [217], [352], [353]. Indeed, the mechanistic model is a backward-

looking modeling approach in which the degradation is the input and the output is the cell's voltage and capacity. Thus, when a cell is in equilibrium, the IC-DV approach can quantify its electrochemical properties as well as its various degradation modes (LLI, LAM) [217]. The IC and DV curves can be used to study the degradation mechanism both qualitatively and quantitatively [230]. Tanim et al. [255] recently investigated the lithiation voltage profile and demonstrated that reversible lithium stripping is dependent on the level of over-lithiation in the graphite electrode. Capacity fading was observed using IC analysis on 13 cells cycled at a low temperature (-10 °C) under diverse conditions such as varying charge current rates, charge cut-off voltages, and charge cut-off current [210].

2.2.4.1.4 Coulombic Efficiency (CE)

Coulombic efficiency (CE) is defined as the ratio of energy (Q_d) a LiB outputs during discharge to the energy (Q_c) a LiB takes in during charge [354].

$$CE = \frac{Q_d}{Q_c} \quad (2-12)$$

When lithium plating occurs on the anode surface during the charging cycles, the CE decreases. As a result, CE can be recognized as a method for detecting lithium plating. Smith et al. [355] advised four important aspects to correctly measure the CE: (i) accuracy of the set current, (ii) precision of the voltage measurement, (iii) duration between voltage measurements, and (iv) precisely controlled cell temperature. Burns et al. [356] investigated lithium plating by plotting CE versus charging current rates. As shown in Figure 8 (B), there is a considerable variation in the capacity loss rates of cells charged at temperatures above 2 C. Furthermore, with a charging rate of 1C at 12 °C, they found a considerable amount of lithium plating. The CE versus charging rate at various

temperatures was recorded (Figure 2-29 (C)), with a minor drop in CE occurring as the deposited lithium began to consume the active lithium. They also proved the presence of lithium plating on graphite electrodes for cells cycled at charging current rates of 2 C for 50 °C and 0.5 C for 12 °C [356].

Table 2-9. Advantages and disadvantages physical characterization of surface morphologies for lithium plating detection

Techniques	In-situ	Ex-situ	Advantages	Disadvantages
Scanning Electron Microscope (SEM)	✓	✓	(a) Suitable for large morphology change (b) Applicable to all types of cells (c) More effective to monitor the detrimental formation of dendrites directly	(a) Only applicable on batteries using solid polymer or inorganic SSE in in-situ condition (b) Risks of surface contamination were always present (c) Not applicable for quantitative studies in dynamic condition (d) The requirement of an extra high vacuum
Optical Microscopy	✓	✓	(a) Instantly distinguish the surface change (b) Able to monitor lithium stripping/plating during operation	(a) Resolution not as high as of SEM (b) Not applicable for quantitative studies in dynamic condition (c) Resolution is too low for most of the nanoscale materials (d) Required to design an optical cell for in-situ investigation
Atomic Force Microscopy (AFM)	✓		(a) Imaging at the atomic level (b) Three-dimensional (3D) image (c) Visibility of Li surface including boundaries, ridgelines, flat areas	(a) Not suitable for inspection of dendrite formation (b) Not applicable for quantitative studies in dynamic condition (c) Destructive method (surface scratching needed in the contact mode) (d) Risks of surface contamination were always present
Transmission Electron Microscope (TEM)	✓	✓	(a) Suitable for large morphology change (b) Dynamic evolution of interfaces at high tempo-spatial resolutions (c) Observation of SEI mechanisms and structures at the nanoscale (d) Observing microstructures in real-time (using open cell)	(a) The requirement of an extra high vacuum (b) Require solid-state electrolyte and ionic liquid (volatile organic electrolytes are incompatible with the high-vacuum environment) (c) Surface damage due to the beam effect (80/300keV) (d) Low spatial/energy resolution due to the presence of various stimuli along the beam path

Nuclear Magnetic Resonance Spectroscopy (NMR)	✓	✓	(a) Quantitative method (b) Provide a non-equilibrium state during charging/discharging (c) Processes in a non-invasive manner (d) Observe the change in intensity proportional to the lithium content of each stage	(a) Risks of surface contamination were always present on Ex-situ condition
---	---	---	---	---

Table 2-10. Advantages and disadvantages physical characterization of surface chemistry for lithium plating.

Techniques	In-situ	Ex-situ	Advantages	Disadvantages
Fourier Transform Infrared (FTIR)	✓	✓	(a) Non-destructive method (b) High surface sensitivity at the molecular level (c) Qualitative/quantitative analysis	(a) Only suitable for detecting the organic components (b) Low reflectance intensity and broad (c) Expensive material for in-situ experiments (d) Damages the electrode surface (in contact mode)
X-ray Photoelectron Spectroscopy (XPS)	✓	✓	(a) Provide the 3D structure of surface films (b) Analysis of inorganic components (c) Study surface species (which are not too active in IR)	(a) Damages the electrode surface (b) Modify the oxidation states of elements (c) Requires a vacuum system

Liu et al. [357] measured the CE of four silicon-based electrode materials during cycling (condition: voltage cut off 1.5-0.02 V), and the resulting CE ranged from 95 % to 98 %. The measurement equipment used in this procedure must be highly precise to detect any variations in voltage and current. However, Tanim et al. [255] recently demonstrated that the CE approach could not be precise and dependable for detecting lithium plating in a full cell over extended cycling. When only small amounts of lithium are deposited, high precision coulombmeters are required. Otherwise, if the amount of deposited lithium is

significant, conventional testers or measurement devices can be used [255] [356], [358]. Furthermore, the rest period has a considerable impact on the CE method, as it cannot distinguish stripping from the plating process [359].

2.2.4.1.5 Electrochemical Impedance Spectroscopy (EIS)

EIS is a quantitative approach for analyzing battery behavior and determining electrochemical kinetics throughout the lithium insertion-extraction process [351]. Lithium deposition has been studied in Li/Li₄Ti₅O₁₂ battery cells based on ionic liquid electrolytes during several charging/discharging cycles by EIS [307]. In another study by the same author, a correlation between the surface area of the electrolyte and lithium metal (formation of lithium dendrites) with $R_{cc} + R_{SEI}$ was introduced. They showed that a decrease in the $R_{cc} + R_{SEI}$ value corresponds to an increase in the interfacial area between the electrolyte and lithium metal electrode [360]. As shown in Figure 2-29 (D), using a conventional electrolyte (LiPF₆ in EC/DMC) resulted in the formation of lithium dendrites [307]. The $R_{cc} + R_{SEI}$ values of LiPF₆ in EMIM-TFSA/EC and LiPF₆ in EMIM-TFSA/PC do not show any decrease. However, there could be additional factors causing a drop-in $R_{cc} + R_{SEI}$ values. EIS measurements are often conducted using laboratory equipment. Nevertheless, Nazer et al.[361] proposed an online EIS technique for implementation in the BMS of HEVs and EVs. They measured electrochemical impedance using broadband excitation signals (pseudo-random binary sequences (PRBSs), random white noise, swept sine, swept square, and a square wave). The proposed system, however, was noisy and could result in an impedance error value at high frequencies [361].

2.2.5 Recent Non-Destructive Approaches for Detecting Lithium Plating

In addition to these electrochemical and physical detection methods, simpler techniques for studying lithium plating have been proposed. According to the literature, when transitioning from a completely unlithiated condition to lithiated LiC_6 (intercalation of lithium), the total volume of the graphite anodes might rise by 10% [229], [362]. The extra volume changes can also be caused by the deposited lithium on the graphite. As a result, detecting changes in cell thickness can be a beneficial strategy for detecting lithium plating [363], [364]. There is a correlation between the volume change and lithium plating, which determines the expected extent of volume gain due to deposited lithium Figure 2-34 (A) [362]. In Ref. [362], a customized setup was provided to measure the thickness of a 20Ah pouch cell during cycling with varied currents and temperatures, as illustrated in Figure 2-30 (B). Due to the reversibility of lithium plating, it was shown that the cell thickness increases rapidly during the lithium plating condition and reduces during the rest time (Figure 2-30 (C)). This method is straightforward and valid, but it necessitates the use of an accurate device to measure cell thickness. Furthermore, this approach is only applicable to pouch cells. It should be also noted that it is not possible to differentiate volume changes due to gassing reactions with lithium plating [365].

Ultrasonic acoustic approaches have recently been used to study LiB behavior [366]–[368]. The propagation and reflection of soundwaves is the fundamental principle of the ultrasonic method. For the first time, Hsieh et al. [369] and colleagues used this approach to measure SOC and SOH in a pouch cell. The ultrasonic investigation can be divided into two modes [370]: (i) pulse-echo mode, which uses a transducer that can either be glued or pressed onto the cell casing. In this case, a voltage pulse is sent out towards the object (cell)

and the pulse is reflected back to the transducers. (ii) Through-transmission mode, which employs two separate transducers, one of which serves as a transmitter and the other as a receiver; a voltage pulse is transmitted from the transceiver and travels through the object material (cell), arriving at the receiver, which is installed on the opposite side of the object. Gold et al. [368] proposed a linear model with ultrasonic pulse frequencies ranging from 200 kHz to 2.25 MHz, which is lower than the one used in prior studies to measure SOC in one cycle. Bommier et al. [366] recently employed the electrochemical acoustic (EA) technique to study SEI formation in NMC/SiGr pouch cells. Due to gassing reactions that occurred during the first SEI formation/lithiation of the silicon particles, the acoustic signal was lost during the first 40 hours of charging. They demonstrated that the acoustic signal is significantly attenuated in the presence of a gaseous environment. Moreover, they found a correlation between the passivation of the silicon particles and the acoustic time-of-flight (TOF) shift.

For the first time, Bommier et al. [371] used the ultrasonic approach to detect lithium plating in a pouch cell. Commercial 210-mAh lithium-ion cells were ultrasonically tested in through-transmission mode. Figure 2-30 (D) shows a schematic of the ultrasonic setup. In their attempt, they established a connection between the acoustic signal and lithium plating. When the cell was charged with 1C and discharged with C/10, the acoustic signal was quickly attenuated at the second cycle ($t=20$ h) and reappeared at the 18th cycle ($t=195$ h), as shown in Figure 2-30 (E) [371]. Meanwhile, the cell capacity was reduced from 0.210 Ah to 0.195 Ah, and they suspected that the loss of acoustic signal was due to lithium plating. However, the loss of the acoustic signal, according to the literature, is a strong sign of a gassing reaction in the cell, and because distinguishing between lithium plating and

gas reaction is difficult, it cannot be utilized as an indication for lithium plating. As a result, they discovered that employing an acoustic signal alone is ineffective. In the second attempt, they decided to measure the shifts (time-of-flight) in the full acoustic waveforms [371]. Cells were cycled twice at C/15 for both charge and discharge and then a CC charge with a fixed capacity of 0.210 Ah (no voltage cutoff) was applied to trigger lithium plating. As shown in Figure 2-30 (F), they found a significant difference at the endpoints of the TOF shifts of the cells that were cycled with fixed-capacity charge (1 C) than the cells that were cycled with a C/15 charge. It was shown that there is a correlation between TOF endpoints differences and lithium plating. They proved the efficiency of this strategy using various ex-situ characterization methods, such as ex-situ SEM, as shown in Figure 2-30 (G) [371].

Table 2-11. Advantages and disadvantages of on-line electrochemical lithium plating detection techniques.

Techniques	BMS	Advantages	Disadvantages
Measurement of Coulombic Efficiency	-	(a) Applicable to all types of cells (b) Suitable for identification of side reactions in early stages	(a) Inaccurate results if another parasitic reaction happens (Oxidation, loss of active materials) (b) Expensive equipment
Voltage Plateau after charging	✓	(a) Non-destructive method (b) Suitable for on-board implementation (c) No requirement for special and expensive equipment	(a) Needs slow discharge rate (b) Availability of abnormal exothermic peaks (c) The importance of the lithium deposited areas (d) Highly depends on internal cell characteristics
Third Lithium Reference Electrode	-	(a) Quantitative evaluation of different electrochemical aspects (b) Reliable method	(a) Safety (Short circuit) (b) Not applicable in Commercial cells (c) Require modifying cell design and fabrication (complicated implementation)
Electrochemical impedance spectroscopy (EIS)	✓	(a) Suitable for study LiB characteristics (b) Non-destructive method Suitable for on-board implementation (c) Fast analyzing period (25/min/cell)	(a) Reduction in cell performance after RE insertion (b) Require complicated computation (c) The cell must be in the equilibrium state
Incremental Capacity (IC) Differential Voltage (DV)	✓	(a) Non-destructive method (b) Suitable for on-board implementation (c) Ideal for identification and quantification of DM	(a) Required small currents for discharge curves (b) Slow analyzing period (10 h/cell)

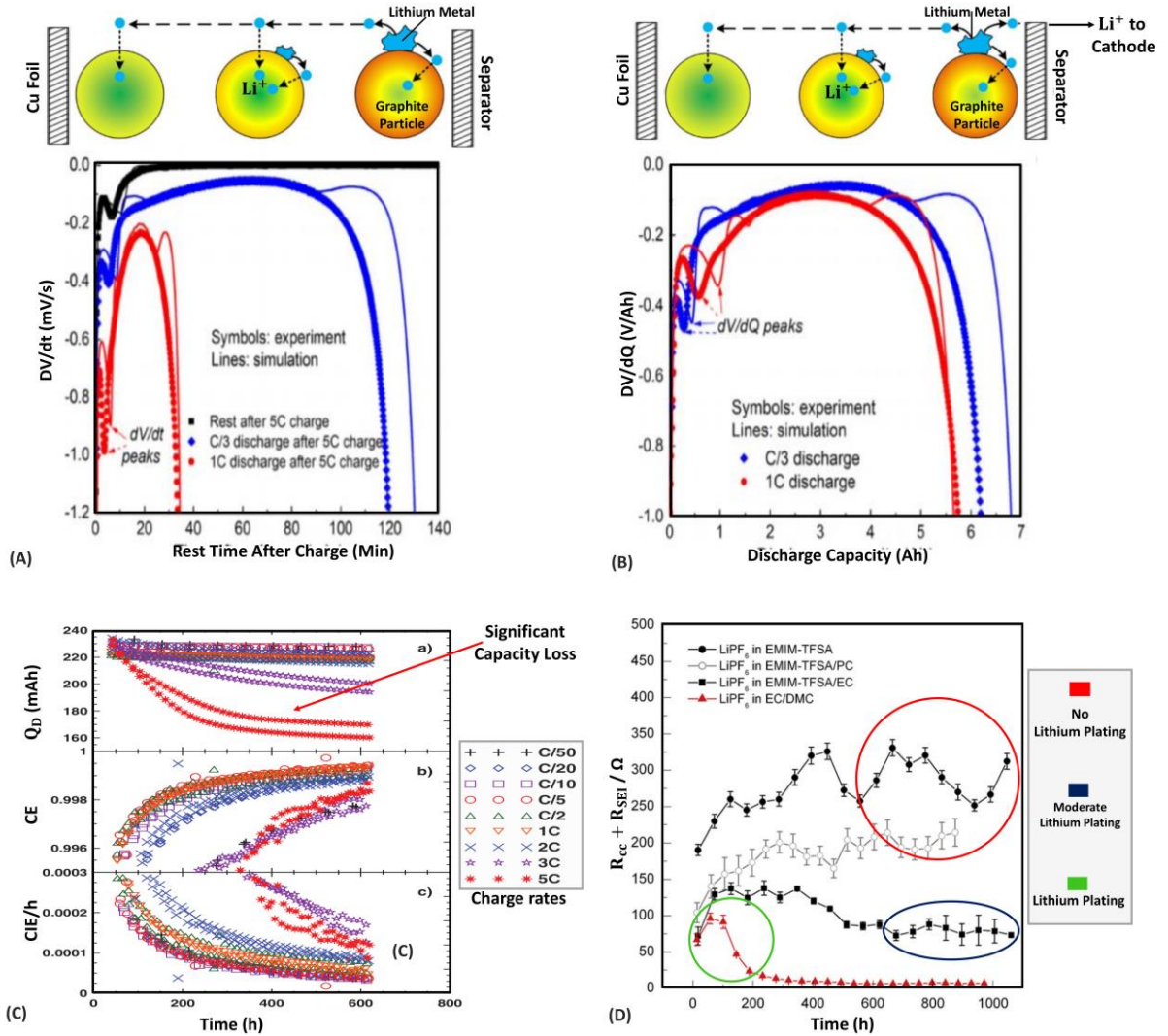


Figure 2-29: Electrochemical Methods. (A) Differential voltage over time (dV/dt) for the two discharge cases and the 5C charge relaxation event, as well as a schematic diagram of the anode's internal characteristics at the start of relaxation. During relaxation Li^+ ions that are not consumable at the separator travel and diffuse through the electric field (migration) and concentration gradient (diffusion) towards the foil, where they are intercalated into graphite (Reprinted from Yang et al. [234] with permission of Elsevier). (B) Differential voltage over capacity (dV/dQ) in the discharge phase because of discharge capability and a schematic diagram of the anode's internal characteristics at the start of discharge. During discharge, Li^+ ions formed by Li stripping near the separator have three destinations: they are intercalated into graphite, they travel to the cathode to deliver output current, and they move under an electrical field (migration) and a concentration gradient (diffusion) towards the foil and are intercalated along the path into graphite (Reprinted from Yang et al. [234] with permission of Elsevier). (C) Cycling data versus time extracted by a high-precision charger. A two-stage charge process is applied on pouch cells at different rates from (C/50 to 5C) at 30 °C ((a) Capacity, (b) Coulombic efficiency, (c) Coulombic inefficiency per hour) (Reprinted from Burns et al. [356] with permission of Electrochemical Society). (D) Resistance values $R_{CC} + R_{SEI}$ as a function of time for various electrolyte solutions (Reprinted from Schweikert et al. [307] with permission of Elsevier).

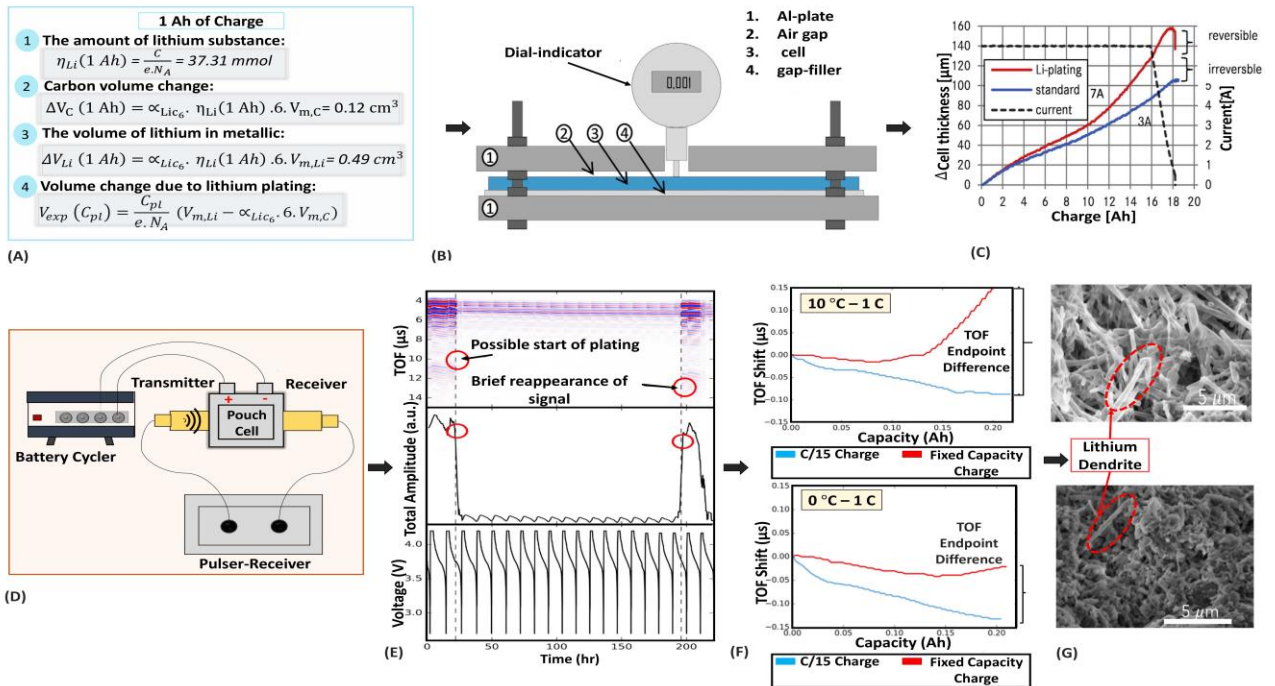


Figure 2-30: Non-Destructive Approaches for Detecting Lithium Plating.

(A) Theoretical relation between volume gain and lithium plating. (B) Schematic of the setup for in-operando measurements of pouch cell thickness during the lithium plating (resolution 1 μm). (C) Significant changes in the cell thickness at the charge current of 7 A due to lithium plating (Reprinted from Bitzer et al.[362] with permission of Elsevier). (D) Schematic of the in-operando acoustic detection setup for studying lithium plating. (E) Acoustic plots consist of three distinct panels, which are, from top to bottom, a heatmap of acoustic time of flight (s), total amplitude of waveforms in random components, and a voltage versus time curve corresponding to the adjoined waveforms. (F) The difference in acoustic TOF shifts during the C/15 charge and the fixed-capacity charge of 0.210 Ah at different temperatures was measured when the cell was cycled at 10 $^{\circ}\text{C}$ with a fixed capacity charge of 1 C. The cell was cycled with a fixed capacity charge of 1 C at 0 $^{\circ}\text{C}$ (G) Ex-situ SEM measurement: electrodes were washed in (DMC) and dried in an argon-filled box for 2 hours at 40 $^{\circ}\text{C}$. Scale bars: 5 μm (Reprinted from Bommier et al. [371] with permission of Cell Reports).

2.2.6 Model-Based Investigation of Lithium Plating

In order to optimize the battery design and develop more practical charging protocols, modeling would be an appropriate solution [221], [372]. There are several different approaches to model LiBs: electrochemical models, equivalent-circuit battery models (ECM), thermal models, electrical models, mechanical models, and molecular models [373]. Modeling can provide us with the exact time of lithium plating and the location of

the deposited lithium on the electrode surface. Newman [374] and co-workers introduced the first battery performance model.

2.2.6.1 Electrochemical Models of Lithium Plating

Electrochemical models based on the porous electrode theory and lithium concentration solution have been widely used to study lithium plating in LiBs. The electrochemical models cover both particle level and cell level dynamics. At the particle level, the mass conservation and diffusion dynamics at both electrodes are explained based on Fick's law [375]. At the cell level, it needs to describe the flow of lithium-ion into the electrolyte, the diffusion of lithium in the active material, and the electron charge transfer in the lithium-ion intercalation process happening at the surface of the active material. All of them are based on the porous-electrode model. The cell level and particle level dynamics are coupled through the local reaction current based on charge conservation. The properties of materials can be estimated based on the electrical measurements of the full cell [376]. The lithium plating criteria can be divided into two different kinds: (i) A saturation concentration at the interface; lithium plating would happen when the concentration of lithium-ions at the electrode interface reaches the saturation level of $0.077 \text{ mol cm}^{-3}$ [243]. (ii) The interfacial overpotential; when the overpotential (η) is lower than 0 V against Li/Li⁺, lithium plating would occur [193], [243], [285]. These criteria are applied in the electrochemical models to predict or suppress lithium plating. Arora et al. [224] made the first attempt to develop a physics-based mathematical model for investigating lithium plating on the negative electrode (graphite and coke) during charge and overcharge. This macro-homogeneous model was based on the work of Doyle and Newman [374]. Kinetic and thermodynamic parameters (e.g. transfer coefficient (α_a, α_c), exchange current density (i_0)) were adopted

into the model to simulate the electrochemical reactions, mass transport, and other physical processes.

They assumed lithium plating is partially reversible, meaning that all of the deposited lithium reacts with the electrolyte to produce a new SEI or dead lithium. They found that the particle size and electrode thickness can influence the lithium plating phenomena [224]. As long as the electrode is thinner and has a smaller particle size, lithium plating is less favorable compared to thicker electrodes with larger particles. However, many other features could be adopted to this model to study lithium deposition in an overcharge reaction. Moreover, this model cannot capture the edge effects of the cell, which have a specific impact on the accumulation of the lithium-ions on the anode electrode during the charging process [377].

In another approach by Ge et al. [243] who used Newman's electrochemical model, also known as a pseudo-two-dimensional (P2D) model, studied lithium plating at low temperatures. They divided the total electrochemical reaction current density into two parts: the lithium intercalation current j_1 and the lithium deposition current j_2 : [243],

$$j = j_1 + j_2 \quad (2-13)$$

Both of them could be described by the Butler-Volmer equation:

$$j_1 = j_{0,1} \left[\exp\left(\frac{\alpha_a F}{RT} \eta_1\right) - \exp\left(-\frac{\alpha_c F}{RT} \eta_1\right) \right] \quad (2-14)$$

where $j_{0,1}$ is the exchange intercalation current, α_a and α_c are the transfer coefficients which generally equal to 0.5, and η_1 is the over-potential for intercalation reaction.

$$j_2 = \min \left\{ 0, \quad j_{0,2} \left[\exp\left(\frac{\alpha_{a,2} F}{RT} \eta_2\right) - \exp\left(-\frac{\alpha_{c,2} F}{RT} \eta_2\right) \right] \right\} \quad (2-15)$$

where $j_{0,2}$ is the exchange plating current, $\alpha_{a,2}$ and $\alpha_{c,2}$ are the transfer coefficients which are generally taken to be 0.3 and 0.7, respectively, and η_2 is the over-potential for lithium plating reaction. When the overpotential (η_2) is lower than 0 V against Li/Li⁺, lithium plating would occur. They found that during low temperature charging when the overpotential (η_2) is minimum, the lithium-ions start to accumulate at the anode-separator interface and then move into the anode electrode. This model also proposed a multi-step charging process that can charge the cell fast and safely without incurring lithium plating at low temperatures [243]. However, the model validation has been carried out with few data points.

A P2D-modeling has been presented by Tang et al. [377] to study lithium plating during cell charging. They found that increasing the thickness of the negative electrode can hinder the deposition of lithium, specifically at the edge of the electrode. In another interesting approach by Tippmann et al.[376] built a P2D electrochemical model combined with a 0D thermal model for operation at low temperatures to predict the aging effects over different temperatures (-25 °C to 40 °C) and currents (0.1 C to 6 C). They used COMSOL Multiphysics 4.2 for performing the simulation and compared the obtained results with EIS experiments. However, the implementation of this model into BMS is not highlighted due to the cost and time-consuming simulations while using the porous electrode theory.

Computational cost is also one of the problematic challenges in lithium plating modeling due to a large number of governing equations (e.g. ten non-linear and multidimensional partial differential in spatial directions x, r, t) that are required to be solved at the same time with the highly non-linear algebraic expression for transport and kinetic parameters [378].

Liu et al. [236] developed a model that couples lithium plating with SEI growth, allowing

simulating concurrent lithium dendrite growth, SEI growth, SEI penetration and regrowth. Their work highlights the effect of SEI in lithium plating. Boovaragavan et al. [378] proposed a reformulated physics-based model for real-time parameter estimation. Their model can simulate porous model equations in 15-45 ms with only 29-49 differential-algebraic equations (DAEs) while using the rigorous model, it takes 90-120s with at least 4800 DAEs. This model is suitable for predicting the capacity fade, but it has only been validated at the 2C rate of discharge [378]. A reduced-order model (ROM) was created by Perkins et al. [379], who defined five different assumptions, such as keeping the cell always in the quasi-equilibrium state for studying lithium plating during overcharge. This model is an optimized version of the Arora model to speed up the calculation of the governing equation in the ROM versus the physical-based model. They could decrease the calculation time to 1/5000 while utilizing ROM comparing to using the physical-based model. This ROM can only be implemented for short pulse lengths (less than 10s) due to the quasi-equilibrium. Thus, it can recognize the boundary between the time that lithium plating would occur or not in the charging-current process [379]. A physics-based model by Yang et al. [380] studied the aging behaviors attributed to lithium plating and SEI growth of a plug-in electric vehicle (PEV) battery over a normal charge/discharge current at the ambient temperature. This model considered the SEI growth and lithium plating rate to explain linear and nonlinear behavior during cycling. The linear aging stage is linked to SEI growth. The transition stage from linear to nonlinear aging is associated with lithium plating. Recently, Lin et al. [375] proposed a data-driven strategy that uses long short-term memory (LSTM) to monitor anode electrode potential in real-time to prevent lithium plating. Because physics-based model implementation is complex, time-consuming, and

requires extensive manual tuning, real-time LSTM is far more precise and computationally efficient and can be easily integrated into the BMS. The LSTM model can complete the entire test in 87 seconds, whereas the physics-based model takes 7 hours and 44 minutes.

2.2.7 Operational Phase Summary

The topic of lithium plating phenomena has been widely investigated in many aspects over the last decade. However, some problems remain in terms of accurate and reliable detection methods, mechanisms, prediction, and prevention. In light of this, in this section, challenges and prospects are introduced from four aspects: mechanisms, detection methods, modeling, material components, and optimized charging protocols.

Chapter 3 : Methodologies

3.1 Manufacturing Phase: Method Details

3.1.1 Section Overview (Pseudocapacitors Electrode Fabrication via ULPING)

⁷The development pathway for enhanced electrode materials has begun in the production of ESDs such as batteries and supercapacitors (SCs) [381] [382], [383]. Although carbon-based supercapacitors have demonstrated success, their low capacitance and poor conductivity limit their use in fast-evolving technologies [384]. To address this, significant research has been conducted on various synthesis methods utilizing different transition metals (TMs) to manipulate the structure of electrode materials for supercapacitors [385]–[387]. The synthesis of electrode materials with unique architecture, well-engineered diffusion channels/pathways, and uniform porous surface structures can be achieved through well-designed synthesis strategies [388], [389]. However, conventional synthesis methods such as chemical vapor deposition, solvothermal, physical vapor deposition, and hydrothermal techniques are time-consuming and require high thermal budgets, resulting in inadequate controllability and outcomes [390], [391]. For instance, the current manufacturing process takes around 24 to 48 hours to synthesize the active material needed for charge storage.

Therefore, in this study, we propose a technique called ultra-short laser pulses for in-situ nanostructure generation (ULPING), which is a powerful tool for controlling electrode

⁷ This section is based on a previously published article:

Kavian Khosravinia, A. Kiani. "Unlocking pseudocapacitors prolonged electrode fabrication via ultrashort laser pulses and machine learning", *iScience*, Cell Press. The material is reproduced here with permission from the publisher, [Cell Press].

morphology while maintaining a low thermal budget for supercapacitors [392], [393]. Table 3-1 summarizes the advantages of our proposed laser processing technique (ULPING) over conventional nano-synthesis methods for fabricating enhanced electrode materials. This technique is carried out under ambient conditions. Compared to conventional synthesis strategies, laser processing technology is considered a green nanofabrication technology because no surfactants or capping agents are required during the process [394]. Additionally, the ULPING process is environmentally friendly because no byproducts or hazardous reducing chemicals are required for the reaction, and the outcome is not a separate byproduct but rather a particular in-situ modification of the substrate [395]. The laser processing technique can be digitally controlled using a computer-aided design with various parameters, including power, pulse repetition rate, frequency, scan speed, and specific pattern formation.

The benefits mentioned above have led to a rise in interest in researching the production of nanostructured surfaces with enlarged specific surface areas using laser techniques. One recent example of this development is the use of ULPING to fabricate electrode materials for pseudocapacitors, which are one of three types of supercapacitors, along with electric double-layer (EDL) capacitors and hybrid capacitors [396]. Pseudocapacitors are composed of electrochemically active electrode materials, such as conducting polymers (CPs) and transition metals (NiO, CuO, TiO, ZnO, MnO, RuO₂) [397].

Table 3-1. Comparison of conventional synthetic methods and ULPING.

Conditions	Conventional Synthetic Methods	ULPING
Experimental setup	Complicated (multi-step)	Simple (single step in ambient condition)
Technological route/Pattern of the electrodes	Mostly separate products from the substrate/No	Add modification directly on substrate material/Yes
Target material	All materials	All solid materials/Polymers (transition metals)
Collection after procedure	Post-processing/binding	Not needed
Environmentally friendly	Non-Environmentally friendly	Green method
Experimental cost and time	High-cost and time-consuming	Low-cost and quick

Pseudocapacitors store electrical energy by the Faradaic charge-transfer process of selectively adsorbed ions and de-solvated ions caused by electro-sorption, redox reactions, or intercalation on the electrode surface [398], [399].

Considering the use of TMs as an electrode for pseudocapacitors, the need for an oxide layer to swap the oxidation state for rapid redox of TMs specifies the pseudocapacitor's functioning characteristic. Thus, using ULPING under ambient settings can accomplish the conditions as it can efficiently and sustainably generate a porous oxide layer. Recently, our group used ULPING on two different TM sheets, namely Ni and Ti, to form an oxide layer, namely NiO and TiO, in ambient conditions using different laser parameters [392], [400], [401]. In our previous work, we studied the effects of scan speed and pulse repetition rate or frequency on Ni substrate [392]. Although the frequency samples did not demonstrate many differences, we observed a progressive increase in performance as the scan speed

was decreased. The scan speed of 10 mm s^{-1} demonstrated the best results, mainly due to the slower beam path travel allowing for better nanostructure generation and more phase transformation of Ni into NiO. An areal capacitance of 92.682 mF/cm^2 was observed at a discharge current of 1 mA/cm^2 . In another study from our group, Gholami et. al [400] used laser pulses to grow Titania 3D nanonetworks (T3DN) on Ti-metal sheets under ambient conditions. They compared the number of laser treatments to a bare Ti control sheet and discovered that treating the same surface twice with high-intensity laser pulses produces an areal capacitance of 6.91 mF cm^{-2} . Self-grown 3D nanostructures are formed as a result of a series of ultrafast events that take place as electromagnetic radiation pulses irradiate the surface of the substrate or target material. From both studies, the active surfaces were binder-less and were produced in a single step with no chemicals using the ULPING approach.

The distinctiveness, novelty, simplicity, and effectiveness of the ULPING approach for producing efficient electrode materials for pseudocapacitors were validated in both studies. Nevertheless, there is still room for improvement in this research area due to the direct connection between the controlling input laser parameters and the material properties of the generated nanostructures on the substrate. This improvement room can be divided into two major levels: the material level and the control/data-driven level. Some of the most important research questions that are going to be answered here are: how the other TMs will behave electrochemically as pseudocapacitor electrodes when they are fabricated using the ULPING method? Furthermore, how will the input laser parameters or fabrication parameters actually impact the electrochemical behaviors of the produced samples? Finally, how can data-driven approaches, particularly machine learning (ML) techniques,

provide insights into the correlation between fabrication parameters (structural features) and pseudocapacitor electrochemical behavior or performance metrics? It is crucial to find out the answers to the above questions since we believe ULPING has great potential to use in the pseudocapacitor-related industry.

In this account, we describe our group's progress in fabricating electrodes with ULPING on bare Ti sheets and using ML to accelerate electrode design in two different but related phases. Figure 3-1 illustrates the experimental setup of a typical ULPING technique. In the first phase, we fabricated 31 electrodes with various T3DN structural features by combining 31 different laser parameters (power (P), frequency (F), pulse duration (PD), and scanning speed (SS)). From here on, the various samples presented would be referred to by their abbreviated names. Using the electrodes we fabricated, we then proceeded to prototype 496-coin cells, where all 31 electrodes were individually coupled with each other, following the mix-and-match matrix. Next, to assess the impact of laser parameter variation on the T3DN properties, we investigated all 496 prototyped coin cells using various characterization techniques. Scanning electron microscopy (SEM) and energy-dispersive X-ray (EDX) spectroscopy were used to analyze the material properties, while electrochemical behavior was studied using a potentiostat with cyclic voltammetry (CV), galvanostatic charge-discharge (GCD) electrochemical impedance spectroscopy (EIS).

In the second phase, studying this enormous number of samples allows us to delve one level deeper using ML algorithms to understand the relationship between fabrication parameters and pseudocapacitor performance metrics. To accomplish this, we conducted a large-scale empirical comparison of three commonly encountered supervised learning

algorithms in the energy field, namely Gaussian process regression (GPR), random forest (RF), and artificial neural network (ANN).

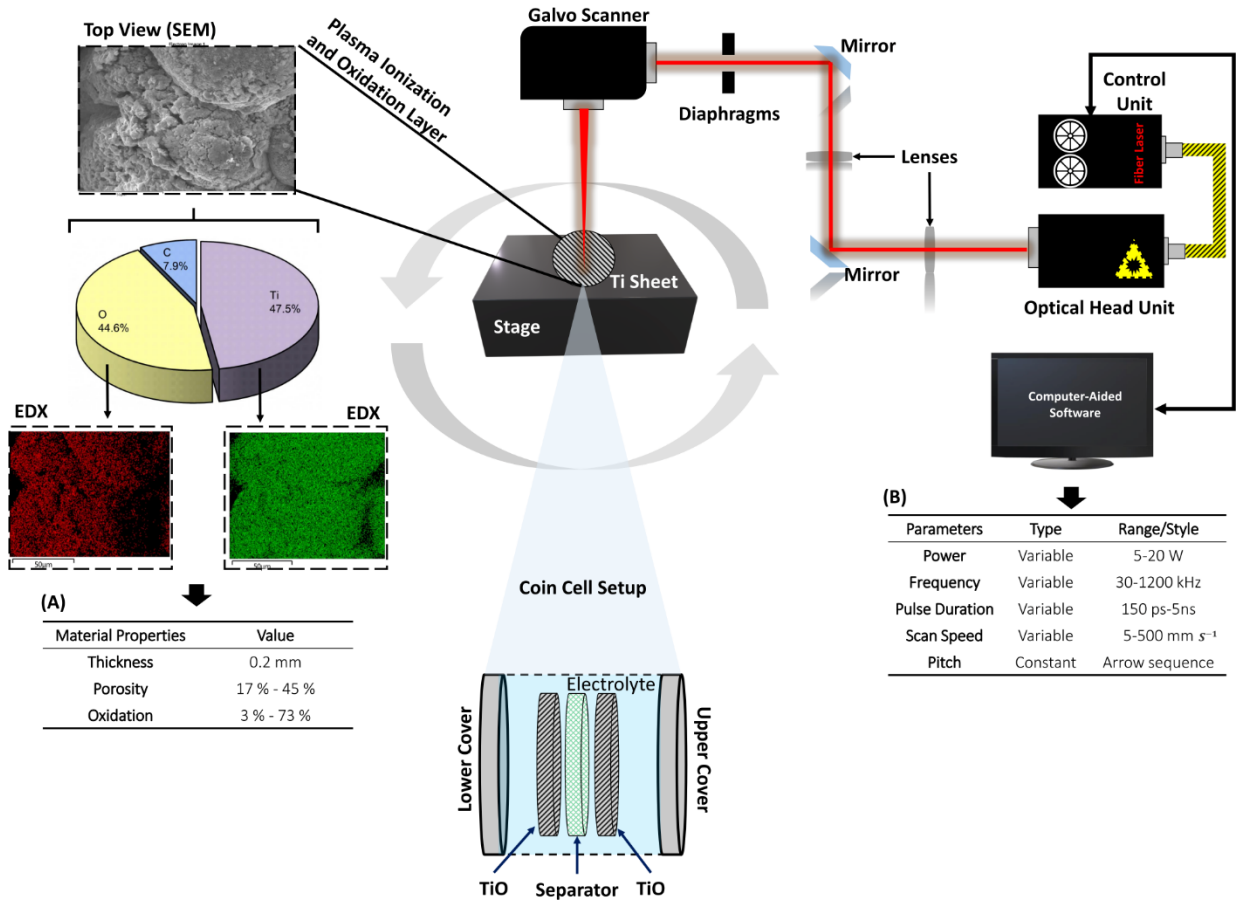


Figure 3-1: Schematic diagram of the experimental setup for the formation of a TiO layer with ULPING approach. (A). Laser parameters can be adjusted using computer-aided software (Marking Mate 2.7). (B) An example of TiO properties and specimen components derived using a combination of several characterization instruments (SEM and EDS) and specified software (ImageJ).

The purpose of this comparison was to evaluate their computing efficiency, accuracy, and applicability for predicting the electrochemical behavior performance of pseudocapacitors. Our findings revealed that this research can provide promising methods for employing ULPING to fabricate nanostructures on TMs that have the potential to be used in pseudocapacitor electrodes.

3.1.2 Experimental Phase

One of the goals of this research is to use ML algorithms to predict the electrochemical behavior of pseudocapacitors fabricated using the ULPING approach. The methodology for achieving this objective is divided into two major phases: experimental and computational. The experimental phase describes the fabrication of electrodes via UPLING, the assembly of pseudocapacitor coin cells, the material, and the electrochemical characterization. The computational phase demonstrates how a large dataset can be generated from the experimental phase and how it can aid in ML-based model development for predicting various electrochemical performance parameters. This information is also included in the key resources table.

3.1.2.1 Preparation of Pseudocapacitors Electrode

In the experiment, a commercial Ti (CAS: 7440-32-6) with a thickness of 0.2 mm (Grade 4) was used as a sample. Ti sheets were polished and cleaned with acetone before being rinsed with DI water. As shown in Figure 3-1, the sample is exposed to the ambient atmosphere with no elaborate shielding (chamber requirement). The pulse ionization was carried out using a 150-picosecond laser pulse system (IPG Laser Model: YLPP-1-150 V-30) at a constant wavelength of 1060 nm (see Figure 3-2). The 7.6 mm laser diameter was lowered to 6 mm using an iris diaphragm before being focused on an XY galvanometer scanner (JD2208 by Sino-Galvo). This scanner provided a theoretical laser spot diameter of 20 μm by using an F-theta lens with a focal length of 63.5 mm, an input aperture of 14 mm, and a beam displacement of 18.7 mm. The pulse laser beam is directed to a platform carrying the Ti sheet. The imprinted profile was designed using Marking Mate 2.7 as CAD

software, which allows the laser patterning parameters such as scanning speed and pitch to be specified. Figure 3-1 (A) indicates the laser parameters used in the experiment.

A total of 31 distinct samples were prepared using parameters such as power ranging from 5 to 20 W, frequency ranging from 30 to 1200 kHz, pulse duration ranging from 150 ps to 5 ns, scan speed ranging from 5 to 500 mm s⁻¹, and a constant pitch pattern (arrow sequence). The center distance between two consecutive lines pulsed by a laser beam is called pitch. The irradiated samples were punched into 6 mm circle discs containing TiO as active material, with an area of 27.2 mm² (see Figure 3-3). To the best of the authors' knowledge, this is the largest sample preparation for pseudocapacitor electrodes through ULPING that has ever been conducted. The laser parameters for each sample are listed below (see Table 3-2).

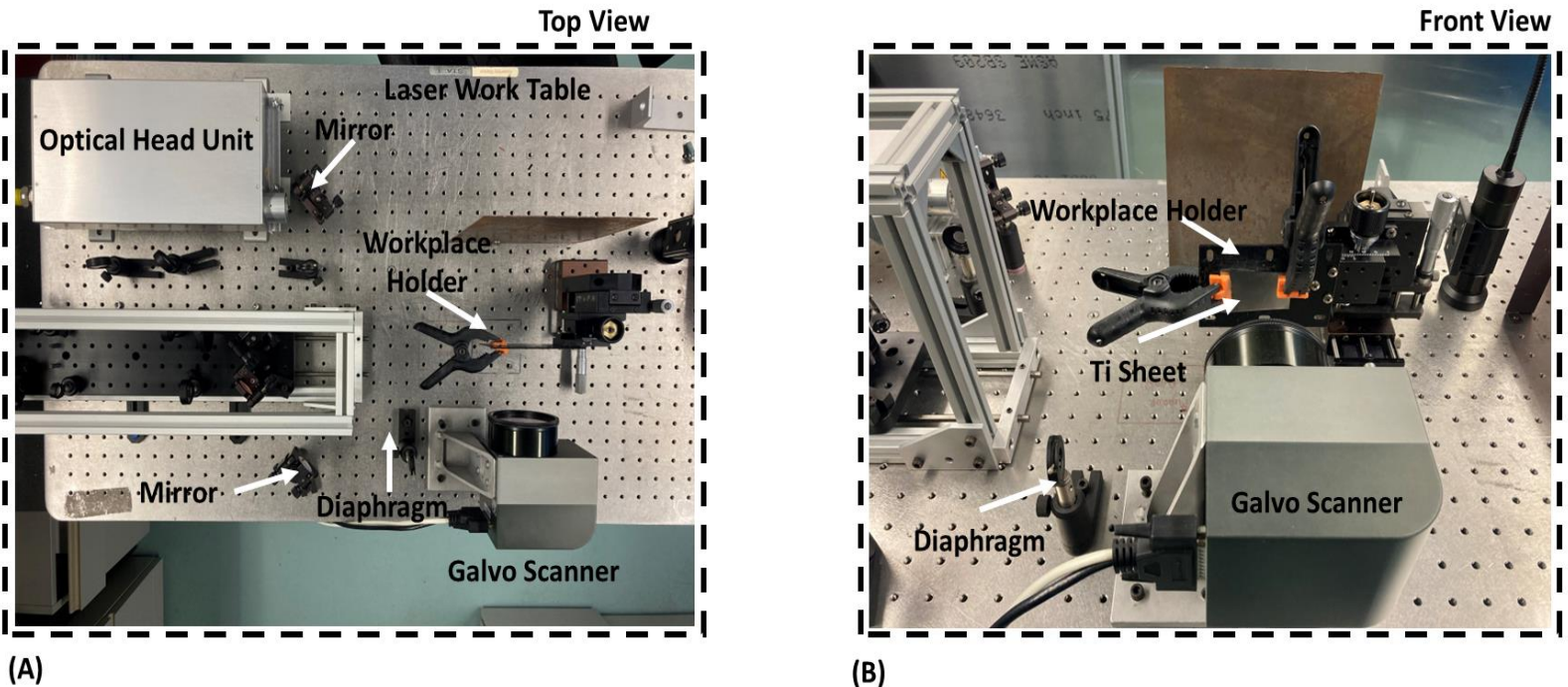


Figure 3-2: ULPING method worktable. (A) Top view. (B) Front view.

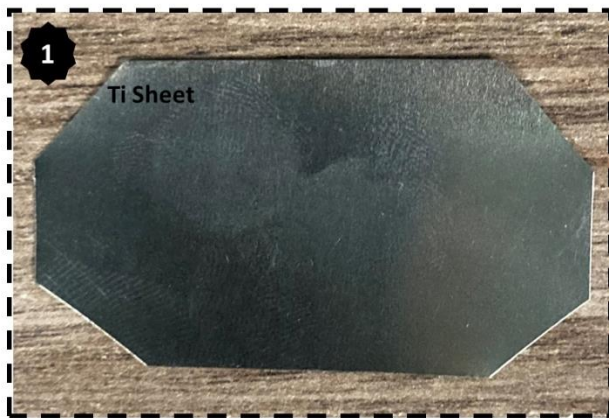
Table 3-2. Laser variables for different samples

Laser Variables	Samples	Power (W)	Frequency(kHz)	Pulse Duration (ns)	Scan Speed (mm s ⁻¹)
Power/Scan Speed	P1	5	1200	0.15	10
	P2	8	1200	0.15	10
	PN1-1	10	1200	0.15	10
	PN2-2	12	1200	0.15	10
	P3	15	1200	0.15	100
	P3-1	15	1200	0.15	200
	P3-2	15	1200	0.15	500
	P4	20	1200	0.15	100
	P4-1	20	1200	0.15	200
	P4-2	20	1200	0.15	500
Frequency/Pulse Duration	F1	10	600	0.15	10
	F2	10	750	0.15	10
	F4	10	900	0.15	10
	F5	10	1050	0.15	10
	PD1	10	100	1	10
	PD2	10	400	1	10
	PD3	10	800	1	10
	PD4	10	1200	1	10
	PD5	10	60	2	10
	PD5-1	10	100	2	10
	PD5-2	10	400	2	10
	PD5-3	10	800	2	10
	PD5-4	10	1200	2	10
	PD6	10	60	5	10
	PD6-1	10	100	5	10
	PD6-2	10	400	5	10
PD6-3	10	800	5	10	
PD6-4	10	1200	5	10	
Scan Speed	S1	10	1200	0.15	40
	S2	10	1200	0.15	50
	S3	10	1200	0.15	60

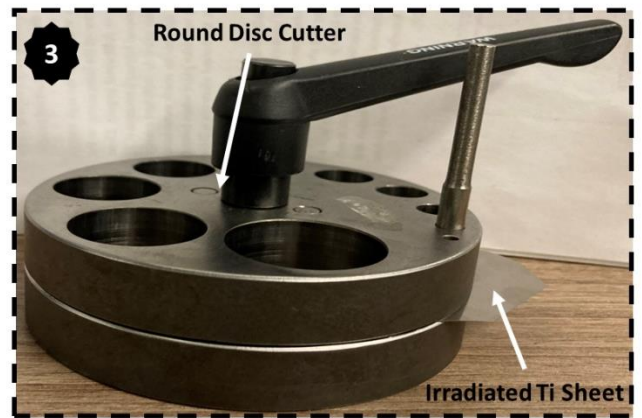
3.1.2.2 Material Characterization

The next stage in this experimental setup is to use various techniques to analyze the surface characterization of the prepared electrodes. Images of the surface topography and composition of the materials were obtained using scanning electron microscopy (SEM-Hitachi High-Tech Global- FlexSEM 1000). The Energy Dispersive X-Ray (EDX-Hitachi High-Tech Global- FlexSEM 1000) spectroscopy equipment was utilized for element

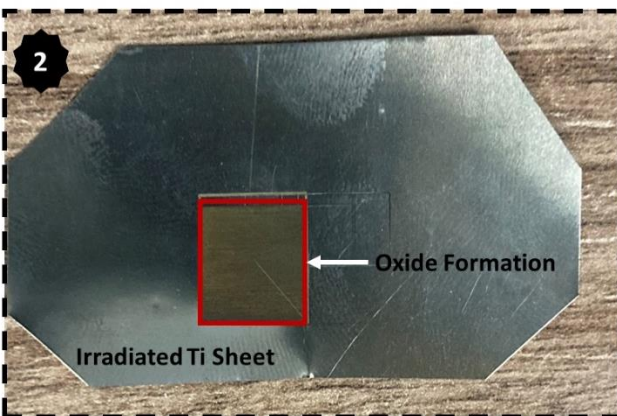
analysis or chemical characterization of the materials, where the presence of oxidized material can be determined, as illustrated in Figure 3-1(B).



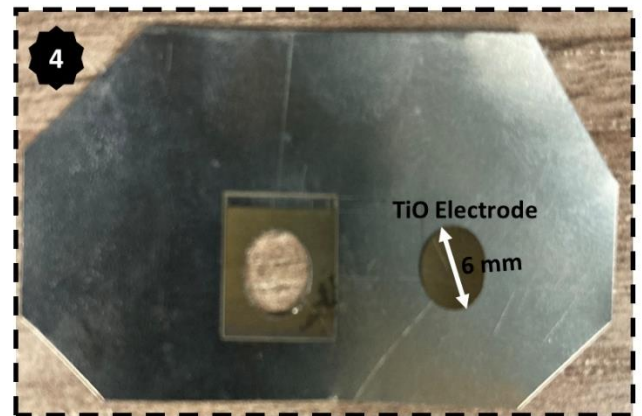
(A)



(C)



(B)



(D)

Figure 3-3: TiO electrode preparation. (A) Cleaned Ti sheet. (B) Oxide forming (TiO after irradiation via ULPING method). (C) The irradiation samples were punched into 6 mm circle discs using a round disc cutter. (D). TiO electrode is prepared.

3.1.2.3 Electrochemical Analysis

The final stretch is to investigate the electrochemical performance of the electrodes that have been fabricated. A two-electrode configuration (coin cell) was carried out, as shown in Figure 3-4, in which two symmetric coin shapes were punched into a 6mm disc and separated by a 1M sodium sulfate (Na_2SO_4 - CAS: 7757-82-6) electrolyte-soaked separator. This coin cell system was acquired from MTI Corp (NO. 2GXA21012) and is simple to assemble. All experiments were carried out in an ambient condition. To understand and analyze the electrochemical analyses of the prepared coin cells, an SP-150 Biologic Potentiostat was used (this information is also included in the key resources table). All the coin cell configurations were subjected to CV, GCD, and EIS. CV tests were carried out at scan rates of 500 mV/s (stable potential of -1V to 1V), 50 mV/s (stable potential of -0.8V to 0.8V), and EIS testing at a perturbation voltage of 50 mV/s at frequencies ranging from 100 mHz to 100 kHz. GCD experiments were carried out at potentials ranging from -0.8V to 0.8V and current densities ranging from 0.25 mA/cm². These tests aid in determining the efficacy of the fabrication scope through laser assistance in the creation of the oxide layer due to irradiation and ablation. As previously stated, we generated 31 electrodes with diverse T3DN structural properties by combining 31 different laser parameters to better understand the relationship between laser parameters and sample electrochemical performance (see Figure 3-5).

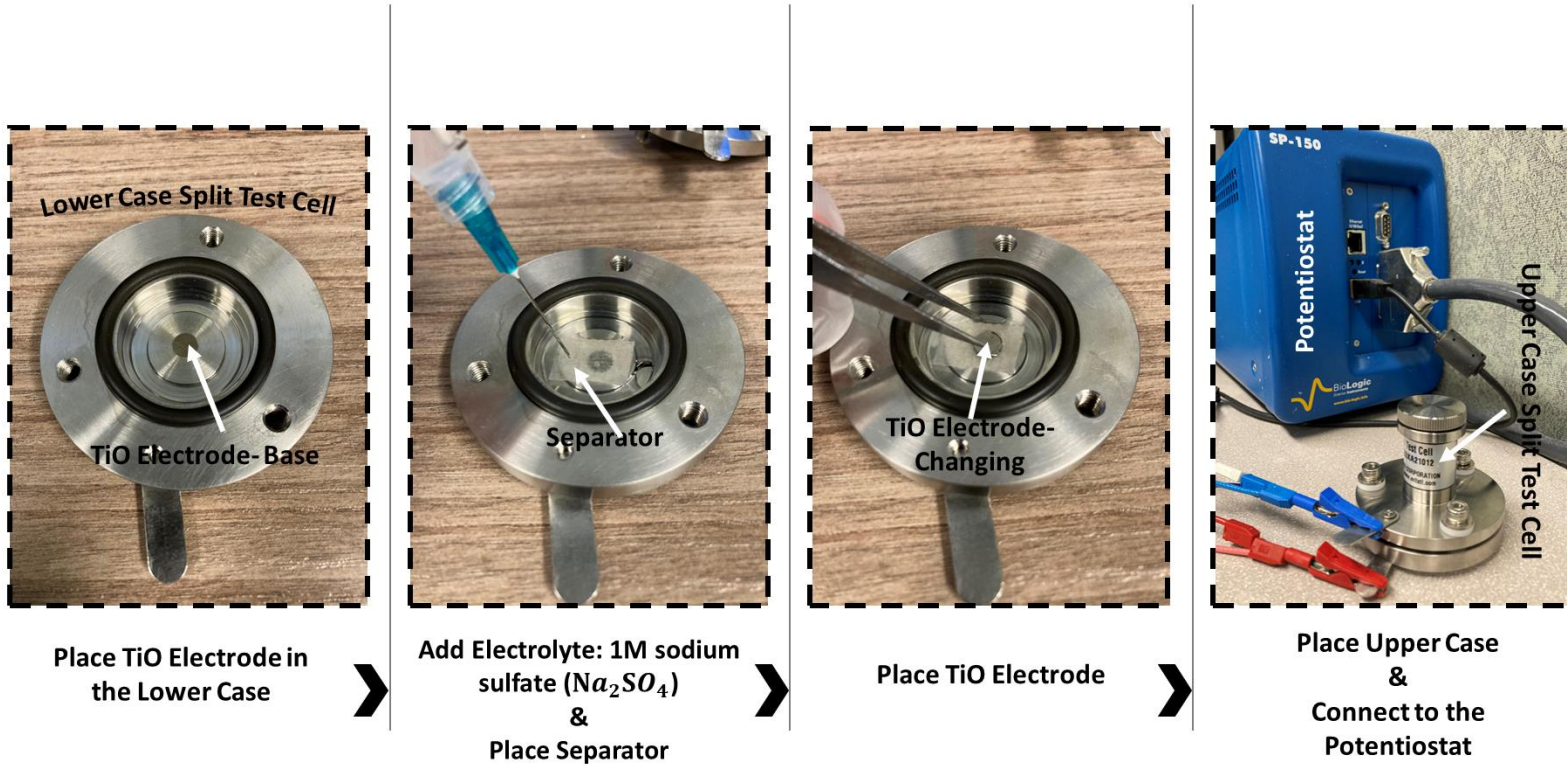


Figure 3-4: Coin cell electrochemical analysis setup.

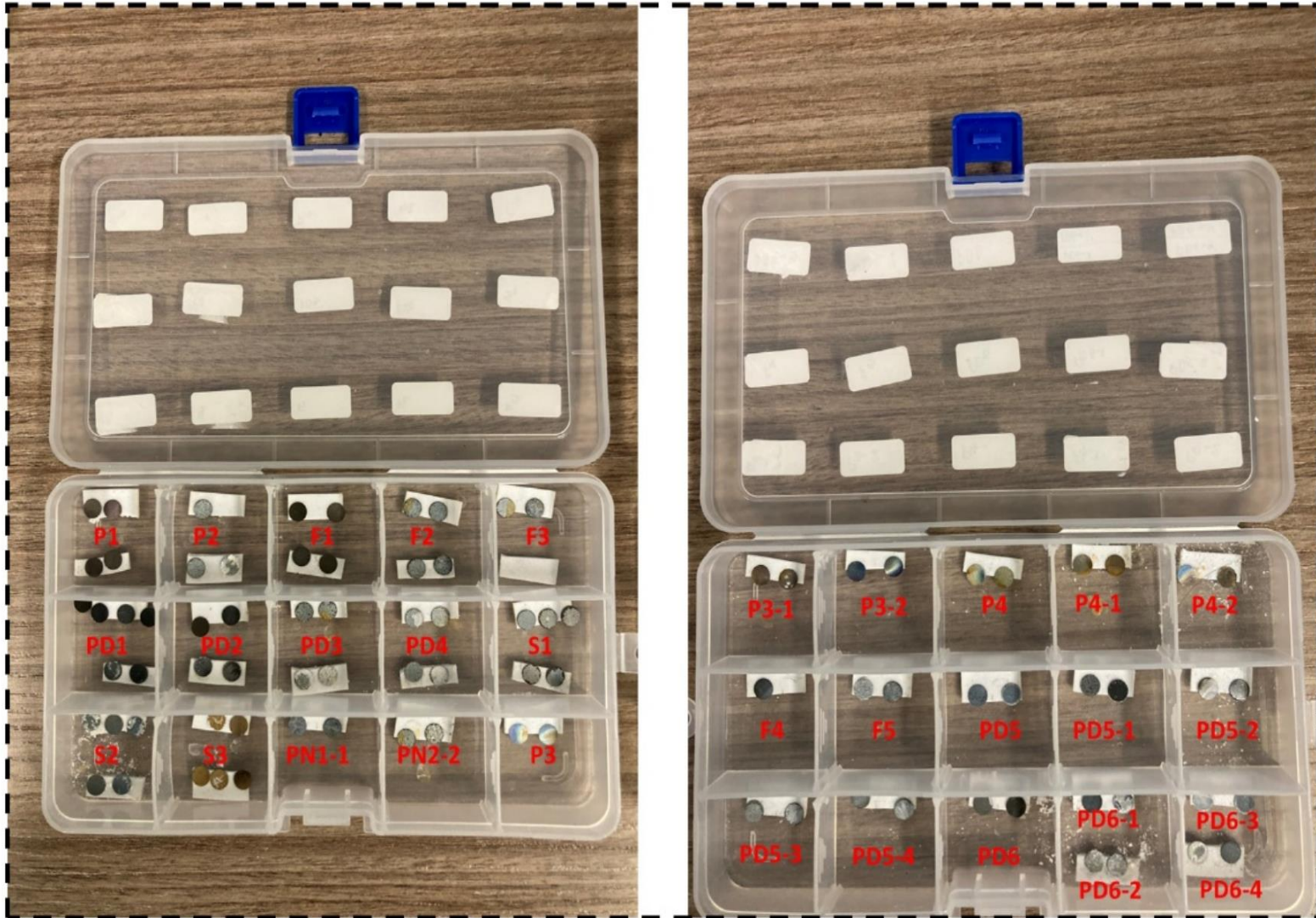
3.1.2.3.1 Specific Areal Capacitance, Energy Density, Power Density Calculation

The specific areal capacitance of each sample can be calculated from the GCD curve based on the following equation,

$$C_A = \frac{J \times \Delta t}{\Delta V}, \text{ where } J = \frac{i}{A} \quad (3-1)$$

Where J is the areal current density (0.25 mA cm^{-2}), Δt is the discharge time from fully charged ($0.8V$) to fully discharged ($-0.8V$), and ΔV is the stable potential window [392], [402]. Appendix A contains the MATLAB code for specific areal capacitance calculation.

To evaluate the practical strength of the fabricated electrodes two important parameters, energy density (E_S) and power density (P_S) can be determined based on their specific areal capacitance using equations (2) and (3) [399], [403].



(A)

Figure 3-5: 31 fabricated electrodes via ULPING.

$$E_S = \frac{1}{2C_A\Delta V^2} \quad (3-2)$$

$$P_S = 3600E_S/\Delta t \quad (3-3)$$

Where C_A is the specific areal capacitance calculated from GCD, ΔV is the potential window and Δt is the discharge time [404].

3.1.2.4 Porosity Estimation

The porosity of each sample was estimated by adjusting the threshold of the 100-micron SEM pictures of all the samples until the software completely emphasized the porous structure. For geometrical measures, ImageJ assumes a 5% margin of error (Wayne Rasband at the National Institutes of Health, USA) [405].

3.1.3 Computational Phase

It is important to emphasize that one of the main objectives of this research was to employ ML algorithms to forecast the electrochemical behavior of the pseudocapacitors fabricated through laser treatment. However, the accuracy and performance of ML algorithms depend largely on the quality and quantity of data. An unbalanced dataset can lead to overfitting and under-fitting issues, which is why it is essential to generate a large and accurate dataset for training the ML algorithm. The dataset generation/preparation and model development procedure are divided into four stages, as shown in Figure 3-6. The first stage describes how to build a large dataset from the experimental setup. The resulting dataset must then be structured and prepared for use in various ML methods. The most beneficial features from the dataset are selected using statistical approaches. Finally, three distinct ML

algorithms are constructed and trained on the dataset to predict the electrochemical performance of the pseudocapacitors, including impedance and specific areal capacitance.

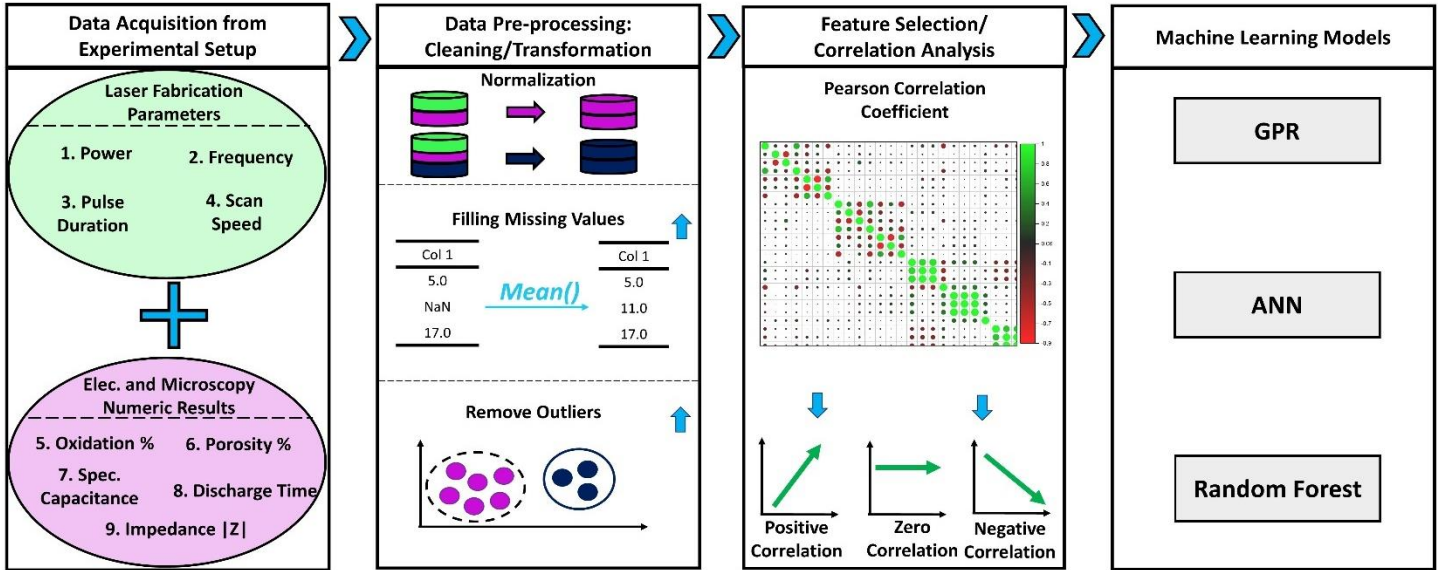


Figure 3-6: Dataset generation and preparation steps. Stage 1: data were collected from the experimental setup, including laser fabrication parameters and results of electrochemical and microscopy analysis. Stage 2: the data was pre-processed, which involved cleaning and transformation to ensure the dataset was ready for use in the ML algorithm. Stage 3: feature selection was used to finalize the dataset and select the most important features for use in the ML algorithm. Stage 4: the ML algorithms were trained on the dataset to predict the electrochemical behavior of the pseudocapacitors.

3.1.3.1 Data Acquisition from Experimental Setup

As employing laser treatment for pseudocapacitor electrode fabrication is a new research method, no specific dataset is publicly or privately available. By dataset, we refer to the information acquired from various pseudocapacitors by microscopy and electrochemical analysis, including electrode morphology and structural parameters, as well as other operational conditions values like discharge rate, electrode impedance, specific areal capacitance, and voltage window. To address this limitation, we prepared 31 electrodes, which allowed us to expand our experiments while also providing a large dataset for ML algorithms. To produce a large dataset, we introduced a unique mix-and-match testing

matrix. Using this matrix, we tested each of the 31 prepared electrodes individually against itself and the other electrodes, with all the necessary information gathered from the electrochemical analysis. The principle of the matrix is very simple and straightforward, as shown in Figure 3-7. For the first coin cell setup, for example, we used 1M salt as the electrolyte solution, and electrode P1 (the base electrode) was positioned in the lower cover of the MTI coin cell setup, with the same P1 electrode located on top of it. This procedure was repeated 31 times, with the P1 electrode serving as the base and the other top electrode serving as the changing electrode. The P2 electrode was likewise tested 30 times with itself and other electrodes, except for P1, which was tested in the previous column (shown with the red circle). This testing technique was continued until S4, which was tested only once with itself. Based on this matrix, we assembled all 496 sets of electrodes together. All 496-coin cell configurations were subjected to CV, GCD, and EIS, with the same setup configurations specified in the previous section.

3.1.3.2 Dataset for Machine Learning Algorithms

Including laser fabrication parameters in the experimental data will provide additional information about their relationship with the electrochemical behavior of the pseudocapacitors. According to Figure 3-6, several quantitative values were recorded, and they can be classified into two groups: laser fabrication parameters, microscopy, and electrochemical analysis (numeric results). These parameters influence the physical and chemical properties of the pseudocapacitor electrode, including its surface area, porosity, and crystal structure, which in turn impact the electrochemical performance.

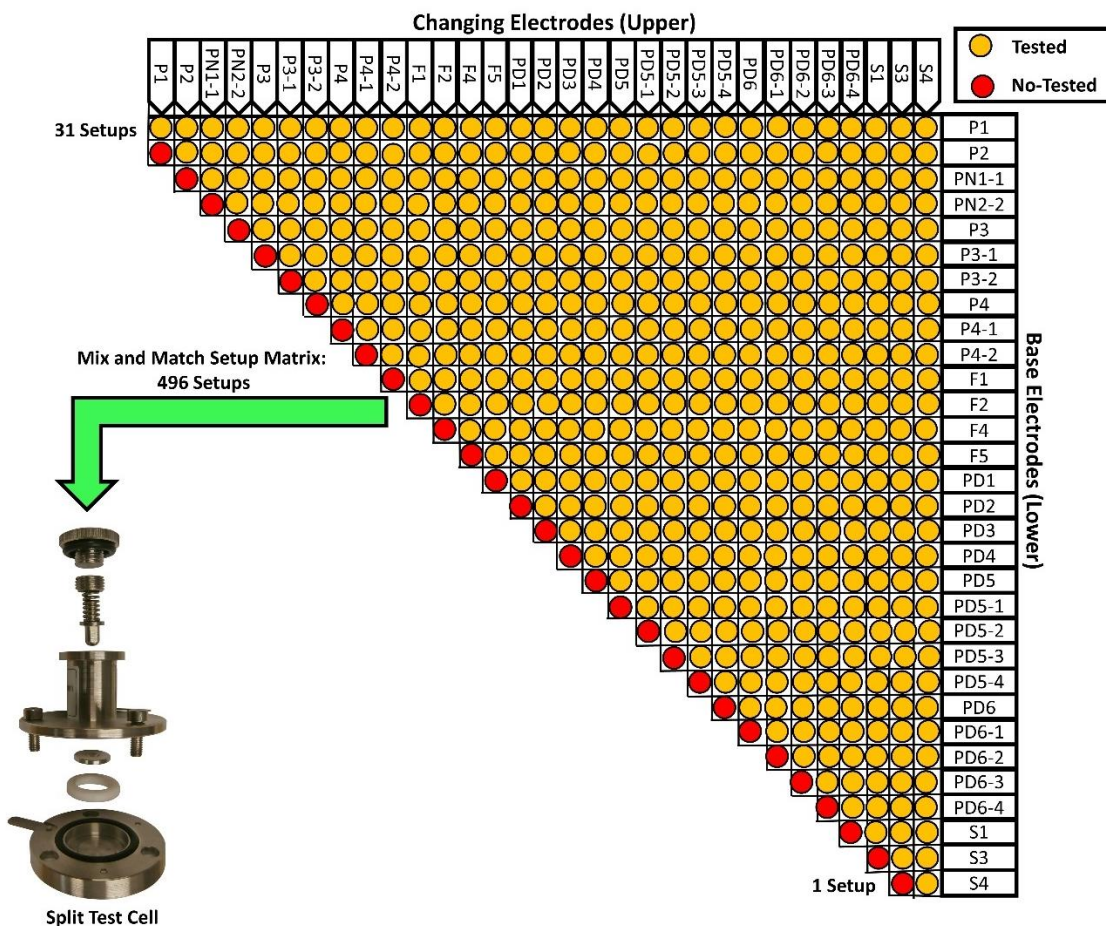


Figure 3-7: Data generation steps from the experimental setup. A one-of-a-kind mix-and-match testing matrix is introduced where each of the 31 prepared electrodes is individually tested against itself and the other electrodes.

Additionally, including microscopy and electrochemical analysis results will provide more comprehensive information about the electrode's structural and electrochemical characteristics. Overall, combining these different types of data will allow for a more thorough analysis of the relationship between laser fabrication parameters and pseudocapacitor performance. The following laser fabrication parameters were recorded: power (W), frequency (kHz), pulse duration (ps-ns), and scan speed (mm s^{-1}) for both electrodes (base and changing electrodes). The electrochemical analysis yielded multiple

variables, including discharge time (S), specific areal capacitance (mF/cm^2), and capacity ($\text{mA}\cdot\text{h}$). Additionally, the impedance (Ohm), phase angle ($|Z|$ -degree $^\circ$), and real impedance (ohm) are recorded at lower and higher frequencies. Several numerical parameters such as oxidation (%), Ti/oxidation ratio (%), and porosity (%) are obtained from the microscopy analysis for both electrodes. The recorded data is considered the final raw dataset from the experimental setup.

3.1.3.3 Dataset Pre-processing for Machine Learning Algorithms

The experimental data are used as input for the data-driven models. Since we are engaging with a regression problem in this study, input features are critical to the accuracy and robustness of the results [406], [407]. Therefore, employing a suitable data pre-processing strategy may be advantageous in boosting the prediction accuracy of a supervised ML system. Figure 3-6 depicts the data pre-processing approach applied, which contains data cleaning and transformation (removing outliers, filling in missing values, and normalizing). The proposed data pre-processing generates a complete and clean dataset free of extraneous information for predicting the electrochemical behavior performance of the fabricated electrodes.

The first step is data cleaning, which involves removing erroneous, incomplete, or duplicate data from a dataset. This process includes removing outliers and filling in missing values, among other techniques. Outliers can cause issues with certain models and removing them may improve model performance. The simplest nonparametric technique for detecting outliers in a one-dimensional feature space is numeric outlier detection. The interquartile range (IQR) is used to identify outliers. In a box-and-whisker plot, the IQR is

represented by the width of the box. The first and third quartiles (Q_1 and Q_3), for example, are calculated. An outlier is then defined as a data point X_i that falls outside of the interquartile range [408]. Outliers that fall outside of the typical data range or have a very low likelihood of occurring are deleted from the raw dataset.

In the next step, we detect missing values. Missing values resulting from sampling system errors are an unavoidable challenge in the experimental procedure. Depending on the dataset, various statistical methodologies can be used to fill in missing values. For example, we used the statistical mean method to fill in the missing values in the raw dataset [406].

Finally, we apply normalization to the data. This process scales the magnitudes of the values to significantly lower values. Normalization can help improve the convergence rate and reduce negative effects. In this investigation, we normalized the input dataset to the range of [-1, 1] using the following equation:

$$x' = \frac{(x - x_{min})}{x_{max} - x_{min}} \quad (3-4)$$

where x_{max} is the maximum value, and x_{min} is the minimum value of input vector x . Appendix A contains the Python code for data pre-processing.

3.1.3.4 Feature Selection with Correlation Analysis

To achieve a compacted dataset, a data dimensionality reduction approach must be applied. One of the common methods to detect and remove redundant and irrelevant features is the feature selection approach based on correlation analysis [409]. To evaluate the relationship between two variables, we employed a common statistical approach known as Pearson's correlation coefficient analysis. The Pearson correlation coefficient (r) expresses the

strength of the linear relationship between variables. It exhibits correlations with a moderate-to-high positive or negative correlation (close to -1 or 1), whereas those with a low correlation are presented (value close to 0). In general, the higher the correlation between input features and output of a data-driven model, the better the model's accuracy. Its formula is as follows [410],

$$r = \frac{\sum_{i=1}^N (x_i - \bar{x})(y_i - \bar{y})}{(N - 1)\sigma_x \sigma_y} \quad (3-5)$$

where x_i is the feature sequence, y is the target output, \bar{x} and \bar{y} are their average values, and the variable σ is the standard deviation [410],

$$\sigma = \sqrt{\frac{\sum_{i=1}^n (x - \bar{x})^2}{(N - 1)}} \quad (3-6)$$

The calculation's usage of mean and standard deviation implies that the two data samples must have a Gaussian or Gaussian-like distribution. We used correlation analysis for removing the less important predictor variables. In our case, since we're dealing with a regression task when two or more independently correlated features are presented in a dataset, the model can use either of these correlated features as a predictor without explicitly selecting one over the others. However, once one of them is used, the importance of the others reduces significantly because the first characteristic effectively removes the impurity that they can remove. As a result, we performed Pearson correlation analysis to identify and delete strongly associated elements. For this experiment, we set the threshold at 0.7. Considering the correlation analysis, the scan speed (base electrode) is eliminated from the laser fabrication parameters. The oxidation and Ti/oxidation ratio for the base electrode are eliminated based on the microcopy numerical results. Furthermore, the impedance at higher frequencies, as well as the real impedance at lower and higher

frequencies, are eliminated from electrochemical analysis. A low-dimensional training dataset $D \in \mathbb{R}^{n \times m}$, consisting of the remaining variables is constructed, where m represents the number of features and n represents the number of samples. The remaining features are shown in Figure 3-8.

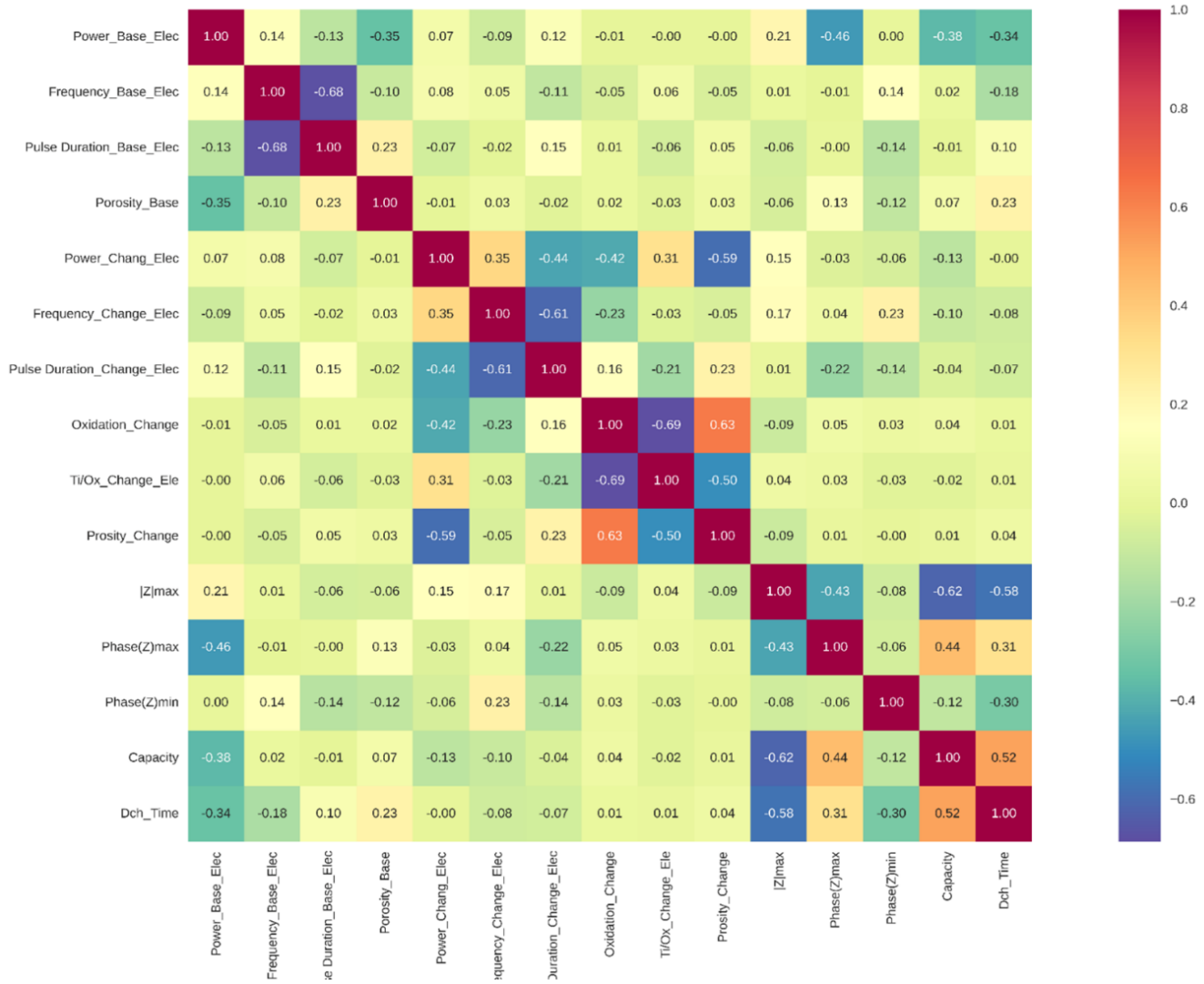


Figure 3-8: Heatmap of a correlation matrix. The threshold is set to 0.7 and the feature above the threshold is eliminated from the dataset.

3.1.3.5 Electrochemical Behavior Prediction Using Regression Machine Learning Algorithms

We present a large-scale empirical comparison of three typical learning algorithms available in the literature, particularly in the supercapacitor community, to evaluate their computing efficiency, accuracy, and applicability for design techniques in this section. Indeed, we make every effort to investigate the space parameters and common variations of each learning method as fully as computationally possible. The three learning algorithms used to predict the electrochemical behavior of the fabricated pseudocapacitor electrodes are RF, GPR, and ANN. Each learning method is developed in Python and executed on a laptop with a 2.59 GHz Intel Core i7-5600U CPU and 8 GB of RAM. This information is also included in the key resources table.

3.1.3.5.1 Gaussian Process Regression for Electrochemical Behavior Prediction

GPR is an efficient solution for estimating nonlinear functions when specifying parametric forms for unknown processes is problematic due to nonparametric modelling and probabilistic predictions [411]. The GP is generated by extending multivariate Gaussian distributions to infinite dimensions, which can be thought of as a distribution over functions and is used to characterize continuous functions. The Gaussian distribution is reflected in the appropriate probability distribution over function $f(x)$ for any finite inputs as follows [411]:

$$f(x) \sim GP(m(x), k_f(x_i, x_j)) \quad (3-7)$$

where the mean and covariance functions are represented by $m(x)$, and $k_f(x_i, x_j)$ respectively, and are expressed by,

$$m(x) = E(f(x)) \quad (3-8)$$

$$k_f(x_i, x_j) = E[(f(x_i) - m(x_i))(f(x_j) - m(x_j))] \quad (3-9)$$

Where $E()$ is the expectation value, $m(x)$ is considered zero for the sake of simplicity, and

$K_f(x_i, x_j) = \delta_f^2 \exp(\frac{-(x_i - x_j)^2}{2l^2})$ is the radial basic kernel function (RBF) [412]. δ_f is the

kernel function's amplitude, and l is the distance measure's length scale. The prior

distribution of outputs z in our regression problem is as follows [411],

$$z \sim N(0, k(x, x') + \sigma_n^2 l_n) \quad (3-10)$$

where N is the normal distribution, σ_n is the noise parameter, x , and x' are considered

training and test set respectively. Thus, y' the predicted output would mirror the joint prior

distribution with the training output y [411],

$$\begin{bmatrix} y \\ y' \end{bmatrix} \sim N(0, \begin{bmatrix} k(x, x) + \sigma_n^2 l_n & k(x, x') \\ k(x, x')^T & k(x', x') \end{bmatrix}) \quad (3-11)$$

The covariance matrices between the training and testing sets are given in the preceding

equation. Furthermore, the n points in the training phase are required to maximize the

hyperparameters (θ) in the covariance function. An efficient optimization solution is to

minimize the negative log marginal probability $L(\theta)$ [411];

$$\begin{cases} L(\theta) = \frac{1}{2} \log[\det \lambda(\theta)] + \frac{1}{2} y^T \lambda^{-1}(\theta) y + \frac{n}{2} \log(2\pi) \\ \lambda(\theta) = k(\theta) + \sigma_n^2 l_n \end{cases} \quad (3-12)$$

Then the predicted y' is determined for x' based on the corresponding conditional

distribution as;

$$p(y'|x', x, y) \sim N(y'|y^-, cov(y')) \quad (3-13)$$

Where,

$$\begin{cases} y^- = k(x, x')^T [k(x, x) + \sigma_n^2 l_n]^{-1} y \\ cov(y') = k(x', x') - k(x, x')^T [k(x, x) + \sigma_n^2 l_n]^{-1} k(x, x') \end{cases} \quad (3-14)$$

where $y^{-'}$ represents the associated forecast mean values, and $cov(y')$ is a variance matrix that represents the uncertainty range of these predictions [411].

3.1.3.5.2 Random Forest Regression for Electrochemical Behavior Prediction

Random forest generates hundreds of distinct decision trees, each with its own regression function. The average of all decision tree outputs is the RF regression forecast from all trees. Classification and regression trees (CART) are a statistical model that can be used to address classification or regression predictive modeling problems [413]. Every decision tree has decision nodes and leaf nodes that evaluate each fed-in sample with a test function and route it to different branches based on the features. Assume the training dataset $TD = \{(X_1, y_1, \dots, (X_n, y_n))\}$, for this regression problem, where n is the number of instances. The procedure for constructing the RF regression model is as follows,

Construction of Random Forest Regression [414]

Step 1: The bootstrap approach is used to randomly select N samples from the entire dataset (TD), and N regression trees are formed; the out-of-bag (OOB) data that are not selected can be utilized as the testing set (which in our case did not happen) [415].

Step 2: Replace the sample obtained from Step1 ($z_n^i = 1, \dots, B$).

Step 3: Fit a tree based on the B , the results for each train i would be $y_i' = G_i(X, Z_n^i)$.

Step 4: The outputs of all trees are then averaged to perform the aggregate. As a result, the output estimation y_i' can be determined by; $y_i' = \frac{1}{B} \sum_{i=1}^B G_i(X, Z_n^i)$.

To execute RF regression, just two parameters must be changed: the number of trees and the number of random features for each split in the forest to build. Appendix A contains the Python code for random forest regression model building.

3.1.3.5.3 Artificial Neural Network for Electrochemical Behavior Estimation

An ANN regression model is developed in Python using a multilayer perceptron (MLP) with MLP Regressor from the Sci-kit learn library [412]. MLP, as shown in Figure 3-9, is

the most basic type of feed-forward network. The units are stacked in a series of layers, with each layer containing a number of identical units. MLP has fully connected neurons in each layer, each with its own weight. The first layer is the input layer, and its units take the input features' values. The final layer is the output layer, which contains one unit for each value that the network outputs. All of the layers in between are referred to as hidden layers. In our work, for example, the input layer has 12 features, 1 hidden layer, 64 neurons, and one output layer with one unit. The mean square error (MSE) is used to determine the loss function during training, as illustrated in the following equation [416];

$$MSE = \frac{1}{K} \sum_{i=1}^K (y(i) - \hat{y}(i))^2 \quad (3-15)$$

Where $y(i)$ present the experimental value, $\hat{y}(i)$ is the estimated value and K is the number of data points. Due to its fast convergence and validation accuracy with big datasets, the Adam optimization algorithm is used for updating weights, and a constant learning rate of 0.001 is used. The model is run over 400 epochs with a batch size of 16. The following equation describes the hidden layer's output activation:

$$v_j^l = f\left(\sum_{i=1}^{j-1} (w_{ji}^l \alpha_i)\right) \quad (3-16)$$

Where l is the hidden layer index, j is the number of neurons in the l^{th} hidden layer such that $j \in Z^+$, $j-1$ is the number of neurons in the $(l-1)^{th}$ hidden layer, and α is the number of features for the layers. The activation function is denoted by $f(\cdot)$. We used the rectifier linear unit (ReLU) as the activation functions [417]. Also, the weight (w_{ji}^l) between layers

are being randomly initialized. MPL modelling takes into account several phases, which are represented in seven steps:

Construction of Multi-Layer Perceptron

Step 1: Feeding normalized experimental data

Step 2: Building the network

Step 3: Configuring the network

Step 4: Initializing the weights and biases

Step 5: Training the network

Step 6: Validating the network

Step 7: Using the network

Appendix A contains the Python code for MLP model construction.

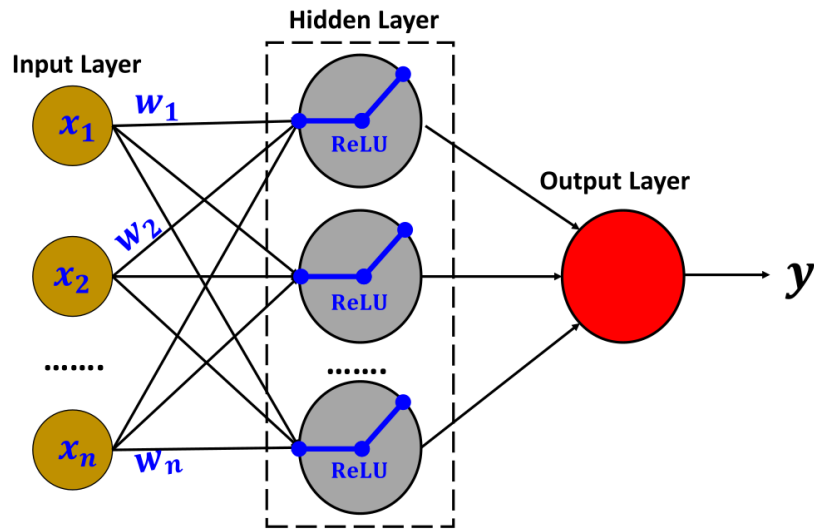


Figure 3-9: Multi-Layer Perceptron with one hidden layer.

3.1.3.6 Training and Test Sets

In general, we divided the dataset into training and testing sets. We utilize the training set to train the model and the testing set to validate the model. The dataset is randomly mixed and divided into 80% training and 20% test data (370 cycles for training and the remaining for validating). The training splits from each pseudocapacitor dataset are pooled into a single dataset. The model's accuracy is then determined by evaluating its performance

using an error metric. This approach, however, is not particularly accurate because our dataset is not very large, and it can be improved. As a result, we used K-fold CV by separating the data into folds and ensuring that each fold is used as a testing set at some time. In other words, the training data is divided into K equal-length segments, with each fold serving as a testing set at some point. Consider 10-fold cross-validation (K=10) as an example. The data set is divided into ten folds in this case. The model is trained 10 times in the first iteration, with one of the segments serving as the test set (validation set) and the rest as the training set. This procedure is repeated until each of the ten folds has served as the testing set. The resulting root mean squares error (RMSE) is then averaged, and the RMSE is determined as a result.

3.1.3.7 Model Performance Metrics

To evaluate the performance of the proposed models, we use the following criteria: root mean square error (RMSE) and coefficient of determination (R^2). We use RMSE as a standard error-index and calculate it for both the expected and actual values. The RMSE's mathematical equation is as follows:

$$RMSE = \sqrt{\frac{1}{K} \sum_{i=1}^K (y(i) - \hat{y}(i))^2} \quad (3- 17)$$

Where $y(i)$ present the experimental value, $\hat{y}(i)$ is the estimated value and K is the number of data points. R^2 expresses the quality of fitting a regression model and ranges

from 0 to 1, the higher the R^2 , the better the model fits the dataset. R^2 is close to 1 is better and close to 0 is worse [416]. The following formula represented R^2 ,

$$R^2 = 1 - \frac{\sum_{i=1}^K (\hat{y}(i) - \bar{y}(i))^2}{\sum_{i=1}^K (y(i) - \bar{y}(i))^2} \quad (3-18)$$

Where $y(i)$ present the experimental value, $\hat{y}(i)$ is the estimated value, $\bar{y}(i)$ is the mean value of all the data points, and K is the number of data points.

3.1.4 Optimization of Pseudocapacitors Electrode Fabrication Strategy

⁸The aim of this section is to accomplish three objectives. The first objective is to generate a dataset from the experimental setup. The second objective involves utilizing the generated dataset to train an artificial neural network (ANN) model for forecasting the electrochemical behavior of pseudocapacitors fabricated through laser treatment. The final objective is to incorporate a meta-heuristic optimization algorithm, utilizing the trained ANN model, to determine the most optimal laser fabrication parameters. The dataset generation and preparation, the development of the model, and the optimization process are separated into four stages, as depicted in Figure 3-10.

One of the objectives of this work was to theoretically predict the electrochemical performance of a pseudocapacitor fabricated using the ULPING method. To achieve this, an ANN model was constructed and optimized to predict the impedance ($|Z|$) and specific capacitance of the pseudocapacitor. The developed models provide new insights into the modeling and theoretical prediction of such pseudocapacitors. The MLP model was found to be effective in forecasting $|Z|$ and specific capacitance, as demonstrated by the low error values (RMSE) obtained for this model.

⁸ This section is based on a previously published article:
Kavian Khosravinia, A. Kiani. "Optimizing the Operation Strategy of the ULPING Technique for Enhancing Capacitance of Supercapacitor Electrodes, using ANN and SA Algorithms", ACS Omega. The material is reproduced here with permission from the publisher, [American Chemical Society].

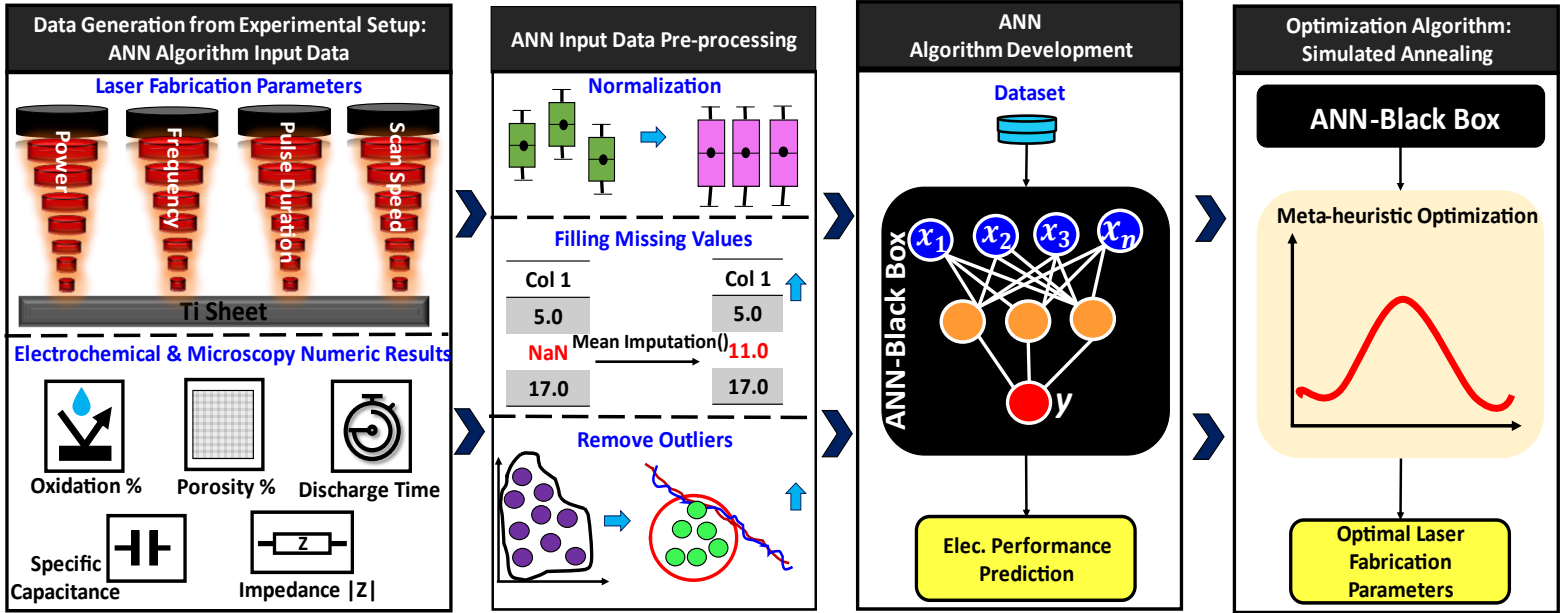


Figure 3-10: The modeling and optimization process consist of four stages. Stage 1: involves the generation of a comprehensive dataset from the experimental setup, which includes information on laser fabrication parameters and results of electrochemical and microscopy analysis. Stage 2: the generated dataset is structured and prepared for the next stage. Stage 3: ANN is built and trained on the dataset to forecast electrochemical performance measures, such as impedance and specific areal capacitance, of pseudocapacitors. Stage 4: the trained ANN is employed in a meta-heuristic optimization algorithm to identify the optimal laser fabrication parameters.

3.1.4.1 Optimization Algorithm Selection

In our approach, we use simulated annealing (SA) as an optimization algorithm to maximize the objective function of a trained MLP model. The MLP model is treated as a black box, and we aim to find the most optimal laser fabrication parameters by maximizing a specific capacitance value. In this section, we first discuss the rationale behind using the SA algorithm and then explain how we formulate the optimization problem using SA.

3.1.4.1.1 Simulated Annealing

SA is a heuristic optimization algorithm that is based on the Monte Carlo search method and resembles the cooling process used for molten metals during annealing. SA typically starts with a random initialization, and the current state is then stochastically perturbed to reach a new state [418], [419]. In the case of molten metals, the internal energy (E) tends to decrease spontaneously, but higher internal energy levels can also be accepted with a certain probability. For optimization purposes, the internal energy can be regarded as the fitness function, and the mechanism for accepting the new solution is based on the Metropolis algorithm. The Metropolis algorithm dictates that the probability of accepting a new solution is related to the annealing temperature, which is given by equation (3-19). This equation shows that the probability of acceptance increases at higher temperatures, while at lower temperatures, the solution tends to remain unchanged [420], [421].

$$P_{ij} = \begin{cases} 1 & , E_j < E_i \\ \exp\left(-\frac{E_j - E_i}{T}\right) & , E_j \geq E_i \end{cases} \quad (3-19)$$

The probability of accepting the current solution (P_{ij}) is determined by the Metropolis algorithm, where "i" represents the previous iteration, and "j" refers to the current iteration. The optimizing function is the internal energy (E), and the annealing temperature (T) determines the probability of accepting the new solution. The process involves several iterations to search for the optimal solution, and the temperature is gradually reduced at an extremely slow rate to ensure the precision of the solution. At the end of each iteration,

annealing takes place, and the annealing temperature is reduced using equation (3-20) [421], [422],

$$T_{K+1} = T_K * K \quad (3-20)$$

where " K " represents the annealing rate. This is because slower annealing tends to provide better precision. The global search for a feasible solution depends on the number of iterations, which can be increased by using a higher annealing temperature and a slower cooling scheme. This approach can lead to better performance by allowing the algorithm to explore a wider range of solutions. Additionally, the independent initialization of the algorithm allows for a more comprehensive search for the optimal solution.

3.1.4.1.2 Simulated Annealing Implementation for Laser Parameter Fabrication

The SA method is implemented based on the laser fabrication parameters and the trained MLP model. In algorithm 1, the first step is to call the trained MLP function using a vector x_n , which includes all eight laser fabrication parameters for asymmetric optimal design, and four laser fabrication parameters for symmetric optimal design. The SA algorithm recommends two sets of four laser parameters for asymmetric optimal design, which fabricate two different electrodes, and one set of laser fabrication parameters for symmetric optimal design, which fabricate both electrodes.

Various parameters need to be initialized, including the initial temperature, the lower temperature limit, cooling schedule rate, the number of iterations, the objective function, and the initial solution (see Table 3-3). The cooling schedule rate should be moderate, as a too high rate can cause the algorithm to converge to a local optimal solution, while a too slow rate can result in a longer search time [423], [424]. After initializing the parameters,

the initial solution is evaluated using the objective function, which aims to maximize the specific areal capacitance ($\max f(x_n)$). The difference between the current solution value and the previous accepted solution value is calculated, and if the difference is less than zero, the solution corresponding to the current function value is updated to the solution after the loop is solved [425]. If not, the solution corresponding to the current function value is updated to the solution after the loop with a certain probability [425]. This process will be repeated N times where N is the number of iterations in each temperature. The current temperature is updated using the cooling schedule rate after each cycle until the end of the cycle, and the optimal solution is obtained at the end of the cycle. Lastly, the SA algorithm recommended eight different laser fabrication parameters for asymmetric optimal design and four different laser fabrication parameters for symmetric optimal design, which can be found in Table 3-4.

Table 3-3. SA parameters for optimal electrode design.

Parameters	Description	Value
T_{max}	initial temperature	1000
T_{min}	lower temperature limit	0.001
K	Cooling schedule	0.9
$N_{iteration}$	Iterations per temperature	1000

Algorithm 1: SA for Optimal Electrode Design

1: $f(x_n); x_n = \{x_1, x_2, x_3, x_4, x_5, x_6, x_7, x_8\}$	▶ Call the MLP function based on the input laser parameters (power, frequency, pulse duration, and scan speed).
2: $T = T_{max};$ $K = 0.9;$ $N = 1000;$	▶ set the initialization of all parameters, including temperature T , iteration N , cooling rate K .
3: $x_{current} = rand(x_n);$	▶ Random initial solution.
4: $f(x_n) \rightarrow$ Specific areal capacitance $f(x_n)$	▶ The initial solution is evaluated using the objective function.
5: While $T > T_{max}$	▶ Verify the temperature of the outer loop.
6: $N = 1:1000$ $x_{n,new} = Generator(x_n)$	▶ Change one parameter in x_n in the constraint range (Range of parameters when have limits based on other parameters)
7: Evaluate: $f(x_{n,new})$	▶ Calculate change of energy level.
if $f(x_{n,new}) > f(x_n)$ accept	▶ Integrating the solution for improvement.
else $\left\{ \begin{array}{l} x_{rej} \\ \text{if } e^{-\{f(x_n) - f(x_{n,new})\}} < rand(0,1) \end{array} \right.$	▶ Acceptance with probability function.
end	▶
$T = T * K$	▶ Reduce the temperature
if $T < T_{min}$	▶ End of optimization
end	

Table 3-4. SA optimal laser fabrication parameters for electrode design.

Optimal Solutions	Base Electrode				Changing Electrode			
	Power (W)	Frequency (KHz)	Pulse Duration (ns)	Scan Speed (mm/s)	Power (W)	Frequency (KHz)	Pulse Duration (ns)	Scan Speed (mm/s)
Asymmetric (OPT-ASY)	13	100	2	5	17	600	1	290
Symmetric (OPT-SYM)	20	600	1	10	20	600	1	10

3.2 Operational Phase: Method Details

3.2.1 Section Overview (Anode Potential Prediction for Lithium Plating Mitigation)

⁹ One of the primary limitations of EVs today is the lengthy recharging time of LiBs, which can take several hours compared to the 3-7 minute refueling time of the gas-fueled car [426]. Therefore, the US Department of Energy's current goal is to increase charging speed by offering extreme fast charging (XFC), which allows an electric vehicle to recharge to 80 percent of full capacity in less than 15 minutes [427]. A minimum of 300 kW charging power is necessary to achieve the 15-minute recharge time for a big battery pack size (for example, >90 kWh) [428].

However, reaching extreme fast charging is often failed due to the increased formation of anodic lithium deposits or lithium plating in the LiB community [429]. During ideal charging conditions, the potential of lithium intercalation into graphite is in the range of 65-200 mV vs. Li^+/Li^0 potential and no lithium plating occurs at this level as shown in Figure 3-11 (b) [429]. During harsh charging conditions, however, charge transfer kinetics in the electrolyte and solid-state diffusion are hindered, causing anode potential to fall below the potential of lithium metal and causing lithium plating to occur (Figure 3-11 (a)) [429]. While some of the plated lithium can be stripped reversibly, the remainder (irreversible portion) can react with the electrolyte to form a secondary solid electrolyte

⁹ This section is based on a previously published article: Kavian Khosravinia, X. Lin. "Toward Enhanced Anode Potential Prediction of Lithium-ion Batteries: Using Optimized Ensemble Selection Approach for Lithium Plating Mitigation", Journal of The Electrochemical Society. The material is reproduced here with permission from the publisher, [IOPSCIENCE].

interphase (SEI) layer [227]. It can also form a high-impedance "dead" lithium film that is electrically isolated from the graphite anode and remains irreversible, increasing the internal resistance and also decreasing the energy density [295]. The irreversible portion contributes to capacity fading through the loss of lithium inventory (LLI), whereas the fully reversible portion does not contribute to capacity fading [217], [218]. In severe circumstances, the accumulated lithium might also form dendrites, which can develop and permeate the separator.

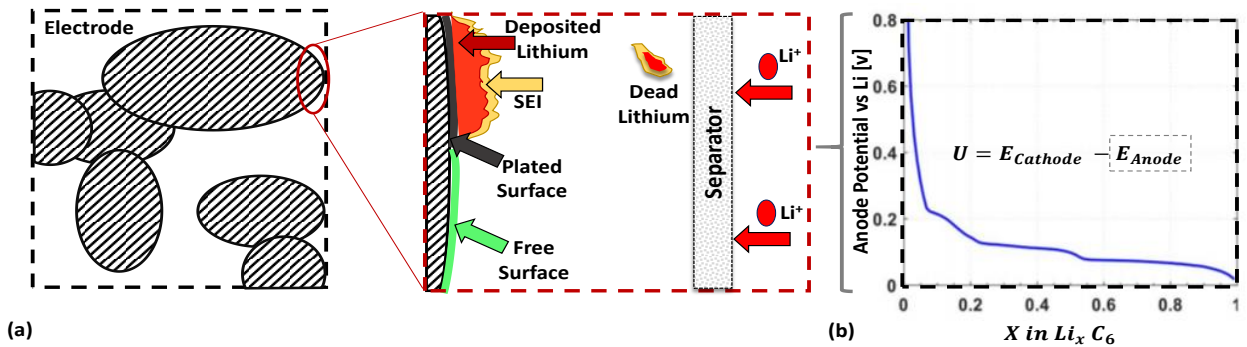


Figure 3-11: (a) Schematic of lithium plating on the graphite anode electrode. The primary SEI layer (yellow color) is formed at the anode surface during the first charge of the cell to protect the electrode. Because the primary SEI layer prevents electrons from making direct contact with the electrolyte, metallic lithium (red color) is deposited between the primary SEI layer and graphite particles. (b) Charge curve of graphite anode potential, X-axis shows the state of lithiation, and the Y-axis shows the anode potential [375].

Detection of lithium plating is not straightforward, and often only indirect proof is given through the aging behavior, the discharged cell voltage, or post-mortem analysis. On the other hand, there are several methods for directly detecting lithium plating, such as physical characterization approaches for both surface morphologies and chemistry, which are extensively employed in fundamental studies. They can provide a detailed understanding of the lithium plating process in the laboratory, but not a mechanistic understanding, and they are not practical in actual engineering applications (EV applications) [342]. As

mentioned earlier, lithium plating occurs when the anode potential drops below 0 V (vs. Li^+/Li^0), and measuring/estimating the anode potential, E_{anode} , (vs. Li^+/Li^0) could give direct proof of the lithium plating. The lower the anode potential, the higher the lithium plating rate. Therefore, real-time prediction of anode potential is the first step to preventing lithium plating. The anode potential must be accurately monitored in real-time during fast charging to prevent lithium plating.

Therefore, the measurement/estimation of the anode potential as an effective and direct evidence approach to detecting lithium plating has garnered a lot of interest in the literature. Anode potential measurement/estimation of LiBs is commonly predicted using three methods, namely, direct measurement, electrochemical models (physics-based model) estimation, and data-driven methods.

The first of these methods often make use of a third reference electrode (RE) as a measuring device to directly measure the anode potential [430]. The anode potential can be measured by inserting the RE into the cell using a certain setup (machinery). It is impossible to overestimate the importance of RE materials and cell designs in the insertion process. Several studies have been carried out to demonstrate how to construct and incorporate the RE into LiBs, as well as where the best position for the RE is to reduce ohmic drop while improving measurement accuracy [431], [432]. Waldmann et al. [235] used a novel technique by positioning the RE near the anode's current collecting tab, which has a higher current density. Due to the limited diffusivity of lithium-ions in graphite at low temperatures and high SOC, they discovered that lithium-ions begin to accumulate near the

anode interface. Nonetheless, due to safety concerns, RE has yet to be used in any commercial cells or real-time LiB applications for measuring electrochemical properties.

Electrochemical models offer another method for estimating the anode potential, as they can cover both the particle and cell levels of a lithium-ion cell and simulate the anode potential. Ge et al. [243] investigated lithium plating at low temperatures using Newman's electrochemical model, also known as a pseudo-two-dimensional (P2D) model. They split the overall electrochemical reaction current density into two parts: lithium intercalation current and lithium deposition current, which could both be described by the Butler-Volmer equation. They discovered that during low-temperature charging, when the overpotential is minimal, lithium ions begin to collect at the anode-separator interface and eventually move inside the anode electrode [243]. However, the model validation was done with only a few data points. Tang et al. [377] also presented a P2D model to investigate lithium plating during cell charging. They discovered that increasing the thickness of the negative electrode can hinder lithium deposition, particularly around the electrode's edge. Another interesting approach by Tipmann et al. [376] also built a P2D electrochemical model combined with a 0D thermal model for operation at low temperatures in order to anticipate the aging effects throughout a range of temperatures (-25 °C to 40 °C) and currents (0.1 C to 6 C). They used COMSOL to run the simulation and compared the obtained results to EIS experiments.

However, in all the previous investigations, both practical and theoretical concerns make developing a proper model for LiB anode potential estimation challenging. From a practical point of view, the model-based anode potential estimation model requires extensive study,

laborious experiments, and a lengthy timeframe. On the theoretical side, model-based anode potential estimation approaches rely on an extensive understanding of battery chemistry, physics, and chemical reactions, which is made up of many complex mathematical equations, complicating the battery model development and parameter estimation. As a result, due to both practical and theoretical considerations, the integration of these models into battery management systems (BMS) is not advised, making it impractical for use in real-time control tasks.

Recently, to overcome the drawbacks of the above approaches, data-driven methods have been gaining remarkable attention as machine learning techniques rapidly advance. The machine learning-based anode potential estimation algorithms make use of a mass of data and powerful models to estimate the anode potential with little prior knowledge of battery internal characteristics and chemical reactions. Hence it can be the ideal solution to address the complex and nonlinear characteristics of LiBs. In a recent paper, we proposed a data-driven approach that utilizes the long short-term memory (LSTM) architecture to estimate the anode potential in real-time for lithium plating prevention [375]. The LSTM model can complete the entire test within 87 s whilst it takes the physics-based model about 7.44 h [375]. Another data-driven method based on a common machine learning technique was proposed in [433], where the authors used linear regression and random forest techniques to develop a prediction model. They used a P2D model as a benchmark to validate their findings (the random forests model reduces the root mean square error to 2.6 mV). However, they did not consider driving charging profiles in their study which may decrease their model accuracy.

Based on these two studies, we can conclude that data-driven approaches can predict the fundamental characteristics of battery aging without requiring knowledge of the electrochemical principles of the battery, and thus are easier to implement, computationally inexpensive, and less complex than model-based methods. Nevertheless, the accuracy and performance of data-driven techniques are heavily reliant on the quality and quantity of data, as an unbalanced dataset leads to overfitting and underfitting problems. Furthermore, selecting hyperparameters for machine technique algorithms through ineffective trial and error increases computing complexity, such as poor training speed and data fitting difficulty, resulting in inadequate anode potential results. On the other hand, the data-driven anode potential estimation has not been investigated thoroughly to examine and introduce a proper regression algorithm for anode potential estimation where it could be computationally efficient and accurate enough to be suitable for online implementation. Therefore, a large-scale empirical evaluation of four supervised learning methods and their optimal combination not only resolves the computational burden of machine technique algorithms but also produces great results in LiBs anode potential estimation.

In this section, I present a new method for accurate anode potential estimation using an optimized ensemble selection approach. The goal of this approach is to combine several models in order to improve the prediction accuracy in regression applications. The results reveal that the developed approach is accurate and resilient since it can estimate anode potential under a variety of operating conditions.

3.2.2 Experimental Setup for Anode Potential Prediction

The anode potential is a key signal in this study due to its direct relationship to lithium plating. As previously stated, obtaining anode potential from a lithium-ion cell is not as simple as determining other measurable cell parameters such as voltage, current, and temperature. This section explains how a physics-based model with thermal dynamics can determine the anode potential by mimicking the cell behavior. As shown in Figure 3-12, the dataset generation procedure is divided into three stages, which are detailed in the following subsections.

3.2.2.1 Data Acquisition from Experimental Setup

A commercial cylindrical cell LG INR18650F1L (high-energy-density) cell is used in this study. This battery has a minimum capacity of 3.35 Ah, a voltage range of 3.6 V – 4.2 V, and a maximum specified charging rate of 0.5C. The anode and cathode of this cell are made of graphite and Lithium Nickel Manganese Cobalt Oxide (NMC), respectively. The LG INR18650F1L is connected to a Neware battery test device (Neware CT-22), and an infrared thermometer MLX90614 is mounted to the battery holder and is used to monitor the surface temperature of the test battery cell. Multiple experiments, including 0.1C, 0.5C, 1C, and 2C charging cycles, were conducted using the constant current-constant voltage (CC-CV) charging protocol.

According to the literature, however, in the constant voltage phase, the anode potential does not decrease [434]. As a result, the constant voltage phase was ignored in this study. The experimental data, which included current, voltage, and surface temperature measurements, were recorded every second and stored in the host computer.

3.2.2.2 Physics-Based Model Parameterization for Anode Potential Prediction

In the second stage, a physics-based model with electrochemical and thermal dynamics is used to mimic cell behavior and to provide the dataset needed for further processing. The anode potential is calculated using a high-fidelity model that was developed in our prior work [221] but tuned for the current cell chemistry. For the sake of simplicity, the anode potential computation process using a physics-based model (COMSOL) is shown in Figure 3-13. The first step is to safely open the battery to be modeled after a full discharge and perform internal cell measurements (see Figure 3-14). Cell parameters that could not be measured directly were found in the literature. Meanwhile, cell identification data such as voltage, current, and temperature are recorded at various C-rates (data captured in stage 1). The data is then compared to the model's simulation results to validate its performance. The predicted voltage and surface temperature responses are compared to experimental data (data captured in stage 1) in Figure 3-15 (A and B). The Root Mean Square Error (RMSE) of the voltage and the temperature are, respectively, 19.8 mV and 0.38°C. The tunable parameters were manually modified (a selection is shown in Table 3-5) until a user-defined RMSE was reached on all C-rates. After the model validation was finished, recorded current profiles from experiments at various C-rates (0.1C, 0.5C, 1C, 2C) and EV driving current profiles (UDDS, HWFET, US06, US06-HWY, MANHATTAN, NYCC, WVUSUB, and EUDC) with different initial SOC (0.35-0.90) are used as inputs. Note that the EV driving current profiles are generated from an electric vehicle with a mass of 1254 kg driving through multiple driving cycles. The EV driving current profiles have been scaled to match the LG INR18650 F1L battery. Finally, the anode potential was determined using the physics-based model at various C-rates.

Table 3-5. Battery model parameters.

Parameter Name	Anode Electrode	Separator	Cathode Electrode
Electrode Thickness (m)	68.3×10^{-6}	13.1×10^{-6}	34.7×10^{-6}
Particle radius ((m)	5.15×10^{-6}		1.8×10^{-6}
Active Material Volumetric Fraction ε_1	0.8876		0.9714
Max. solid-phase Concentration $c_{i,max}$ ($mol\ m^{-3}$)	30000		50000
Charge transfer Coefficient α_a, α_c	0.5		0.5

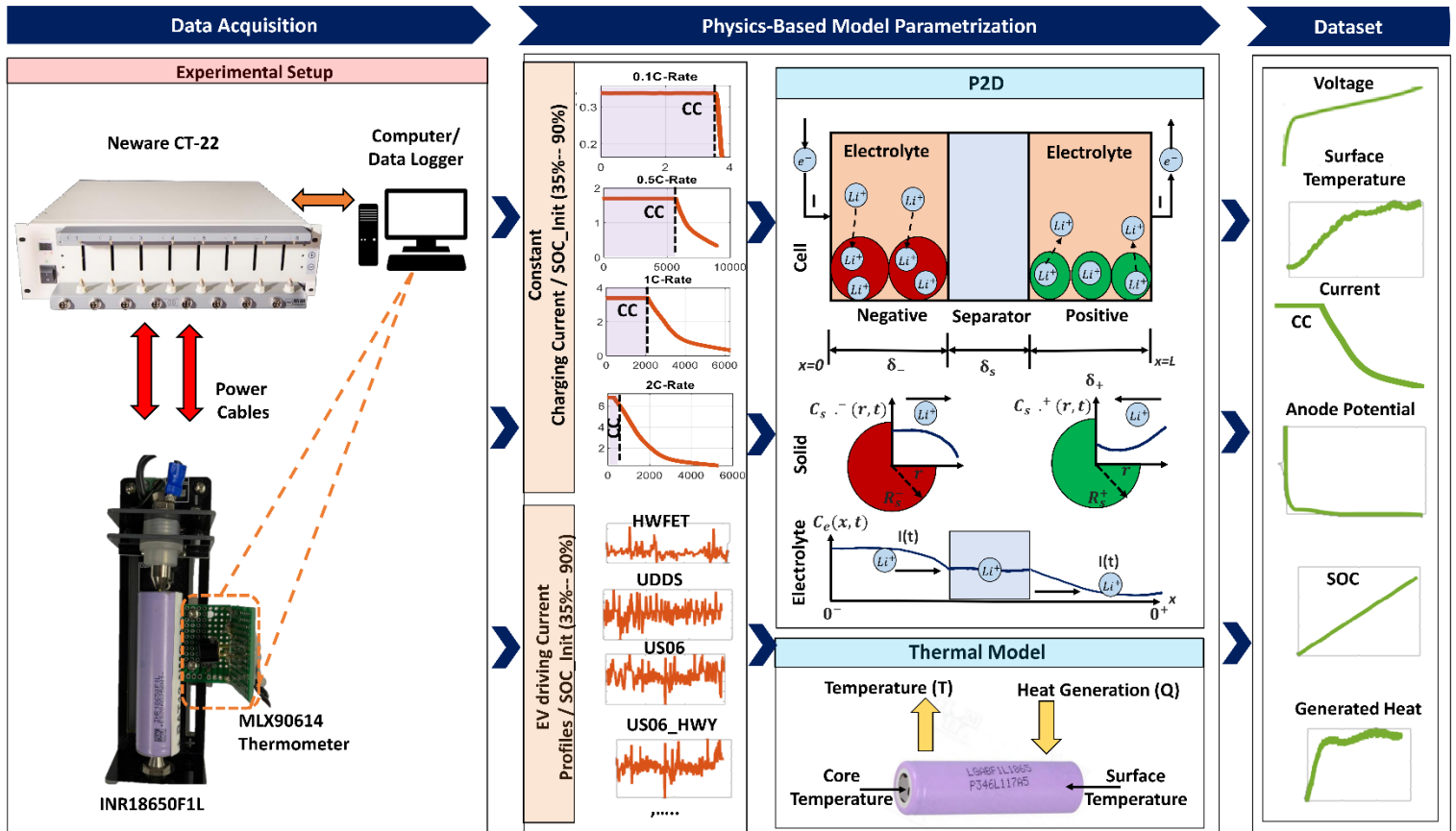


Figure 3-12: Experiment setup and data generation steps based on a physics-based model. Stage 1: data acquisition from experimental setup (CCCV charging protocol was used). Stage 2: physics-based-model parameterization (CC phase was extracted and used as input for the model). Stage 3: final dataset for use in data-driven approaches.

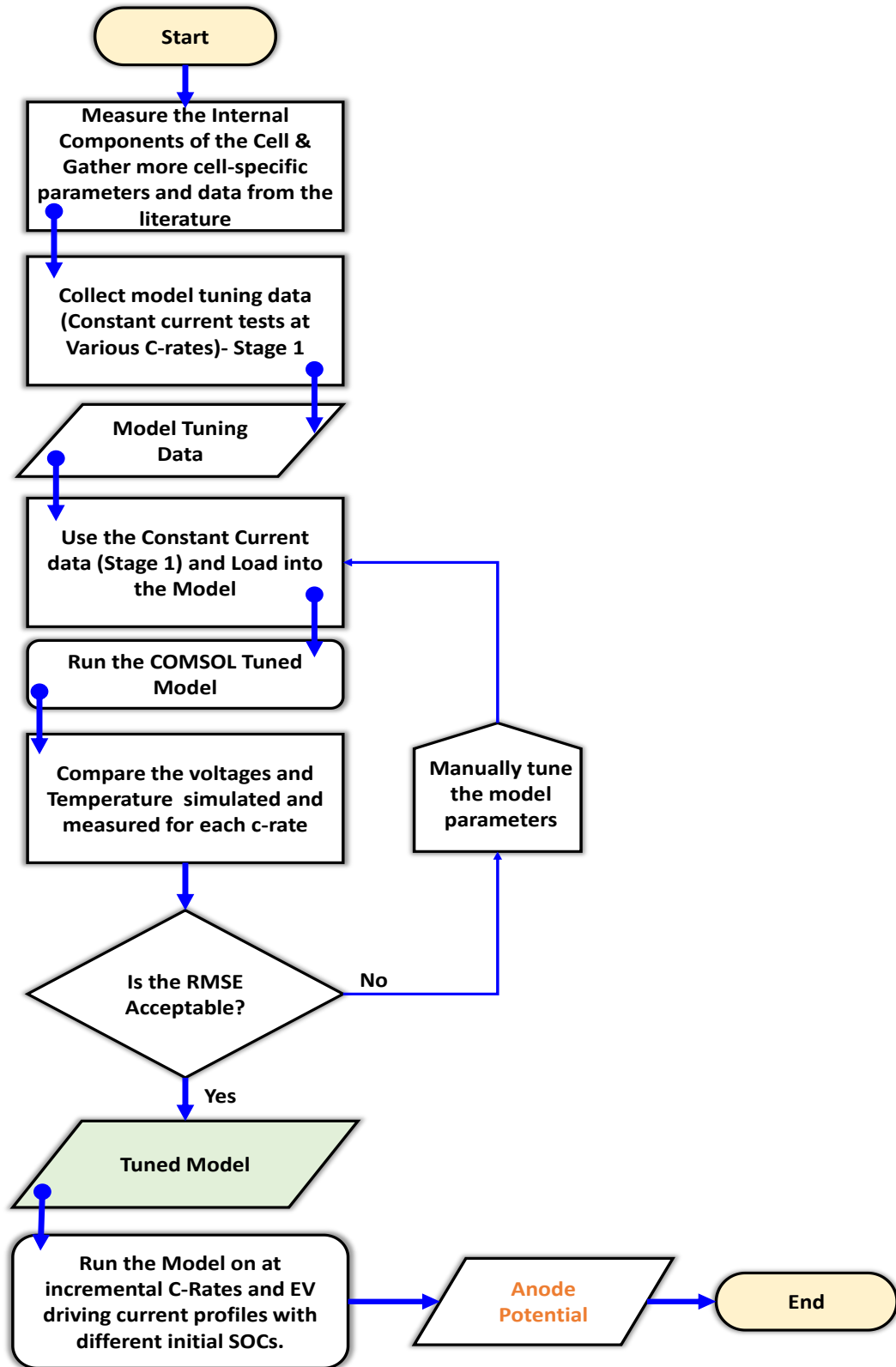


Figure 3-13: Flowchart for anode potential prediction through physics-based model (COMSOL).

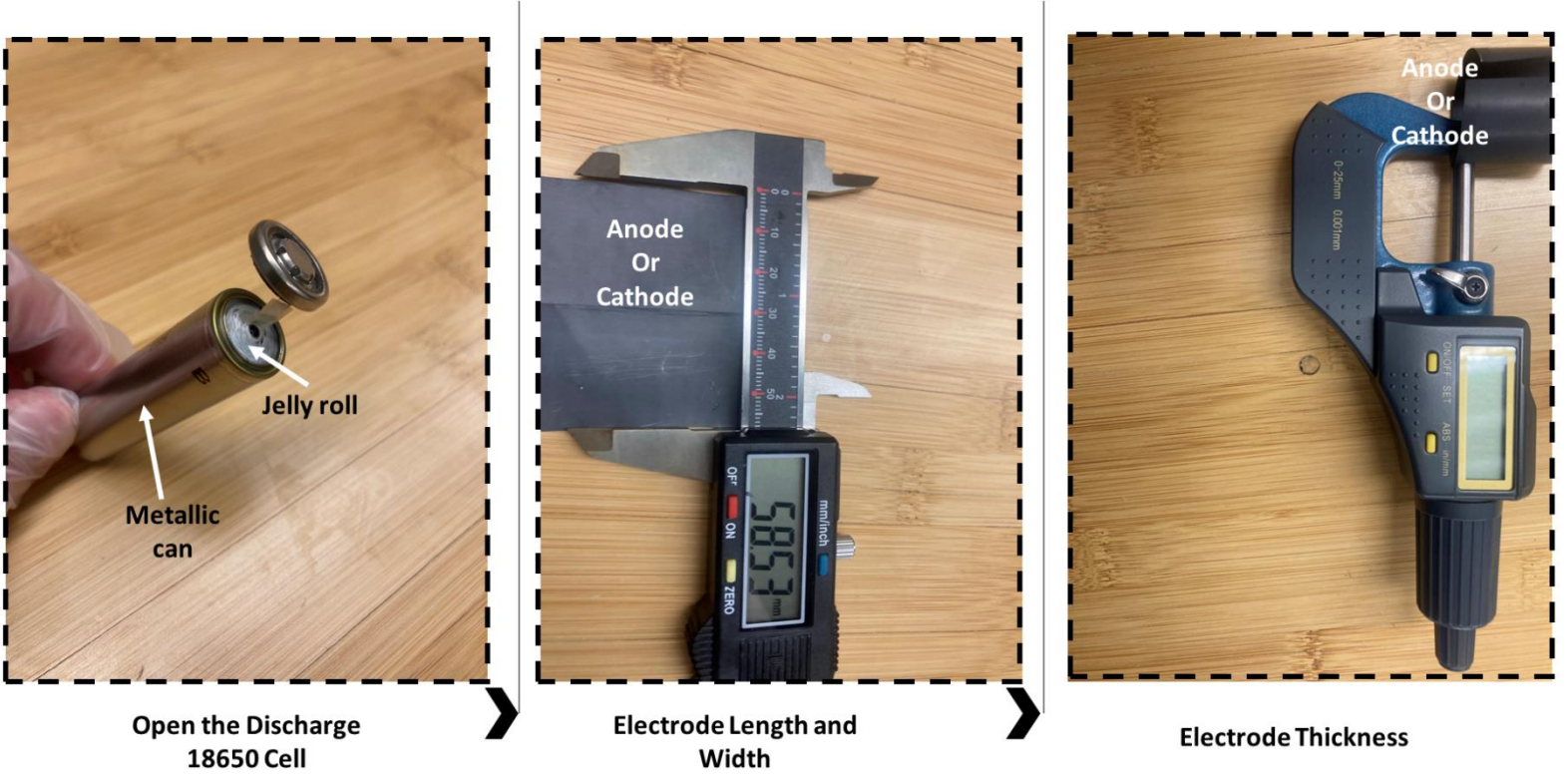
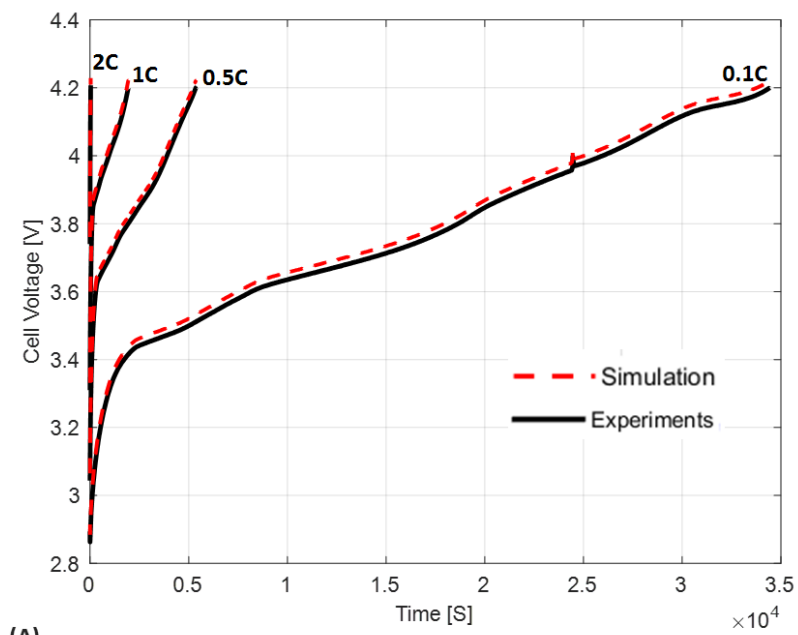
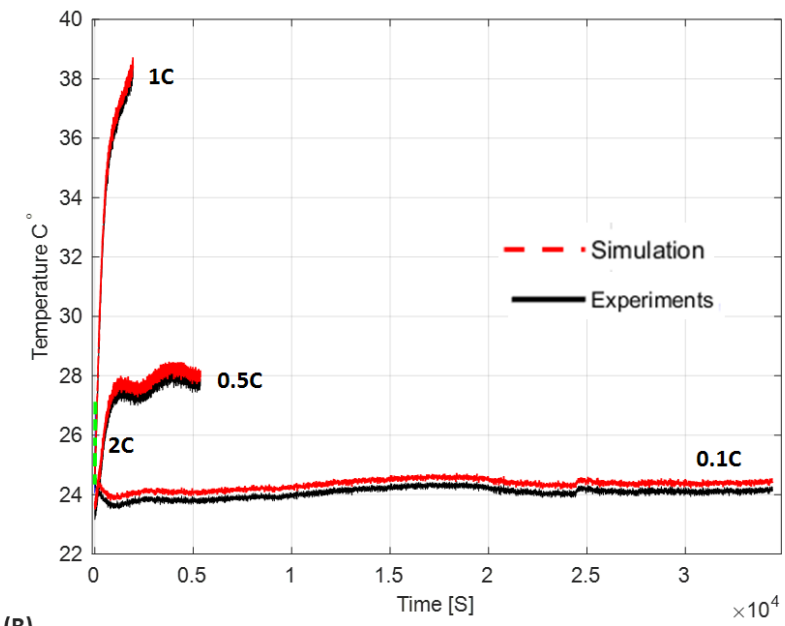


Figure 3-14: Disassembly of an 18650 cell and internal measurements.



(A)



(B)

Figure 3-15: (A) Voltage comparison between model prediction and experimental data. (B) Surface temperature comparison between model prediction and experimental data.

3.2.2.2.1 Physics-Based Battery and Thermal Model Theories

This study's battery model is comprised of an electrochemical model and a two-state thermal model (Figure 3-12). In this study, a commercial cylindrical cell LG INR18650 F1L is used. One of the elements described by the model is the charge-transfer-kinetic (Butler-Volmer equation) of the cell shown in Figure 3-16 (Eqn. (10)). The expression considers the influence of the overpotential η (see the relationship with anode potential in Eqn. (12)) on the cell's local reaction current j_{loc} , as well as other constants such as the charge transfer coefficients for the anode and cathode materials a_a , a_c . a_s is the active surface area per unit volume, i_0 is the exchange current density, R_{SEI} is the resistance due to the SEI layer and F is Faraday's constant. The anode potential vs. Li^+/Li^0 , abbreviated as the anode potential (ϕ), is calculated by comparing the solid phase potential of the anode (Φ_1) to the solution phase potential of the surrounding electrolyte (Φ_2) as measured by an inserted lithium metal. The anode potential and overpotential relationship is shown in Eqn. 12 in Figure 3-16, where U_1 is the anode's open circuit potential and $\phi = \Phi_1 - \Phi_2$. We attempted to simplify the model description by summarizing all the mathematical equations and their relationships in Figure 3-16. More information, however, can be found in our previous publications and these references [372], [375], [435].

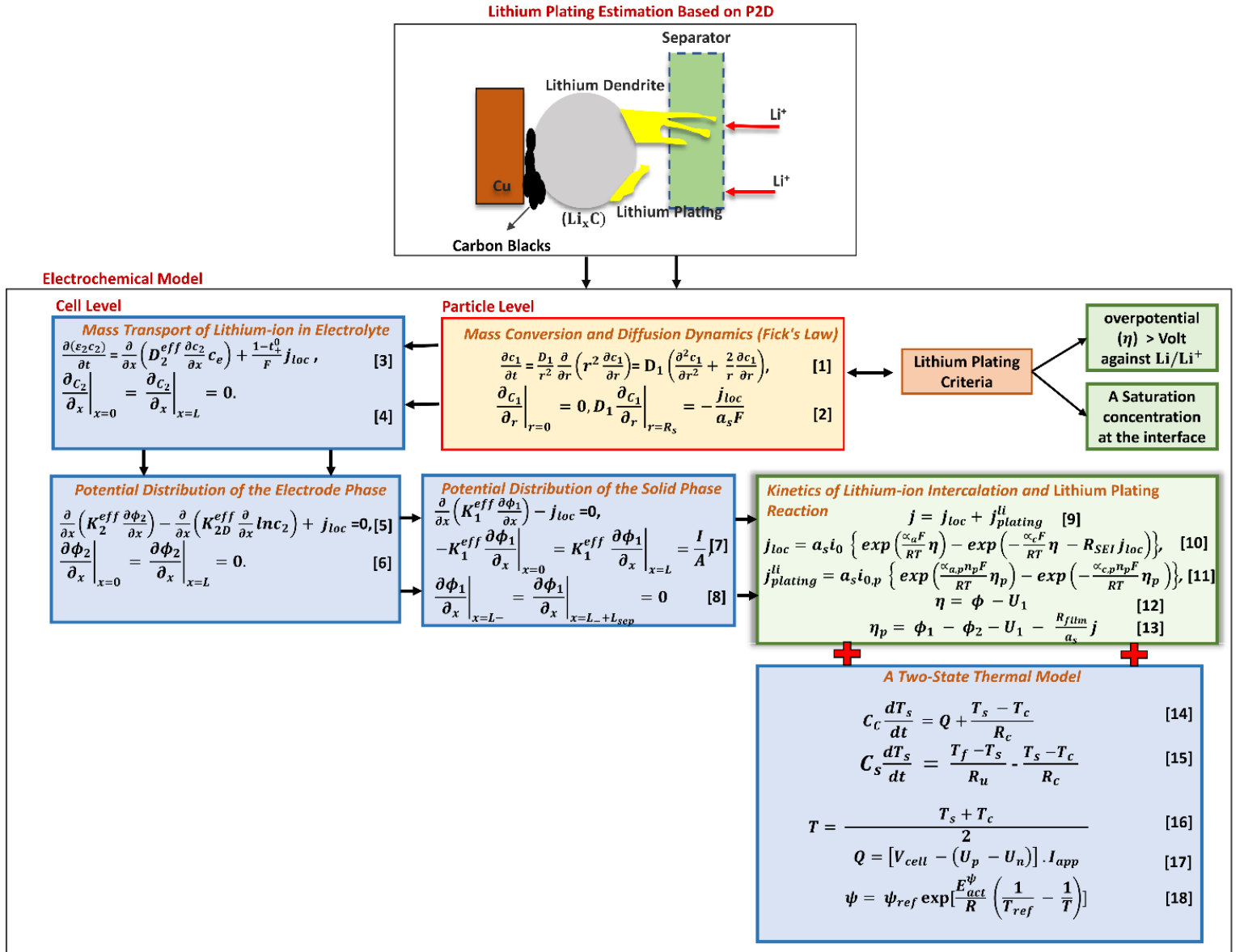


Figure 3-16: A Model-based Approach for Lithium Plating Detection.

3.2.2.3 Anode Potential Dataset for Machine Learning Algorithms

The experimentally validated physics-based model was used to generate a large amount of data at various C-rates and EV driving current profiles. The following variables were recorded: voltage $V(t)$, surface temperature $T_s(t)$, current $I(t)$, anode electrode potential

$\phi(t)$, state of charge $SOC(t)$, time (t), and generated heat $Q(t)$. The recorded data is the final raw dataset from the experimentally validated physics-based model and is ready for further processing for usage in the data-driven approach.

3.2.3 Anode Potential Dataset Preparation for Machine Learning Algorithms

Input features are crucial to the accuracy and robustness of all ML algorithms. Hence, applying an appropriate data pre-processing strategy is beneficial to the prediction accuracy of a supervised ML algorithms [406], [407]. The data pre-processing strategy used is represented in Figure 3-17, which includes anode potential dataset (input dataset), data cleaning/transformation (removing outliers, filling missing values, time-domain synchronization, and normalizing), correlation analysis, and feature subset selection. The developed data pre-processing strategy generated a complete and clean dataset that was free of irrelevant features for estimating anode potential.

The variables generated from the experimentally validated physics-based model are used as inputs for the data-driven models. The raw dataset, however, must be cleaned and structured before it can be used to develop and train machine learning models. The dataset preparation for data-driven techniques is described in the following section (see Figure 3-17).

3.2.3.1 Data Cleaning and Transformation

The process of correcting or removing inaccurate, incomplete, or duplicate data within a dataset is referred to as data cleaning. This procedure primarily consists of but is not limited to, removing outliers, filling missing values, and time-domain synchronization.

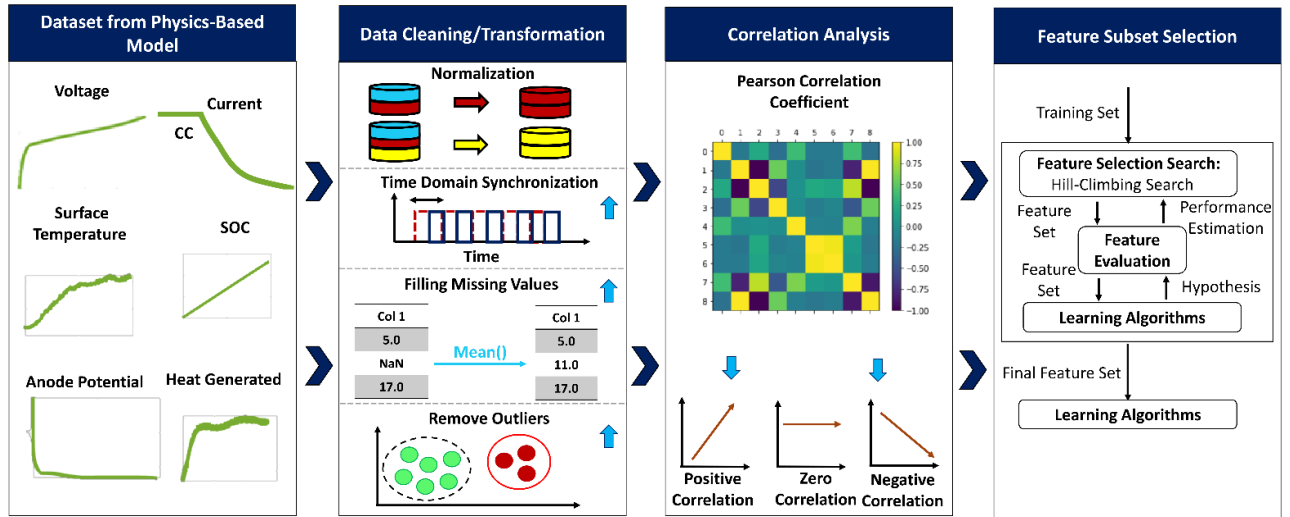


Figure 3-17: Anode Potential Dataset Preparation for Machine Learning Algorithms (lithium plating mitigation).

Outliers can cause issues with certain types of models due to large values throwing up the outputted prediction and removing them generally improves the model’s performance. Outliers that fall outside of the normal data range or have extremely low probability are removed from the raw dataset.

The missing values due to the error of the sampling system is an unavoidable problem in the experimental process. The missing values can be filled using many statistical approaches depending on the dataset, where we used the statistical mean method to fill the missing values in the raw dataset. The time-based interpolation approach is used to synchronize all of the data based on the timestamp of each dataset (Figure 3-17) [406]. There is frequently a considerable gap between the maximum and minimum values inside a feature.

When normalization is conducted, the magnitudes of the values are scaled to significantly low values. Data normalization can improve the pace of convergence and reduce the

negative effect of data redundancy (Figure 3-17). The input dataset in this investigation was normalized to the range [-1, 1], as represented in the following equation,

$$x' = \frac{(x - x_{min})}{x_{max} - x_{min}} \quad (3-21)$$

where x_{max} is the maximum value, and x_{min} is the minimum value of input vector x .

3.2.3.2 Correlation Analysis

We used the common statistical approach known as Pearson's correlation coefficient analysis to calculate the correlation between the input and the output variables. Pearson's correlation coefficient (r) summarizes the strength of the linear link between two data samples. It can express the correlation between each attribute and the output variable (anode potential) and choose only those characteristics with a moderate-to-high positive or negative correlation (near -1 or 1) while discarding those with a low correlation (value close to 0). Generally, the higher the correlation between the input features and the output of a data-driven model, the better the model's accuracy. Pearson's correlation coefficient's formula is as follows [410],

$$r = \frac{\sum_{i=1}^N (x_i - \bar{x})(y_i - \bar{y})}{(N - 1)\sigma_x \sigma_y} \quad (3-22)$$

Where N is the number of samples, i is the index within the sample set, \bar{x} and \bar{y} are their average values, and σ is the standard deviation defined by [433],

$$\sigma = \sqrt{\frac{\sum_{i=1}^N (x_i - \bar{x})^2}{(N - 1)}} \quad (3-23)$$

The mean and standard deviation implies that the two data samples must have a Gaussian or Gaussian-like distribution. The correlation coefficient, which is the result of the calculation, can be analyzed to better understand the relationship (Table 3-6). Based on the

last column of the Table 2, the variables with the highest correlation to the anode potential are: current ($r = -0.98$), voltage ($r = -0.87$), generated heat ($r = 0.54$), surface temperature ($r = -0.15$), and SOC ($r = -0.14$). A few trends can be seen by plotting the variables from the dataset against the anode potential (see Figure 3-18), such as a quadratic relationship between the generated heat to the anode potential.

Table 3-6. Pearson correlation coefficient between the input variables vs output variables.

	Voltage	SOC	Generated Heat	Surface Temperature	Current	Anode Potential
Voltage	1.00000	0.605207	-0.452091	0.058226	0.799753	-0.872705
SOC	0.605207	1.00000	-0.016814	-0.119350	0.014133	-0.147484
Generated Heat	-0.452091	-0.016814	1.00000	-0.086703	-0.572239	0.541186
Surface Temperature	0.058226	-0.119350	-0.086703	1.00000	0.164145	-0.158255
Current	0.799753	0.014133	-0.572239	0.164145	1.00000	-0.987867
Anode Potential	-0.872705	-0.147484	0.541186	-0.158255	-0.987867	1.00000

3.2.3.3 Feature Subset Selection

To achieve a compacted dataset, a data dimensionality reduction approach must be applied. One of the common methods to detect and remove redundant and irrelevant features is the feature subset selection approach [409]. The feature subset selection can be divided into two types, wrapper-based, which was used in this study, and filter-based [436]. This technique employs a learning algorithm as a base learner and evaluates the algorithm's performance on a dataset with various subsets of attributes selected. In our example, we used the most common regression algorithms, which include linear regression, support vector regression (SVR), random forests regression (RF), and gaussian process regression (GPR), all of which may consider both linear and non-linear variables. The wrapper

method, as illustrated in Figure 3-17, is based on a simple concept in which the learning algorithm is regarded as a black box. The feature subset selection method searches for a good subset by including the learning algorithm in the evaluation function. The wrapper method searches the space of possible parameters. A state space, an initial state, a termination condition, and a search technique are all required for a search. Since hill-climbing and best-first search are common search strategies, we employed hill-climbing in this paper. The accuracy estimation algorithm (RMSE) is used to estimate the accuracy of the learning algorithm. The learning algorithm is applied to the dataset, which is often partitioned into internal training and holdout sets with different sets of features removed. The feature subset with the highest evaluation is chosen as the final set on which to conduct the learning algorithm. Considering the feature subset selection method and correlation analysis and based on the findings that the random forest algorithm performs the best, a low-dimensional training dataset $D \in \mathbb{R}^{N \times m}$, consisting of four variables, namely, the voltage, the surface temperature, the current, and the SOC can be obtained, where m represents the number of features and N represents the number of samples.

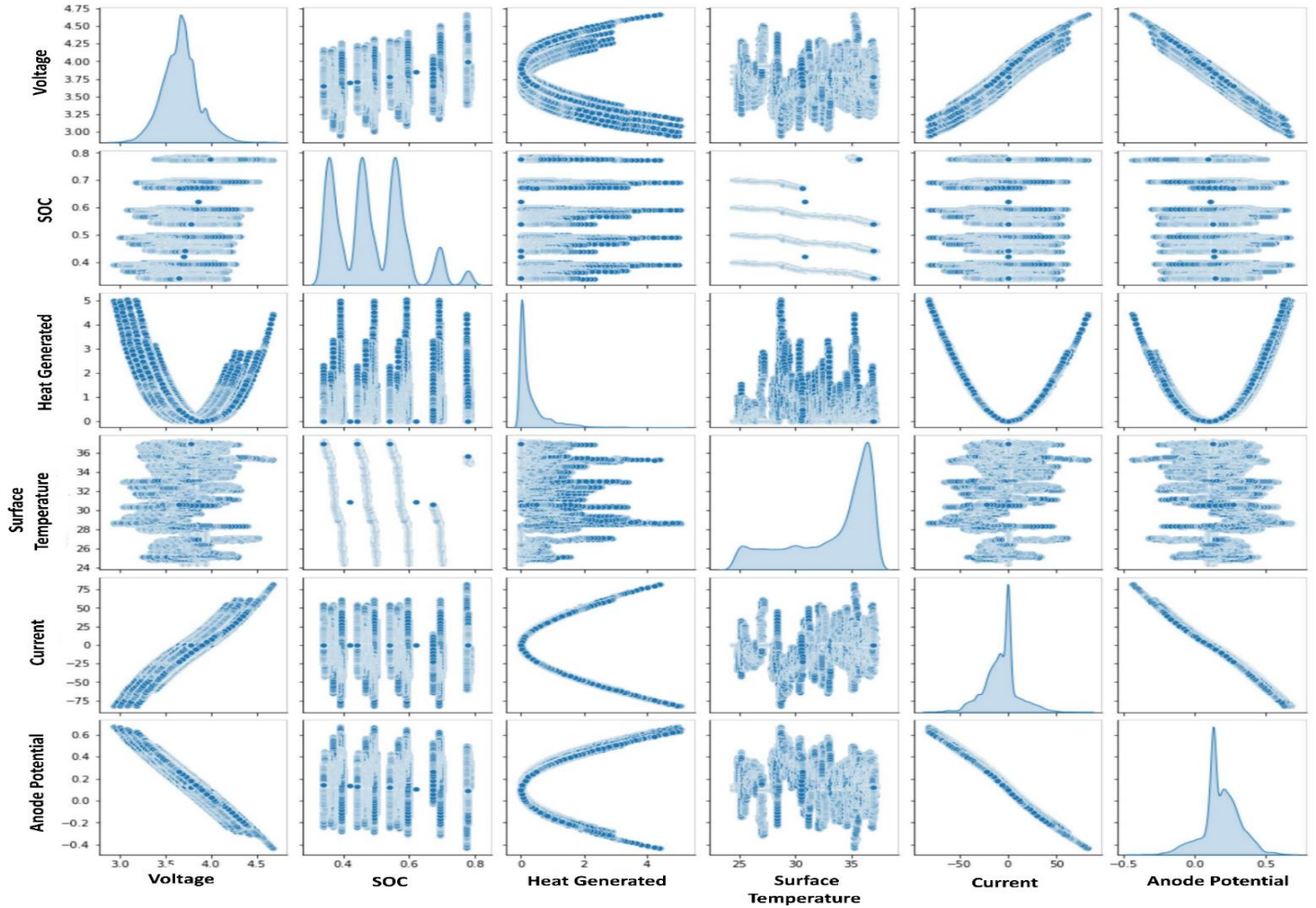


Figure 3-18: Illustration of pairwise relationships for the dataset features, and the diagonal plots show the distribution of features in the dataset.

3.2.3.4 Training and Testing Dataset

As illustrated in Figure 3-19, the dataset is separated into two subsets: training and testing. The prepared data from four different driving cycles, namely, US06, US06-HWY, HWFET, and UDDS (with varied sets of initial SOC's ranging from 0.4 to 0.90), and constant charging profiles are concatenated to generate the training data stream. This procedure generates a large amount of data, which will cover the battery conditions under various operating circumstances and assist in providing a more accurate model. The test

data stream is formed by four separate driving cycles: EUDC, NYCC, MANHATTAN, and WVUSUB, each with a different set of initial SOC's ranging from 0.35 to 0.85. Unlike the training data which concatenates all the data from different current profiles to form a long training data stream, the test data for each driving profile remains separate.

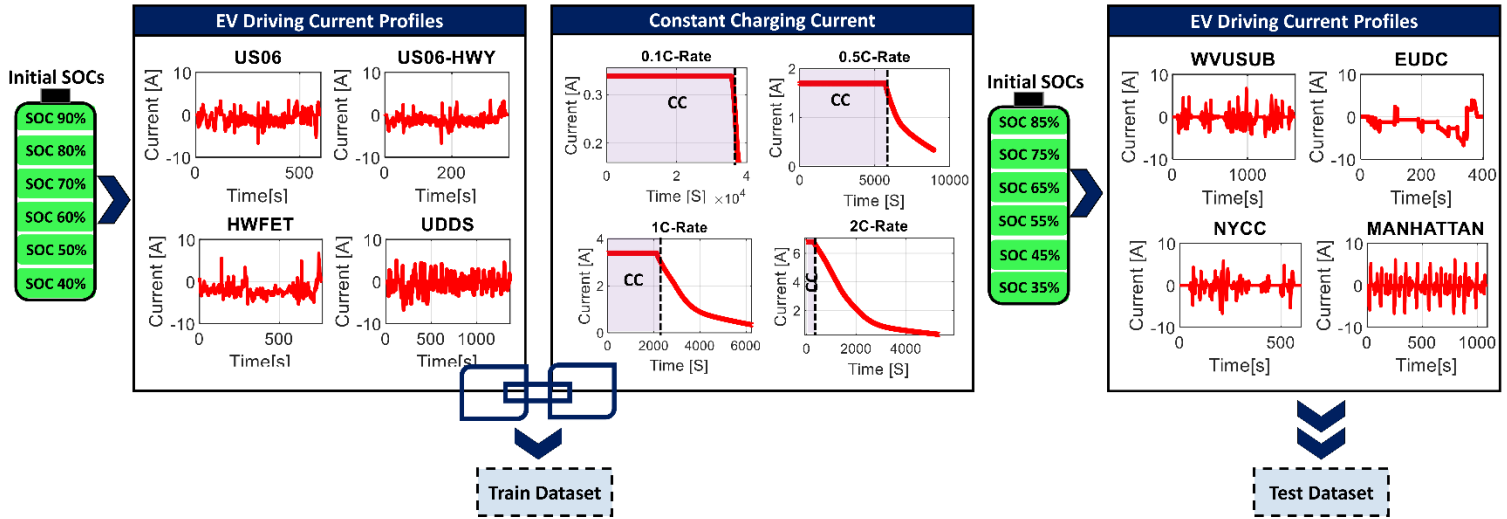


Figure 3-19: Training and Test Data Splitting.

3.2.4 Machine Learning for Anode Potential Prediction

3.2.4.1 Anode Potential Estimation Based on Regression Machine Learning Algorithms

In this section, we present a large-scale empirical comparison of four common supervised learning algorithms found in the literature, particularly in the battery community, to evaluate their computational efficiency, accuracy, and suitability for online implementation. Indeed, we attempt to explore the space parameters and common variations for each learning algorithm as thoroughly as is computationally feasible. All of the four learning algorithms (linear regression, RF, SVR, and GPR) were fit on the training dataset and tested with four different driving cycles. Each learning algorithm is

implemented using Python and WEKA data mining tools on a laptop with a 2.59 GHz Intel Core i7-5600U CPU and 8 GB of internal memory.

3.2.4.1.1 Linear Regression Model for Anode Potential Estimation:

The concept behind the linear regression is to represent the class (anode potential (ϕ)) as a linear combination of properties with predefined weights [417]:

$$y = w_0 + w_1d_1 + w_2d_2 + \dots + w_kd_k \quad (3-24)$$

where y is the class, d_1, \dots, d_k are the attribute values (current, voltage, and SOC) and w_0, \dots, w_k are weights. Therefore, the predicted value (estimated anode potential) for the first instance's class can be expressed as,

$$w_0d_0^{(1)} + w_1d_1^{(1)} + w_2d_2^{(1)} + \dots + w_kd_k^{(1)} = \sum_{j=0}^k w_jd_j^1 \quad (3-24)$$

Where the superscript (1) denotes that it is the first instance. The least-squares linear regression method involves selecting the coefficients w_j in order to minimize the sum of the squares of these differences throughout all training datasets. Assume there are n training instances: use a superscript to indicate the i^{th} one (i). The difference is thus the sum of the squares of the differences [417];

$$\sum_{i=1}^n (y^i - \sum_{j=0}^k w_jd_j^i)^2 \quad (3-25)$$

where the expression inside the parentheses represents the difference between the actual class of the i^{th} instance and its predicted class. We should minimize this sum of squares by choosing optimal coefficients. Overfitting occurs when a model learns the details and noise of the training data too accurately to the point where it negatively impacts the

performance of the model on new data. In order to reduce the overfitting in the linear regression model, a regularization term is added,

$$\sum_{i=1}^n (y^i - \sum_{j=0}^k w_j d_j^i)^2 + \lambda \sum_{i,j=1}^n (w_j d_j^i)^2 \quad (3-26)$$

Where λ is the regularization coefficient, which indeed controls the degree of regularization[417]. This stops the model from putting too much weight on specific training instances by assigning them big coefficients unless this results in a proportionally large drop in error. The final equation has the following regression coefficient fits;

$$\begin{aligned} \phi = & -0.2404 \times V + 0.102 \times SOC + (-0.005 \times T_s) + (-0.0048 \times I) \\ & + 0.9946 \end{aligned} \quad (3-27)$$

3.2.4.1.2 Support Vector Regression for Anode Potential Estimation:

SVR is first applied to linear regression issues and can also deal with nonlinear regression problems after introducing the kernel trick. ε -SVR is a common SVR model in the literature that uses limited training set $D = \{(x_i, y_i) \mid i = 1, 2, \dots, l\}$, ($x_i \in R^n$ is an n -dimensional sample input and $y_i \in R$ is a sample output). In the event of nonlinearity in the training sample, SVR transforms space nonlinear problems to linear problems in a high-dimensional space using a nonlinear mapping and substitutes the inner product of the sample vector with kernel function $K(x_i, x_j)$. As a result, the specific implementation of the method of the SVR is as follows [437]:

$$f(x) = (w \times f(x)) + b.F \quad (3-28)$$

Where $f(x)$ is the prediction function (anode potential (ϕ)), w is the weight, and b is the deviation value. It should be noted that the sample points are distributed independently and identically [437].

Outside of the training sample collection, optimal solutions w and b for an unknown value x could be identified, resulting in $|f(x) - (w \cdot x) - b| \leq \varepsilon$. The problem is similar to attempting to solve the following optimization problem,

$$\min_{w,b} \phi(x) = \frac{1}{2} \|w\|^2 = \frac{1}{2} (w \cdot w) \quad (3-29)$$

$$\text{Subject to } \begin{cases} y_i - ((w \cdot x) + b) \leq \varepsilon \\ ((w \cdot x) + b - y_i) \leq \varepsilon \end{cases} \quad i=1, 2, \dots, l \quad (3-30)$$

Where $\varepsilon > 0$ is the insensitive loss function. If the sample data problem's $f(x)$ cannot be computed with confidence ε while importing slack variables ξ and $\hat{\xi}$, the problem can be converted into [437],

$$\min_{w,b,\xi,\hat{\xi}} \phi(x) = \frac{1}{2} \|w\|^2 + C \sum_{i=1}^l (\xi + \hat{\xi}) \quad (3-31)$$

$$\text{Subject to } \begin{cases} y_i - ((w \cdot x_i) + b) \leq \varepsilon + \xi_i \\ ((w \cdot x_i) + b - y_i) \leq \varepsilon + \hat{\xi}_i \\ \xi_i, \hat{\xi}_i \geq 0 \end{cases} \quad i = 1, 2, \dots, l \quad (3-32)$$

Where $C > 0$ is the punishment quantity, and the severity of the penalty varies with the degree of ε . To convert the minimization problem into a dual problem, the Lagrangian function is used [437],

$$\begin{aligned} \max Q(a_i - \hat{a}_i) = & -\frac{1}{2} \sum_{i,j=1}^l (a_i - \hat{a}_i) (a_i - \hat{a}_i) (x_i \cdot x_j) - \\ & \varepsilon \sum_{i=1}^l (a_i + \hat{a}_i) + \sum_{i=1}^l x_i (a_i - \hat{a}_i) \end{aligned} \quad (3-33)$$

$$\text{Subject to } \begin{cases} \sum_{i=1}^l (a_i - \hat{a}_i) = 0 \\ a_i, \hat{a}_i \in [0, C], \quad i = 1, 2, \dots, l \end{cases} \quad (3-34)$$

Therefore, the SVR model for nonlinear regression is as follows,

$$f(x) = \sum_{i=1}^l (a_i - \hat{a}_i)K(x_i, x) + b \quad (3-35)$$

Where $f(x)$ is the predicted anode potential (ϕ), $K(x_i - x) = \exp(-\frac{|x_i - x|^2}{\delta^2})$ is the radial basic kernel function (RBF), and δ is the width of the function parameters[437]. The SVR model has three hyper-parameters (C, ε, δ) based on the above equations. The WEKA tool's grid search approach is used to identify the values of these hyper-parameters.

Three evaluation criteria are used to assess the performance of the proposed models: root mean square error (RMSE), anode potential prediction error, and model training time. We adopted the RMSE as a representative error index, where it was calculated for the predicted values against simulation values using four different test-driving cycles. Each test dataset contains a different set of initial SOCs; in our case, we consider 35% SOC to be the lowest value, 65% SOC to be the average value, and 85% to be the maximum value, in order to cover most battery operation circumstances. The mathematical equation of the RMSE is expressed as follows:

$$RMSE = \sqrt{\frac{1}{N} \sum_{i=1}^N (y_i - \hat{y}_i)^2} \quad (3-36)$$

Where y_i present the simulated anode potential, \hat{y}_i is the estimated value and N is the number of samples and i is the measurement index.

The anode potential prediction error is used to evaluate the prediction accuracy,

$$Anode\ potential_{error} = Anode\ potential_{prediction} - Anode\ potential_{real} \quad (3-37)$$

$Time_{tr}$ is the model training time and is used to evaluate modeling efficiency.

3.2.5 Optimized Ensemble Selection for Anode Potential Prediction

This section describes how to develop an optimized ensemble selection model for anode potential estimation. The objective of this research was to examine a variety of regression algorithms in the context of fast charging and use them to create the ensemble model. Linear regression, RF, SVR, and GPR are the studying learning algorithms. We chose these for two main reasons: they are widely used in the battery field to estimate battery parameters such as the SOC, the capacity, and the remaining useful life, and they have been thoroughly explored in the previous sections, providing us with the opportunity to illustrate the superiority of using ensemble selection rather than a single learning algorithm.

3.2.5.1 Creation of the Optimized Ensemble

We investigated four different learning algorithms for anode potential prediction, but no one approach is superior because their performance is entirely dependent on the properties of the dataset. Intuitively, the purpose of ensemble selection is to detect and combine the strengths of these distinct algorithms to produce a sum greater than the parts [438]. This is accomplished by developing a library that is designed to be as broad as feasible to capitalize on a wide range of distinct learning algorithms.

The operating principle of ensemble selection is divided into two primary phases. The first phase, known as ensemble overproduction (composition of the model library (ML)), involves the generation of a huge number of models. The second phase, or choice phase (ensemble construction), involves selecting a subset of models from the models generated in the first phase.

In the first stage, we constructed an ML using the WEKA data mining tool to create the ML and the ensemble selection. All the learners and their settings were changed based on the learner settings provided by the software. In practice, the ML creation step is as follows:

Composition of Model Library (ML)

Step 1: Choose a variety of learning algorithms to serve as parent regression algorithms. In our example, as shown in Table 3-8, four regression algorithms were chosen as parent regression algorithms: linear regression, RF, SVR, and GPR.

Step 2: Select a wide range of learning algorithm settings (changing the parameter) for each parent regression algorithm.

Step 3: Build the ML, which is a collection of 533 models that are derived from the four-parent regression algorithm (see Table 3-8 for details).

The models are combined in an ML in the second phase of ensemble selection to attain optimal accuracy. The basic ensemble selection process is as follows:

- 1) Begin with an empty ensemble.
- 2) Then include in the ensemble the model from the library that maximizes the ensemble's performance on a hill-climb (validation) set in terms of error metric (RMSE).
- 3) Afterward, repeat Step 2 for a certain number of iterations or until all the models are used.
- 4) Finally, return the ensemble with the best performance on the hill-climb (validation) set from the nested collection of ensembles [439].

Thus, the technique used is a forward selection procedure that chooses models from a pool and repeatedly adds them to the ensemble based on a predefined criterion. The forward ensemble selection algorithm is shown in Table 3-7 (pseudocode). The current subset, S , is initialized to the empty set in the forward selection, and the procedure appends to S at each step the regressor $h \in H \setminus S$ that optimizes an evaluation function $f_{FS}(S, h, D)$. Based on the data, D , this function evaluates the addition of h to S . It may, for example, return the RMSE of the sub ensemble $S \cup \{h\}$ on the data set D by simply averaging the regressors' decisions. $H = \{h_t, t = 1, 2, \dots, N\}$ denotes the set of base regressors that create the ensemble.

Table 3-7. The pseudocode of the forward selection method.

Require: Ensemble of regressor H , the evaluation function f_{FS} and set D

- 1: $S = \emptyset$
 - 2: While $S \neq H$
 - 3: $h_t = \arg \max f_{FS}(S, h, D)$
 - 4: $S = S \cup \{h_t\}$
 - 5: **end While**
-

As a result, ES begins the ensemble building process by selecting a model at random from the ML. A subset of models is formed by adding models one at a time. If the ensemble's evaluation criterion is higher than the previous step's evaluation criterion (RMSE in our case), then more models are added to the existing ensemble. When the ensemble of size $k + 1$ model shows a score lower than the ensemble of size k , the iterative procedure ends.

3.2.5.2 Evaluation Measure

The forward selection strategy employed in ensemble selection typically causes over-fitting. To check for over-fitting, we use the hill-climbing technique to test the ensemble model with training sets of varying sizes. At each stage, ensemble selection adds a model from the library to the ensemble that maximizes the ensemble's performance on the saved hill-climbing data. In addition, we use ensemble selection with 5-fold cross-validation. For each iteration of ES, five models are picked at random during the ensemble generation process. During the ensemble construction process, candidate ensembles must be rated against a validation dataset. The RMSE is used as the scoring metric here to identify the model that best optimizes the performance of the ensemble formed by adding, or removing, a model from the existing ensemble. In forward selection, the RMSE is determined for a model h about the present sub ensemble S and the set of instances D as follows:

$$RMSE_{FS}(S, h, D) = \sqrt{\frac{1}{N|S|} \sum_{i=1}^S \sum_{j=1}^S (h_i(x_j) - y_j)^2 + \frac{1}{N} \sum_{j=1}^S (h(x_j) - y_j)^2} \quad (3-38)$$

The RMSE computation is based on the ensemble decision in all cases of the pruning dataset. The complexity of these measurements is thus $O(|S|N)$. However, if the predictions of the current ensemble are updated gradually each time a learner is inserted or withdrawn from it, the complexity can be reduced to $O(N)$.

3.2.5.3 Stopping Criteria

As previously stated, ensemble selection continues with the current iteration until there is no model in the library that, when added to the ensemble of size $k + 1$ model, shows a lower score than the ensemble of size k .

3.2.5.4 Combination of Models

When the stopping criteria is met, the model selection is completed, and an ensemble selection (ζ) from the library is chosen. The selected models in ε are then tested individually over the test dataset (D) according to the mechanics of the base learner, yielding the matrix of uncombined raw model outputs Z ($Z = \zeta(Y)$). When the uncombined final output Z is combined, it is denoted by P and is a composite function of the raw output of each constituent learner. The model combination is the process of getting to P from Z , and can be as simple as a weighted average of each model's raw outputs over the test points. We aggregate the estimates using a simple linear function. For instance, x , the ensemble output is $h_s(x) = \frac{1}{|S|} \sum_{i=1}^{|S|} h_i(x)$. The final sub-ensemble chosen has the lowest RMSE on the evaluation set (we use a linear function for model combination). In conclusion, each ensemble is a weighted average of models, and the average of a group of ensembles is a simple weighted average of the base learners.

Table 3-8. Summary of model configurations used in this study.

Algorithm	# Models in Library	Parameter	Values
Linear Regressions	153	Regularization Parameter (Ridge-G)	Ridge {0.05 to 0.000000001} in increments of 0.001.
Support Vector Regression	110	Kernel Gamma Parameter Regularization parameter (C) Polynomial Degree	Polynomial, linear {0.001, 0.005, 0.01, 0.05, 0.1, 0.5, 1, 2} $10^{-7}, 10^{-6}, \dots, 10^{-1}, \dots, 10^3$ 2, 3
Random Forests Regression	160	Number of trees	10, 25, 50, 100
Gaussian Process Regression	110	Kernel RBF Gamma Parameter Polynomial Degree	RBF, Polynomial {0.001, 0.005, 0.01, 0.05, 0.1, 0.5, 1} 2, 3, 8

The following settings were used to train the algorithms (the rest of the parameters were left at their default values): Linear regressions: We have changed the Ridge parameter (G) ranging from {0.05 to 0.000000001} in increments of 0.001. SVRs: In SVR, we use most kernels that are linear, polynomial degree 2 and 3, and 8 radial kernels ($\gamma \in \{0.001, 0.005, 0.01, 0.05, 0.1, 0.5, 1, 2\}$) and change the regularization parameter C by factors of ten from 10^{-7} to 10^3 . We use Platt's technique to transform SVR outputs into probabilities by fitting them to a sigmoid to make the SVR predictions consistent with other models. RFs: We used 2 values for the confidence factor {0.25, 0.5}, and 2 values for Laplace smoothing ({true, false}). Each tree is bagged in 25 segments. Each tree trained on a bootstrap sample, as well as the final bagged ensemble averaging all of these trees, is added to the library. GPR: In GPR, we use most kernels that are RBF, and polynomial degree 2 and 3, and 8 radial kernels ($\gamma \in \{0.001, 0.005, 0.01, 0.05, 0.1, 0.5, 1, 2\}$).

Chapter 4 : Results and Discussion (Manufacturing Phase)

4.1 Results of Fabricated Pseudocapacitor Electrodes via ULPING

4.1.1 Morphology and Structural Properties of Selected Electrodes

¹⁰After the completion of sample preparation, 12 samples were chosen to be analyzed and observed for structural and morphological alterations. The basic concept of laser-induced porous structures is that a higher surface area and more porosity on the electrode surface can lead to better capacitance behaviors by enabling more ions to be adsorbed during the charge and discharge process. Moreover, a higher oxidized surface area means more available redox-active sites. To illustrate these changes more clearly, the samples were divided into four groups, with one of the laser parameters varied while keeping the others constant. In the scan speed group, for example, the laser parameters power (10 W), frequency (1200 kHz), and pulse duration (0.15 ns) remain constant while the scan speed changes from 40 (mm s^{-1}) in S1 to 50 (mm s^{-1}) and 60 (mm s^{-1}) in S2 and S3, respectively. The frequency is varied in the frequency group, the power is changed in the power group, and the pulse duration is varied in the pulse duration group, while the rest of the laser parameters remain constant in each group. It appears that the laser ablation parameters have a significant impact on the surface morphology of the treated samples. The SEM images and EDX results in Figure 4-1 demonstrate that the surface properties of the ablated samples vary depending on the laser parameters used. The scan speed group shows some

¹⁰ This section is based on a previously published article:
Kavian Khosravinia, A. Kiani. "Unlocking pseudocapacitors prolonged electrode fabrication via ultrashort laser pulses and machine learning", iScience, Cell Press. The material is reproduced here with permission from the publisher, [Cell Press].

of the most significant differences, with sample S3 displaying only minor modifications to the pretreatment Ti surface, while sample S2 shows a slightly better surface but still lacks the desired porous structure for increased surface area (see Figures 4-1 (A, B, and C)). These differences may be attributed to the amount of time allotted for the laser beam to traverse and ablate the surface, which affects the resulting surface morphology. The slower scan speed used for S1 allowed for more energy to be transferred or induced onto the Ti substrate's surface, resulting in more extensive surface oxidation and the growth of a self-standing 3D nanostructured oxide layer. This is why S1 showed the "broccoli-like" macroporous structure and a white and black oxide layer, indicating increased surface area and redox active sites. The constant pulse duration used for S1 and S2 ensured that the ablation process was consistent, while the varied scan speeds allowed for more or less ablation to occur, resulting in different surface properties. Another distinction among samples is the degree of oxidation that happened during the laser irradiation procedure, which is shown in EDX results. This indicates that the slower scan speeds allow for more time for the laser to interact with the titanium substrate, leading to increased oxidation and a higher percentage of oxygen detected in the EDX map spectrum. On the other hand, higher scan speeds result in less interaction time and, therefore, lower oxidation and a higher percentage of titanium detected. The EDX map spectrum indicates the existing elements for each sample as a percentage. S1 has the highest percentage of oxygen detection (45%) and the lowest percentage in Ti traces (55%). As the scan speed increases, the oxygen percentage declines; S2 shows reduced oxygen detection percentage traces (23.4%) and an increase in Ti traces (76.6%). S3 with the highest scan speed had the highest Ti percentage (82.9%) and the lowest oxygen traces (17.1%).

It's worth noting that although it was not easy to differentiate the oxide layer by visual inspection in the frequency group, the SEM images and EDX results still provide valuable insights into the effects of frequency on the fabricated samples. The differences in the distribution of the porous structure between F4 and F5 could suggest that there is an optimal frequency for achieving a more evenly distributed porous structure. F2, on the other hand, had equally dispersed porous pores that resembled the structure of a porous sponge. The EDX data shows a higher oxidation percentage (44.6%) and a lower Ti percentage (55.4%) at the lower frequency of 750 kHz. This is because the maximum surface temperature of the irradiated zone becomes higher at this frequency as each pulse has more energy. The oxidation percentage decreased from 42.1% to 39.2% as the frequency increased to 900 kHz in F4 and 1050 kHz in F5 (see Figures 4-1 (D, E, and F)). The laser plasma plume is more stable at 1050 kHz, resulting in better agglomeration of ionized atoms and evaporated nanoparticles to form thicker nanofibrous structures. Additionally, the decrease in oxidation percentage and increase in Ti percentage with increasing frequency could indicate that there is a threshold frequency beyond which further increases in frequency do not have a significant impact on the oxidation and surface morphology.

The samples are easily distinguishable by visual inspection of the power group samples. P2, with the lowest power of 8W, kept its shiny black surface. The PN1-1 and PN2-2 at different powers, revealing an extensive black and white surface oxidation layer. Based on the SEM images, P2 showed minimal changes, with a uniform surface structure but the least fiber structure. This is because less power is transferred to the surface. The PN1-1 SEM images show a slightly improved surface, but it is still far from the desired porous

structure required for increased surface area. When the power was increased to 12 W in PN2-2, a spongy porous microstructure was obtained because more energy or power was transferred or induced onto the surface of the Ti substrate to cause a successful phase change (see Figures 4-1 (G, H, and I)). At the same time, the EDX results confirm that as the power increased, so did the oxidation traces in the substrate. P2 with the lowest power has the lowest percentage of oxidation (37.7%). As the power increases, so does the oxidation percentage rate, with the PN1-1 with a power of 10 showing an oxidation percentage of 38.2% and the PN2-2 showing an oxidation rate of 39.6%. The effect of power changes has previously been validated in our work [440], [441]. It's interesting to see how the power level of the laser affects the surface properties of the Ti substrate, especially in terms of the degree of oxidation and the resulting microstructure. It seems that the higher the power, the more energy is transferred to the surface, resulting in a more significant phase change and increased oxidation traces. This, in turn, leads to a more porous microstructure, which is desirable for increased surface area and superior capacitance behavior. It can also be seen in the pulse duration group that changing the laser pulse duration from 1 to 5 ns changes the topology of the electrode surface (see Figures 4-1 (J, K, and L)). The pulse duration is the time measured across a pulse; as the pulse duration increases, the time needed to transfer the laser pulse decreases. The sample PD6-4 with the longest pulse duration has a uniformly distributed structure with visible holes and groves. Although there has been some improvement in PD5-4 as the pulse duration has decreased, there are still many holes and cracked structures. The hair-like or "broccoli-like" macroporous structure can be seen with PD4. These improved surface characteristics are due to the laser's longer pulse duration beam, which allows for a more ablated surface. The

pulse duration group's EDX results follow the same pattern as the scan speed group's. The sample with the shortest pulse duration (PD4) has the highest oxidation percentage (40%). The oxidation rates decreased to 38.2% and 30.9%, respectively, as the pulse duration increased from 2 to 5 ns (longer pulse duration) in PD5-4 and PD6-4. Ultimately, the S3 sample with the slower scan speed yielded the best and most improved structure for surface-dependent reactions in the fabrication of pseudocapacitance electrodes [440], [442], [443]. In comparison to other samples, S3 exhibited a greater maximum area and oxidation at a given surface area. The primary objective of this section, however, was not to identify the best sample, but rather to highlight the effect of altering laser parameters in response to changes in the oxidation pattern.

4.1.2 Electrochemical Performance of Selected Electrodes

To validate the findings from microscopy and characterization analysis regarding the impact of laser parameters on surface characterization improvement, an electrochemical analysis was conducted. The electrochemical analysis consisted of CV, GCD, and EIS to assess the coherence with structural modifications.

4.1.2.1 Cyclic Voltammetry

CV is a powerful and widely used electrochemical technique for studying the reduction and oxidation processes of molecular species as well as the capacitive behavior of electrochemical devices. Figure 4-2 illustrates the CV curves of all selected electrodes (S1, S2, S3, F2, F4, F5, P2, PN1-1, PN2-2, PD4, PD5-4, and PD6-4) in 1M sodium sulfate (Na_2SO_4) electrolyte with a potential range of -0.8 - 0.8V and a scan rate of 50 mVs^{-1} .

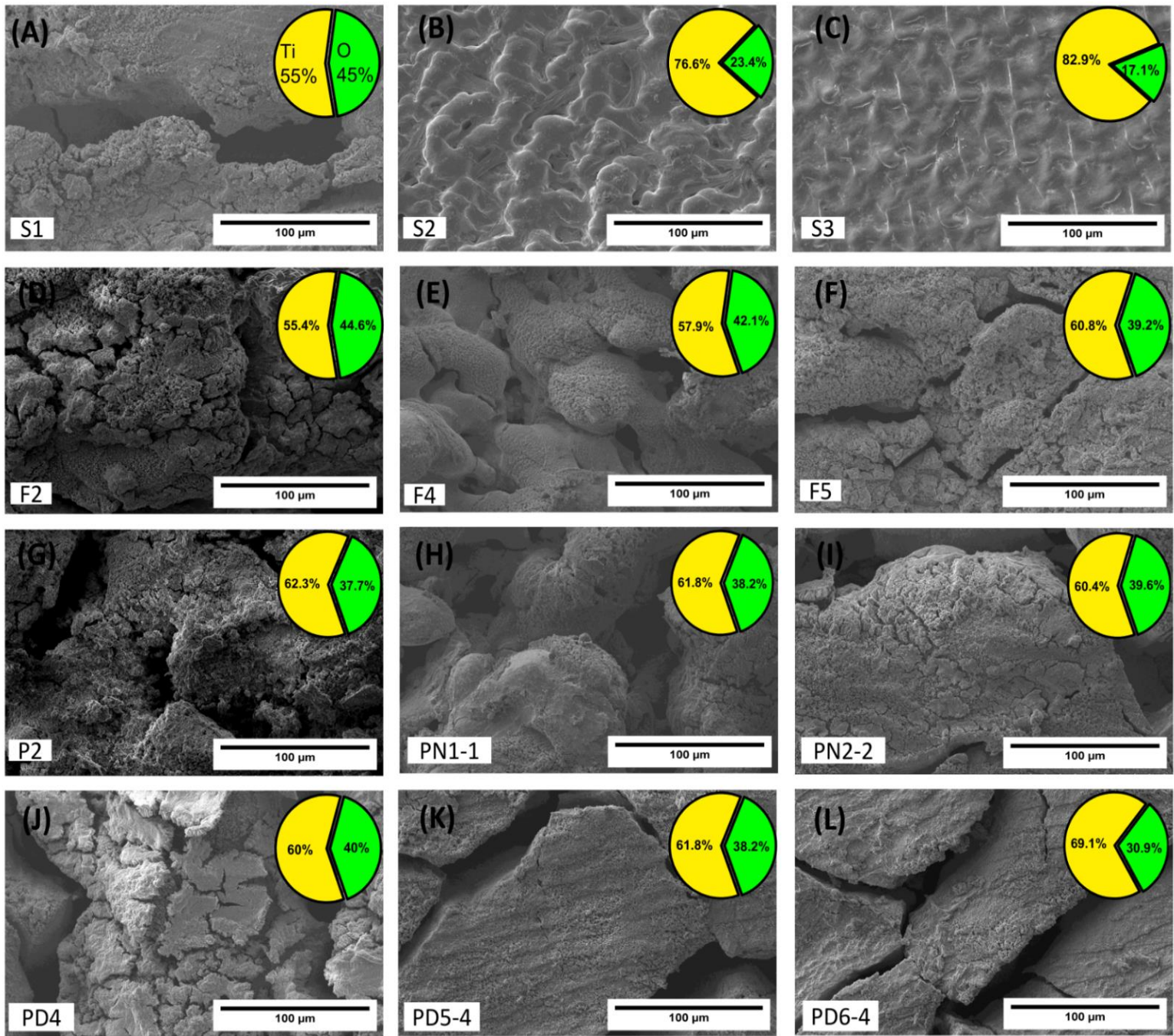


Figure 4-1: Morphological characterization using SEM images with EDX element mapping (weight %) of 12 selected samples. The EDX analysis demonstrated the presence of Ti and O species in the samples. The samples analyzed were as follows: (A-C) S1, S2, and S3 at x500 magnification (100 μm); (D-F) F2, F4, and F5 at x500 magnification (100 μm); (G-I) P2, PN1-1, and PN2-2 at x500 magnification (100 μm); and (J-L) PD-4, PD5-4, and PD6-4 at x500 magnification (100 μm).

The electrochemical performance of the samples may be affected by the electrolyte composition, which we did not consider because it was consistent across all setups. The redox peaks demonstrate excellent reversibility and rapid kinetics taking place at the oxide surface. The capacitive nature of the samples is apparent in the range of -0.8V to 0.8V. The rapid, reversible redox behavior and capacitive characteristics of the samples confirm the presence of pseudocapacitance, thus verifying the device as a pseudocapacitor.

Compared to the other groups, the scan speed group exhibited the best capacitive performance. S3, which had the fastest scan speed, had the lowest current density of 0.028 mA at 0.8 V due to its low oxidation and surface area (Figure 4-2 (A)). Meanwhile, S2's current density at 0.8 V (0.05048 mA) improved slightly as the scan speed decreased, which can be attributed to its increased surface area and oxidation rate. When the scan speed in S1 is reduced to 40 mm s^{-1} , an approximately rectangular-shaped CV curve with the maximum rechargeable current density is observed, indicating the best enhancement in super-capacitive performance as expected from an ideal capacitor. The super-capacitive performance of both S1 and S2 samples is improved, with current densities of 0.07525 mA and 0.05048 mA, respectively, at 0.8 V. The CV curve obtained for S1 is several orders of magnitude larger than the CV curves obtained for other samples in all groups, indicating significantly greater performance. S1's superior performance can be attributed mainly to its faster oxidizing rate and the presence of 3D nanoporous structures, which lead to the best performance among all samples in the CV findings. As previously mentioned, the improved pattern resulting from changing the laser parameters is evident in the CV curves of all other sample groups as well. Among the frequency, power, and pulse duration groups, F2 with the lowest frequency, PN2-2 with the highest power, and P4 with the shortest pulse

duration exhibit the best supercapacitive performance (see Figures 4-2(B, C, and D)). Based on the SEM images and EDX data, it is possible to deduce that both surface area and oxidation rate play major roles in the electrodes' electrochemical behavior.

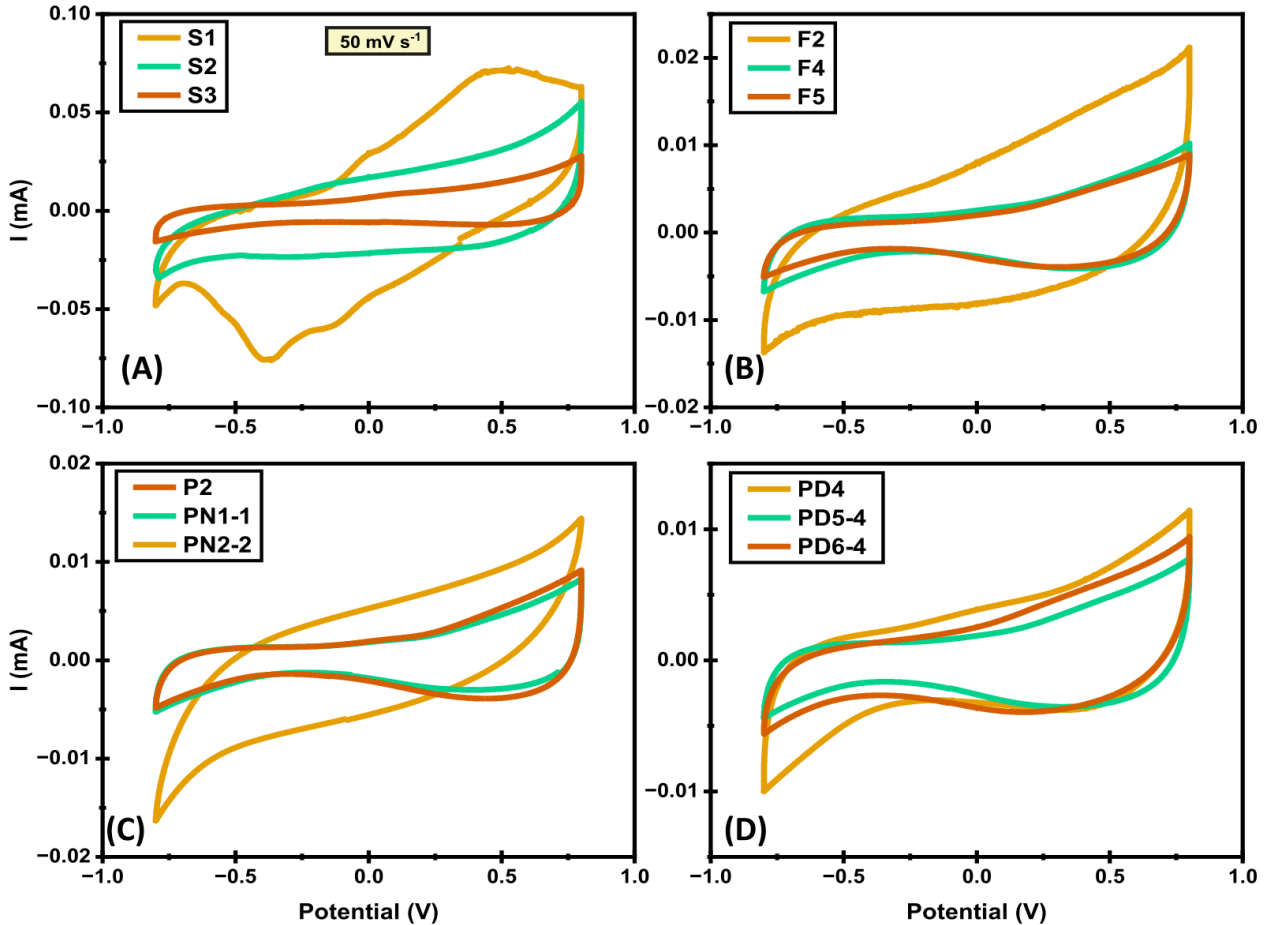


Figure 4-2: CV curves at a scan rate of 50 mVs^{-1} . (A) S1 exhibits superior redox and capacitive capabilities compared to the other samples due to its faster oxidizing rate and the presence of 3D nanoporous structures. (B) Among the samples with different frequencies, F2 shows better charge storage capacity compared to the other samples. (C) Increasing the power in PN-2-2 leads to an improvement in the capacitive behavior of the sample. (D) PD4 with the shorter pulse duration shows better electrochemical performance compared to the other samples.

4.1.2.2 Galvanostatic Charge-Discharge

GCD was employed to characterize the fabricated samples, as it has a relatively direct physical relationship with the capacitive charge. During the GCD test, the discharge and

charge curves were analyzed for all cell setups, which used a constant current density of 0.25 mA cm^{-2} for charging and discharging in the stable potential range of -0.8 V to 0.8 V . Figure 4-3 depicts the GCD plot of all sample groups, which, like the CV and microscopy results, confirms the existence of an improvement pattern in all cell setups as a result of the laser parameter change. S1 shows superior performance not only within the scan speed samples but also across other sample groups. S1 depleted stored charges in 8.18 seconds, while S2 and S3 depleted in 3.8 and 1.4 seconds, respectively (see Figure 4-3(A)). Reduction in the redox event primarily causes the charge depletion. Furthermore, the improved specific surface area significantly contributes to S1's excellent performance. The slower scan speed of the laser beam in S1 and S2 allows for a larger area to be irradiated per second compared to S3. Figure 4-3 (B) depicts the discharge curve for the frequency samples group. The discharge time for F2 with the lowest frequency was 0.894 seconds, which was consistent with the microscopy analysis, which revealed that F2 has an equally dispersed porous pores structure. The depletion stored charge decreased from 0.30 seconds to 0.25 seconds as the frequency increased in F4 and F5. The improvement pattern can also be seen in the power and pulse duration sample groups. The PN2-2 with the highest power has the best performance in the power samples group, taking 0.35 seconds to fully discharge from 0.8V to -0.8V . While P2 and PN1-1 take 0.26 and 0.15 seconds, respectively, to deplete the stored charge. Improved surface morphology contributes to improved electrochemical behavior (Figure 4-3 (C)). The pulse duration group's best performance is displayed by PD4, which discharges in 0.5 seconds and has a macroporous structure resembling fiber or broccoli, according to the microscopy analysis. The longer pulse duration beam of the laser allows for a more ablated surface, which results in superior

surface properties. The discharge time decreased as the pulse duration increased, with PD5-4 discharged in 0.30. While PD6-4 discharged the stored charge in 0.25 seconds despite having the largest pulse length and a non-uniformly distributed structure (Figure 4-3(D)).

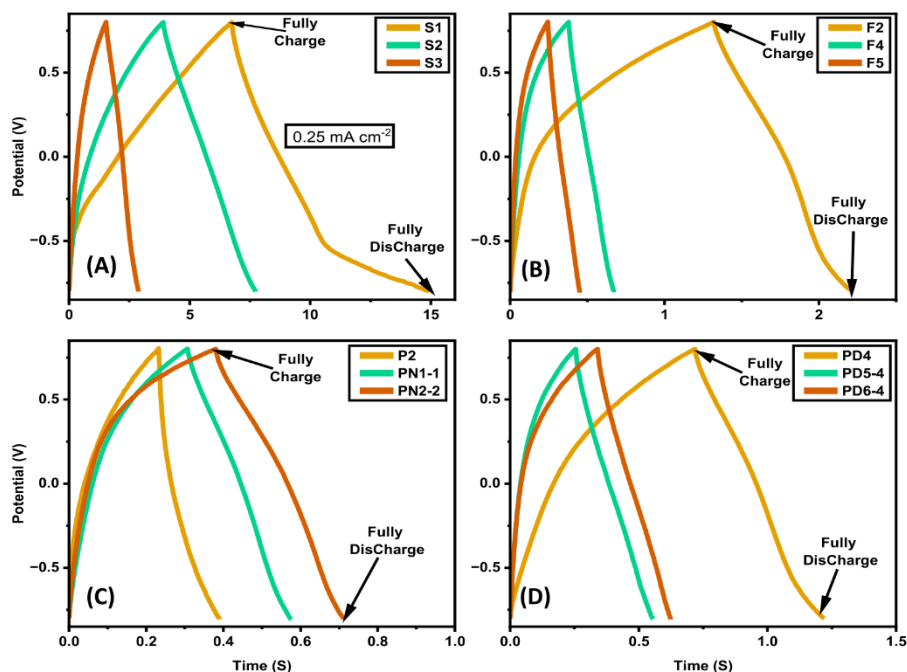


Figure 4-3: GCD Curves were generated at a constant current density of 0.25 mA cm⁻². (A) S1 exhibits a larger charge depletion compared to S2 and S3. (B) F2 has the longest discharge duration in the frequency samples. (C) PN2-2 shows a longer charge depletion compared to other samples. (D) The discharge time of the PD4 with the shortest pulse duration is the longest.

4.1.2.3 Electrochemical Impedance Spectroscopy

Another electrochemical technique that is commonly used in conjunction with CV is electrochemical impedance spectroscopy (EIS). EIS is based on a low-amplitude alternating current (AC) signal with a continuous DC bias. To analyze the samples, EIS measurements were performed on all sample groups over a range of frequencies from 100 mHz to 100 kHz, and their Nyquist and Bode plots are presented in Figure 4-4. The

improvement pattern was also evident in the EIS results, which further confirmed the relationship between increased electrode surface area and improved electrochemical behavior. Specifically, the impedance data for each sample group were represented as a sum of their real and imaginary portions, as shown in Figures 4-4 (A, D, G, and J). The summation of real and imaginary components can be as high as 80000 Ohm.cm² in P2 and as low as 2700 Ohm.cm² in S1. Electrode conductivity is a crucial parameter that can be extracted from EIS measurements. Figures 4-4 (B, E, H, and K) show the electrode impedance plotted against frequency for each sample group. Among all the samples, S1, which had the best surface area for interfacial charge storage, exhibited the lowest electrode resistivity (2678 Ohm.cm²). Additionally, the samples with the highest performance in microscopy, CV, and GCD also demonstrated lower electrode resistivity. F2, the top-performing sample in the frequency group, had a resistivity of 17681 Ohm. cm², while PN2-2 has a value of 19442 Ohm. cm² and PD4 have a value of 34241 Ohm. cm². The Bode plot was used to analyze the capacitance behavior and diffusion properties of the samples, as shown in Figures 4-4 (C, F, I, and L). Generally, the Bode plot displays the phase angle versus frequency, with the ideal capacitance phase angle being -90°. Both the Nyquist and Bode analyses reveal a clear trend: the best samples of each group show the least impedance with the least phase angle near -90° in the lower frequency. For instance, in the scan speed group, the S1 phase angle value is extremely close to -80°, the F2 value is close to -70°, and the PN2-2 and PD4 values are also close to -80° and -70°, respectively. These results demonstrate that samples with superior surface areas exhibit improved charge transfer, better electrochemical behavior (lower impedance), and phase angle values that approach the ideal capacitance phase angle. It is worth noting that the electrolyte used in

this study was a simple salt solution with a lower conductivity than strong acidic or basic water solutions.

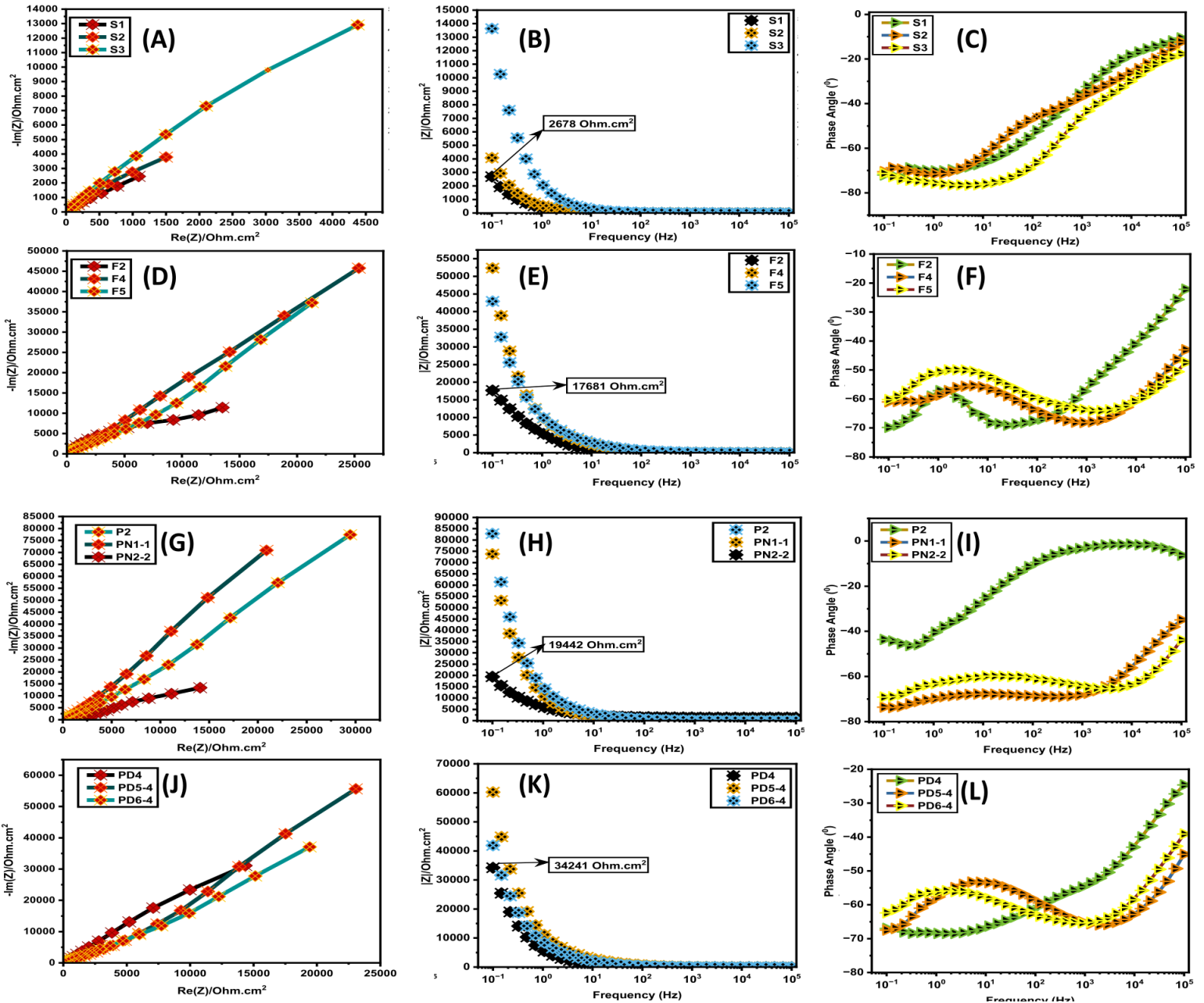


Figure 4-4: EIS Analysis. (A, D, G, J) The Nyquist plot for all the selected samples. (B, E, H, K) For each sample, a basic impedance vs frequency curve was plotted. (C, F, I, L) The Bode plot (phase angle vs frequency) was plotted for all the samples. The Nyquist and impedance versus frequency plots were used to evaluate the electrode conductivity, while the Bode plot was used to investigate the capacitance behavior and diffusion properties of the samples.

Furthermore, the electrochemical performance of the selected samples was studied based on specific areal capacitance, energy density, and power density. Interestingly, the outstanding specific areal capacitance of 2.8833 mF/cm² was achieved at 0.25 mA/cm² with maximum energy density and power density output of 0.003690624 Wh/cm² and 1.62622355 W/cm² respectively, as shown in the Ragone plot depicted in Figure 4-5. For additional morphological analysis, the software ImageJ was used to estimate topological features associated with the ablated surface by examining SEM pictures. The specific areal capacitance, energy density, power density, and porosity of all the samples are shown in Table 4-1. The improving trend can also be seen here; as the surface area expanded, so did the specific areal capacitance and porosity.

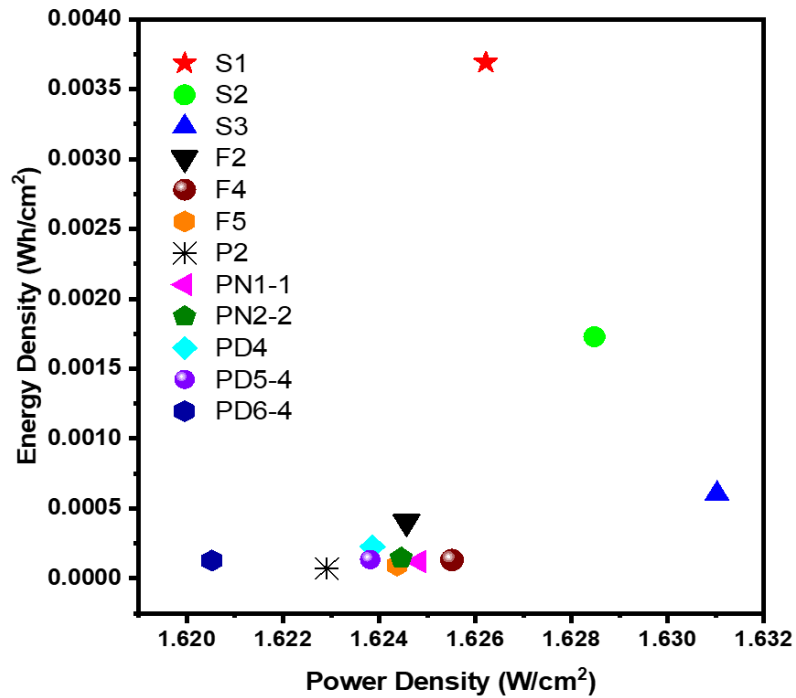


Figure 4-5: Ragone Plot. The energy density and power density of the selected samples is determined based on the calculated specific areal capacitance at a current density of 0.25 mA/cm².

Table 4-1. Summary of the specific areal capacitance, porosity, energy density, and power density of the selected samples.

Sample	Specific Areal Capacitance(mF/cm ²) @ Current density (0.25 mA/cm ²)	Porosity (%)	Energy Density (Wh/cm ²)	Power Density (W/cm ²)
S1	2.8833	45.92	0.003690624	1.62622355
S2	1.3500	15.34	0.001728	1.628481675
S3	0.4743	5.4	0.000607104	1.631025672
F2	0.3155	40.14	0.00040384	1.624565873
F4	0.1029	34.47	0.000131712	1.625516627
F5	0.0723	32.17	0.000092544	1.624370551
P2	0.0554	27.41	0.000070912	1.622906548
PN1-1	0.0939	33.64	0.000120192	1.624826136
PN2-2	0.1163	37.76	0.000148864	1.624463171
PD4	0.1762	36.65	0.000225536	1.623859241
PD5-4	0.1054	32.28	0.000134912	1.623815446
PD6-4	0.0997	30.02	0.000127616	1.620520635

4.1.3 Electrochemical Performance of All 496 Coin Cells

The electrochemical behavior of all 496 prototyped coin cells was evaluated based on three distinct characteristics: specific areal capacitance, discharge duration with a constant current density of 0.25 mA/cm², and maximum impedance $|Z|$ value at the lowest frequency (see STAR Methods for details). Figures 4-6 (A and B) show that the electrochemical behavior of samples with varied manufacturing parameters can be greatly improved or unimproved when tested together. For example, the sample set P1-PD2, where the P1 electrode is the base electrode and the PD2 electrode is the changing electrode, shows high specific areal capacitance and discharge time of 5.7 mF/cm² and 16.1 S, respectively, while demonstrating low impedance of 2493.2 Ohm.cm² (Figure 4-6 (C)). In contrast, the PD1-P3-2 sample set shows the poorest performance among the other samples, with low discharge time and specific areal capacitance of 3.1 seconds and 1.1 mF/cm², respectively,

and a high impedance of 32946 Ohm.cm². These results demonstrate that the electrochemical behavior of pseudocapacitors is highly dependent on the manufacturing parameters and the combination of electrodes used in a single-cell setup. This is yet another proof that the enhanced surface area has an impact on the electrochemical behavior of the fabricated electrode.

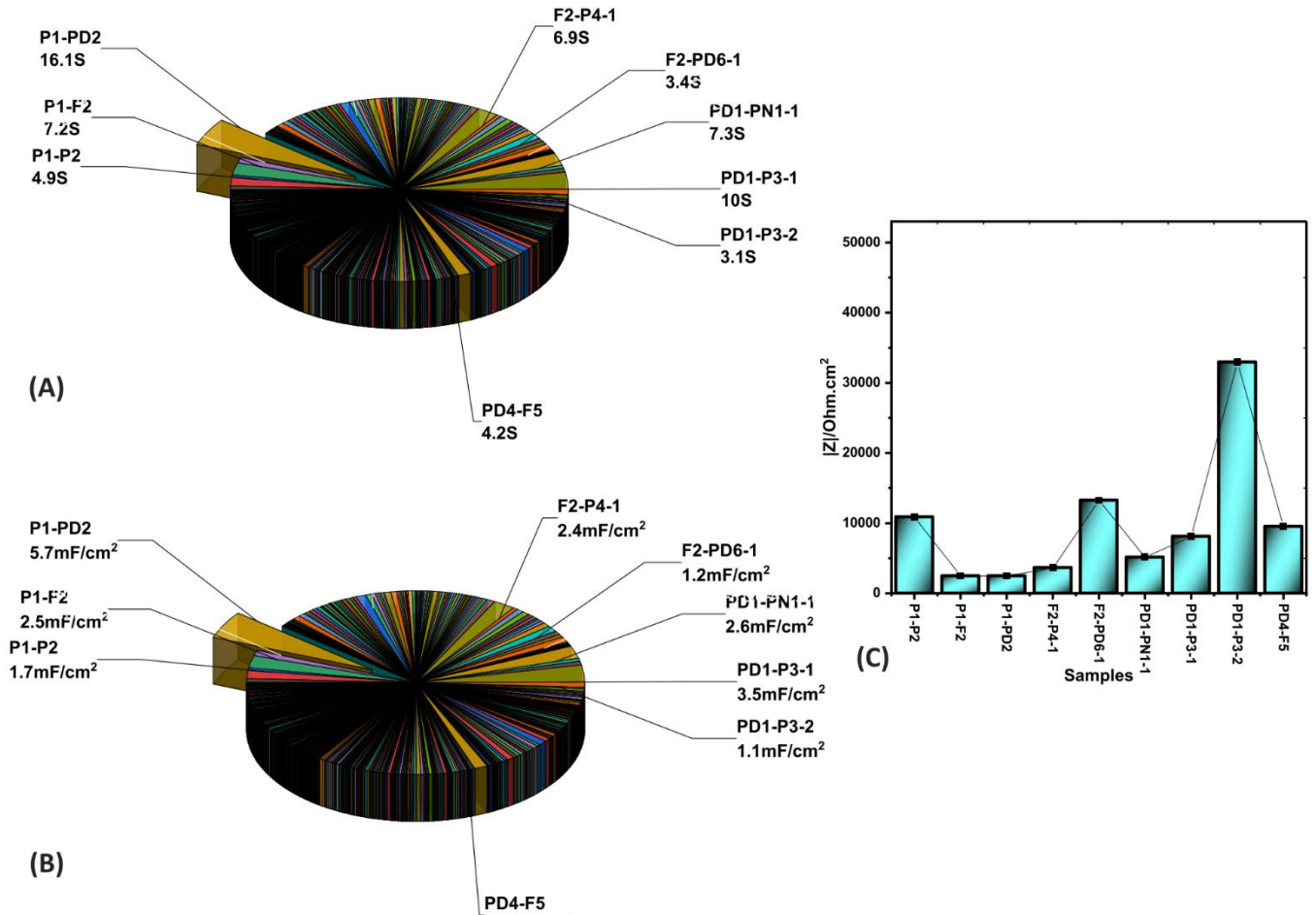


Figure 4-6: The Electrochemical Analysis for All 496 Coin cell Setups. (A) a pie chart is presented, showing the discharge time of all tested samples with a constant current density of 0.25 mA cm⁻². The sample set P1-PD2 displayed the longest discharge time among all tested samples, suggesting excellent electrochemical performance. (B) a pie chart showing the specific areal capacitance for all tested samples. Once again, the sample set P1-PD2 exhibited the highest specific areal capacitance of 5.7 mF/cm². (C) a bar chart indicating the impedance |Z| (maximum value at the lowest frequency) for all coin cell setups. The sample set P1-PD2 displayed a low impedance of 2493.2 Ohm.cm², indicating a better-conducting material compared to other tested samples.

4.2 Electrochemical Behavior Prediction of Pseudocapacitor Electrodes via Machine Learning Algorithms

4.2.1 Specific Capacitance and Impedance Prediction Based on Test Dataset

To predict the electrochemical behavior of the fabricated pseudocapacitors, we utilized three machine learning algorithms: RF, GPR, and ANN. To evaluate the efficacy of each training model in predicting electrochemical behavior metrics, we loaded the trained model with the test dataset. The dataset is split between 80% training data and 20% test data. Figure 4-7 displays the parity plots of the test sets for each of the ML models trained on the dataset. In Figures 4-7 (A, C, and E), the actual specific capacitance values are plotted against predicted values for all models. The RMSE score can be as low as 0.1107 while the R^2 score can be as high as 0.8338, demonstrating the importance of the bootstrap approach in RF for learning the non-linear electrochemical behavior of pseudocapacitors. There is a significant increase in RMSE scores 0.4900 and 0.4791, as well as a fall in R^2 scores 0.7691 and 0.7638 for MLP and GPR, respectively. It reveals that MLP and GPR have lower robustness than RF but can still achieve acceptable predictive accuracy. RF outperformed in predicting specific capacitance. The actual $|Z|$ values are plotted against the predicted values for all the models in Figures 4-7 (B, D, and F). MLP achieves an RMSE of 0.0512 and an R^2 score of 0.9975 for predicting impedance $|z|$, which is a much lower RMSE and higher R^2 value than the other models in this study. GPR, on the other hand, performs worse than RF because it has the highest RMSE value of 0.5080 and the lowest R^2 score of 0.7594. The GPR model's high RMSE values and low R^2 scores highlight the nonlinear nature of pseudocapacitors. As also indicated in Table 4-2, RF outperforms GPR in all cases, with

only minor differences in RMSE and R^2 scores. It is evident that GPR is not a suitable model for forecasting the non-linear electrochemical behavior of a pseudocapacitor ($|Z|$).

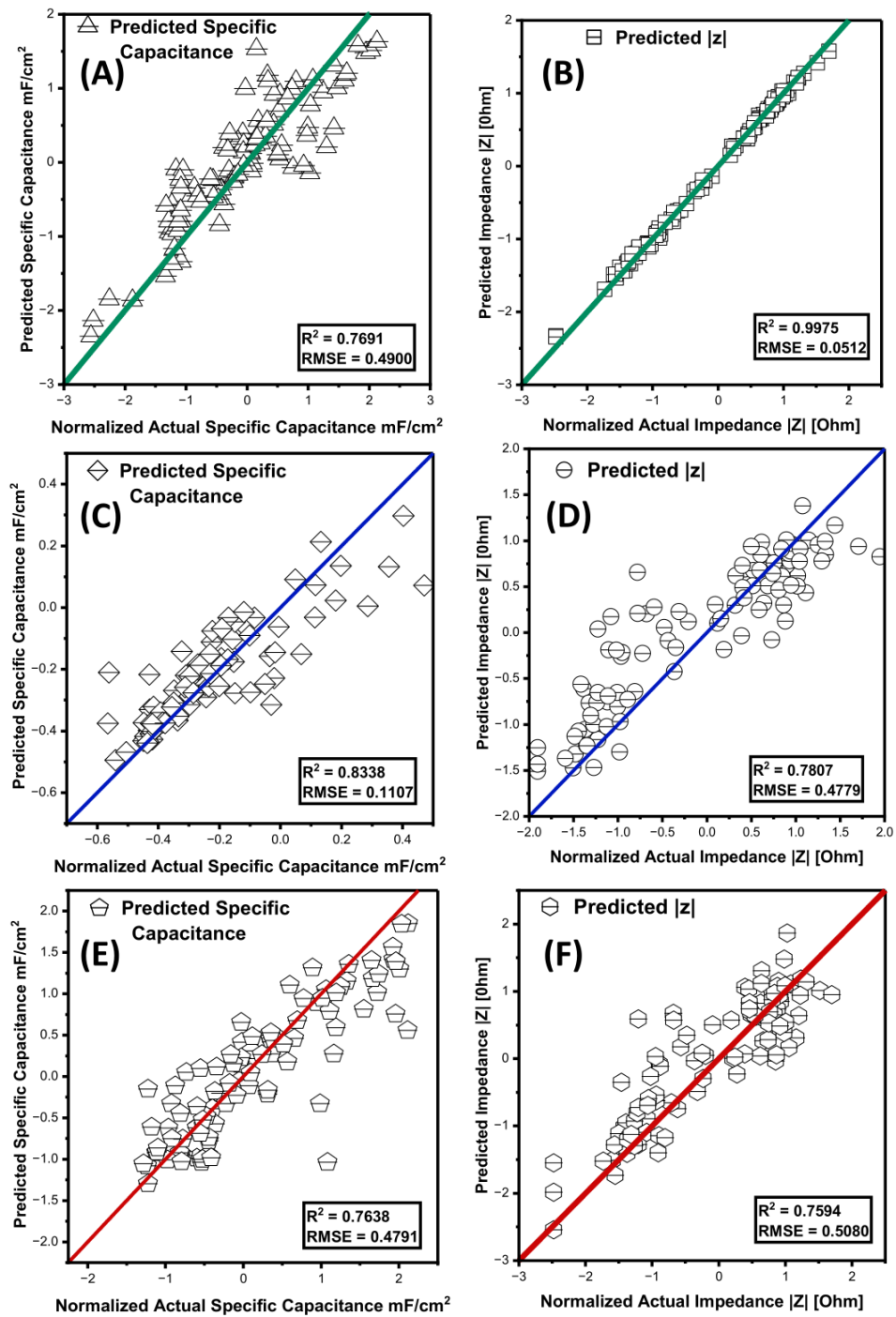


Figure 4-7: Comparison between experimental values for $|Z|$ and specific areal capacitance values and predictions made using the test set. (A-B) MLP. (C-D) RF. (E-F) GPR.

4.2.2 Specific Capacitance and Impedance Prediction Based on Cross Validation

Additionally, to verify regression accuracy, we used cross-validation (CV) to evaluate all ML models on a limited data sample. We compared the RMSE scores of all three developed learning algorithms (see Table 4-3). As expected, the MLP approach outperformed the RF and GPR approaches, with the lowest RMSE score of 0.0393 for predicting the $|Z|$ value. The RF and GPR models had the highest RMSE scores, with values of 0.5125 and 0.5033, respectively. Moreover, RF had the lowest RMSE score for forecasting specific capacitance, as it did in the dataset-splitting technique, whereas the RMSE score increased dramatically in the MLP and GPR models.

Table 4-2. Performance comparison of ML algorithms on the test dataset.

Learning Algorithms	MLP		RF		GPR	
	RMSE	R ²	RMSE	R ²	RMSE	R ²
Impedance $ Z $ [Ohm]	0.0512	0.9975	0.4479	0.7807	0.5080	0.7594
Specific Capacitance [mF/cm ²]	0.4900	0.7691	0.1107	0.8338	0.4791	0.7638

Table 4-3. Performance comparison of ML algorithms based on cross-validation.

Learning Algorithms	MLP	RF	GPR
Performance Metrics	RMSE	RMSE	RMSE
Impedance $ Z $ [Ohm]	0.0393	0.5125	0.5033
Specific Capacitance [mF/cm ²]	0.4401	0.1182	0.4797

4.3 Discussion and Summary

The changes in linearity graphs achieved by individual models are due to differences in their mathematical construction. The MLP model is better suited for predicting $|Z|$, whereas the RF model is better suited for predicting specific capacitance. For example, the R^2 value indicates that the MLP model provides the best fit for $|Z|$ ($R^2 = 0.9975$). When an RF model is used for $|Z|$ ($R^2 = 0.7807$), the fit is the least accurate when compared to the GPR and MLP. Similarly, for the specific capacitance, the RF model provides the best fit ($R^2 = 0.8338$). When using a GPR model for specific capacitance ($R^2 = 0.7638$), the fit is the least accurate when compared to the MLP.

In summary, we aimed to build a theoretical bridge between the fabricated pseudocapacitors (experimental data) and their electrochemical performance via data-driven ML approaches. Therefore, we divided this research into two major phases. The first section describes a single, simple, and environmentally friendly in-situ procedure for generating TiO by irradiating a Ti sheet with an ultra-short, pulses laser for a pseudocapacitor electrode. Whereas the results show that the tuning laser parameters have an effect on the electrochemical performance of the fabricated pseudocapacitors. With a single and rapid electrode fabrication method, a specific areal capacitance of 2.8333 mF/cm² at a current density of 0.25 mA/cm² was achieved for an S1 sample with the lowest scan speed. In the second section, we tried to shed new light on the modeling and prediction of the electrochemical behavior performance of fabricated pseudocapacitors. Several data-driven ML algorithms were used in this study to simulate the electrochemical behavior of pseudocapacitors, such as impedance and specific capacitance. These models use numerous mathematical constructs to predict behavior as accurately as possible. The MLP

and RF models were determined to be the most effective for forecasting $|Z|$, and the specific capacitance of its effectiveness can be described in terms of the lowest error values (RMSE) obtained for this model compared to other tested models. Based on our findings, the ranking of accuracy for the constructed ML models in predicting the impedance ($|Z|$) value is as follows: GPR, RF, and MLP. The findings reveal that MLP has the highest accuracy for predicting impedance ($|Z|$) value with an RMSE of 0.0512. Additionally, the constructed ML models' accuracy in predicting specific capacitance values can be ranked in descending order as follows: first, the MLP model, followed by the GPR model, and finally, the RF model. RF has the best performance for specific capacitance with an RMSE of 0.1107. However, we believed that the RF model could predict the electrochemical behavior performance metrics fairly well since it ranked the best for predicting impedance ($|Z|$) value and the second for specific capacitance. This study presents the importance and efficacy of the in-situ laser irradiation technique for creating a metal oxide layer on a Ti sheet under ambient conditions. Moreover, it underscores the potential of ML algorithms as a tool for constructing mathematical models to forecast the electrochemical behavior of pseudocapacitors, thereby facilitating the development of optimal electrodes. We have high confidence that the results of this study will yield potential solutions for the economical and ecologically sound production of pseudocapacitor electrodes.

4.4 Optimization for Enhancing Electrochemical Behavior of Pseudocapacitors Electrode

4.4.1 Morphology and Structural Properties of Optimized Electrodes

¹¹Following the optimization of sample preparation, six samples were selected for analysis of structural and morphological changes. Laser-induced porous structures offer increased surface area and porosity, which enhances the electrode's capacitance behavior by enabling more ions to adsorb during charge and discharge processes. Additionally, increased oxidized surface area offers more available redox-active sites. We compared the non-optimized and optimized sample sets to illustrate these changes more clearly. In the non-optimized sample group, S2 and S4 were selected, where the laser parameters remained constant with power set to 10 W, frequency set to 900 kHz, and pulse duration of 0.15 ns, while the scan speed set at 10 (mm s⁻¹). For S4, all the parameters remained the same as S2, except the frequency was increased to 1200 kHz. In the optimized samples we selected OPT-SYM and OPT-ASY (see Table 3-4). Results indicate that laser ablation parameters significantly impact the surface morphology of treated samples. Figure 4-8 depicts SEM images and EDX results showing that surface properties of ablated samples vary depending on the laser parameters used.

SEM images were taken of all samples under both x500 (100 μm) and x3,000 (10 μm) magnification, as depicted in Figure 4-8. The OPT-SYM and OPT-ASY methods exhibit

¹¹ This section is based on a previously published article: Kavian Khosravinia, A. Kiani. "Optimizing the Operation Strategy of the ULPING Technique for Enhancing Capacitance of Supercapacitor Electrodes, using ANN and SA Algorithms", ACS Omega. The material is reproduced here with permission from the publisher, [American Chemical Society].

some significant differences. Samples S4 and S4 display only minor modifications to the pretreatment Ti surface, whereas sample S2 shows a slightly better surface but still lacks the desired porous structure to increase surface area (refer to Figures 4-8 (A-D)). The differences in the distribution of the porous structure between S2 and S4 suggest that there might be an optimal frequency for achieving a more evenly distributed porous structure. EDX data indicates a higher oxidation percentage (28.2%) and a lower Ti percentage (71.8%) at the lower frequency of 900 kHz, as the maximum surface temperature of the irradiated zone becomes higher at this frequency with each pulse having more energy. The oxidation percentage decreases to 23.3% as the frequency increases to 1200 kHz. The decrease in oxidation percentage and increase in Ti percentage with increasing frequency could indicate a threshold frequency beyond which further increases in frequency do not have a significant impact on the oxidation and surface morphology.

On the other hand, the surface morphology of the optimized samples is distinct. The slower scan speed and lower frequency used for OPT-ASY (1) allowed for more energy to be transferred or induced onto the Ti substrate's surface, resulting in more extensive surface oxidation and the growth of a self-standing 3D nanostructured oxide layer. This is why OPT-ASY (1) shows the "broccoli-like" macroporous structure and a white and black oxide layer, indicating increased surface area and redox active sites (see Figure 4-8 (I and J)). OPT-ASY (2), on the other hand, with higher scan speed (290 mm s⁻¹) and frequency and lower pulse duration shows a uniformly distributed structure with visible holes and grooves without any 3D nanostructured oxide layer (Figure 4-8 (G and H)). When the power was increased to 20 W in OPT-SYM with a scan speed of 10 (mm s⁻¹), a spongy porous

microstructure was obtained because more energy or power was transferred or induced onto the surface of the Ti substrate, causing a successful phase change Figure 4-8 (E). At x3,000 magnification, the SEM image of OPT-SYM shows millions of micro granules that have grown and agglomerated on top of the standing structures, which closely resembles the top view of a broccoli (see Figure 4-8 (F)). The formation of these standing structures is consistent throughout the entire surface. These differences may also be attributed to the amount of time allotted for the laser beam to traverse and ablate the surface, affecting the resulting surface morphology. Another distinction among samples is the degree of oxidation that occurred during the laser irradiation procedure, which is shown in the EDX results. This indicates that slower scan speeds on OPT-ASY (1) and OPT-SYM allow for more time for the laser to interact with the titanium substrate, leading to increased oxidation and a higher percentage of oxygen detected in the EDX map spectrum. In contrast, higher scan speeds in OPT-ASY (2) result in less interaction time and, therefore, lower oxidation and a higher percentage of titanium detected. Despite the frequency increase, morphology still exhibits a fibrous and porous microstructure, highlighting the importance of power and scan speed. It is interesting to see how the power level and scan speed of the laser affect the surface properties of the Ti substrate, especially in terms of the degree of oxidation and the resulting microstructure. It appears that the higher the power and the lower the scan speed, the more energy is transferred to the surface, resulting in a more significant phase change and increased oxidation traces. This, in turn, leads to a more porous microstructure, which is desirable for increased surface area and superior capacitance behavior.

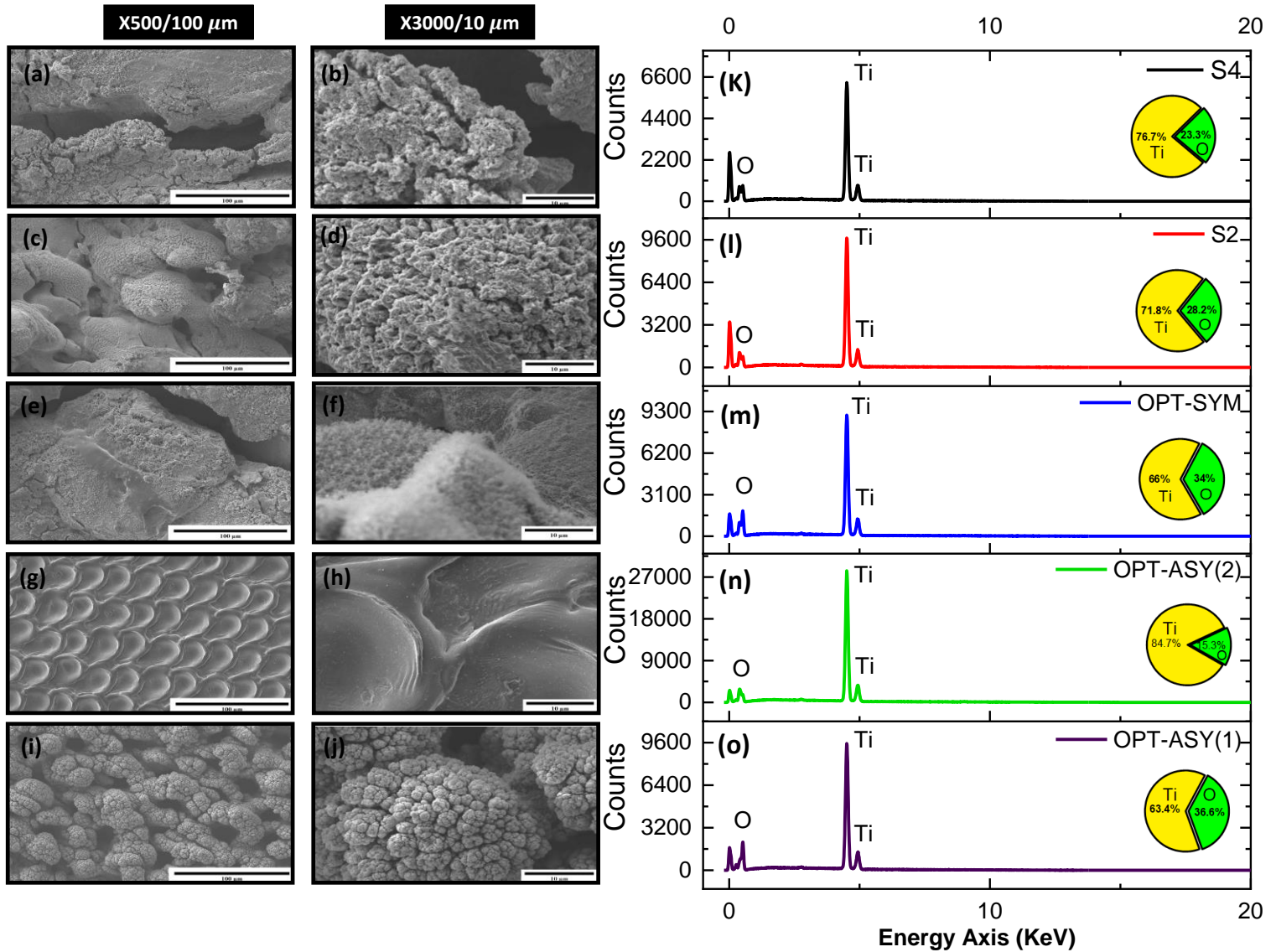


Figure 4-8: Morphological characterization was conducted using SEM images with EDX element mapping (weight %). The EDX data demonstrates elemental composition and presence of oxygen caused during laser irradiation. The samples analyzed were: S4 at x500 magnification (100 μm) and x3000 magnification (10 μm) (a and b, respectively); S2 at x500 magnification (100 μm) and x3000 magnification (10 μm) (c and d, respectively); OPT-SYM at x500 magnification (100 μm) and x3000 magnification (10 μm) (e and f, respectively); OPT-ASY (2) at x500 magnification (100 μm) and x3000 magnification (10 μm) (g and h, respectively); OPT-ASY(1) at x500 magnification (100 μm) and x3000 magnification (10 μm) (i and j, respectively). The EDX results are presented in images (k-o). Images (b, d, f, h, and j) were taken at x3000 magnification (10 μm) to provide a closer view of the samples.

The X-ray diffraction (XRD) analysis was employed to confirm the presence of micro and nano web-like structures of titanium oxide in one electrode. The XRD patterns revealed the formation of a crystalline structure consisting of rutile and anatase phases, as shown in Figure 4-9. The dominant phase was found to be rutile, as evidenced by the major peaks observed at 26.8° , 35.6° , 40.5° , 53.6° , 63.4° , 68.6° , and 69.4° , which correspond to (1 1 0), (1 0 1), (1 1 1), (2 1 1), (3 1 0), (3 0 1), and (1 1 2), respectively (according to JCPDS card No. 88–1175) [444], [445]. The anatase phase was also present, with peaks observed at 38.4° , 55.9° , and 62.3° corresponding to (0 0 4), (2 0 0), and (2 0 4), respectively (according to JCPDS card No. 21–1272) [400], [445], [446]. The anatase phase is known for its higher surface area and narrow band, which make it more suitable for energy conversion applications. However, it is also known to have more surface defects. On the other hand, the rutile phase is generally known for its tetragonal crystal structure, higher density, and thermal stability, making it more durable and suitable for higher power applications. The presence of a mixed state allows for a combination of both phases on the surface, which may provide a desirable combination of properties for various applications. XPS was conducted on all the samples to analyze the surface chemical bonding and cation oxidation states of the laser-assisted fabrication. The XPS survey spectrum for one of the samples (Figure 4-10 (A)) confirms that the film mainly consists of titanium and oxygen, with some additional carbon. A similar composition is observed in the survey spectra for the OPT-ASY (1) sample. The high-resolution XPS spectrum of the Ti 2p region shown in Figure 4-10 (B) is deconvoluted into two peaks, Ti 2p_{3/2} and Ti 2p_{1/2}, which are located at 458.91 and 464.58 eV, respectively [447], [448]. This is a typical signature for stoichiometric TiO. The O 1s core-level spectra for OPT-ASY (1) are shown in Figure 4-9 (C), and the

decomposition is performed using two contributions denoted as O_I (530.38 eV) and O_{II} (531.84 eV) [449]. The low-energy peak O_I is assigned to the Ti-O bond, while the peak at higher binding energies, O_{II}, corresponds to C-O bonds [449].

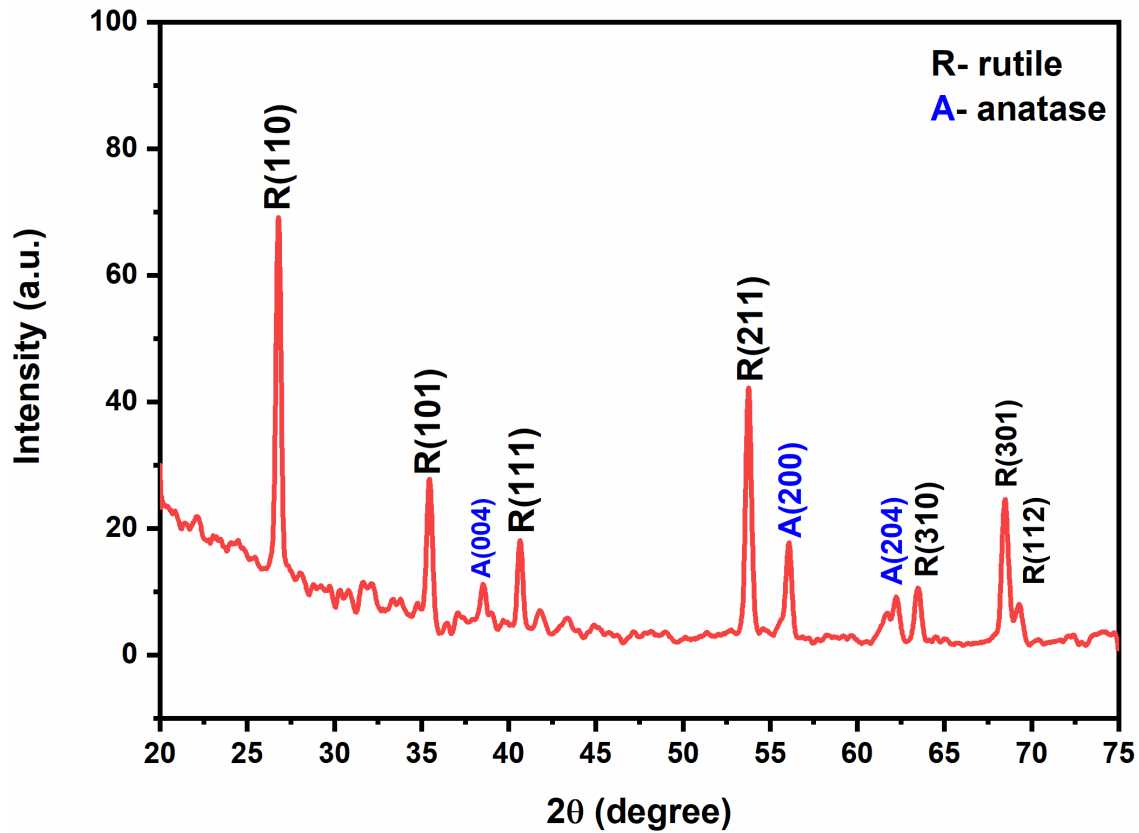


Figure 4-9: XRD analysis of electrode fabricated using the ULPING technique.

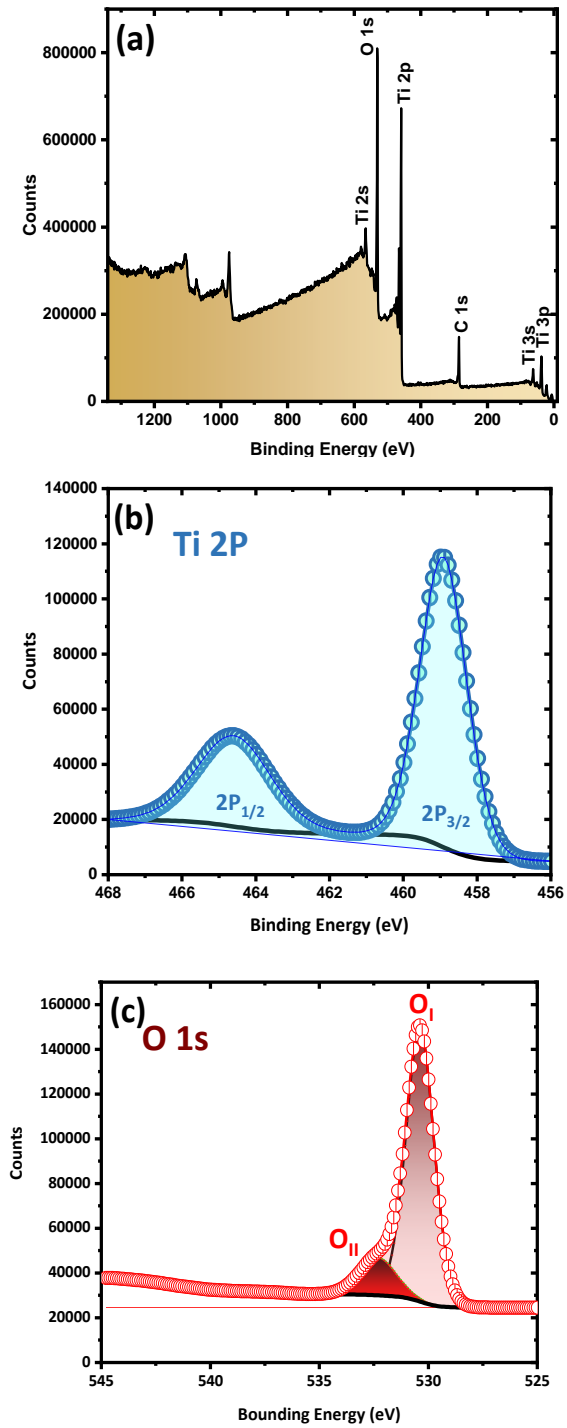


Figure 4-10: (a) A survey scan of the XPS spectrum demonstrates Ti and O species. (b) Ti 2p peak (c) O 1s core levels with deconvoluted two peaks.

4.4.2 Electrochemical Properties of Optimized electrodes

The purpose of the electrochemical analysis was to confirm the results obtained from the microscopy and characterization analysis with respect to the effect of laser parameters on surface characterization improvement. The electrochemical analysis included cyclic voltammetry (CV), galvanostatic charge-discharge (GCD), and electrochemical impedance spectroscopy (EIS) to determine whether the observed structural modifications had an impact on the electrochemical properties of the samples. The results of the electrochemical analysis were then compared to the findings from the microscopy and characterization analysis to establish a correlation between the two. This allowed for a more complete understanding of the impact of the laser parameters on both the physical and electrochemical properties of the samples.

The electrode's electrochemical redox and capacitive behavior was analyzed using a CV curve. As shown in Figure 4-11 (a-b), the CV curve indicates a typical Faradaic dominant reaction. Figure 4-11 (a-b) illustrates the CV curves of the chosen electrodes in a 1M sodium sulfate (Na_2SO_4) electrolyte, with a potential range of -0.8V to 0.8V and a scan rate of 50 mVs^{-1} , as well as a potential range of -1V to 1V with a scan rate of 500 mVs^{-1} . The electrolyte composition, which remained consistent across all setups, may affect the electrochemical performance of the samples, although it was not considered in this study. The redox peaks exhibited excellent reversibility and rapid kinetics occurring at the oxide surface, while the capacitive nature of the samples was evident in the -0.8V to 0.8V range. The samples' rapid, reversible redox behavior and capacitive characteristics confirm the

presence of pseudocapacitance, thereby confirming the device as a pseudocapacitor from a scientific perspective.

Among the analyzed samples, OPT-ASY demonstrated the best capacitive performance. S2-S4, on the other hand, showed the lowest current density of 0.021 mA at 0.8 V due to their low oxidation and surface area. OPT-SYM's current density at 0.8 V (0.038 mA) improved slightly due to its increased surface area and oxidation rate. At a scan rate of 500 mVs⁻¹, OPT-SYM exhibits a symmetric CV shape, further confirming that the symmetric fabrication parameters recommended by the optimization algorithm result in excellent performance. OPT-ASY, a combination of different laser parameters, showed an approximately rectangular-shaped CV curve with the maximum rechargeable current density, indicating the best enhancement in super-capacitive performance as expected from an ideal capacitor. The CV curve for OPT-ASY was several orders of magnitude larger than that of other samples in all groups, indicating significantly greater performance. OPT-ASY's superior performance was mainly due to its faster oxidizing rate and the presence of 3D nanoporous structures, leading to the best performance among all samples in the CV findings. The SEM images and EDX data suggest that both surface area and oxidation rate play major roles in the electrodes' electrochemical behavior. Additionally, the improved pattern resulting from changing the laser parameters is evident in the CV curves of all other sample groups as well.

GCD test was used to evaluate the capacitive charge of the fabricated samples. The test involved analyzing the discharge and charge curves for all cell setups using a constant current density of 0.25 mA cm⁻² within the stable potential range of -0.8 V to 0.8 V.

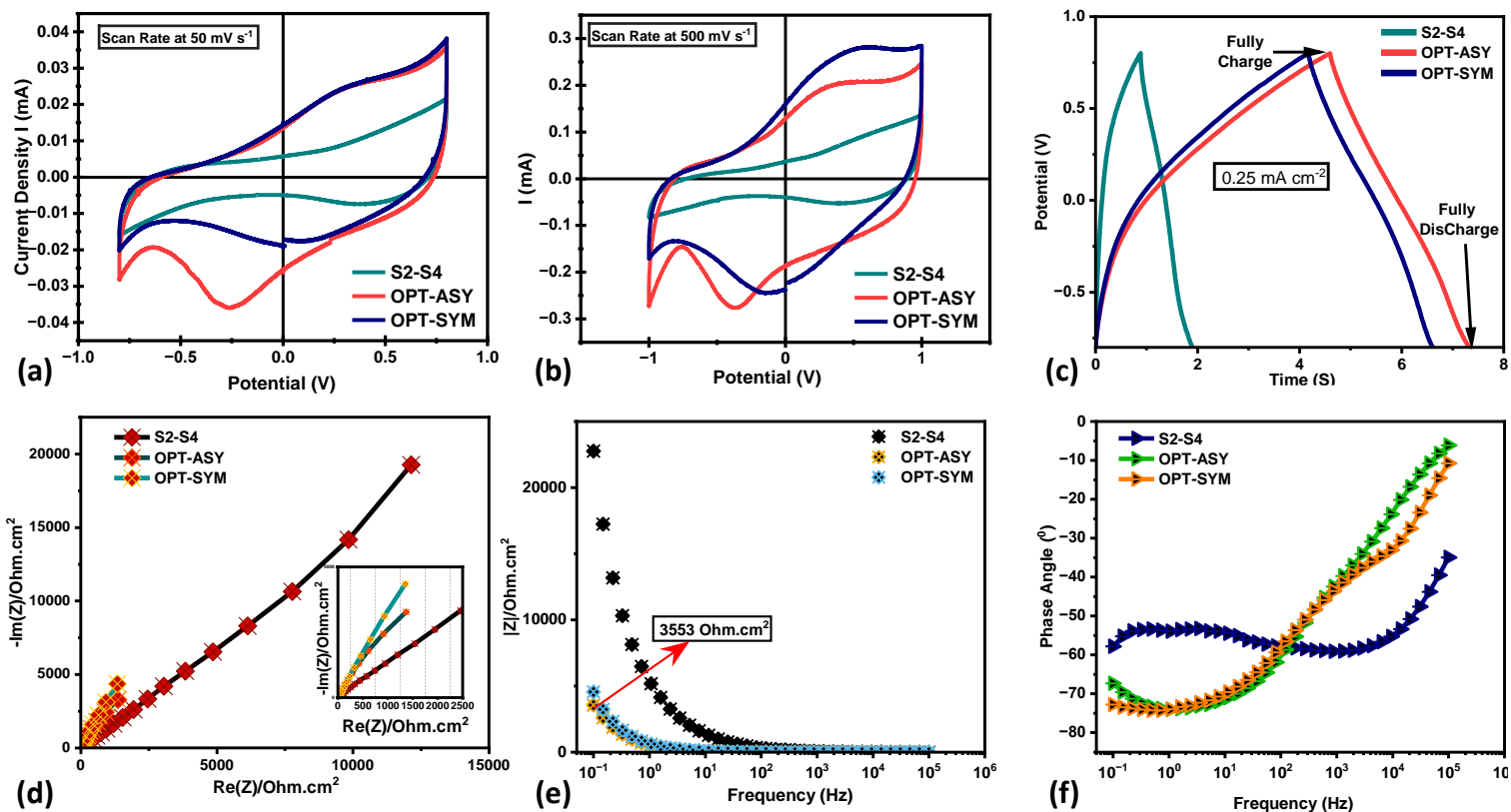


Figure 4-11: (a) The CV profile of all samples at 50 mV s^{-1} scan speed. (b) The CV curve of all samples at 500 mV s^{-1} scan rates. (c) GCD Curves were generated at a constant current density of 0.25 mA cm^{-2} , OPT-ASY exhibits a larger charge depletion compared to OPT-SYM and S2-S4. (d) Nyquist Impedance analysis of all the samples. (e) OPT-ASY demonstrates the least impedance. (f) Bode plot of sample to achieve near 80° phase angle for capacitive characteristics. These results suggest that OPT-ASY is the most promising sample with superior electrochemical behavior, demonstrated by its lower impedance and larger charge depletion in GCD. The CV and GCD curves also indicate that samples with increased surface area perform better. The Nyquist and Bode plots further support this observation, with OPT-ASY showing the least impedance and closest phase angle to the ideal capacitance phase angle. Overall, these findings suggest that optimizing surface area can lead to improved electrochemical performance in the tested samples.

As shown in Figure 4-11 (c), the GCD plot of all sample groups confirmed the improvement pattern resulting from changing the laser parameters, consistent with the CV and microscopy results. OPT-ASY exhibited the best performance, not only within the optimized samples but also across other sample groups, depleting stored charges in 3.1498 seconds. In comparison, OPT-SYM and S2-S4 depleted charges in 2.9091 and 1.015

seconds, respectively. Reduction in the redox event was primarily responsible for charge depletion, and the improved specific surface area significantly contributed to OPT-ASY's and OPT-SYM's excellent performance. Once again, the microscopy analysis revealed an improvement pattern from non-optimized samples to optimized samples, demonstrating the crucial role of improved surface morphology in enhancing the electrochemical behavior of the samples.

EIS is frequently used in conjunction with CV. EIS is based on a continuous DC bias and a low amplitude alternating current (AC) signal. EIS measurements were performed on all sample groups spanning a frequency range of 100 mHz to 100 kHz to examine the samples, and their Nyquist and Bode graphs are shown in Figure 4-11 (d-f). The pattern of improvement was also visible in the EIS measurements, confirming the link between increased electrode surface area and enhanced electrochemical performance. Figure 4-11 (d) shows how the impedance data for each sample were represented as a sum of their real and imaginary sections. The summation of real and imaginary components can be as high as 20000 Ohm.cm² in S2-S4 and as low as 3500 Ohm.cm² in OPT-ASY. Electrode conductivity is a crucial parameter that can be extracted from EIS measurements. Figure 4-11 (e) shows the electrode impedance plotted against frequency for each sample group. Among all the samples, the optimized sample, OPT-ASY, which had the best surface area for interfacial charge storage, exhibited the lowest electrode resistivity (3554 Ohm.cm²). Indeed, both optimized samples with the highest performance in microscopy, CV, and GCD also demonstrated lower electrode resistivity. The Bode plot was utilized to analyze the capacitance behavior and diffusion properties of the samples, as shown in Figure 4-11

(f). Generally, the Bode plot displays the phase angle versus frequency, with the ideal capacitance phase angle being -90° . Both the Nyquist and Bode analyses reveal a clear trend: the best samples of each group show the least impedance with the least phase angle near -90° in the lower frequency. For instance, in the optimized group, the OPT-ASY phase angle value is extremely close to -70° , the OPT-SYM value is close to -75° , and in the non-optimized sample, S2-S4 values are also close to -60° . These results demonstrate that samples with superior surface areas exhibit improved charge transfer, better electrochemical behavior (lower impedance), and phase angle values that approach the ideal capacitance phase angle. It is worth noting that the electrolyte used in this study was a simple salt solution with lower conductivity than strong acidic or basic water solutions.

As we mentioned earlier the specific areal capacitance of each sample can be calculated from the GCD curve based on the equations (3-2) and (3-3). Interestingly, the outstanding specific areal capacitance of 0.9999 mF/cm^2 was achieved at 0.25 mA/cm^2 with maximum energy density and power density output of $0.001279872 \text{ Wh/cm}^2$ and $1.46283734 \text{ W/cm}^2$ respectively. For additional morphological analysis, the software ImageJ was used to estimate topological features associated with the ablated surface by examining SEM pictures. The porosity of each sample was estimated by adjusting the threshold of the 100-micron SEM pictures of all the samples until the software completely emphasized the porous structure. For geometrical measures, ImageJ assumes a 5% margin of error. The specific areal capacitance, energy density, power density, and porosity of all the samples are shown in Table 4-4. The improving trend can also be seen here; as the surface area expanded, so did the specific areal capacitance and porosity.

Table 4-4. Summary of the specific areal capacitance, porosity, energy density, and power density of the selected samples.

Sample	Specific Areal Capacitance(mF/cm²) @ Current density (0.25 mA/cm²)	Porosity (%)	Energy Density (Wh/cm²)	Power Density (W/cm²)
OPT-ASY	0.9999	42.35	0.001279872	1.46283734
OPT-SYM	0.8575	33.35	0.0010976	1.3217019
S2-S4	0.3579	23.8/22.6	0.000458112	1.623886805

4.5 Discussion and Summary

In this study, our first aim was to establish the relationship between the laser parameters used in the fabrication of pseudocapacitor electrodes and their electrochemical performance through data-driven ML approaches. Subsequently, we investigated how an optimization algorithm, simulated annealing, could be used to find the most optimal laser parameters for achieving the most efficient electrochemical performance of the fabricated electrodes. To accomplish this, we generated a large dataset that included laser parameters selected experimentally and electrochemical behavior performance metrics obtained from different microscopy and electrochemistry analyses. We then used artificial neural networks to highlight the relationship between laser parameters and electrochemical performance metrics such as specific areal capacitance and impedance. Finally, we employed a simulated annealing optimization algorithm to maximize the objective function, which, in our case, was the specific capacitance value, and determine the most optimal laser fabrication parameters. Our results showed that the specific areal capacitance increased from 0.3579 mF cm⁻² in non-optimized electrodes to 0.9999 mF cm⁻² at a current density of 0.25 mA cm⁻² in optimized electrodes

Chapter 5 : Results and Discussion (Operational Phase)

5.1 Evaluation Performance of Machine Learning Algorithms for Anode Potential Prediction

First, we evaluate each training model's ability to predict the anode potential using the training data set. The predictions are based on four driving cycles and four constant charge profiles, as indicated in Table 5-1. As expected, the RMSE value is low in most of the conditions because the models are trained on training data. The maximum RMSE occurs during the MANHATTAN driving cycle when the initial SOC is 70% and the GPR algorithm is used. The EUDC and NYCC have the lowest RMSE for driving cycles with an initial SOC of 70% when employing the RF algorithm. The 2.4 mV RMSE is obtained for constant charging profiles ranging from 0.1C to 2C, which is less than the driving profiles.

To evaluate the efficacy of each training model (linear regression, RF, SVR, GPR) in predicting the anode potential, the trained model is loaded with the test dataset, which is compiled from a variety of driving cycles and initial SOCs. Figure 5-1 compares the predicted anode potential from different learning algorithms to the estimated anode potential from the physics-based model. The MANHATTAN driving cycle, with an initial SOC of 65%, was selected as an example for this comparison (for full comparison, see

¹² This section is based on a previously published article: Kavian Khosravinia, X. Lin. "Toward Enhanced Anode Potential Prediction of Lithium-ion Batteries: Using Optimized Ensemble Selection Approach for Lithium Plating Mitigation", Journal of The Electrochemical Society. The material is reproduced here with permission from the publisher, [IOPSCIENCE].

Figure 5-4). Based on the comparison (see Table 5-2), it is found that the RMSE for the RF algorithm on the EUDC driving cycle can be as low as 2.5 mV, which is satisfactory. The maximum RMSE occurs during the MANHATTAN driving cycle when the GPR algorithm is used (42.6 mV). Furthermore, we discovered that the linear and RF algorithms have the lowest RMSE in all driving cycles with an initial SOC of 65%, whereas the SVR and GPR algorithms have the lowest RMSE in drive cycles with an initial SOC of 35%. In order to evaluate the prediction accuracy, the anode potential prediction error is applied. Figure 5-2 presents the error of each algorithm by displaying the difference between an estimated and an actual value. In particular, GPR has the highest error rate in all time-varying driving cycles when compared to the other methods, whereas SVR and RF have the lowest error rate. Table 5-2 summarizes the anode potential estimation error, which shows that the RF performs significantly better on most of the time-varying drive cycles when compared with the other methodologies. It should be noted that the high performance of the RF has also been proven in the literature for anode potential prediction [433].

Table 5-1. Performance comparison of different learning algorithms on the training dataset.

Learning Algorithm	US06-RMSE [mV]			US06-HWY -RMSE [mV]			HWFET -RMSE [mV]			UDDS -RMSE [mV]			Constant Charging		
	40%	70%	90%	40%	70%	90%	40%	70%	90%	40%	70%	90%	40%	70%	90%
Linear Regression	33.4	11.3	27.3	32.9	15.3	27.8	32.5	16.9	28.4	34.2	11.9	25.4	11.27	10.2	15.1
RF	11.1	2.5	4.8	8.6	3.6	6.2	7.9	2.5	6.1	9.4	2.8	5.4	4.65	2.4	2.6
SVR	4.1	9.2	13.8	4.3	9.5	15.6	4.7	8.9	15.9	5.0	8.1	13.9	5.44	5.6	6.83
GPR	31.1	32.3	30.9	31.7	40.4	32.3	31.0	39.2	35.6	29.8	32.4	30.3	15.27	17.6	18.3

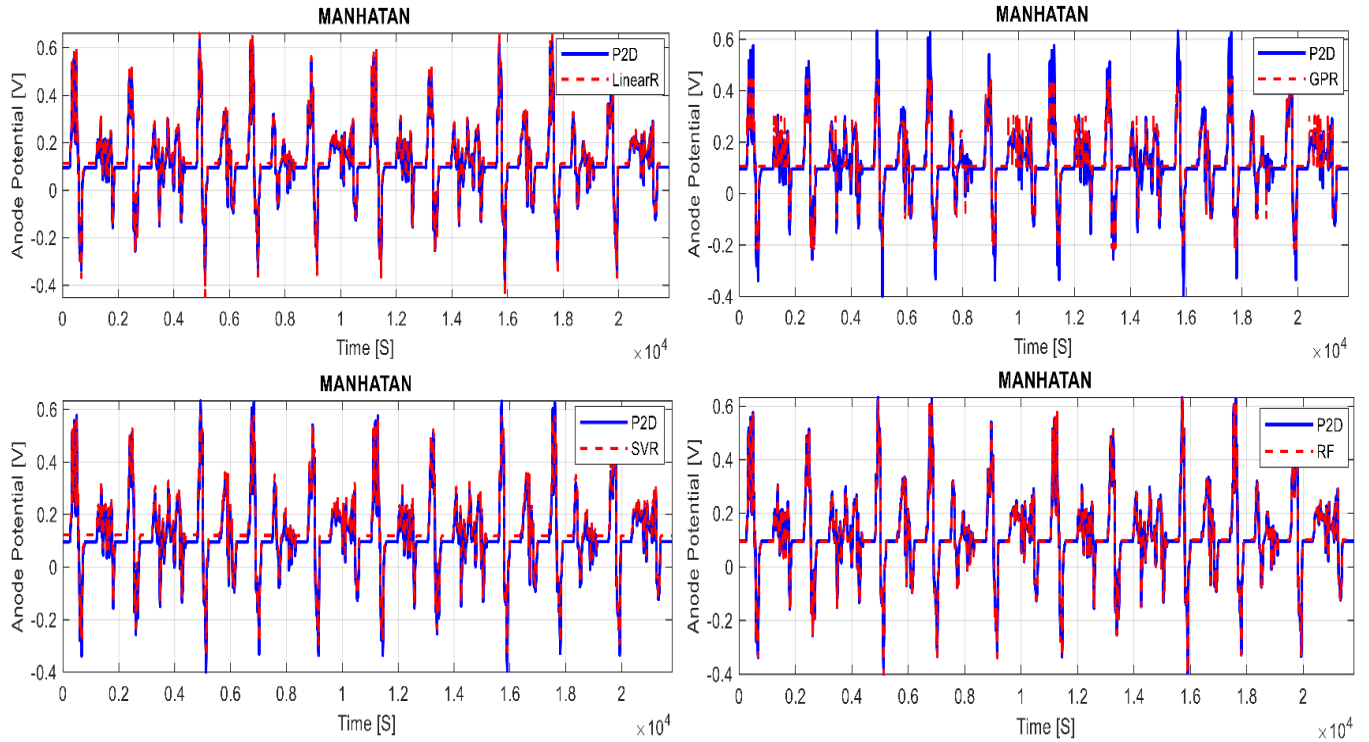


Figure 5-1: Comparison of the anode potential predictions on the test data (EV driving current profile -Manhattan) with the initial SOCs of 65% between the physics-based model and linear regression, gaussian process regression, support vector regression and random forests regression.

5.2 valuation Performance of Optimized Ensemble Selection for Anode Potential Prediction

Predictions on the test dataset are made to evaluate the adaptability of the developed ensembles selection algorithm. We compared the RMSE value of the ensemble selection to the other four developed learning algorithms and the physics-based model as the study's benchmark (see Table 5-2). Figure 5-3 compares the predicted anode potential from the ensemble selection with the physics-based model on the four different driving cycles with the initial SOC of 65% as an example for this comparison (full comparison is provided in Appendix-III). As expected, the ensemble selection approach performs well. The

maximum RMSE for the WVUSUB driving cycle with an initial SOC of 65 % is 6.3 mV, while the minimum is 2.1 mV for the MANHATTAN driving cycle with an initial SOC of 65 %. As a result, the ensemble selection algorithm is well trained, and the above data indicate the ensemble selection algorithm's efficacy in forecasting the anode potential at different operating conditions. Figure 5-4 depicts the error of the ensemble selection algorithm vs RF by showing the difference between an estimated and an actual value. In the MANHATTAN, NYCC, and WVUSUB driving cycles, RF has the highest error rate, whereas in the EUDC with an initial SOC of 35 % RF has the lowest error rate.

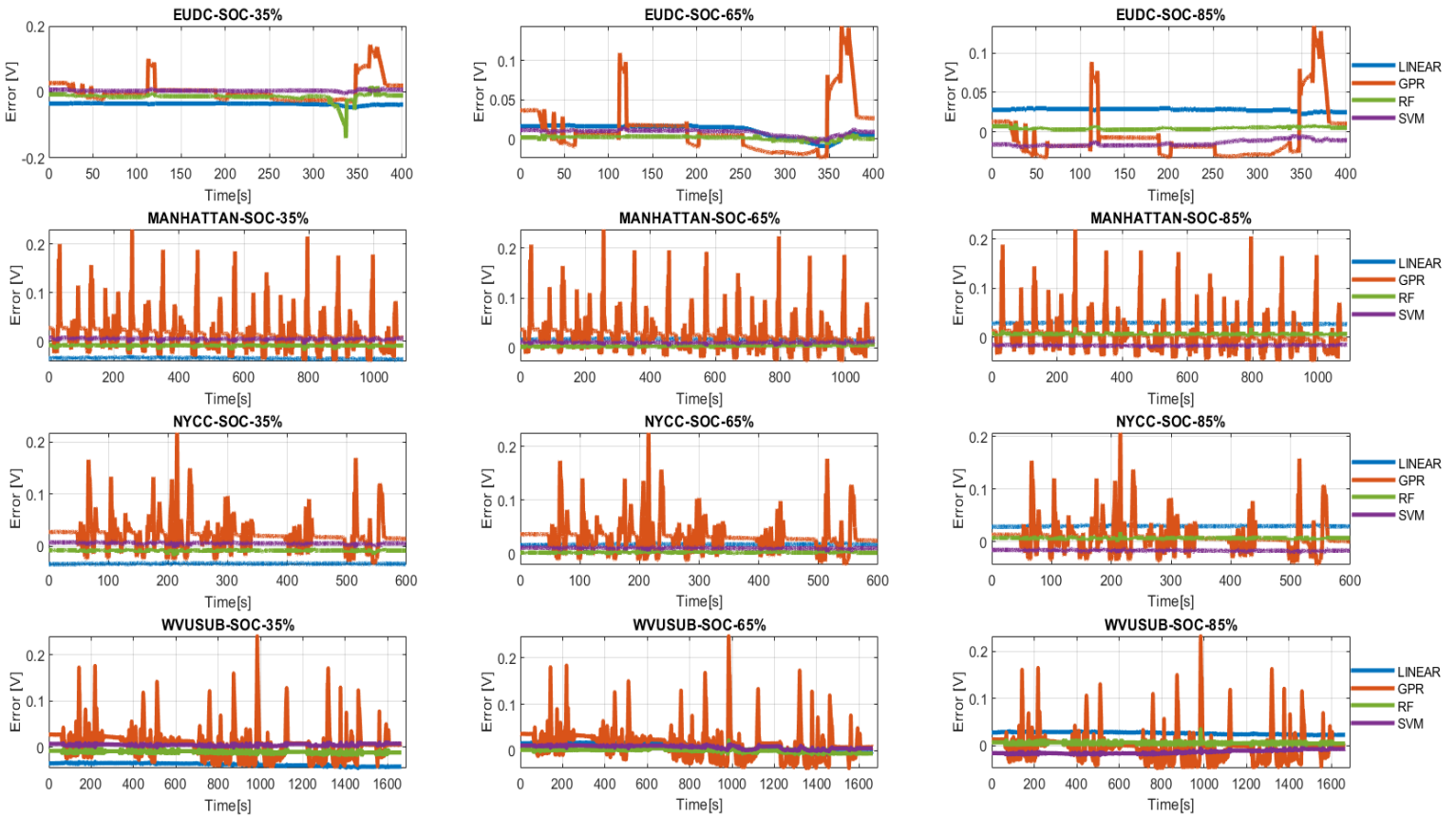


Figure 5-2: Anode Potential Estimation Error on the Test Data with the initial SOC of 35%, 65%, and 85% (linear regression-blue curve, GPR-orange curve, RF-green curve, SVR-purple curve).

Table 5-2. Performance comparison of different learning algorithms and the developed ES model on the test dataset.

Learning Algorithms	EUDC-RMSE [mV]			MANHATTAN-RMSE [mV]			NYCC-RMSE [mV]			WVUSUB-RMSE [mV]		
	35%	65%	85%	35%	65%	85%	35%	65%	85%	35%	65%	85%
Linear Regression	35.6	12.1	28.0	34.9	16.5	28.6	33.6	17.2	29.5	37.6	12.5	26.5
RF	11.6	2.5	5.0	9.1	3.7	6.4	8.8	2.6	6.4	10.6	3.2	5.8
SVR	4.6	9.9	14.7	5.0	10.3	16.8	5.5	10.2	17.1	5.2	8.5	14.1
GPR	33.2	33.9	32.3	33.4	42.6	34.6	32.4	42.1	35.6	31.5	35.4	32.3
Ensemble Selection	11.9	2.3	2.6	4.9	2.1	2.4	2.2	2.3	3.1	5.1	6.3	3.8

5.3 Discussion and Summary

The average training time and testing time are significant factors when considering a method from a practical standpoint. The offline fitting time of the models and the estimated online prediction time are compared. Table 5-3 compares the average time required to train and test each model individually. COMSOL Multiphysics is used to solve the physics-based model, which is based on partial differential equations. To make this comparison, all of the developed models, as well as the full-order physics-based model, are run through the whole test data set on the Intel i7-5600 CPU. There are 3628 degrees of freedom in the full-order physics-based PDE model, taking about 8.14h to complete the computation required. It is clear that the offline training and prediction time increases linearly, the offline training time for a linear regression model is about 0.03s while for the ensemble selection is 2218.39s. However, the prediction time for the linear regression, SVR, GPR, RF, and the ensemble selection is less than 1s which is very low compared to the physics-based model. The concern here is determining how much the average training and testing time restricts the proposed model's applicability. The answer is highly dependent on the

goal of the proposed method; if the goal is to develop an optimized fast charging protocol that is highly sensitive to the accuracy of the predicted anode potential, then this cost can be ignored because the proposed ensemble selection achieves the highest accuracy for the majority of battery operating conditions. Even though, in practice, online implementation is highly important.

Generally, at that stage, the trained model is uploaded to a GPU for example, and the average time can be reduced further. Since previously employing a GPU reduced the computing time of an LSTM network from 87s to 14s in our previous work [375].

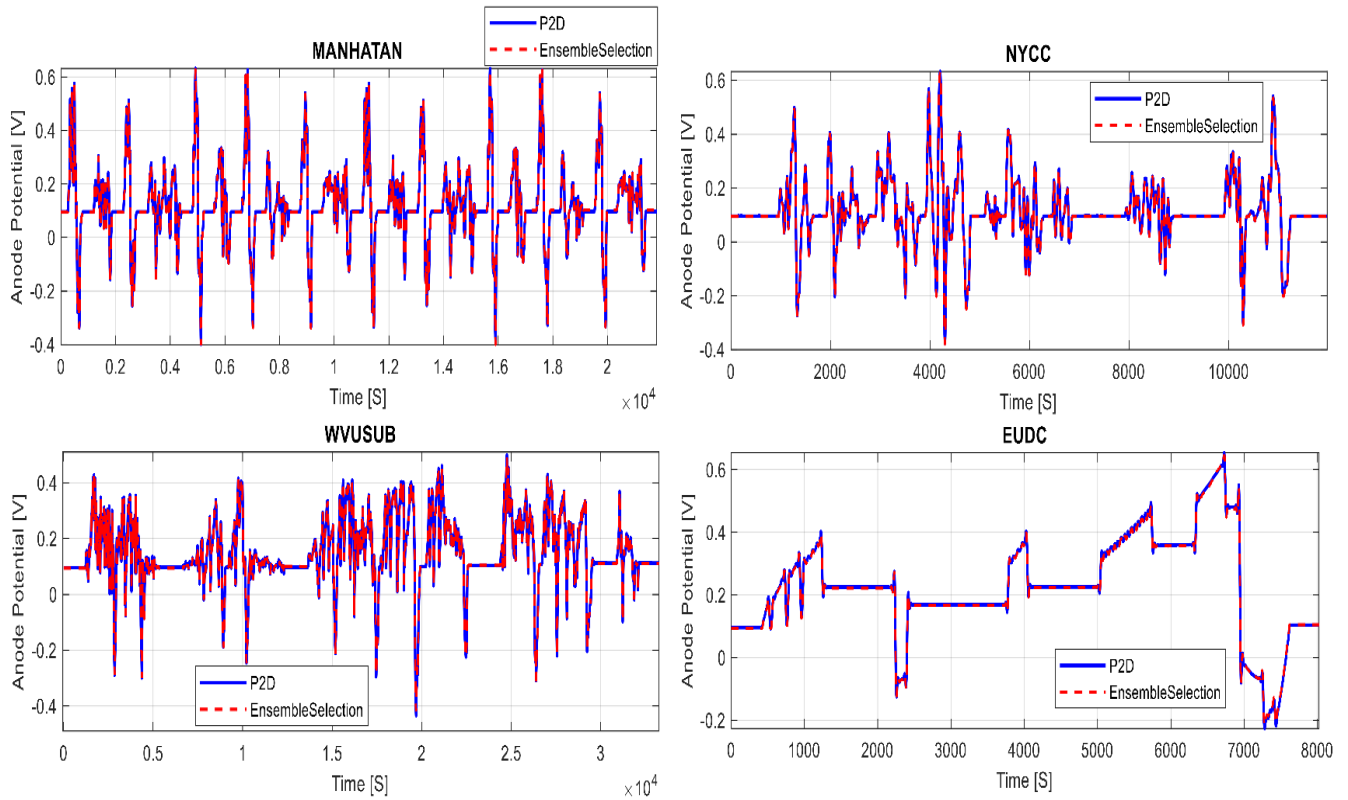


Figure 5-3: Comparison of Anode Potential Predictions on the Test Data (EV Driving Current Profiles) with the Initial SOCs of 65% between Physics-Based Model and Ensemble Selection.

Table 5-3. Average training and testing time of the proposed method and different learning algorithms.

Model	Avg. Training Time [s]	Avg. Prediction Time [s]
Linear regression	0.03s	0.001s
SVR	0.30s	0.01s
RF regression (100 Trees)	2.08s	0.06s
GPR	16.8s	0.5s
Ensemble Selection	2218.39s (0.62h)	0.8s
Physics-based model	29304s (8.14h)	29304s (8.14h)

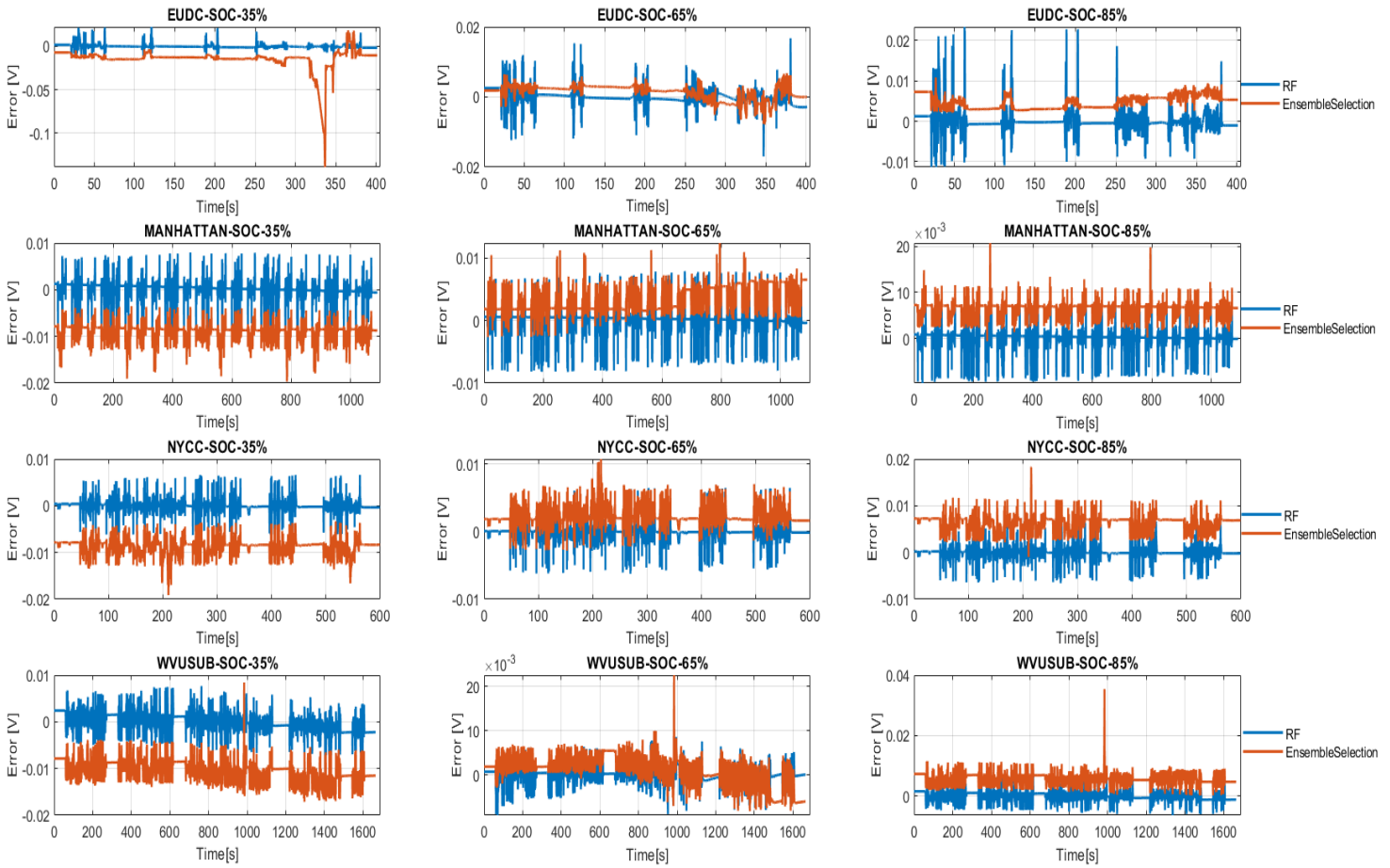


Figure 5-4: Anode Potential Estimation Error for Ensemble Selection Model and RF.

The complex, non-linear, and path-dependent nature of battery degradation, particularly lithium plating, poses some difficulty in developing an explicit model to detect or accurately capture the lithium plating. Given that data-driven approaches are superior to model-based approaches in terms of enhanced learning capability, high accuracy, and low computational complexity, they are ideal for addressing the complex and nonlinear characteristics of lithium-ion batteries. To take advantage of the data-driven features and avoid lithium plating, an ensemble selection approach is proposed to obtain an accurate estimation of the anode electrode potential. It should be noted that the data-driven method's prediction accuracy is greatly dependent on the input features. A data pre-processing method and correlation analysis are used to extract features that have high correlations with the anode potential. The feature subset selection method is used to remove redundancy in a high-dimensional data set and to generate a set with compacted data. This compacted dataset includes the most frequently measured signals in the battery management system, such as charging/discharging current, cell voltage, SOC, and battery surface temperature. The compacted dataset was first analyzed using four common regression algorithms, including linear regression, random forests, support vector regression, and gaussian process regression. Then, an ensemble selection model is built, which is trained using as many learning methods and control parameters as possible for the issue. The trained ensemble selection model can reliably estimate the anode electrode potential under various operating conditions. The results show that the ensemble selection model is effective at predicting the anode potential of lithium-ion batteries. For driving cycles, the lowest estimation RMSE is only 2.1 mV.



Figure 5-5: Anode Potential Predictions on the Test Data with the Initial SOC's of 35%, 65%, and 85% Using 4 Common Regression Algorithms. REF (red curve-Physics-based model), Linear regression (green curve), Gaussian process regression (blue curve), Random forests (pink curve), and Support vector regression (yellow curve).

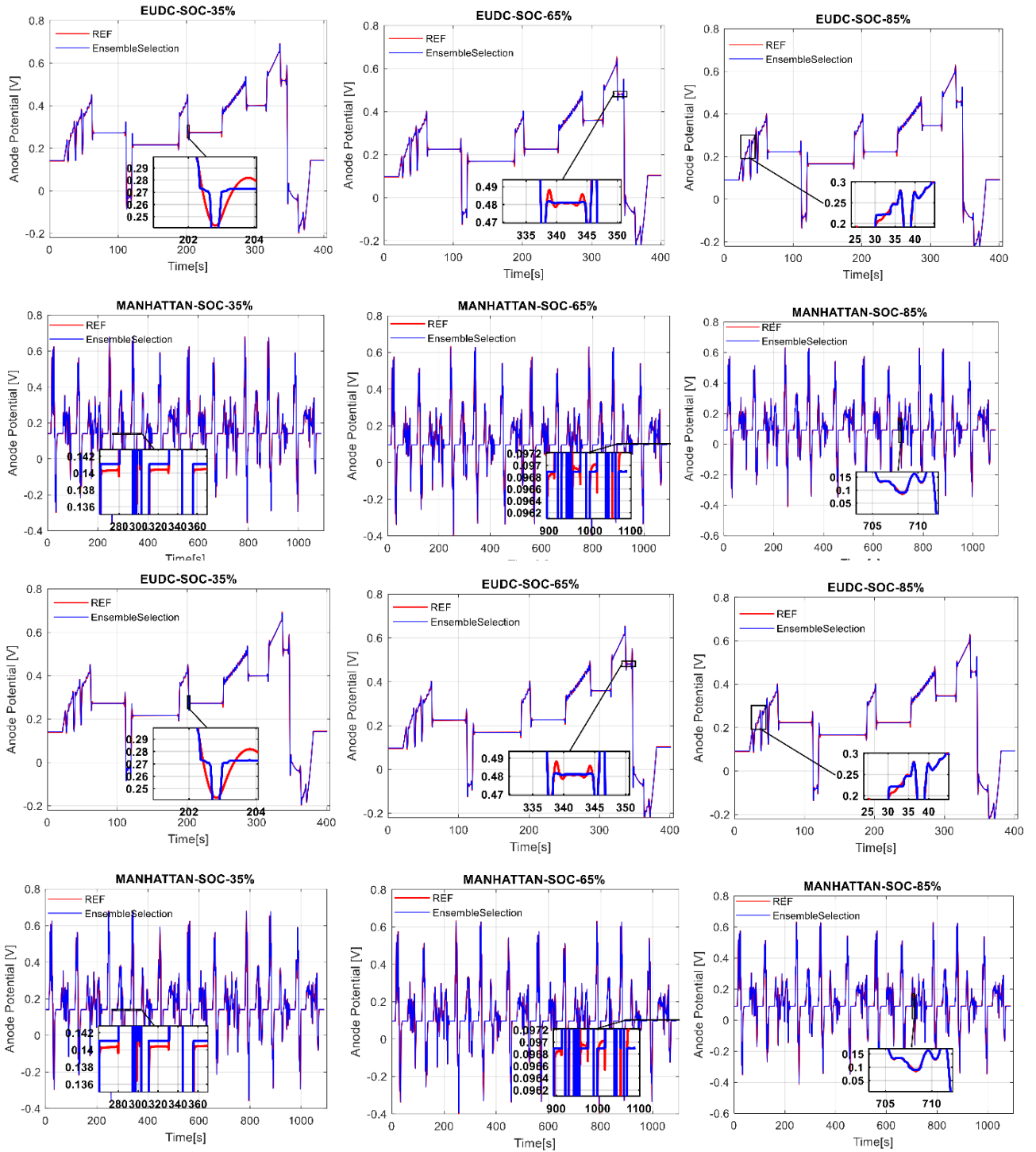


Figure 5-6: Anode Potential Predictions on the Test Data with the Initial SOC's of 35%, 65%, and 85% Using Ensemble Selection Algorithm and Physics-Based Model (REF).

Chapter 6 : Conclusions

The current status of sustainable development and climate change is extremely concerning. The globe is facing tremendous problems as a result of the effects of climate change on the environment, society, and the economy. As humans, we must take steps to limit our carbon footprint and alleviate the effects of climate change. This includes switching to renewable energy sources, minimizing waste and consumption, and promoting sustainable habits in all aspects of life.

In this thesis, we aim to examine this concern from a different perspective by delving deeper into the material life cycle chain. We focus on the life cycle (degradation) of electrochemical energy storage devices during both the manufacturing and operational phases.

In the manufacturing section, we demonstrate how an efficient electrochemical energy storage device (pseudocapacitor) can be built using a simple, single-step ultra-short laser pulses for in-situ nanostructure generation (ULPING) method. Our results reveal that this method is a green synthesis technique that can fabricate a pseudocapacitor electrode in less than 10 minutes, which can be used as an effective energy storage device. The fabricated pseudocapacitor can be electrically charged in less than 5 seconds at a constant current density of 0.25 mA/cm^2 and can hold the charge between 1 to 8 seconds in some of the electrodes.

In the second section, we aimed to provide new insights into the modeling and prediction of the electrochemical behavior performance of the fabricated pseudocapacitors. Several data-driven machine learning (ML) algorithms were utilized in this study to simulate the

electrochemical behavior of pseudocapacitors, such as impedance and specific capacitance. These models employ numerous mathematical constructs to predict behavior as accurately as possible. The Multilayer Perceptron (MLP) and Random Forest (RF) models were found to be the most effective for forecasting $|Z|$, and the specific capacitance. Their effectiveness can be described in terms of the lowest error values (RMSE) obtained for these models compared to other tested models.

This thesis highlights the significance and effectiveness of the in-situ laser irradiation technique for creating a metal oxide layer on a Ti sheet under ambient conditions. Furthermore, it emphasizes the potential of ML algorithms as a tool for constructing mathematical models to forecast the electrochemical behavior of pseudocapacitors, thereby facilitating the development of optimal electrodes.

The laser fabrication parameters were experimentally selected to achieve high-performance pseudocapacitors. Thus, we used an optimization algorithm to assess whether we could improve the electrochemical behavior performance of the pseudocapacitors. One of the primary objectives of this section was to determine the optimal laser fabrication parameters to attain the highest specific areal capacitance. We employed a simulated annealing (SA) optimization algorithm to evaluate the trained MLP model as a black box and maximize the objective function, which, in our case, is a specific capacitance value, to identify the most optimal laser fabrication parameters. Using SA, we found the optimal laser fabrication parameters that increased the specific areal capacitance to $0.9999 \text{ mF cm}^{-2}$ at a current density of 0.25 mA cm^{-2} . Our findings reveal that this research offers promising methods for employing ULPING to fabricate nanostructures on transition metals (TMs)

that have the potential to be used in pseudocapacitor electrodes. Moreover, it highlights the importance of utilizing data-driven approaches in electrode design procedures.

In the operational phase, we studied one of the most detrimental degradation mechanisms that occur during the fast-charging process, known as the deposition of metallic lithium or lithium plating, in another EESD, lithium-ion batteries. Lithium plating occurs when the anode potential drops below 0V (vs. Li^+/Li^0), and the lower the anode potential, the higher the lithium plating rate. Thus, predicting the anode potential in real-time is an ideal way to prevent lithium plating.

We propose a machine learning approach based on an ensemble selection that accurately predicts the anode potential under various charging conditions. To achieve a large input dataset with high correlation with anode potential, we applied data pre-processing, correlation analysis, and feature subset selection. The ensemble selection model is built using the compacted dataset, and the predictions achieve high accuracy, with only a maximum Root Mean Square Error of 2.1 mV on the driving cycles.

According to the experimental results, the proposed ensemble selection model achieves adequate results for anode potential predictions at driving cycle and constant charging profiles. Our study highlights the importance of utilizing machine learning techniques in predicting and preventing degradation mechanisms in electrochemical energy storage devices such as lithium-ion batteries.

6.1 Limitations of study

This thesis used the ULPING fabrication technique on a Ti sheet to generate an oxide layer for use as pseudocapacitor electrodes. While the obtained results were satisfactory, with a

specific areal capacitance of $2.8333 \text{ mF cm}^{-2}$ at a current density of 0.25 mA cm^{-2} , the experimental selection of laser fabrication parameters may have limited the achievement of the optimal electrochemical performance. Therefore, one of the future directions of this study is to determine the optimal laser fabrication parameters to achieve the highest specific areal capacitance based on the other optimization algorithms. In addition, this study focuses on the most used ML algorithms applicable to predicting electrochemical behavior. However, other advanced ML algorithms may also perform well for this prediction task, and their potential use in future research should be explored. Furthermore, as the performance of ML models is highly problem-dependent, the application of the proposed models to other electrode properties requires additional validation.

In the operational phase, the proposed method achieves good anode potential estimation results for a fresh LiB, but there are still certain difficulties under certain conditions, such as the battery's performance degradation over time. The formation and growth of different aging mechanisms will affect the charging habit of the battery as it ages. As a result, the proposed method's accuracy and robustness must be examined under different aging cycles, and the state of health as an input parameter would also aid in capturing any variance generated by an aging cell.

Bibliography

- [1] M. Ashby, *Materials and the Environment: Eco-informed Material Choice: Second Edition*. Elsevier Inc., 2012. doi: 10.1016/C2010-0-66554-0.
- [2] R. Ali, T. M. N. T. Mansur, N. H. Baharudin, and S. I. S. Hassan, “Environmental impacts of renewable energy,” *Electric Renewable Energy Systems*, pp. 519–546, 2016, doi: 10.1016/B978-0-12-804448-3.00021-9.
- [3] D. Welsby, J. Price, S. Pye, and P. Ekins, “Unextractable fossil fuels in a 1.5 °C world,” *Nature*, vol. 597, no. 7875, pp. 230–234, Sep. 2021, doi: 10.1038/s41586-021-03821-8.
- [4] B. K. Kim, S. Sy, A. Yu, and J. Zhang, “Electrochemical Supercapacitors for Energy Storage and Conversion,” *Handbook of Clean Energy Systems*, pp. 1–25, 2015, doi: 10.1002/9781118991978.hces112.
- [5] S. Shiraishi, *Electric Double Layer Capacitors*, vol. 2, no. 1. Elsevier Ltd, 2003. doi: 10.1016/B978-008044163-4/50027-9.
- [6] T. Brousse, D. Bélanger, and J. W. Long, “To Be or Not To Be Pseudocapacitive?,” *J Electrochem Soc*, vol. 162, no. 5, pp. A5185–A5189, 2015, doi: 10.1149/2.0201505jes.
- [7] B. E. Conway, V. Birss, and J. Wojtowicz, “The role and utilization of pseudocapacitance for energy storage by supercapacitors,” *J Power Sources*, vol. 66, no. 1–2, pp. 1–14, 1997, doi: 10.1016/S0378-7753(96)02474-3.
- [8] B. E. Conway, “Transition from ‘Supercapacitor’ to ‘Battery’ Behavior in Electrochemical Energy Storage,” 1991. Accessed: Aug. 12, 2022. [Online]. Available: <https://iopscience.iop.org/article/10.1149/1.2085829/pdf>
- [9] Y. Gogotsi and R. M. Penner, “Energy Storage in Nanomaterials - Capacitive, Pseudocapacitive, or Battery-like?,” *ACS Nano*, vol. 12, no. 3. American Chemical Society, pp. 2081–2083, Mar. 27, 2018. doi: 10.1021/acsnano.8b01914.

- [10] E. Herrero, L. J. Buller, and H. D. Abruña, “Underpotential deposition at single crystal surfaces of Au, Pt, Ag and other materials,” *Chemical Reviews*, vol. 101, no. 7, pp. 1897–1930, Jul. 2001. doi: 10.1021/cr9600363.
- [11] D. Rochefort and A. L. Pont, “Pseudocapacitive behaviour of RuO₂ in a proton exchange ionic liquid,” *Electrochem commun*, vol. 8, no. 9, pp. 1539–1543, Sep. 2006, doi: 10.1016/j.elecom.2006.06.032.
- [12] C. C. Hu, K. H. Chang, M. C. Lin, and Y. T. Wu, “Design and tailoring of the nanotubular arrayed architecture of hydrous RuO₂ for next generation supercapacitors,” *Nano Lett*, vol. 6, no. 12, pp. 2690–2695, Dec. 2006, doi: 10.1021/nl061576a.
- [13] S. Zhao et al., “Determining the Electrochemically Active Area of IrO_x Powder Catalysts in an Operating Proton Exchange Membrane Electrolyzer,” *ECS Trans*, vol. 69, no. 17, pp. 877–881, Sep. 2015, doi: 10.1149/06917.0877ecst.
- [14] B. Li et al., “Electrolytic-anion-redox adsorption pseudocapacitance in nanosized lithium-free transition metal oxides as cathode materials for Li-ion batteries,” *Nano Energy*, vol. 72, Jun. 2020, doi: 10.1016/j.nanoen.2020.104727.
- [15] M. L. Foresti, M. Innocenti, F. Forni, and R. Guidelli, “Electrosorption valency and partial charge transfer in halide and sulfide adsorption on Ag(111),” *Langmuir*, vol. 14, no. 24, pp. 7008–7016, Nov. 1998, doi: 10.1021/la980692t.
- [16] E. Kim, W. T. Leverage, Y. Liu, I. M. White, W. E. Bentley, and G. F. Payne, “Redox-capacitor to connect electrochemistry to redox-biology,” *Analyst*, vol. 139, no. 1, pp. 32–43, 2014, doi: 10.1039/C3AN01632C.
- [17] L. Zhang and X. S. Zhao, “Carbon-based materials as supercapacitor electrodes,” *Chem Soc Rev*, vol. 38, no. 9, pp. 2520–2531, Aug. 2009, doi: 10.1039/b813846j.
- [18] T. Chen, C. Xiang, Y. Zou, F. Xu, and L. Sun, “All-Solid High-Performance Asymmetric Supercapacitor Based on Yolk-Shell NiMoO₄/V₂CT_x@Reduced Graphene Oxide and Hierarchical Bamboo-Shaped MoO₂@Fe₂O₃/N-Doped

- Carbon,” *Energy and Fuels*, vol. 35, no. 12, pp. 10250–10261, Jun. 2021, doi: 10.1021/acs.energyfuels.1c00913.
- [19] H. Zhang, G. Cao, Z. Wang, Y. Yang, Z. Shi, and Z. Gu, “Growth of manganese oxide nanoflowers on vertically-aligned carbon nanotube arrays for high-rate electrochemical capacitive energy storage,” *Nano Lett*, vol. 8, no. 9, pp. 2664–2668, Sep. 2008, doi: 10.1021/nl800925j.
- [20] L. Z. Fan, Y. S. Hu, J. Maier, P. Adelhelm, B. Smarsly, and M. Antonietti, “High electroactivity of polyaniline in supercapacitors by using a hierarchically porous carbon monolith as a support,” *Adv Funct Mater*, vol. 17, no. 16, pp. 3083–3087, Nov. 2007, doi: 10.1002/adfm.200700518.
- [21] D. Hulicova-Jurcakova et al., “Effect of surface phosphorus functionalities of activated carbons containing oxygen and nitrogen on electrochemical capacitance,” *Carbon N Y*, vol. 47, no. 6, pp. 1576–1584, May 2009, doi: 10.1016/j.carbon.2009.02.006.
- [22] X. Yu et al., “Emergent Pseudocapacitance of 2D Nanomaterials,” *Advanced Energy Materials*, vol. 8, no. 13. Wiley-VCH Verlag, May 04, 2018. doi: 10.1002/aenm.201702930.
- [23] Y. Liu, S. P. Jiang, and Z. Shao, “Intercalation pseudocapacitance in electrochemical energy storage: recent advances in fundamental understanding and materials development,” *Materials Today Advances*, vol. 7. Elsevier Ltd, Sep. 01, 2020. doi: 10.1016/j.mtadv.2020.100072.
- [24] C. Choi et al., “Achieving high energy density and high power density with pseudocapacitive materials,” *Nature Reviews Materials*, vol. 5, no. 1. Nature Research, pp. 5–19, Jan. 01, 2020. doi: 10.1038/s41578-019-0142-z.
- [25] J. Liu et al., “Advanced Energy Storage Devices: Basic Principles, Analytical Methods, and Rational Materials Design,” *Advanced Science*, vol. 5, no. 1. Wiley-VCH Verlag, Jan. 01, 2018. doi: 10.1002/advs.201700322.

- [26] B. E. Conway and L. Bai, "Determination of the adsorption behaviour of 'overpotential-deposited' hydrogen-atom species in the cathodic hydrogen-evolution reaction by analysis of potential-relaxation transients," *Journal of the Chemical Society, Faraday Transactions 1: Physical Chemistry in Condensed Phases*, vol. 81, no. 8, pp. 1841–1862, 1985, doi: 10.1039/F19858101841.
- [27] J. P. Zheng and T. R. Jow, "A New Charge Storage Mechanism for Electrochemical Capacitors," *J Electrochem Soc*, vol. 142, no. 1, pp. L6–L8, 1995, doi: 10.1149/1.2043984.
- [28] V. Augustyn et al., "High-rate electrochemical energy storage through Li + intercalation pseudocapacitance," *Nat Mater*, vol. 12, no. 6, pp. 518–522, 2013, doi: 10.1038/nmat3601.
- [29] T. Brezesinski, J. Wang, S. H. Tolbert, and B. Dunn, "Ordered mesoporous α -MoO₃ with iso-oriented nanocrystalline walls for thin-film pseudocapacitors," *Nat Mater*, vol. 9, no. 2, pp. 146–151, 2010, doi: 10.1038/nmat2612.
- [30] W. Chen, C. Xia, and H. N. Alshareef, "One-step electrodeposited nickel cobalt sulfide nanosheet arrays for high-performance asymmetric supercapacitors," *ACS Nano*, vol. 8, no. 9, pp. 9531–9541, 2014, doi: 10.1021/nn503814y.
- [31] J. Xiao, L. Wan, S. Yang, F. Xiao, and S. Wang, "Design hierarchical electrodes with highly conductive NiCo₂S₄ nanotube arrays grown on carbon fiber paper for high-performance pseudocapacitors," *Nano Lett*, vol. 14, no. 2, pp. 831–838, 2014, doi: 10.1021/nl404199v.
- [32] X. Xiong et al., "Controlled synthesis of NiCo₂S₄ nanostructured arrays on carbon fiber paper for high-performance pseudocapacitors," *Nano Energy*, vol. 16, pp. 71–80, 2015, doi: 10.1016/j.nanoen.2015.06.018.
- [33] D. Linzen, S. Buller, E. Karden, and R. W. de Doncker, "Analysis and evaluation of charge-balancing circuits on performance, reliability, and lifetime of supercapacitor systems," *IEEE Trans Ind Appl*, vol. 41, no. 5, pp. 1135–1141, Sep. 2005, doi: 10.1109/TIA.2005.853375.

- [34] J. Zhang, Y. Cui, and G. Shan, "Metal oxide nanomaterials for pseudocapacitors," 2017. Accessed: Aug. 12, 2022. [Online]. Available: <https://arxiv.org/abs/1905.01766>
- [35] S. W. Tsai, L. Hackl, A. Kumar, and C. H. Hou, "Exploring the electrosorption selectivity of nitrate over chloride in capacitive deionization (CDI) and membrane capacitive deionization (MCDI)," *Desalination*, vol. 497, no. 1, p. 114764, Jan. 2021, doi: 10.1016/j.desal.2020.114764.
- [36] T. Y. Ying, K. L. Yang, S. Yiacoumi, and C. Tsouris, "Electrosorption of ions from aqueous solutions by nanostructured carbon aerogel," *J Colloid Interface Sci*, vol. 250, no. 1, pp. 18–27, Jun. 2002, doi: 10.1006/jcis.2002.8314.
- [37] Z. Hai and S. Zhuiykov, "Functionalizing New Intercalation Chemistry for Sub-Nanometer-Scaled Interlayer Engineering of 2D Transition Metal Oxides and Chalcogenides," *Adv Mater Interfaces*, vol. 5, no. 7, Apr. 2018, doi: 10.1002/admi.201701385.
- [38] M. Rajapakse et al., "Intercalation as a versatile tool for fabrication, property tuning, and phase transitions in 2D materials," *NPJ 2D Mater Appl*, vol. 5, no. 1, Dec. 2021, doi: 10.1038/s41699-021-00211-6.
- [39] F. A. Soto et al., "Tuning the Solid Electrolyte Interphase for Selective Li- and Na-Ion Storage in Hard Carbon," *Advanced Materials*, vol. 29, no. 18, 2017, doi: 10.1002/adma.201606860.
- [40] D. Aurbach et al., "Recent studies on the correlation between surface chemistry, morphology, three-dimensional structures and performance of Li and Li-C intercalation anodes in several important electrolyte systems," *J Power Sources*, vol. 68, no. 1, pp. 91–98, 1997, doi: 10.1016/S0378-7753(97)02575-5.
- [41] K. Zhang et al., "Pseudocapacitive Behavior and Ultrafast Kinetics from Solvated Ion Cointercalation into MoS₂ for Its Alkali Ion Storage," *ACS Appl Energy Mater*, vol. 2, no. 5, pp. 3726–3735, 2019, doi: 10.1021/acsaem.9b00445.

- [42] K. Xu, "Electrolytes and interphases in Li-ion batteries and beyond," *Chem Rev*, vol. 114, no. 23, pp. 11503–11618, 2014, doi: 10.1021/cr500003w.
- [43] Q. Wei et al., "High-Energy and High-Power Pseudocapacitor–Battery Hybrid Sodium-Ion Capacitor with Na⁺ Intercalation Pseudocapacitance Anode," *Nanomicro Lett*, vol. 13, no. 1, pp. 1–13, 2021, doi: 10.1007/s40820-020-00567-2.
- [44] S. Sopčić, R. Peter, M. Petravić, and Z. Mandić, "New insights into the mechanism of pseudocapacitance deterioration in electrodeposited MnO₂ under negative potentials," *J Power Sources*, vol. 240, pp. 252–257, 2013, doi: 10.1016/j.jpowsour.2013.04.008.
- [45] Y. G. Wang and Y. Y. Xia, "A new concept hybrid electrochemical supercapacitor: Carbon/LiMn₂O₄ aqueous system," *Electrochem Commun*, vol. 7, no. 11, pp. 1138–1142, 2005, doi: 10.1016/j.elecom.2005.08.017.
- [46] S. Chu and A. Majumdar, "Opportunities and challenges for a sustainable energy future," *Nature*, vol. 488, no. 7411, pp. 294–303, Aug. 16, 2012. doi: 10.1038/nature11475.
- [47] X. H. Xia, J. P. Tu, X. L. Wang, C. D. Gu, and X. B. Zhao, "Hierarchically porous NiO film grown by chemical bath deposition via a colloidal crystal template as an electrochemical pseudocapacitor material," *J Mater Chem*, vol. 21, no. 3, pp. 671–679, Jan. 2011, doi: 10.1039/c0jm02784g.
- [48] H. Tian et al., "Theoretical Investigation of 2D Layered Materials as Protective Films for Lithium and Sodium Metal Anodes," *Adv Energy Mater*, vol. 7, no. 13, Jul. 2017, doi: 10.1002/aenm.201602528.
- [49] C. Xia, W. Chen, X. Wang, M. N. Hedhili, N. Wei, and H. N. Alshareef, "Highly stable supercapacitors with conducting polymer core-shell electrodes for energy storage applications," *Adv Energy Mater*, vol. 5, no. 8, Apr. 2015, doi: 10.1002/aenm.201401805.
- [50] J. B. Mitchell, W. C. Lo, A. Genc, J. Lebeau, and V. Augustyn, "Transition from Battery to Pseudocapacitor Behavior via Structural Water in Tungsten Oxide,"

- Chemistry of Materials, vol. 29, no. 9, pp. 3928–3937, May 2017, doi: 10.1021/acs.chemmater.6b05485.
- [51] S. Lou, Y. Zhao, J. Wang, G. Yin, C. Du, and X. Sun, “Ti-Based Oxide Anode Materials for Advanced Electrochemical Energy Storage: Lithium/Sodium Ion Batteries and Hybrid Pseudocapacitors,” *Small*, vol. 15, no. 52, pp. 1–44, 2019, doi: 10.1002/sml.201904740.
- [52] X. Hou et al., “Metal Organic Framework Derived Core-Shell Structured Co₉S₈@N-C@MoS₂ Nanocubes for Supercapacitor,” *ACS Appl Energy Mater*, vol. 1, no. 7, pp. 3513–3520, 2018, doi: 10.1021/acsaem.8b00773.
- [53] J. B. Cook et al., “Mesoporous MoS₂ as a Transition Metal Dichalcogenide Exhibiting Pseudocapacitive Li and Na-Ion Charge Storage,” *Adv Energy Mater*, vol. 6, no. 9, pp. 1–12, 2016, doi: 10.1002/aenm.201501937.
- [54] R. Wang et al., “Elucidating the Intercalation Pseudocapacitance Mechanism of MoS₂-Carbon Monolayer Interoverlapped Superstructure: Toward High-Performance Sodium-Ion-Based Hybrid Supercapacitor,” *ACS Appl Mater Interfaces*, vol. 9, no. 38, pp. 32745–32755, 2017, doi: 10.1021/acsami.7b09813.
- [55] E. Pomerantseva and Y. Gogotsi, “Two-dimensional heterostructures for energy storage,” *Nat Energy*, vol. 2, no. 7, Jul. 2017, doi: 10.1038/nenergy.2017.89.
- [56] A. M. Hashem et al., “Improvement of the electrochemical performance of nanosized α -MnO₂ used as cathode material for Li-batteries by Sn-doping,” *J Alloys Compd*, vol. 509, no. 40, pp. 9669–9674, Oct. 2011, doi: 10.1016/j.jallcom.2011.07.075.
- [57] X. Chen, Q. Su, J. Yu, M. Wei, G. Guo, and Y. Wang, “Experimental study on the degradation mechanism of LaCoO₃-based symmetric supercapacitors,” *RSC Adv*, vol. 11, no. 41, pp. 25170–25178, Jul. 2021, doi: 10.1039/d1ra03362j.
- [58] C. M. Julien and A. Mauger, “Nanostructured MnO₂ as electrode materials for energy storage,” *Nanomaterials*, vol. 7, no. 11. MDPI AG, Nov. 17, 2017. doi: 10.3390/nano7110396.

- [59] C. Zhong, Y. Deng, W. Hu, J. Qiao, L. Zhang, and J. Zhang, "A review of electrolyte materials and compositions for electrochemical supercapacitors," *Chemical Society Reviews*, vol. 44, no. 21. Royal Society of Chemistry, pp. 7484–7539, Nov. 07, 2015. doi: 10.1039/c5cs00303b.
- [60] A. M. Bittner et al., "Ageing of electrochemical double layer capacitors," *J Power Sources*, vol. 203, pp. 262–273, Apr. 2012, doi: 10.1016/j.jpowsour.2011.10.083.
- [61] C. Zhong, D. Sun, Y. Deng, W. Hu, J. Qiao, and J. Zhang, "Compatibility of electrolytes with inactive components of electrochemical supercapacitors," in *Electrolytes for Electrochemical Supercapacitors*, CRC Press, 2016, pp. 255–274. doi: 10.1201/b21497-4.
- [62] M. R. Palacín, P. Simon, and J. M. Tarascon, "Nanomaterials for Electrochemical Energy Storage: the Good and the Bad," *Acta Chim. Slov*, vol. 63, pp. 417–423, 2016, doi: 10.17344/acsi.2016.2314.
- [63] L. Mao, K. Zhang, H. S. On Chan, and J. Wu, "Nanostructured MnO₂/graphene composites for supercapacitor electrodes: The effect of morphology, crystallinity and composition," *J Mater Chem*, vol. 22, no. 5, pp. 1845–1851, Feb. 2012, doi: 10.1039/c1jm14503g.
- [64] J. B. Arnott and S. W. Donne, "Examining Manganese Dioxide," *J Electrochem Soc*, vol. 154, no. 8, p. A776, 2007, doi: 10.1149/1.2745643.
- [65] G. J. Browning and S. W. Donne, "Proton diffusion in γ -manganese dioxide," *J Appl Electrochem*, vol. 35, no. 9, pp. 871–878, Sep. 2005, doi: 10.1007/s10800-005-4738-1.
- [66] Y. G. Zhu, Y. Wang, Y. Shi, Z. X. Huang, L. Fu, and H. Y. Yang, "Phase transformation induced capacitance activation for 3D graphene-CoO nanorod pseudocapacitor," *Adv Energy Mater*, vol. 4, no. 9, pp. 1–8, Jun. 2014, doi: 10.1002/aenm.201301788.

- [67] S. Cheng et al., “Phase evolution of an alpha MnO₂-based electrode for pseudocapacitors probed by in operando Raman spectroscopy,” *Nano Energy*, vol. 9, pp. 161–167, 2014, doi: 10.1016/j.nanoen.2014.07.008.
- [68] Y. Mizuno et al., “Fabrication of LiCoO₂ crystal layers using a flux method and their application for additive-free lithium-ion rechargeable battery cathodes,” *Cryst Growth Des*, vol. 14, no. 4, pp. 1882–1887, Apr. 2014, doi: 10.1021/cg5000217.
- [69] C. Hu et al., “Carbon-Based Metal-Free Catalysts for Energy Storage and Environmental Remediation,” *Advanced Materials*, vol. 31, no. 13, pp. 1–14, Mar. 2019, doi: 10.1002/adma.201806128.
- [70] T. Purkait et al., “Electrochemically customized assembly of a hybrid xerogel material: Via combined covalent and non-covalent conjugation chemistry: An approach for boosting the cycling performance of pseudocapacitors,” *J Mater Chem A Mater*, vol. 8, no. 14, pp. 6740–6756, Apr. 2020, doi: 10.1039/d0ta02477e.
- [71] D. P. Dubal, G. S. Gund, R. Holze, and C. D. Lokhande, “Mild chemical strategy to grow micro-roses and micro-woolen like arranged CuO nanosheets for high performance supercapacitors,” *J Power Sources*, vol. 242, pp. 687–698, 2013, doi: 10.1016/j.jpowsour.2013.05.013.
- [72] D. P. Dubal, G. S. Gund, R. Holze, H. S. Jadhav, C. D. Lokhande, and C. J. Park, “Surfactant-assisted morphological tuning of hierarchical CuO thin films for electrochemical supercapacitors,” *Dalton Transactions*, vol. 42, no. 18, pp. 6459–6467, 2013, doi: 10.1039/c3dt50275a.
- [73] P. Simon and Y. Gogotsi, “Perspectives for electrochemical capacitors and related devices,” *Nature Materials*, vol. 19, no. 11. *Nature Research*, pp. 1151–1163, Nov. 01, 2020. doi: 10.1038/s41563-020-0747-z.
- [74] D. R. Rolison et al., “Multifunctional 3D nanoarchitectures for energy storage and conversion,” *Chem Soc Rev*, vol. 38, no. 1, pp. 226–252, Dec. 2009, doi: 10.1039/b801151f.

- [75] A. C. Nwanya et al., “Facile Synthesis of Nanosheet-like CuO Film and its Potential Application as a High-Performance Pseudocapacitor Electrode,” *Electrochim Acta*, vol. 198, pp. 220–230, Apr. 2016, doi: 10.1016/j.electacta.2016.03.064.
- [76] C. D. Lokhande, D. P. Dubal, and O. S. Joo, “Metal oxide thin film based supercapacitors,” *Current Applied Physics*, vol. 11, no. 3. Elsevier B.V., pp. 255–270, 2011. doi: 10.1016/j.cap.2010.12.001.
- [77] X. Zhang et al., “High-power and high-energy-density flexible pseudocapacitor electrodes made from porous CuO nanobelts and single-walled carbon nanotubes,” *ACS Nano*, vol. 5, no. 3, pp. 2013–2019, Mar. 2011, doi: 10.1021/nn1030719.
- [78] A. Vlad, N. Singh, J. Rolland, S. Melinte, P. M. Ajayan, and J. F. Gohy, “Hybrid supercapacitor-battery materials for fast electrochemical charge storage,” *Sci Rep*, vol. 4, Mar. 2014, doi: 10.1038/srep04315.
- [79] T. S. Mathis, N. Kurra, X. Wang, D. Pinto, P. Simon, and Y. Gogotsi, “Energy Storage Data Reporting in Perspective—Guidelines for Interpreting the Performance of Electrochemical Energy Storage Systems,” *Adv Energy Mater*, vol. 9, no. 39, pp. 1–13, 2019, doi: 10.1002/aenm.201902007.
- [80] D. P. Dubal et al., “Metal–Organic Framework (MOF) Derived Electrodes with Robust and Fast Lithium Storage for Li-Ion Hybrid Capacitors,” *Adv Funct Mater*, vol. 29, no. 19, 2019, doi: 10.1002/adfm.201900532.
- [81] T. Liu and Y. Li, “Addressing the Achilles’ heel of pseudocapacitive materials: Long-term stability,” *InfoMat*, vol. 2, no. 5. Blackwell Publishing Ltd, pp. 807–842, Sep. 01, 2020. doi: 10.1002/inf2.12105.
- [82] V. D. Patake, S. S. Joshi, C. D. Lokhande, and O. S. Joo, “Electrodeposited porous and amorphous copper oxide film for application in supercapacitor,” *Mater Chem Phys*, vol. 114, no. 1, pp. 6–9, Mar. 2009, doi: 10.1016/j.matchemphys.2008.09.031.
- [83] S. Ahankari, D. Lasrado, and R. Subramaniam, “Advances in materials and fabrication of separators in supercapacitors,” *Cite this: Mater. Adv*, vol. 3, p. 1472, 2022, doi: 10.1039/d1ma00599e.

- [84] Y. M. Shulga, S. A. Baskakov, V. A. Smirnov, N. Y. Shulga, K. G. Belay, and G. L. Gutsev, "Graphene oxide films as separators of polyaniline-based supercapacitors," *J Power Sources*, vol. 245, pp. 33–36, 2014, doi: 10.1016/j.jpowsour.2013.06.094.
- [85] C. G. Cameron, "Cold Temperature Optimization of Supercapacitors," *ECS Trans*, vol. 41, no. 22, pp. 121–132, May 2012, doi: 10.1149/1.3693068/XML.
- [86] D. Weingarh, A. Foelske-Schmitz, and R. Kötz, "Cycle versus voltage hold - Which is the better stability test for electrochemical double layer capacitors?," *J Power Sources*, vol. 225, pp. 84–88, Mar. 2013, doi: 10.1016/j.jpowsour.2012.10.019.
- [87] S. Wang et al., "Battery state estimation methods," *Battery System Modeling*, pp. 125–156, 2021, doi: 10.1016/B978-0-323-90472-8.00001-9.
- [88] J. Muñoz, A. K. Cuentas-Gallegos, M. Robles, A. Guillén-López, D. R. Lobato-Peralta, and J. E. Pascoe-Sussoni, "Lignin-Derived Materials for Supercapacitors," 2022.
- [89] I. Belenkaya, A. Matvienko, and A. Nemudry, "Ferroelasticity of SrCo_{0.8}Fe_{0.2}O_{3- δ} perovskite-related oxide with mixed ion-electron conductivity," *J Appl Crystallogr*, vol. 48, no. 1, pp. 179–188, Feb. 2015, doi: 10.1107/S1600576714027770.
- [90] K. Wang, L. Zhang, B. Ji, and J. Yuan, "The thermal analysis on the stackable supercapacitor," *Energy*, vol. 59, pp. 440–444, Sep. 2013, doi: 10.1016/j.energy.2013.07.064.
- [91] K. Wang, L. Li, H. Yin, T. Zhang, and W. Wan, "Thermal modelling analysis of spiral wound supercapacitor under constant-current cycling," *PLoS One*, vol. 10, no. 10, Oct. 2015, doi: 10.1371/journal.pone.0138672.
- [92] M. Boota and Y. Gogotsi, "MXene—Conducting Polymer Asymmetric Pseudocapacitors," *Adv Energy Mater*, vol. 9, no. 7, pp. 1–8, 2019, doi: 10.1002/aenm.201802917.

- [93] M. R. Lukatskaya et al., “Ultra-high-rate pseudocapacitive energy storage in two-dimensional transition metal carbides,” *Nat Energy*, vol. 2, no. 8, pp. 1–12, 2017, doi: 10.1038/nenergy.2017.105i.
- [94] S. E. Burkhardt et al., “Tailored redox functionality of small organics for pseudocapacitive electrodes,” *Energy Environ Sci*, vol. 5, no. 5, pp. 7176–7187, 2012, doi: 10.1039/c2ee21255b.
- [95] S.-C. Pang, M. A. Anderson, and T. W. Chapman, “Novel Electrode Materials for Thin-Film Ultracapacitors: Comparison of Electrochemical Properties of Sol-Gel-Derived and Electrodeposited Manganese Dioxide,” *J Electrochem Soc*, vol. 147, no. 2, p. 444, 2000, doi: 10.1149/1.1393216.
- [96] D. Titus, E. James Jebaseelan Samuel, and S. M. Roopan, *Nanoparticle characterization techniques*. Elsevier Inc., 2019. doi: 10.1016/b978-0-08-102579-6.00012-5.
- [97] J. Zhao and X. Liu, *Electron microscopic methods (TEM, SEM and energy dispersal spectroscopy)*, 2nd ed. Elsevier Ltd., 2022. doi: 10.1016/b978-0-12-822974-3.00013-6.
- [98] K. Malaie, M. R. Ganjali, T. Alizadeh, and P. Norouzi, “Hydrothermal growth of magnesium ferrite rose nanoflowers on Nickel foam; application in high-performance asymmetric supercapacitors,” *Journal of Materials Science: Materials in Electronics*, vol. 29, no. 1, pp. 650–657, 2018, doi: 10.1007/s10854-017-7958-3.
- [99] R. Dhilip Kumar, Y. Andou, M. Sathish, and S. Karuppuchamy, “Synthesis of nanostructured Cu-WO₃ and CuWO₄ for supercapacitor applications,” *Journal of Materials Science: Materials in Electronics*, vol. 27, no. 3, pp. 2926–2932, 2016, doi: 10.1007/s10854-015-4111-z.
- [100] R. D. Kumar, Y. Andou, and S. Karuppuchamy, “Microwave-assisted synthesis of Zn-WO₃ and ZnWO₄ for pseudocapacitor applications,” *Journal of Physics and Chemistry of Solids*, vol. 92, pp. 94–99, 2016, doi: 10.1016/j.jpccs.2016.01.022.

- [101] J. Xie, X. Sun, N. Zhang, K. Xu, M. Zhou, and Y. Xie, "Layer-by-layer B-Ni(OH)₂/graphene nanohybrids for ultraflexible all-solid-state thin-film supercapacitors with high electrochemical performance," *Nano Energy*, vol. 2, no. 1, pp. 65–74, 2013, doi: 10.1016/j.nanoen.2012.07.016.
- [102] C. Colpitts and A. Kiani, "Synthesis of bioactive three-dimensional silicon-oxide nanofibrous structures on the silicon substrate for bionic devices' fabrication," *Nanomaterials and Nanotechnology*, vol. 6, no. 1, 2016, doi: 10.5772/62312.
- [103] T. Li, X. Z. Yuan, L. Zhang, D. Song, K. Shi, and C. Bock, "Degradation Mechanisms and Mitigation Strategies of Nickel-Rich NMC-Based Lithium-Ion Batteries," *Electrochemical Energy Reviews*, vol. 3, no. 1. Springer Science and Business Media B.V., pp. 43–80, Mar. 01, 2020. doi: 10.1007/s41918-019-00053-3.
- [104] Y. Wang, Y. Song, and Y. Xia, "Electrochemical capacitors: Mechanism, materials, systems, characterization and applications," *Chem Soc Rev*, vol. 45, no. 21, pp. 5925–5950, 2016, doi: 10.1039/c5cs00580a.
- [105] L. A. Bromberg, J. Xia, R. Rooney, and N. Dimitrov, "Enhanced adhesion of continuous nanoporous Au layers by thermochemical oxidation of glassy carbon," *Coatings*, vol. 4, no. 3, pp. 416–432, 2014, doi: 10.3390/coatings4030416.
- [106] M. Toupin, T. Brousse, and D. Bélanger, "Charge storage mechanism of MnO₂ electrode used in aqueous electrochemical capacitor," *Chemistry of Materials*, vol. 16, no. 16, pp. 3184–3190, 2004, doi: 10.1021/cm049649j.
- [107] E. Miniach and G. Gryglewicz, "Solvent-controlled morphology of bismuth sulfide for supercapacitor applications," *J Mater Sci*, vol. 53, no. 24, pp. 16511–16523, 2018, doi: 10.1007/s10853-018-2785-3.
- [108] R. Bolagam, R. Boddula, and P. Srinivasan, "One-step preparation of sulfonated carbon and subsequent preparation of hybrid material with polyaniline salt: a promising supercapacitor electrode material," *Journal of Solid State*

Electrochemistry, vol. 21, no. 5, pp. 1313–1322, May 2017, doi: 10.1007/s10008-016-3487-x.

- [109] P. Asen and S. Shahrokhian, “A High Performance Supercapacitor Based on Graphene/Polypyrrole/Cu₂O-Cu(OH)₂ Ternary Nanocomposite Coated on Nickel Foam,” *Journal of Physical Chemistry C*, vol. 121, no. 12, pp. 6508–6519, 2017, doi: 10.1021/acs.jpcc.7b00534.
- [110] A. Ehsani, A. A. Heidari, and H. M. Shiri, “Electrochemical Pseudocapacitors Based on Ternary Nanocomposite of Conductive Polymer/Graphene/Metal Oxide: An Introduction and Review to it in Recent Studies,” *Chemical Record*, vol. 19, no. 5, pp. 908–926, 2019, doi: 10.1002/tcr.201800112.
- [111] H. Wang et al., “In situ NMR spectroscopy of supercapacitors: Insight into the charge storage mechanism,” *J Am Chem Soc*, vol. 135, no. 50, pp. 18968–18980, 2013, doi: 10.1021/ja410287s.
- [112] J. M. Griffin, A. C. Forse, W. Y. Tsai, P. L. Taberna, P. Simon, and C. P. Grey, “In situ NMR and electrochemical quartz crystal microbalance techniques reveal the structure of the electrical double layer in supercapacitors,” *Nat Mater*, vol. 14, no. 8, pp. 812–819, 2015, doi: 10.1038/nmat4318.
- [113] K. Selvaraj et al., “Supercapacitor and high k properties of CNT-PbS reinforced quinoxaline amine based polybenzoxazine composites,” *Soft Matter*, vol. 18, no. 46, pp. 8779–8791, Oct. 2022, doi: 10.1039/d2sm00737a.
- [114] H. B. Li et al., “Amorphous nickel hydroxide nanospheres with ultrahigh capacitance and energy density as electrochemical pseudocapacitor materials,” *Nat Commun*, vol. 4, no. May, pp. 1–7, 2013, doi: 10.1038/ncomms2932.
- [115] M. Khot and A. Kiani, “Synthesis of self-grown nanostructured NiO via pulse ionization for binderless pseudocapacitor electrode,” *J Energy Storage*, vol. 55, Nov. 2022, doi: 10.1016/j.est.2022.105779.
- [116] S. A. Ebrahim, M. E. Harb, M. M. Soliman, and M. B. Tayel, “Preparation and characterization of a pseudocapacitor electrode by spraying a conducting polymer

- onto a flexible substrate,” *Journal of Taibah University for Science*, vol. 10, no. 2, pp. 281–285, 2016, doi: 10.1016/j.jtusci.2015.07.004.
- [117] A. Sumboja, C. Y. Foo, J. Yan, C. Yan, R. K. Gupta, and P. S. Lee, “Significant electrochemical stability of manganese dioxide/polyaniline coaxial nanowires by self-terminated double surfactant polymerization for pseudocapacitor electrode,” *J Mater Chem*, vol. 22, no. 45, pp. 23921–23928, Dec. 2012, doi: 10.1039/c2jm32456c.
- [118] H. Xia et al., “Hierarchically Structured Co_3O_4 @Pt@ MnO_2 Nanowire Arrays for High-Performance Supercapacitors,” *Sci Rep*, vol. 3, Oct. 2013, doi: 10.1038/srep02978.
- [119] A. Bello et al., “High-performance symmetric electrochemical capacitor based on graphene foam and nanostructured manganese oxide,” *AIP Adv*, vol. 3, no. 8, Aug. 2013, doi: 10.1063/1.4819270.
- [120] A. Sumboja, C. Y. Foo, J. Yan, C. Yan, R. K. Gupta, and P. S. Lee, “Electronic Supporting Information (ESI) for Significant Electrochemical Stability of Manganese Dioxide/Polyaniline Coaxial Nanowires by Self-Terminated Double Surfactant Polymerization for Pseudocapacitor Electrode,” 2012.
- [121] A. Gholami and A. Kiani, “Laser-induced nanofibrous titania film electrode: A new approach for energy storage materials,” *J Energy Storage*, vol. 31, Oct. 2020, doi: 10.1016/j.est.2020.101654.
- [122] G. Wang, L. Zhang, and J. Zhang, “A review of electrode materials for electrochemical supercapacitors,” *Chem Soc Rev*, vol. 41, no. 2, pp. 797–828, 2012, doi: 10.1039/c1cs15060j.
- [123] I. Lesov, S. Tcholakova, M. Kovadjieva, T. Saison, M. Lamblet, and N. Denkov, “Role of Pickering stabilization and bulk gelation for the preparation and properties of solid silica foams,” *J Colloid Interface Sci*, vol. 504, pp. 48–57, 2017, doi: 10.1016/j.jcis.2017.05.036.

- [124] W. Wang, Q. Hao, W. Lei, X. Xia, and X. Wang, "Graphene/SnO₂/polypyrrole ternary nanocomposites as supercapacitor electrode materials," *RSC Adv*, vol. 2, no. 27, pp. 10268–10274, 2012, doi: 10.1039/c2ra21292g.
- [125] P. Asen, S. Shahrokhian, and A. Irajizad, "One step electrodeposition of V₂O₅/polypyrrole/graphene oxide ternary nanocomposite for preparation of a high performance supercapacitor," vol. 42, no. 33, 2017. doi: 10.1016/j.ijhydene.2017.07.008.
- [126] V. Aranganathan and A. Nityananda Shetty, "Synthesis and characterization of reduced- graphene oxide/ nickel oxide/ polyaniline ternary nanocomposites for supercapacitors.," *Mater Today Proc*, vol. 5, no. 2, pp. 8852–8861, 2018, doi: 10.1016/j.matpr.2017.12.317.
- [127] W. Sun, R. Zheng, and X. Chen, "Symmetric redox supercapacitor based on micro-fabrication with three-dimensional polypyrrole electrodes," *J Power Sources*, vol. 195, no. 20, pp. 7120–7125, 2010, doi: 10.1016/j.jpowsour.2010.05.012.
- [128] C. Xu, L. Wu, S. Hu, H. Xie, and X. Zhang, "A Heavily Surface-Doped Polymer with the Bifunctional Catalytic Mechanism in Li-O₂ Batteries," *iScience*, vol. 14, pp. 312–322, 2019, doi: 10.1016/j.isci.2019.03.016.
- [129] R. Bolagam, R. Boddula, and P. Srinivasan, "Synthesis of highly crystalline polyaniline with the use of (Cyclohexylamino)-1-propanesulfonic acid for supercapacitor," *J Appl Electrochem*, vol. 45, no. 1, pp. 51–56, 2015, doi: 10.1007/s10800-014-0753-4.
- [130] M. R. Hasyim and R. Rajagopalan, "Prediction of Discharge Performances of Pseudocapacitors Using Their Impedance Characteristics," *J Electrochem Soc*, vol. 167, no. 1, p. 013536, 2020, doi: 10.1149/1945-7111/ab6722.
- [131] G. Han et al., "Sandwich-structured MnO₂/polypyrrole/reduced graphene oxide hybrid composites for high-performance supercapacitors," *RSC Adv*, vol. 4, no. 20, pp. 9898–9904, 2014, doi: 10.1039/c3ra47764a.

- [132] K. Makgopa et al., “A high-rate aqueous symmetric pseudocapacitor based on highly graphitized onion-like carbon/birnessite-type manganese oxide nanohybrids,” *J Mater Chem A Mater*, vol. 3, no. 7, pp. 3480–3490, Feb. 2015, doi: 10.1039/c4ta06715k.
- [133] H. Peng et al., “Hierarchical MoS₂-Coated V₂O₃ composite nanosheet tubes as both the cathode and anode materials for pseudocapacitors,” *Electrochim Acta*, vol. 277, pp. 218–225, 2018, doi: 10.1016/j.electacta.2018.04.219.
- [134] S. M. Jung, D. J. Preston, H. Y. Jung, Z. Deng, E. N. Wang, and J. Kong, “Porous Cu Nanowire Aerosponges from One-Step Assembly and their Applications in Heat Dissipation,” *Advanced Materials*, vol. 28, no. 7, pp. 1413–1419, 2016, doi: 10.1002/adma.201504774.
- [135] Y. C. Chen et al., “Structurally Deformed MoS₂ for Electrochemically Stable, Thermally Resistant, and Highly Efficient Hydrogen Evolution Reaction,” *Advanced Materials*, vol. 29, no. 44, pp. 1–11, 2017, doi: 10.1002/adma.201703863.
- [136] Y. Yang et al., “The Role of Geometric Sites in 2D Materials for Energy Storage,” *Joule*, vol. 2, no. 6, pp. 1075–1094, 2018, doi: 10.1016/j.joule.2018.04.027.
- [137] K. H. Shin et al., “Biomimetic composite architecture achieves ultrahigh rate capability and cycling life of sodium ion battery cathodes,” *Appl Phys Rev*, vol. 7, no. 4, 2020, doi: 10.1063/5.0020805.
- [138] M. S. Javed et al., “High performance solid state flexible supercapacitor based on molybdenum sulfide hierarchical nanospheres,” *J Power Sources*, vol. 285, pp. 63–69, 2015, doi: 10.1016/j.jpowsour.2015.03.079.
- [139] B. Radisavljevic and A. Kis, “Mobility engineering and a metal-insulator transition in monolayer MoS₂,” *Nat Mater*, vol. 12, no. 9, pp. 815–820, 2013, doi: 10.1038/nmat3687.
- [140] P. Roy, S. Berger, and P. Schmuki, “TiO₂ nanotubes: Synthesis and applications,” *Angewandte Chemie - International Edition*, vol. 50, no. 13, pp. 2904–2939, 2011, doi: 10.1002/anie.201001374.

- [141] C. Wang, K. Adair, and X. Sun, "All-Solid-State Lithium Metal Batteries with Sulfide Electrolytes: Understanding Interfacial Ion and Electron Transport," *Acc Mater Res*, vol. 3, no. 1, pp. 21–32, 2022, doi: 10.1021/accountsmr.1c00137.
- [142] Y. Sun et al., "A Novel Organic 'Polyurea' Thin Film for Ultralong-Life Lithium-Metal Anodes via Molecular-Layer Deposition," *Advanced Materials*, vol. 31, no. 4, pp. 1–9, 2019, doi: 10.1002/adma.201806541.
- [143] Y. Zhao et al., "Natural SEI-Inspired Dual-Protective Layers via Atomic/Molecular Layer Deposition for Long-Life Metallic Lithium Anode," *Matter*, vol. 1, no. 5, pp. 1215–1231, 2019, doi: 10.1016/j.matt.2019.06.020.
- [144] H. Wang et al., "Atomic Layer Deposition of Amorphous TiO₂ on Carbon Nanotube Networks and Their Superior Li and Na Ion Storage Properties," *Adv Mater Interfaces*, vol. 3, no. 21, 2016, doi: 10.1002/admi.201600375.
- [145] Y. T. Weng et al., "Spatially Confined MnO₂ Nanostructure Enabling Consecutive Reversible Charge Transfer from Mn(IV) to Mn(II) in a Mixed Pseudocapacitor-Battery Electrode," *Adv Energy Mater*, vol. 5, no. 18, pp. 1–10, 2015, doi: 10.1002/aenm.201500772.
- [146] K. W. Nam, M. G. Kim, and K. B. Kim, "In situ Mn K-edge X-ray absorption spectroscopy studies of electrodeposited manganese oxide films for electrochemical capacitors," *Journal of Physical Chemistry C*, vol. 111, no. 2, pp. 749–758, 2007, doi: 10.1021/jp063130o.
- [147] F. Ataherian and N. L. Wu, "1.2 Volt manganese oxide symmetric supercapacitor," *Electrochem Commun*, vol. 13, no. 11, pp. 1264–1267, 2011, doi: 10.1016/j.elecom.2011.08.028.
- [148] M. Kim and J. Kim, "Redox deposition of birnessite-type manganese oxide on silicon carbide microspheres for use as supercapacitor electrodes," *ACS Appl Mater Interfaces*, vol. 6, no. 12, pp. 9036–9045, 2014, doi: 10.1021/am406032y.

- [149] L. bo Jiang, X. zhong Yuan, J. Liang, J. Zhang, H. Wang, and G. ming Zeng, “Nanostructured core-shell electrode materials for electrochemical capacitors,” *J Power Sources*, vol. 331, pp. 408–425, 2016, doi: 10.1016/j.jpowsour.2016.09.054.
- [150] Y. Fang, B. Y. Guan, D. Luan, and X. W. (David) Lou, “Synthesis of CuS@CoS₂ Double-Shelled Nanoboxes with Enhanced Sodium Storage Properties,” *Angewandte Chemie - International Edition*, vol. 58, no. 23, pp. 7739–7743, Jun. 2019, doi: 10.1002/anie.201902583.
- [151] Z. Shi, S. Wei, H. Zuo, M. Huang, J. Shi, and H. Wang, “Boosting capacitance and energy density by construction NiCoO₂/CoS₂ nanocomposites arrays as pseudocapacitor,” *J Alloys Compd*, vol. 881, 2021, doi: 10.1016/j.jallcom.2021.160627.
- [152] T. F. Yi, P. P. Peng, X. Han, Y. R. Zhu, and S. Luo, “Interconnected Co₃O₄@CoNiO₂@PPy nanorod and nanosheet composite grown on nickel foam as binder-free electrodes for Li-ion batteries,” *Solid State Ion*, vol. 329, no. October 2018, pp. 131–139, 2019, doi: 10.1016/j.ssi.2018.12.002.
- [153] M. Gao et al., “Core-shell Cu_{2-x}S @ CoS₂ heterogeneous nanowire array with superior electrochemical performance for supercapacitor application,” *Electrochim Acta*, vol. 323, p. 134839, 2019, doi: 10.1016/j.electacta.2019.134839.
- [154] Y. G. Zhu et al., “Design and synthesis of NiO nanoflakes/graphene nanocomposite as high performance electrodes of pseudocapacitor,” *RSC Adv*, vol. 3, no. 42, pp. 19409–19415, 2013, doi: 10.1039/c3ra42091d.
- [155] M. Zhi, C. Xiang, J. Li, M. Li, and N. Wu, “Nanostructured carbon-metal oxide composite electrodes for supercapacitors: A review,” *Nanoscale*, vol. 5, no. 1, pp. 72–88, Jan. 2013, doi: 10.1039/c2nr32040a.
- [156] M. S. Wu, Y. P. Lin, C. H. Lin, and J. T. Lee, “Formation of nano-scaled crevices and spacers in NiO-attached graphene oxide nanosheets for supercapacitors,” *J Mater Chem*, vol. 22, no. 6, pp. 2442–2448, Feb. 2012, doi: 10.1039/c1jm13818a.

- [157] K. Lota, A. Sierczynska, and G. Lota, “Supercapacitors Based on Nickel Oxide/Carbon Materials Composites,” *International Journal of Electrochemistry*, vol. 2011, pp. 1–6, 2011, doi: 10.4061/2011/321473.
- [158] S. Wu, K. K. Hui, K. K. Hui, K. Ho Kim, and K. San Hui, “Ultrathin porous NiO nanoflake arrays on nickel foam as an advanced electrode for high performance asymmetric supercapacitors,” pp. 1–9, 2016.
- [159] V. Ganesh, S. Pitchumani, and V. Lakshminarayanan, “New symmetric and asymmetric supercapacitors based on high surface area porous nickel and activated carbon,” *J Power Sources*, vol. 158, no. 2 SPEC. ISS., pp. 1523–1532, Aug. 2006, doi: 10.1016/j.jpowsour.2005.10.090.
- [160] X. Liu et al., “Heterostructured Co-NTC@Co₃S₄ as an anode material for asymmetric pseudocapacitors,” *CrystEngComm*, vol. 24, no. 19, pp. 3621–3629, 2022, doi: 10.1039/d2ce00300g.
- [161] T. T. Nguyen, J. Balamurugan, N. H. Kim, and J. H. Lee, “Hierarchical 3D Zn-Ni-P nanosheet arrays as an advanced electrode for high-performance all-solid-state asymmetric supercapacitors,” *J Mater Chem A Mater*, vol. 6, no. 18, pp. 8669–8681, 2018, doi: 10.1039/c8ta01184b.
- [162] W. Kukułka, K. Kierzek, N. Stankiewicz, X. Chen, T. Tang, and E. Mijowska, “Well-Designed Porous Graphene Flakes for Lithium-Ion Batteries with Outstanding Rate Performance,” *Langmuir*, vol. 35, no. 39, pp. 12613–12619, Oct. 2019, doi: 10.1021/acs.langmuir.8b03477.
- [163] J. Zhang, T. Zhang, D. Yu, K. Xiao, and Y. Hong, “Transition from ZIF-L-Co to ZIF-67: A new insight into the structural evolution of zeolitic imidazolate frameworks (ZIFs) in aqueous systems,” *CrystEngComm*, vol. 17, no. 43, pp. 8212–8215, 2015, doi: 10.1039/c5ce01531f.
- [164] I. Jeong, D. Y. Han, J. Hwang, W. J. Song, and S. Park, “Foldable batteries: from materials to devices,” *Nanoscale Advances*, vol. 4, no. 6. Royal Society of Chemistry, pp. 1494–1516, Feb. 03, 2022. doi: 10.1039/d1na00892g.

- [165] G. Ma et al., "High-performance aqueous asymmetric supercapacitor based on $\text{K}_0.3\text{WO}_3$ nanorods and nitrogen-doped porous carbon," *J Power Sources*, vol. 330, pp. 219–230, Oct. 2016, doi: 10.1016/j.jpowsour.2016.09.022.
- [166] H. Xie et al., "3D nitrogen-doped graphene/ $\text{Co}(\text{OH})_2$ -nanoplate composites for high-performance electrochemical pseudocapacitors," *RSC Adv*, vol. 4, no. 106, pp. 61753–61758, 2014, doi: 10.1039/c4ra10333e.
- [167] L. Jiang and Z. Fan, "Design of advanced porous graphene materials: From graphene nanomesh to 3D architectures," *Nanoscale*, vol. 6, no. 4, pp. 1922–1945, Feb. 21, 2014. doi: 10.1039/c3nr04555b.
- [168] H. Wang, H. S. Casalongue, Y. Liang, and H. Dai, " $\text{Ni}(\text{OH})_2$ nanoplates grown on graphene as advanced electrochemical pseudocapacitor materials," *J Am Chem Soc*, vol. 132, no. 21, pp. 7472–7477, Jun. 2010, doi: 10.1021/ja102267j.
- [169] J. S. Lee, S. I. Kim, J. C. Yoon, and J. H. Jang, "Chemical vapor deposition of mesoporous graphene nanoballs for supercapacitor," *ACS Nano*, vol. 7, no. 7, pp. 6047–6055, Jul. 2013, doi: 10.1021/nn401850z.
- [170] Z. Niu, J. Chen, H. H. Hng, J. Ma, and X. Chen, "A leavening strategy to prepare reduced graphene oxide foams," *Advanced Materials*, vol. 24, no. 30, pp. 4144–4150, Aug. 2012, doi: 10.1002/adma.201200197.
- [171] X. Cao, Z. Yin, and H. Zhang, "Three-dimensional graphene materials: Preparation, structures and application in supercapacitors," *Energy and Environmental Science*, vol. 7, no. 6. Royal Society of Chemistry, pp. 1850–1865, 2014. doi: 10.1039/c4ee00050a.
- [172] Y. Meng et al., "All-graphene core-sheath microfibers for all-solid-state, stretchable fibriform supercapacitors and wearable electronic textiles," *Advanced Materials*, vol. 25, no. 16, pp. 2326–2331, Apr. 2013, doi: 10.1002/adma.201300132.
- [173] H. Yoon, "Current trends in sensors based on conducting polymer nanomaterials," *Nanomaterials*, vol. 3, no. 3, pp. 524–549, Sep. 2013, doi: 10.3390/nano3030524.

- [174] T. Liu et al., “Polyaniline and polypyrrole pseudocapacitor electrodes with excellent cycling stability,” *Nano Lett*, vol. 14, no. 5, pp. 2522–2527, 2014, doi: 10.1021/nl500255v.
- [175] H. Wang, J. Lin, and Z. X. Shen, “Polyaniline (PANi) based electrode materials for energy storage and conversion,” *Journal of Science: Advanced Materials and Devices*, vol. 1, no. 3. Elsevier B.V., pp. 225–255, Sep. 01, 2016. doi: 10.1016/j.jsamd.2016.08.001.
- [176] T. Liu et al., “Supporting Information Polyaniline and Polypyrrole Pseudocapacitor Electrodes with Excellent Cycling Stability,” pp. 1–11.
- [177] Z. S. Wu, G. Zhou, L. C. Yin, W. Ren, F. Li, and H. M. Cheng, “Graphene/metal oxide composite electrode materials for energy storage,” *Nano Energy*, vol. 1, no. 1. pp. 107–131, Jan. 2012. doi: 10.1016/j.nanoen.2011.11.001.
- [178] S. Im et al., “Nanoparticle intercalation-induced interlayer-gap-opened graphene–polyaniline nanocomposite for enhanced supercapacitive performances,” *Appl Surf Sci*, vol. 412, pp. 160–169, 2017, doi: 10.1016/j.apsusc.2017.03.282.
- [179] X. Liu et al., “Three-dimensional and stable polyaniline-grafted graphene hybrid materials for supercapacitor electrodes,” *J Mater Chem A Mater*, vol. 2, no. 37, pp. 15273–15278, Oct. 2014, doi: 10.1039/c4ta03077j.
- [180] Q. Hao, X. Xia, W. Lei, W. Wang, and J. Qiu, “Facile synthesis of sandwich-like polyaniline/boron-doped graphene nano hybrid for supercapacitors,” *Carbon N Y*, vol. 81, no. 1, pp. 552–563, 2015, doi: 10.1016/j.carbon.2014.09.090.
- [181] F. Liu, S. Song, D. Xue, and H. Zhang, “Folded structured graphene paper for high performance electrode materials,” *Advanced Materials*, vol. 24, no. 8, pp. 1089–1094, Feb. 2012, doi: 10.1002/adma.201104691.
- [182] T. G. Yun et al., “All-Transparent Stretchable Electrochromic Supercapacitor Wearable Patch Device,” *ACS Nano*, vol. 13, no. 3, pp. 3141–3150, 2019, doi: 10.1021/acsnano.8b08560.

- [183] X. Cheng, J. Pan, Y. Zhao, M. Liao, and H. Peng, “Gel Polymer Electrolytes for Electrochemical Energy Storage,” *Advanced Energy Materials*, vol. 8, no. 7. Wiley-VCH Verlag, Mar. 05, 2018. doi: 10.1002/aenm.201702184.
- [184] Y. Huang et al., “An Intrinsically Stretchable and Compressible Supercapacitor Containing a Polyacrylamide Hydrogel Electrolyte,” *Angewandte Chemie*, vol. 129, no. 31, pp. 9269–9273, Jul. 2017, doi: 10.1002/ange.201705212.
- [185] X. Zhang, M. Kar, T. C. Mendes, Y. Wu, and D. R. MacFarlane, “Supported Ionic Liquid Gel Membrane Electrolytes for Flexible Supercapacitors,” *Adv Energy Mater*, vol. 8, no. 15, May 2018, doi: 10.1002/aenm.201702702.
- [186] X. Peng et al., “A zwitterionic gel electrolyte for efficient solid-state supercapacitors,” *Nat Commun*, vol. 7, no. May, pp. 1–8, 2016, doi: 10.1038/ncomms11782.
- [187] British Petroleum, “Energy Outlook 2020,” *BP Energy Outlook 2030, Statistical Review*. London: British Petroleum., p. 81, 2020, [Online]. Available: <https://www.bp.com/content/dam/bp/business-sites/en/global/corporate/pdfs/energy-economics/energy-outlook/bp-energy-outlook-2020.pdf>
- [188] K. Popham, “Transportation electrification,” *Smart Cities: Applications, Technologies, Standards, and Driving Factors*, no. January, pp. 109–122, 2017, doi: 10.1007/978-3-319-59381-4-7.
- [189] R. Zhang and S. Fujimori, “The role of transport electrification in global climate change mitigation scenarios,” *Environmental Research Letters*, vol. 15, no. 3, 2020, doi: 10.1088/1748-9326/ab6658.
- [190] IRENA, “Global Renewables Outlook: Energy transformation 2050,” 2020. [Online]. Available: <https://www.irena.org/publications/2020/Apr/Global-Renewables-Outlook-2020>

- [191] É. Latulippe and K. Mo, Outlook for Electric Vehicles and Implications for the Oil Market. 2019, pp. 1–10. [Online]. Available: <https://www.bankofcanada.ca/wp-content/uploads/2019/06/san2019-19.pdf>
- [192] National Resources Canada, “Electric Vehicle Technology Roadmap for Canada: A strategic vision for highway-capable battery-electric, plug-in and other hybrid-electric vehicles,” Natural resources Canada, vol. 1, no. 1, pp. 1–71, 2010.
- [193] Z. Li, J. Huang, B. Yann Liaw, V. Metzler, and J. Zhang, “A review of lithium deposition in lithium-ion and lithium metal secondary batteries,” *J Power Sources*, vol. 254, pp. 168–182, 2014, doi: 10.1016/j.jpowsour.2013.12.099.
- [194] G. Pistoia and B. Liaw, *Green Energy and Technology Behaviour of Lithium-Ion Batteries in Electric Vehicles; Battery Health, Performance, Safety, and Cost*. Springer International Publishing AG, 2017. doi: <https://doi.org/10.1007/978-3-319-69950-9>.
- [195] M. Dubarry, G. Baure, and A. Devie, “Durability and reliability of EV batteries under electric utility grid operations: Path dependence of battery degradation,” *J Electrochem Soc*, vol. 165, no. 5, pp. A773–A783, 2018, doi: 10.1149/2.0421805jes.
- [196] Z. Ma, J. Jiang, W. Shi, W. Zhang, and C. C. Mi, “Investigation of path dependence in commercial lithium-ion cells for pure electric bus applications: Aging mechanism identification,” *J Power Sources*, vol. 274, pp. 29–40, Jan. 2015, doi: 10.1016/j.jpowsour.2014.10.006.
- [197] N. Nitta, F. Wu, J. T. Lee, and G. Yushin, “Li-ion battery materials: Present and future,” *Materials Today*, vol. 18, no. 5, pp. 252–264, 2015, doi: 10.1016/j.mattod.2014.10.040.
- [198] G. Pistoia et al., *Lithium-Ion Batteries Advances and Applications*. Elsevier B.V, 2014. doi: <http://dx.doi.org/10.1016/B978-0-444-59513-3.00001-7>.
- [199] A. Mishra et al., “Electrode materials for lithium-ion batteries,” *Mater Sci Energy Technol*, vol. 1, no. 2, pp. 182–187, 2018, doi: 10.1016/j.mset.2018.08.001.

- [200] S. Goriparti, E. Miele, F. De Angelis, E. Di Fabrizio, R. Proietti Zaccaria, and C. Capiglia, “Review on recent progress of nanostructured anode materials for Li-ion batteries,” *J Power Sources*, vol. 257, pp. 421–443, 2014, doi: 10.1016/j.jpowsour.2013.11.103.
- [201] B. Xu, D. Qian, Z. Wang, and Y. S. Meng, “Recent progress in cathode materials research for advanced lithium ion batteries,” *Materials Science and Engineering R: Reports*, vol. 73, no. 5–6, pp. 51–65, 2012, doi: 10.1016/j.mser.2012.05.003.
- [202] E. R. Logan and J. R. Dahn, “Electrolyte Design for Fast-Charging Li-Ion Batteries,” *Trends Chem*, vol. 2, no. 4, pp. 354–366, 2020, doi: 10.1016/j.trechm.2020.01.011.
- [203] A. Tomaszewska et al., “Lithium-ion battery fast charging: A review,” *eTransportation*, vol. 1, no. August, p. 100011, 2019, doi: 10.1016/j.etrans.2019.100011.
- [204] T. R. Jow, S. A. Delp, J. L. Allen, J.-P. Jones, and M. C. Smart, “Factors Limiting Li + Charge Transfer Kinetics in Li-Ion Batteries ,” *J Electrochem Soc*, vol. 165, no. 2, pp. A361–A367, 2018, doi: 10.1149/2.1221802jes.
- [205] Q. Liu et al., “Understanding undesirable anode lithium plating issues in lithium-ion batteries,” *RSC Adv*, vol. 6, no. 91, pp. 88683–88700, 2016, doi: 10.1039/c6ra19482f.
- [206] T. Waldmann, B. I. Hogg, and M. Wohlfahrt-Mehrens, “Li plating as unwanted side reaction in commercial Li-ion cells – A review,” *J Power Sources*, vol. 384, no. November 2017, pp. 107–124, 2018, doi: 10.1016/j.jpowsour.2018.02.063.
- [207] K. Xu, A. Von Cresce, and U. Lee, “Differentiating contributions to ‘ion transfer’ barrier from interphasial resistance and Li+ desolvation at electrolyte/graphite interface,” *Langmuir*, vol. 26, no. 13, pp. 11538–11543, 2010, doi: 10.1021/la1009994.

- [208] Y. Yamada, Y. Iriyama, T. Abe, and Z. Ogumi, “Kinetics of lithium ion transfer at the interface between graphite and liquid electrolytes: effects of solvent and surface film,” *Langmuir*, vol. 25, no. 21, pp. 12766–12770, 2009, doi: 10.1021/la901829v.
- [209] C. Pastor-Fernández, K. Uddin, G. H. Chouchelamane, W. D. Widanage, and J. Marco, “A Comparison between Electrochemical Impedance Spectroscopy and Incremental Capacity-Differential Voltage as Li-ion Diagnostic Techniques to Identify and Quantify the Effects of Degradation Modes within Battery Management Systems,” *J Power Sources*, vol. 360, pp. 301–318, 2017, doi: 10.1016/j.jpowsour.2017.03.042.
- [210] M. Ouyang et al., “Low temperature aging mechanism identification and lithium deposition in a large format lithium iron phosphate battery for different charge profiles,” *J Power Sources*, vol. 286, pp. 309–320, Jul. 2015, doi: 10.1016/j.jpowsour.2015.03.178.
- [211] J. Vetter et al., “Ageing mechanisms in lithium-ion batteries,” *J Power Sources*, vol. 147, no. 1–2, pp. 269–281, 2005, doi: 10.1016/j.jpowsour.2005.01.006.
- [212] V. Agubra and J. Fergus, “Lithium ion battery anode aging mechanisms,” *Materials*, vol. 6, no. 4, pp. 1310–1325, 2013. doi: 10.3390/ma6041310.
- [213] T. R. Tanim et al., “Extreme Fast Charge Challenges for Lithium-Ion Battery: Variability and Positive Electrode Issues,” *J Electrochem Soc*, vol. 166, no. 10, pp. A1926–A1938, 2019, doi: 10.1149/2.0731910jes.
- [214] C. Birkenmaier, B. Bitzer, M. Harzheim, A. Hintennach, and T. Schleid, “Lithium plating on graphite negative electrodes: Innovative qualitative and quantitative investigation methods,” *J Electrochem Soc*, vol. 162, no. 14, pp. A2646–A2650, 2015, doi: 10.1149/2.0451514jes.
- [215] N. Legrand, B. Knosp, P. Desprez, F. Lapticque, and S. Raël, “Physical characterization of the charging process of a Li-ion battery and prediction of Li plating by electrochemical modelling,” *J Power Sources*, vol. 245, pp. 208–216, 2014, doi: 10.1016/j.jpowsour.2013.06.130.

- [216] C. Pastor-Fernández, T. Bruen, W. D. Widanage, M. A. Gama-Valdez, and J. Marco, “A Study of Cell-to-Cell Interactions and Degradation in Parallel Strings: Implications for the Battery Management System,” *J Power Sources*, vol. 329, pp. 574–585, 2016, doi: 10.1016/j.jpowsour.2016.07.121.
- [217] M. Dubarry, C. Truchot, and B. Y. Liaw, “Synthesize battery degradation modes via a diagnostic and prognostic model,” *J Power Sources*, vol. 219, pp. 204–216, 2012, doi: 10.1016/j.jpowsour.2012.07.016.
- [218] J. S. Edge et al., “Lithium ion battery degradation: what you need to know,” *Physical Chemistry Chemical Physics*, vol. 23, no. 14, pp. 8200–8221, Apr. 2021, doi: 10.1039/D1CP00359C.
- [219] B. V. Ratnakumar and M. C. Smart, “Lithium plating behavior in lithium-ion cells,” *ECS Trans*, vol. 25, no. 36, pp. 241–252, 2010, doi: 10.1149/1.3393860.
- [220] C. R. Birkl, M. R. Roberts, E. McTurk, P. G. Bruce, and D. A. Howey, “Degradation diagnostics for lithium ion cells,” *J Power Sources*, vol. 341, pp. 373–386, Feb. 2017, doi: 10.1016/j.jpowsour.2016.12.011.
- [221] X. Lin, J. Park, L. Liu, Y. Lee, A. M. Sastry, and W. Lu, “A Comprehensive Capacity Fade Model and Analysis for Li-Ion Batteries,” *J Electrochem Soc*, vol. 160, no. 10, pp. A1701–A1710, 2013, doi: 10.1149/2.040310jes.
- [222] F. Grimsman, F. Brauchle, T. Gerbert, A. Gruhle, J. Parisi, and M. Knipper, “Impact of different aging mechanisms on the thickness change and the quick-charge capability of lithium-ion cells,” *J Energy Storage*, vol. 14, pp. 158–162, Dec. 2017, doi: 10.1016/j.est.2017.10.010.
- [223] S. Ahmed et al., “Enabling fast charging – A battery technology gap assessment,” *J Power Sources*, vol. 367, pp. 250–262, 2017, doi: 10.1016/j.jpowsour.2017.06.055.
- [224] P. Arora, M. Doyle, and R. E. White, “Mathematical Modeling of the Lithium Deposition Overcharge Reaction in Lithium-Ion Batteries Using Carbon-Based Negative Electrodes,” 1988.

- [225] R. Chandrasekaran, “Quantification of bottlenecks to fast charging of lithium-ion-insertion cells for electric vehicles,” *J Power Sources*, vol. 271, pp. 622–632, 2014, doi: 10.1016/j.jpowsour.2014.07.106.
- [226] S. Hein and A. Latz, “Influence of local lithium metal deposition in 3D microstructures on local and global behavior of Lithium-ion batteries,” *Electrochim Acta*, vol. 201, pp. 354–365, 2016, doi: 10.1016/j.electacta.2016.01.220.
- [227] S. Hein, T. Danner, and A. Latz, “An Electrochemical Model of Lithium Plating and Stripping in Lithium Ion Batteries,” *ACS Appl Energy Mater*, vol. 3, no. 9, pp. 8519–8531, Sep. 2020, doi: 10.1021/ACSAEM.0C01155/ASSET/IMAGES/LARGE/AE0C01155_0009.JPEG.
- [228] H. Wang et al., “Underpotential lithium plating on graphite anodes caused by temperature heterogeneity,” *Proc Natl Acad Sci U S A*, vol. 117, no. 47, pp. 29453–29461, 2020, doi: 10.1073/pnas.2009221117.
- [229] S. J. Harris, A. Timmons, D. R. Baker, and C. Monroe, “Direct in situ measurements of Li transport in Li-ion battery negative electrodes,” *Chem Phys Lett*, vol. 485, no. 4–6, pp. 265–274, Jan. 2010, doi: 10.1016/j.cplett.2009.12.033.
- [230] A. Barai et al., “A comparison of methodologies for the non-invasive characterisation of commercial Li-ion cells,” *Prog Energy Combust Sci*, vol. 72, pp. 1–31, 2019, doi: 10.1016/j.pecs.2019.01.001.
- [231] M. Ecker, P. Shafiei Sabet, and D. U. Sauer, “Influence of operational condition on lithium plating for commercial lithium-ion batteries – Electrochemical experiments and post-mortem-analysis,” *Appl Energy*, vol. 206, no. November, pp. 934–946, 2017, doi: 10.1016/j.apenergy.2017.08.034.
- [232] X. Zhao, Y. Yin, Y. Hu, and S. Y. Choe, “Electrochemical-thermal modeling of lithium plating/stripping of Li(Ni_{0.6}Mn_{0.2}Co_{0.2})O₂/Carbon lithium-ion batteries at subzero ambient temperatures,” *J Power Sources*, vol. 418, no. February, pp. 61–73, 2019, doi: 10.1016/j.jpowsour.2019.02.001.

- [233] D. Ren et al., “Investigation of Lithium Plating-Stripping Process in Li-Ion Batteries at Low Temperature Using an Electrochemical Model,” *J Electrochem Soc*, vol. 165, no. 10, pp. A2167–A2178, 2018, doi: 10.1149/2.0661810jes.
- [234] X. G. Yang, S. Ge, T. Liu, Y. Leng, and C. Y. Wang, “A look into the voltage plateau signal for detection and quantification of lithium plating in lithium-ion cells,” *J Power Sources*, vol. 395, no. May, pp. 251–261, 2018, doi: 10.1016/j.jpowsour.2018.05.073.
- [235] T. Waldmann et al., “Interplay of operational parameters on lithium deposition in lithium-ion cells: Systematic measurements with reconstructed 3-electrode pouch full cells,” *J Electrochem Soc*, vol. 163, no. 7, pp. A1232–A1238, 2016, doi: 10.1149/2.0591607jes.
- [236] G. Liu and W. Lu, “A model of concurrent lithium dendrite growth, SEI growth, SEI penetration and regrowth,” *J Electrochem Soc*, vol. 164, no. 9, pp. A1826–A1833, 2017, doi: 10.1149/2.0381709jes.
- [237] E. Sahraei, J. Meier, and T. Wierzbicki, “Characterizing and modeling mechanical properties and onset of short circuit for three types of lithium-ion pouch cells,” *J Power Sources*, vol. 247, pp. 503–516, 2014, doi: 10.1016/j.jpowsour.2013.08.056.
- [238] C. J. Orendorff, E. P. Roth, and G. Nagasubramanian, “Experimental triggers for internal short circuits in lithium-ion cells,” *J Power Sources*, vol. 196, no. 15, pp. 6554–6558, Aug. 2011, doi: 10.1016/j.jpowsour.2011.03.035.
- [239] T. R. Tanim et al., “Article Heterogeneous Behavior of Lithium Plating during Extreme Fast Charging Heterogeneous Behavior of Lithium Plating during Extreme Fast Charging,” 2020, doi: 10.1016/j.xcrp.2020.100114.
- [240] D. Anseán et al., “Operando lithium plating quantification and early detection of a commercial LiFePO₄ cell cycled under dynamic driving schedule,” *J Power Sources*, vol. 356, no. October, pp. 36–46, 2017, doi: 10.1016/j.jpowsour.2017.04.072.

- [241] T. Guan et al., “The degradation of LiCoO₂/graphite batteries at different rates,” *Electrochim Acta*, vol. 279, pp. 204–212, Jul. 2018, doi: 10.1016/j.electacta.2018.04.197.
- [242] L. Gireaud, S. Grugeon, S. Laruelle, B. Yrieix, and J. M. Tarascon, “Lithium metal stripping/plating mechanisms studies: A metallurgical approach,” *Electrochem commun*, vol. 8, no. 10, pp. 1639–1649, 2006, doi: 10.1016/j.elecom.2006.07.037.
- [243] H. Ge et al., “Investigating lithium plating in lithium-ion batteries at low temperatures using electrochemical model with NMR assisted parameterization,” *J Electrochem Soc*, vol. 164, no. 6, pp. A1050–A1060, 2017, doi: 10.1149/2.0461706jes.
- [244] M. Petzl, M. Kasper, and M. A. Danzer, “Lithium plating in a commercial lithium-ion battery - A low-temperature aging study,” *J Power Sources*, vol. 275, pp. 799–807, Feb. 2015, doi: 10.1016/j.jpowsour.2014.11.065.
- [245] I. D. Campbell, M. Marzook, M. Marinescu, and G. J. Offer, “How Observable Is Lithium Plating? Differential Voltage Analysis to Identify and Quantify Lithium Plating Following Fast Charging of Cold Lithium-Ion Batteries,” *J Electrochem Soc*, vol. 166, no. 4, pp. A725–A739, 2019, doi: 10.1149/2.0821904jes.
- [246] C. Fear, T. Adhikary, R. E. Carter, A. N. Mistry, C. T. Love, and P. P. Mukherjee, “In Operando Detection of the Onset and Mapping of Lithium Plating Regimes during Fast Charging of Lithium-ion Batteries,” *ACS Appl Mater Interfaces*, 2020, doi: 10.1021/acsami.0c07803.
- [247] F. Ringbeck, C. Rahe, G. Fuchs, and D. U. Sauer, “Identification of Lithium Plating in Lithium-Ion Batteries by Electrical and Optical Methods,” *J Electrochem Soc*, vol. 167, no. 9, p. 090536, 2020, doi: 10.1149/1945-7111/ab8f5a.
- [248] D. Ouyang, Y. He, J. Weng, J. Liu, M. Chen, and J. Wang, “Influence of low temperature conditions on lithium-ion batteries and the application of an insulation material,” *RSC Adv*, vol. 9, no. 16, pp. 9053–9066, 2019, doi: 10.1039/c9ra00490d.

- [249] J. Jaguemont, L. Boulon, and Y. Dubé, “A comprehensive review of lithium-ion batteries used in hybrid and electric vehicles at cold temperatures,” *Appl Energy*, vol. 164, pp. 99–114, 2016, doi: 10.1016/j.apenergy.2015.11.034.
- [250] S. Ma et al., “Temperature effect and thermal impact in lithium-ion batteries: A review,” *Progress in Natural Science: Materials International*, vol. 28, no. 6, pp. 653–666, 2018, doi: 10.1016/j.pnsc.2018.11.002.
- [251] D. Anseán et al., “Operando lithium plating quantification and early detection of a commercial LiFePO₄ cell cycled under dynamic driving schedule,” *J Power Sources*, vol. 356, pp. 36–46, 2017, doi: 10.1016/j.jpowsour.2017.04.072.
- [252] M. Börner et al., “Degradation effects on the surface of commercial LiNi_{0.5}Co_{0.2}Mn_{0.3}O₂ electrodes,” *J Power Sources*, vol. 335, pp. 45–55, 2016, doi: 10.1016/j.jpowsour.2016.09.071.
- [253] X. G. Yang, G. Zhang, S. Ge, and C. Y. Wang, “Fast charging of lithium-ion batteries at all temperatures,” *Proc Natl Acad Sci U S A*, vol. 115, no. 28, pp. 7266–7271, 2018, doi: 10.1073/pnas.1807115115.
- [254] X. G. Yang et al., “Asymmetric Temperature Modulation for Extreme Fast Charging of Lithium-Ion Batteries,” *Joule*, vol. 3, no. 12, pp. 3002–3019, 2019, doi: 10.1016/j.joule.2019.09.021.
- [255] T. R. Tanim, E. J. Dufek, C. C. Dickerson, and S. M. Wood, “Electrochemical quantification of lithium plating: Challenges and considerations,” *J Electrochem Soc*, vol. 166, no. 12, pp. A2689–A2696, 2019, doi: 10.1149/2.1581912jes.
- [256] S. P. Rangarajan, Y. Barsukov, and P. P. Mukherjee, “In operando signature and quantification of lithium plating,” *J Mater Chem A Mater*, vol. 7, no. 36, pp. 20683–20695, 2019, doi: 10.1039/c9ta07314k.
- [257] P. Keil and A. Jossen, “Charging protocols for lithium-ion batteries and their impact on cycle life-An experimental study with different 18650 high-power cells,” *J Energy Storage*, vol. 6, pp. 125–141, May 2016, doi: 10.1016/j.est.2016.02.005.

- [258] L. Zhang, Z. Zhang, P. C. Redfern, L. A. Curtiss, and K. Amine, “Molecular engineering towards safer lithium-ion batteries: A highly stable and compatible redox shuttle for overcharge protection,” *Energy Environ Sci*, vol. 5, no. 8, pp. 8204–8207, 2012, doi: 10.1039/c2ee21977h.
- [259] D. Juarez-Robles, A. A. Vyas, C. Fear, J. A. Jeevarajan, and P. P. Mukherjee, “Overcharge and Aging Analytics of Li-Ion Cells,” *J Electrochem Soc*, vol. 167, no. 9, p. 090547, 2020, doi: 10.1149/1945-7111/ab9569.
- [260] S. Liu, L. Xiong, and C. He, “Long cycle life lithium ion battery with lithium nickel cobalt manganese oxide (NCM) cathode,” *J Power Sources*, vol. 261, pp. 285–291, 2014, doi: 10.1016/j.jpowsour.2014.03.083.
- [261] J. Cannarella and C. B. Arnold, “The Effects of Defects on Localized Plating in Lithium-Ion Batteries,” *J Electrochem Soc*, vol. 162, no. 7, pp. A1365–A1373, 2015, doi: 10.1149/2.1051507jes.
- [262] T. Abe, H. Fukuda, Y. Iriyama, and Z. Ogumi, “Solvated Li-ion transfer at interface between graphite and electrolyte,” *J Electrochem Soc*, vol. 151, no. 8, pp. 1120–1123, 2004, doi: 10.1149/1.1763141.
- [263] M. C. Smart and B. V. Ratnakumar, “Effects of electrolyte composition on lithium plating in lithium-ion cells,” *J Electrochem Soc*, vol. 158, no. 4, 2011, doi: 10.1149/1.3544439.
- [264] C. T. Love, O. A. Baturina, and K. E. Swider-Lyons, “Observation of lithium dendrites at ambient temperature and below,” *ECS Electrochemistry Letters*, vol. 4, no. 2, pp. A24–A27, 2014, doi: 10.1149/2.0041502eel.
- [265] F. Yao et al., “Diffusion mechanism of lithium ion through basal plane of layered graphene,” *J Am Chem Soc*, vol. 134, no. 20, pp. 8646–8654, 2012, doi: 10.1021/ja301586m.
- [266] M. Dubarry, G. Baure, and D. Anseán, “Perspective on State-of-Health Determination in Lithium-Ion Batteries,” *Journal of Electrochemical Energy Conversion and Storage*, vol. 17, no. 4, pp. 1–8, 2020, doi: 10.1115/1.4045008.

- [267] G. Baure and M. Dubarry, “Synthetic vs. Real driving cycles: A comparison of electric vehicle battery degradation,” *Batteries*, vol. 5, no. 2, 2019, doi: 10.3390/batteries5020042.
- [268] S. F. Schuster et al., “Nonlinear aging characteristics of lithium-ion cells under different operational conditions,” *J Energy Storage*, vol. 1, no. 1, pp. 44–53, 2015, doi: 10.1016/j.est.2015.05.003.
- [269] T. Waldmann, M. Wilka, M. Kasper, M. Fleischhammer, and M. Wohlfahrt-Mehrens, “Temperature dependent ageing mechanisms in Lithium-ion batteries - A Post-Mortem study,” *J Power Sources*, vol. 262, pp. 129–135, 2014, doi: 10.1016/j.jpowsour.2014.03.112.
- [270] J.-G. Zhang, W. Xu, and W. A. Henderson, *Lithium Metal Anodes and Rechargeable Lithium Metal Batteries*. Springer Series in Materials Science, 2017. doi: DOI 10.1007/978-3-319-44054-5.
- [271] B. B. Perla and W. Yixuan, *Lithium-Ion Batteries - Solid-Electrolyte Interphase*. Imperial College Press, 2010. doi: 10.1142/9781860946448.
- [272] T. Waldmann et al., “Review—Post-Mortem Analysis of Aged Lithium-Ion Batteries: Disassembly Methodology and Physico-Chemical Analysis Techniques,” *J Electrochem Soc*, vol. 163, no. 10, pp. A2149–A2164, 2016, doi: 10.1149/2.1211609jes.
- [273] N. Williard, B. Sood, M. Osterman, and M. Pecht, “Disassembly methodology for conducting failure analysis on lithium-ion batteries,” *Journal of Materials Science: Materials in Electronics*, vol. 22, no. 10, pp. 1616–1630, 2011, doi: 10.1007/s10854-011-0452-4.
- [274] A. Friesen et al., “Impact of cycling at low temperatures on the safety behavior of 18650-type lithium ion cells: Combined study of mechanical and thermal abuse testing accompanied by post-mortem analysis,” *J Power Sources*, vol. 334, pp. 1–11, 2016, doi: 10.1016/j.jpowsour.2016.09.120.

- [275] T. Rauhala, K. Jalkanen, T. Romann, E. Lust, N. Omar, and T. Kallio, “Low-temperature aging mechanisms of commercial graphite/LiFePO₄ cells cycled with a simulated electric vehicle load profile—A post-mortem study,” *J Energy Storage*, vol. 20, no. October, pp. 344–356, 2018, doi: 10.1016/j.est.2018.10.007.
- [276] A. Iturrondobeitia et al., “Post-Mortem Analysis of Calendar-Aged 16 Ah NMC/Graphite Pouch Cells for EV Application,” *Journal of Physical Chemistry C*, vol. 121, no. 40, pp. 21865–21876, Oct. 2017, doi: 10.1021/acs.jpcc.7b05416.
- [277] M. Kassem and C. Delacourt, “Postmortem analysis of calendar-aged graphite/LiFePO₄ cells,” *J Power Sources*, vol. 235, pp. 159–171, 2013, doi: 10.1016/j.jpowsour.2013.01.147.
- [278] M. Lang et al., “Post mortem analysis of fatigue mechanisms in LiNi_{0.8}Co_{0.15}Al_{0.05}O₂ – LiNi_{0.5}Co_{0.2}Mn_{0.3}O₂ – LiMn₂O₄/graphite lithium ion batteries,” *J Power Sources*, vol. 326, pp. 397–409, 2016, doi: 10.1016/j.jpowsour.2016.07.010.
- [279] M. Storch et al., “Post-mortem analysis of calendar aged large-format lithium-ion cells: Investigation of the solid electrolyte interphase,” *J Power Sources*, vol. 443, no. October, p. 227243, 2019, doi: 10.1016/j.jpowsour.2019.227243.
- [280] Y. Cohen and D. Aurbach, “The use of a special work station for in situ measurements of highly reactive electrochemical systems by atomic force and scanning tunneling microscopes,” *Review of Scientific Instruments*, vol. 70, no. 12, pp. 4668–4675, 1999, doi: 10.1063/1.1150130.
- [281] J. Steiger, D. Kramer, and R. Mönig, “Mechanisms of dendritic growth investigated by in situ light microscopy during electrodeposition and dissolution of lithium,” *J Power Sources*, vol. 261, pp. 112–119, Sep. 2014, doi: 10.1016/j.jpowsour.2014.03.029.
- [282] G. Liu, D. Wang, J. Zhang, A. Kim, and W. Lu, “Preventing Dendrite Growth by a Soft Piezoelectric Material,” 2019, doi: 10.1021/acsmaterialslett.9b00289.

- [283] J. Steiger, D. Kramer, and R. Mönig, “Microscopic observations of the formation, growth and shrinkage of lithium moss during electrodeposition and dissolution,” *Electrochim Acta*, vol. 136, pp. 529–536, Aug. 2014, doi: 10.1016/j.electacta.2014.05.120.
- [284] K. Persson et al., “Lithium diffusion in graphitic carbon,” *Journal of Physical Chemistry Letters*, vol. 1, no. 8, pp. 1176–1180, Apr. 2010, doi: 10.1021/jz100188d.
- [285] C. Uhlmann, J. Illig, M. Ender, R. Schuster, and E. Ivers-Tiffée, “In situ detection of lithium metal plating on graphite in experimental cells,” *J Power Sources*, vol. 279, pp. 428–438, Apr. 2015, doi: 10.1016/j.jpowsour.2015.01.046.
- [286] K. E. Thomas-Alyea, C. Jung, R. B. Smith, and M. Z. Bazant, “In situ observation and mathematical modeling of lithium distribution within graphite,” *J Electrochem Soc*, vol. 164, no. 11, pp. E3063–E3072, 2017, doi: 10.1149/2.0061711jes.
- [287] P. Baudry, M. Armand, M. Gauthier, and J. Masounave, “In situ observation by SEM of positive composite electrodes during discharge of polymer lithium batteries,” *Solid State Ion*, vol. 28–30, no. PART 2, pp. 1567–1571, 1988, doi: 10.1016/0167-2738(88)90421-3.
- [288] M. Shao, “In situ microscopic studies on the structural and chemical behaviors of lithium-ion battery materials,” *J Power Sources*, vol. 270, pp. 475–486, 2014, doi: 10.1016/j.jpowsour.2014.07.123.
- [289] H. J. Chang et al., “Investigating Li Microstructure Formation on Li Anodes for Lithium Batteries by in Situ $^6\text{Li}/^7\text{Li}$ NMR and SEM,” *Journal of Physical Chemistry C*, vol. 119, no. 29, pp. 16443–16451, 2015, doi: 10.1021/acs.jpcc.5b03396.
- [290] I. Yoshimatsu, T. Hirai, and J. ichi Yamaki, “Lithium Electrode Morphology during Cycling in Lithium Cells,” *J Electrochem Soc*, vol. 135, no. 10, pp. 2422–2427, 1988, doi: 10.1149/1.2095351.
- [291] M. Nagao, A. Hayashi, M. Tatsumisago, T. Kanetsuku, T. Tsuda, and S. Kuwabata, “In situ SEM study of a lithium deposition and dissolution mechanism in a bulk-type solid-state cell with a $\text{Li}_2\text{S-P}_2\text{S}_5$ solid electrolyte,” *Physical Chemistry*

- Chemical Physics, vol. 15, no. 42, pp. 18600–18606, Nov. 2013, doi: 10.1039/c3cp51059j.
- [292] D. Chen, S. Indris, M. Schulz, B. Gamer, and R. Mönig, “In situ scanning electron microscopy on lithium-ion battery electrodes using an ionic liquid,” *J Power Sources*, vol. 196, no. 15, pp. 6382–6387, 2011, doi: 10.1016/j.jpowsour.2011.04.009.
- [293] F. Sagane, R. Shimokawa, H. Sano, H. Sakaebe, and Y. Iriyama, “In-situ scanning electron microscopy observations of Li plating and stripping reactions at the lithium phosphorus oxynitride glass electrolyte/Cu interface,” *J Power Sources*, vol. 225, pp. 245–250, Mar. 2013, doi: 10.1016/j.jpowsour.2012.10.026.
- [294] G. Rong et al., “Liquid-Phase Electrochemical Scanning Electron Microscopy for In Situ Investigation of Lithium Dendrite Growth and Dissolution,” *Advanced Materials*, vol. 29, no. 13, 2017, doi: 10.1002/adma.201606187.
- [295] K. R. Tallman et al., “Anode Overpotential Control via Interfacial Modification: Inhibition of Lithium Plating on Graphite Anodes,” *ACS Appl Mater Interfaces*, vol. 11, no. 50, pp. 46864–46874, Dec. 2019, doi: 10.1021/ACSAMI.9B16794/ASSET/IMAGES/LARGE/AM9B16794_0008.JPEG.
- [296] Y. Wu and N. Liu, “Visualizing Battery Reactions and Processes by Using In Situ and In Operando Microscopies,” *Chem*, vol. 4, no. 3, pp. 438–465, 2018, doi: 10.1016/j.chempr.2017.12.022.
- [297] Y. Yuan, K. Amine, J. Lu, and R. Shahbazian-Yassar, “Understanding materials challenges for rechargeable ion batteries with in situ transmission electron microscopy,” *Nat Commun*, vol. 8, no. May, pp. 1–14, 2017, doi: 10.1038/ncomms15806.
- [298] H. Ghassemi, M. Au, N. Chen, P. A. Heiden, and R. S. Yassar, “Real-time observation of lithium fibers growth inside a nanoscale lithium-ion battery,” *Appl Phys Lett*, vol. 99, no. 12, pp. 1–4, 2011, doi: 10.1063/1.3643035.

- [299] X. H. Liu et al., “In situ TEM experiments of electrochemical lithiation and delithiation of individual nanostructures,” *Adv Energy Mater*, vol. 2, no. 7, pp. 722–741, 2012, doi: 10.1002/aenm.201200024.
- [300] B. L. Mehdi et al., “In-situ electrochemical transmission electron microscopy for battery research,” *Microscopy and Microanalysis*, vol. 20, no. 2, pp. 484–492, 2014, doi: 10.1017/S1431927614000488.
- [301] Z. Zeng, W. I. Liang, H. G. Liao, H. L. Xin, Y. H. Chu, and H. Zheng, “Visualization of electrode-electrolyte interfaces in LiPF₆/EC/DEC electrolyte for lithium ion batteries via in situ TEM,” *Nano Lett*, vol. 14, no. 4, pp. 1745–1750, 2014, doi: 10.1021/nl403922u.
- [302] S. Krachkovskiy, M. L. Trudeau, and K. Zaghib, “Application of magnetic resonance techniques to the in situ characterization of Li-ion batteries: A review,” *Materials*, vol. 13, no. 7, 2020, doi: 10.3390/ma13071694.
- [303] J. Arai, Y. Okada, T. Sugiyama, M. Izuka, K. Gotoh, and K. Takeda, “In Situ Solid State ⁷Li NMR Observations of Lithium Metal Deposition during Overcharge in Lithium Ion Batteries,” *J Electrochem Soc*, vol. 162, no. 6, pp. A952–A958, 2015, doi: 10.1149/2.0411506jes.
- [304] F. Chevallier, F. Poli, B. Montigny, and M. Letellier, “In situ ⁷Li nuclear magnetic resonance observation of the electrochemical intercalation of lithium in graphite: Second cycle analysis,” *Carbon N Y*, vol. 61, pp. 140–153, 2013, doi: 10.1016/j.carbon.2013.04.078.
- [305] M. Letellier, F. Chevallier, F. Béguin, E. Frackowiak, and J. N. Rouzaud, “The first in situ ⁷Li NMR study of the reversible lithium insertion mechanism in disorganised carbons,” *Journal of Physics and Chemistry of Solids*, vol. 65, no. 2–3, pp. 245–251, 2004, doi: 10.1016/j.jpcs.2003.10.022.
- [306] J. Arai and R. Nakahigashi, “Study of Li metal deposition in lithium ion battery during low-temperature cycle using in situ solid-state ⁷Li nuclear magnetic

- resonance,” *J Electrochem Soc*, vol. 164, no. 13, pp. A3403–A3409, 2017, doi: 10.1149/2.1921713jes.
- [307] N. Schweikert et al., “Suppressed lithium dendrite growth in lithium batteries using ionic liquid electrolytes: Investigation by electrochemical impedance spectroscopy, scanning electron microscopy, and in situ ^7Li nuclear magnetic resonance spectroscopy,” *J Power Sources*, vol. 228, pp. 237–243, 2013, doi: 10.1016/j.jpowsour.2012.11.124.
- [308] K. Gotoh et al., “In situ ^7Li nuclear magnetic resonance study of the relaxation effect in practical lithium ion batteries,” *Carbon N Y*, vol. 79, no. 1, pp. 380–387, 2014, doi: 10.1016/j.carbon.2014.07.080.
- [309] H. Ota, Y. Sakata, X. Wang, J. Sasahara, and E. Yasukawa, “Characterization of Lithium Electrode in Lithium Imides/Ethylene Carbonate and Cyclic Ether Electrolytes II. Surface Chemistry,” *J Electrochem Soc*, vol. 151, no. 3, 2004, doi: 10.1149/1.1644137.
- [310] J. Wandt, P. Jakes, J. Granwehr, R. A. Eichel, and H. A. Gasteiger, “Quantitative and time-resolved detection of lithium plating on graphite anodes in lithium ion batteries,” *Materials Today*, vol. 21, no. 3, pp. 231–240, 2018, doi: 10.1016/j.mattod.2017.11.001.
- [311] A. Niemöller, P. Jakes, R. A. Eichel, and J. Granwehr, “EPR Imaging of Metallic Lithium and its Application to Dendrite Localisation in Battery Separators,” *Sci Rep*, vol. 8, no. 1, pp. 1–7, 2018, doi: 10.1038/s41598-018-32112-y.
- [312] M. Sathiya, J. B. Leriche, E. Salager, D. Gourier, J. M. Tarascon, and H. Vezin, “Electron paramagnetic resonance imaging for real-time monitoring of Li-ion batteries,” *Nat Commun*, vol. 6, pp. 1–7, 2015, doi: 10.1038/ncomms7276.
- [313] J. Wandt, C. Marino, H. A. Gasteiger, P. Jakes, R. A. Eichel, and J. Granwehr, “Operando electron paramagnetic resonance spectroscopy-formation of mossy lithium on lithium anodes during charge-discharge cycling,” *Energy Environ Sci*, vol. 8, no. 4, pp. 1358–1367, 2015, doi: 10.1039/c4ee02730b.

- [314] K. Luo, M. Yorgancioglu, and D. Keller, "Scanning force microscopy at -25°C," *Ultramicroscopy*, vol. 50, no. 2, pp. 147–155, 1993, doi: 10.1016/0304-3991(93)90005-I.
- [315] K. I. Morigaki and A. Ohta, "Analysis of the surface of lithium in organic electrolyte by atomic force microscopy, Fourier transform infrared spectroscopy and scanning auger electron microscopy," *J Power Sources*, vol. 76, no. 2, pp. 159–166, 1998, doi: 10.1016/S0378-7753(98)00151-7.
- [316] R. Mogi, M. Inaba, Y. Iriyama, T. Abe, and Z. Ogumi, "In situ atomic force microscopy study on lithium deposition on nickel substrates at elevated temperatures," *J Electrochem Soc*, vol. 149, no. 4, Apr. 2002, doi: 10.1149/1.1454138.
- [317] D. Aurbach and Y. Cohen, "The application of atomic force microscopy for the study of Li deposition processes," *J Electrochem Soc*, vol. 143, no. 11, pp. 3525–3532, 1996, doi: 10.1149/1.1837248.
- [318] C. Shen, G. Hu, L. Z. Cheong, S. Huang, J. G. Zhang, and D. Wang, "Direct Observation of the Growth of Lithium Dendrites on Graphite Anodes by Operando EC-AFM," *Small Methods*, vol. 2, no. 2, pp. 1–7, 2018, doi: 10.1002/smtd.201700298.
- [319] Y. Yang et al., "In Situ Electrochemistry of Rechargeable Battery Materials: Status Report and Perspectives," *Advanced Materials*, vol. 29, no. 31, pp. 1–22, 2017, doi: 10.1002/adma.201606922.
- [320] Y. S. Cohen, Y. Cohen, and D. Aurbach, "Micromorphological studies of lithium electrodes in alkyl carbonate solutions using in situ atomic force microscopy," *Journal of Physical Chemistry B*, vol. 104, no. 51, pp. 12282–12291, 2000, doi: 10.1021/jp002526b.
- [321] D. Aurbach, B. Markovsky, I. Weissman, E. Levi, and Y. Ein-Eli, "On the correlation between surface chemistry and performance of graphite negative

- electrodes for Li ion batteries,” *Electrochim Acta*, vol. 45, no. 1, pp. 67–86, 1999, doi: 10.1016/S0013-4686(99)00194-2.
- [322] L. Castro, R. Dedryvère, J. B. Ledeuil, J. Bréger, C. Tessier, and D. Gonbeau, “Aging mechanisms of LiFePO₄//graphite cells studied by XPS: Redox reaction and electrode/electrolyte interfaces,” *J Electrochem Soc*, vol. 159, no. 4, pp. 357–363, 2012, doi: 10.1149/2.024204jes.
- [323] D. Aurbach, I. Weissman, A. Schechter, and H. Cohen, “X-ray Photoelectron Spectroscopy Studies of Lithium Surfaces Prepared in Several Important Electrolyte Solutions. A Comparison with Previous Studies by Fourier Transform Infrared Spectroscopy,” 1996.
- [324] S. Wenzel, T. Leichtweiss, D. Krüger, J. Sann, and J. Janek, “Interphase formation on lithium solid electrolytes - An in situ approach to study interfacial reactions by photoelectron spectroscopy,” *Solid State Ion*, vol. 278, pp. 98–105, 2015, doi: 10.1016/j.ssi.2015.06.001.
- [325] S. S. Harilal, J. P. Allain, A. Hassanein, M. R. Hendricks, and M. Nieto-Perez, “Reactivity of lithium exposed graphite surface,” *Appl Surf Sci*, vol. 255, no. 20, pp. 8539–8543, Jul. 2009, doi: 10.1016/j.apsusc.2009.06.009.
- [326] V. Wood, “X-ray tomography for battery research and development,” *Nat Rev Mater*, vol. 3, no. 9, pp. 293–295, 2018, doi: 10.1038/s41578-018-0053-4.
- [327] P. Pietsch and V. Wood, “X-Ray Tomography for Lithium Ion Battery Research: A Practical Guide,” *Annu Rev Mater Res*, vol. 47, no. 1, pp. 451–479, 2017, doi: 10.1146/annurev-matsci-070616-123957.
- [328] F. Sun et al., “Advancing knowledge of electrochemically generated lithium microstructure and performance decay of lithium ion battery by synchrotron X-ray tomography,” *Materials Today*, vol. 27, no. August, pp. 21–32, 2019, doi: 10.1016/j.mattod.2018.11.003.
- [329] T. Waldmann, R.-G. Scurtu, K. Richter, and M. Wohlfahrt-Mehrens, “18650 vs. 21700 Li-ion cells – A direct comparison of electrochemical, thermal, and

- geometrical properties,” *J Power Sources*, vol. 472, no. July, p. 228614, 2020, doi: 10.1016/j.jpowsour.2020.228614.
- [330] V. Vanpeene, J. Villanova, A. King, B. Lestriez, E. Maire, and L. Roué, “Dynamics of the Morphological Degradation of Si-Based Anodes for Li-Ion Batteries Characterized by In Situ Synchrotron X-Ray Tomography,” *Adv Energy Mater*, vol. 9, no. 18, pp. 1–13, 2019, doi: 10.1002/aenm.201803947.
- [331] D. S. Eastwood et al., “Three-dimensional characterization of electrodeposited lithium microstructures using synchrotron X-ray phase contrast imaging,” *Chemical Communications*, vol. 51, no. 2, pp. 266–268, 2015, doi: 10.1039/c4cc03187c.
- [332] K. J. Harry, D. T. Hallinan, D. Y. Parkinson, A. A. MacDowell, and N. P. Balsara, “Detection of subsurface structures underneath dendrites formed on cycled lithium metal electrodes,” *Nat Mater*, vol. 13, no. 1, pp. 69–73, 2014, doi: 10.1038/nmat3793.
- [333] S. J. An, J. Li, C. Daniel, D. Mohanty, S. Nagpure, and D. L. Wood, “The state of understanding of the lithium-ion-battery graphite solid electrolyte interphase (SEI) and its relationship to formation cycling,” *Carbon N Y*, vol. 105, pp. 52–76, 2016, doi: 10.1016/j.carbon.2016.04.008.
- [334] K. Morigaki, “Analysis of the interface between lithium and organic electrolyte solution,” *J Power Sources*, vol. 104, no. April 2001, pp. 13–23, 2002, doi: [https://doi.org/10.1016/S0378-7753\(01\)00871-0](https://doi.org/10.1016/S0378-7753(01)00871-0).
- [335] Y. Krämer et al., “A New Method for Quantitative Marking of Deposited Lithium by Chemical Treatment on Graphite Anodes in Lithium-Ion Cells,” *Chemistry - A European Journal*, vol. 21, no. 16, pp. 6062–6065, 2015, doi: 10.1002/chem.201406606.
- [336] L. D. Ellis, S. Buteau, S. G. Hames, L. M. Thompson, D. S. Hall, and J. R. Dahn, “A New Method for Determining the Concentration of Electrolyte Components in Lithium-Ion Cells , Using Fourier Transform Infrared Spectroscopy and Machine Learning,” vol. 165, no. 2, pp. 256–262, 2018, doi: 10.1149/2.0861802jes.

- [337] C. M. Burba and R. Frech, "In situ transmission FTIR spectroelectrochemistry: A new technique for studying lithium batteries," *Electrochim Acta*, vol. 52, no. 3, pp. 780–785, Nov. 2006, doi: 10.1016/j.electacta.2006.06.007.
- [338] J. Fan and S. Tan, "Studies on charging lithium-ion cells at low temperatures," *J Electrochem Soc*, vol. 153, no. 6, 2006, doi: 10.1149/1.2190029.
- [339] M. Petzl and M. A. Danzer, "Nondestructive detection, characterization, and quantification of lithium plating in commercial lithium-ion batteries," *J Power Sources*, vol. 254, pp. 80–87, May 2014, doi: 10.1016/j.jpowsour.2013.12.060.
- [340] S. Schindler, M. Bauer, M. Petzl, and M. A. Danzer, "Voltage relaxation and impedance spectroscopy as in-operando methods for the detection of lithium plating on graphitic anodes in commercial lithium-ion cells," *J Power Sources*, vol. 304, pp. 170–180, 2016, doi: 10.1016/j.jpowsour.2015.11.044.
- [341] V. Zinth et al., "Lithium plating in lithium-ion batteries at sub-ambient temperatures investigated by in situ neutron diffraction," *J Power Sources*, vol. 271, pp. 152–159, Aug. 2014, doi: 10.1016/j.jpowsour.2014.07.168.
- [342] U. R. Koleti, T. Q. Dinh, and J. Marco, "A new on-line method for lithium plating detection in lithium-ion batteries," *J Power Sources*, vol. 451, p. 227798, Mar. 2020, doi: 10.1016/J.JPOWSOUR.2020.227798.
- [343] M. C. Smart, B. V Ratnakumar, L. Whitcanack, K. Chin, M. Rodriguez, and S. Surampudi, "Performance Characteristics of Lithium Ion Cells at Low Temperatures," *Proceedings of the Annual Battery Conference on Applications and Advances*, vol. 2002-Janua, pp. 41–46, 2002, doi: 10.1109/BCAA.2002.986366.
- [344] A. N. Jansen, D. W. Dees, D. P. Abraham, K. Amine, and G. L. Henriksen, "Low-temperature study of lithium-ion cells using a Li₂Sn micro-reference electrode," *J Power Sources*, vol. 174, no. 2, pp. 373–379, Dec. 2007, doi: 10.1016/j.jpowsour.2007.06.235.
- [345] D. P. Abraham, S. D. Poppen, A. N. Jansen, J. Liu, and D. W. Dees, "Application of a lithium-tin reference electrode to determine electrode contributions to

- impedance rise in high-power lithium-ion cells,” *Electrochim Acta*, vol. 49, no. 26, pp. 4763–4775, Oct. 2004, doi: 10.1016/j.electacta.2004.05.040.
- [346] Y. Hoshi, Y. Narita, K. Honda, T. Ohtaki, I. Shitanda, and M. Itagaki, “Optimization of reference electrode position in a three-electrode cell for impedance measurements in lithium-ion rechargeable battery by finite element method,” *J Power Sources*, vol. 288, pp. 168–175, 2015, doi: 10.1016/j.jpowsour.2015.04.065.
- [347] H. Nara, D. Mukoyama, T. Yokoshima, T. Momma, and T. Osaka, “Impedance analysis with transmission line model for reaction distribution in a pouch type lithium-ion battery by using micro reference electrode,” *J Electrochem Soc*, vol. 163, no. 3, pp. A434–A441, 2016, doi: 10.1149/2.0341603jes.
- [348] E. McTurk, C. R. Birkl, M. R. Roberts, D. A. Howey, and P. G. Bruce, “Minimally invasive insertion of reference electrodes into commercial lithium-ion pouch cells,” *ECS Electrochemistry Letters*, vol. 4, no. 12, pp. A145–A147, 2015, doi: 10.1149/2.0081512eel.
- [349] L. Somerville, S. Ferrari, M. J. Lain, A. McGordon, P. Jennings, and R. Bhagat, “An in-situ reference electrode insertion method for commercial 18650-type cells,” *Batteries*, vol. 4, no. 2, pp. 1–11, 2018, doi: 10.3390/batteries4020018.
- [350] F. La Mantia, C. D. Wessells, H. D. Deshazer, and Y. Cui, “Reliable reference electrodes for lithium-ion batteries,” *Electrochem commun*, vol. 31, pp. 141–144, 2013, doi: 10.1016/j.elecom.2013.03.015.
- [351] M. Dollé, F. Orsini, A. S. Gozdz, and J. M. Tarascon, “Development of Reliable Three-Electrode Impedance Measurements in Plastic Li-Ion Batteries,” *J Electrochem Soc*, vol. 148, no. 8, pp. 851–857, 2001, doi: 10.1149/1.1381071.
- [352] C. Pastor-Fernández, W. D. Widanage, G. H. Chouchelamane, and J. Marco, “A SoH diagnosis and prognosis method to identify and quantify degradation modes in Li-ion batteries using the IC/DV technique,” *IET Conference Publications*, vol. 2016, no. CP691, pp. 1–6, 2016, doi: 10.1049/cp.2016.0966.

- [353] X. Han, M. Ouyang, L. Lu, J. Li, Y. Zheng, and Z. Li, "A comparative study of commercial lithium ion battery cycle life in electrical vehicle: Aging mechanism identification," *J Power Sources*, vol. 251, pp. 38–54, 2014, doi: 10.1016/j.jpowsour.2013.11.029.
- [354] A. J. Bard and L. R. Faulkner, *Fundamentals and Applications*, vol. 30. 1980. doi: 10.1146/annurev.matsci.30.1.117.
- [355] A. J. Smith, J. C. Burns, S. Trussler, and J. R. Dahn, "Precision measurements of the Coulombic efficiency of lithium-ion batteries and of electrode materials for lithium-ion batteries," *J Electrochem Soc*, vol. 157, no. 2, pp. 196–202, 2010, doi: 10.1149/1.3268129.
- [356] J. C. Burns, D. A. Stevens, and J. R. Dahn, "In-situ detection of lithium plating using high precision coulometry," *J Electrochem Soc*, vol. 162, no. 6, pp. A959–A964, 2015, doi: 10.1149/2.0621506jes.
- [357] Y. Liu, K. Hanai, J. Yang, N. Imanishi, A. Hirano, and Y. Takeda, "Morphology-stable silicon-based composite for Li-intercalation," vol. 168, pp. 61–68, 2004, doi: 10.1016/j.ssi.2004.01.031.
- [358] A. J. Smith, J. C. Burns, and J. R. Dahn, "A high precision study of the coulombic efficiency of Li-Ion batteries," *Electrochemical and Solid-State Letters*, vol. 13, no. 12, pp. 177–179, 2010, doi: 10.1149/1.3487637.
- [359] F. Shi et al., "Lithium metal stripping beneath the solid electrolyte interphase," *Proc Natl Acad Sci U S A*, vol. 115, no. 34, pp. 8529–8534, Aug. 2018, doi: 10.1073/pnas.1806878115.
- [360] N. Schweikert, H. Hahn, and S. Indris, "Cycling behaviour of Li/Li₄Ti₅O₁₂ cells studied by electrochemical impedance spectroscopy," *Physical Chemistry Chemical Physics*, vol. 13, no. 13, pp. 6234–6240, 2011, doi: 10.1039/c0cp01889a.
- [361] R. Al Nazer, V. Cattin, P. Granjon, M. Montaru, and M. Ranieri, "Broadband identification of battery electrical impedance for HEVs," *IEEE Trans Veh Technol*, vol. 62, no. 7, pp. 2896–2905, 2013, doi: 10.1109/TVT.2013.2254140.

- [362] B. Bitzer and A. Gruhle, “A new method for detecting lithium plating by measuring the cell thickness,” *J Power Sources*, vol. 262, pp. 297–302, Sep. 2014, doi: 10.1016/j.jpowsour.2014.03.142.
- [363] M. Bauer, M. Wachtler, H. Stöwe, J. V. Persson, and M. A. Danzer, “Understanding the dilation and dilation relaxation behavior of graphite-based lithium-ion cells,” *J Power Sources*, vol. 317, pp. 93–102, Jun. 2016, doi: 10.1016/j.jpowsour.2016.03.078.
- [364] F. Grimsmann, T. Gerbert, F. Brauchle, A. Gruhle, J. Parisi, and M. Knipper, “Determining the maximum charging currents of lithium-ion cells for small charge quantities,” *J Power Sources*, vol. 365, pp. 12–16, Oct. 2017, doi: 10.1016/j.jpowsour.2017.08.044.
- [365] Q. Q. Liu, D. J. Xiong, R. Petibon, C. Y. Du, and J. R. Dahn, “Gas Evolution during Unwanted Lithium Plating in Li-Ion Cells with EC-Based or EC-Free Electrolytes,” *Journal of The Electrochemical Society*, vol. 163, no. 14, pp. A3010–A3015, 2016, doi: 10.1149/2.0711614jes.
- [366] C. Bommier et al., “Operando Acoustic Monitoring of SEI Formation and Long-Term Cycling in NMC / SiGr Composite Pouch Cells Operando Acoustic Monitoring of SEI Formation and Long-Term Cycling in NMC / SiGr Composite Pouch Cells,” 2020, doi: 10.1149/1945-7111/ab68d6.
- [367] G. Davies et al., “State of Charge and State of Health Estimation Using Electrochemical Acoustic Time of Flight Analysis,” *Journal of The Electrochemical Society*, vol. 164, no. 12, pp. A2746–A2755, 2017, doi: 10.1149/2.1411712jes.
- [368] L. Gold et al., “Probing lithium-ion batteries ’ state-of-charge using ultrasonic transmission e Concept and laboratory testing,” *J Power Sources*, vol. 343, pp. 536–544, 2017, doi: 10.1016/j.jpowsour.2017.01.090.
- [369] A. G. Hsieh et al., “Environmental Science Electrochemical-acoustic time of flight : in operando correlation of physical dynamics with battery charge and health †,” pp. 1569–1577, 2015, doi: 10.1039/c5ee00111k.

- [370] Y. Wu, Y. Wang, W. K. C. Yung, and M. Pecht, "Ultrasonic Health Monitoring of Lithium-Ion Batteries," *Electronics (Switzerland)*, vol. 8, no. 7, 2019, doi: doi:10.3390/electronics8070751.
- [371] C. Bommier et al., "In Operando Acoustic Detection of Lithium Metal Plating in Commercial LiCoO₂/Graphite Pouch Cells," *Cell Rep Phys Sci*, vol. 1, no. 4, p. 100035, 2020, doi: 10.1016/j.xcrp.2020.100035.
- [372] X. Lin, X. Hao, A. Ivanco, Z. Liu, and W. Jia, "Physics-based and control-oriented modeling of diffusion-induced stress in Li-ion batteries," *J Electrochem Soc*, vol. 165, no. 10, pp. A2255–A2266, 2018, doi: 10.1149/2.0971810jes.
- [373] M. Tomasov, M. Kajanova, P. Bracinik, and D. Motyka, "Overview of battery models for sustainable power and transport applications," *Transportation Research Procedia*, vol. 40, pp. 548–555, 2019, doi: 10.1016/j.trpro.2019.07.079.
- [374] M. Doyle, T. Fuller, and J. Newman, "Modeling of galvanostatic charge and discharge of the lithium/ polymer/insertion cell," *J Electrochem Soc*, vol. 140, no. 6, pp. 1526–1533, 1993, doi: 10.1149/1.2221597.
- [375] X. Lin, "Real-Time Prediction of Anode Potential in Li-Ion Batteries Using Long Short-Term Neural Networks for Lithium Plating Prevention," *J Electrochem Soc*, vol. 166, no. 10, pp. A1893–A1904, 2019, doi: 10.1149/2.0621910jes.
- [376] S. Tippmann, D. Walper, L. Balboa, B. Spier, and W. G. Bessler, "Low-temperature charging of lithium-ion cells part I: Electrochemical modeling and experimental investigation of degradation behavior," *J Power Sources*, vol. 252, pp. 305–316, Apr. 2014, doi: 10.1016/j.jpowsour.2013.12.022.
- [377] M. Tang, P. Albertus, and J. Newman, "Two-dimensional modeling of lithium deposition during cell charging," *J Electrochem Soc*, vol. 156, no. 5, 2009, doi: 10.1149/1.3095513.
- [378] V. Boovaragavan, S. Harinipriya, and V. R. Subramanian, "Towards real-time (milliseconds) parameter estimation of lithium-ion batteries using reformulated

- physics-based models,” *J Power Sources*, vol. 183, no. 1, pp. 361–365, 2008, doi: 10.1016/j.jpowsour.2008.04.077.
- [379] R. D. Perkins, A. V. Randall, X. Zhang, and G. L. Plett, “Controls oriented reduced order modeling of lithium deposition on overcharge,” *J Power Sources*, vol. 209, pp. 318–325, Jul. 2012, doi: 10.1016/j.jpowsour.2012.03.003.
- [380] X. G. Yang, Y. Leng, G. Zhang, S. Ge, and C. Y. Wang, “Modeling of lithium plating induced aging of lithium-ion batteries: Transition from linear to nonlinear aging,” *J Power Sources*, vol. 360, pp. 28–40, 2017, doi: 10.1016/j.jpowsour.2017.05.110.
- [381] M. S. Javed et al., “Heterostructured bimetallic–sulfide@layered Ti₃C₂T_x–MXene as a synergistic electrode to realize high-energy-density aqueous hybrid-supercapacitor,” *Nano Energy*, vol. 101, p. 107624, Oct. 2022, doi: 10.1016/j.nanoen.2022.107624.
- [382] Y. Shao et al., “Design and Mechanisms of Asymmetric Supercapacitors,” *Chem Rev*, vol. 118, no. 18, pp. 9233–9280, Sep. 2018, doi: 10.1021/ACS.CHEMREV.8B00252.
- [383] N. Devi and S. S. Ray, “Performance of bismuth-based materials for supercapacitor applications: A review,” *Mater Today Commun*, vol. 25, Dec. 2020, doi: 10.1016/j.mtcomm.2020.101691.
- [384] M. Yu and X. Feng, “Thin-Film Electrode-Based Supercapacitors,” *Joule*, vol. 3, no. 2, Cell Press, pp. 338–360, Feb. 20, 2019. doi: 10.1016/j.joule.2018.12.012.
- [385] C. Choi et al., “Achieving high energy density and high power density with pseudocapacitive materials,” *Nature Reviews Materials*, vol. 5, no. 1. Nature Research, pp. 5–19, Jan. 01, 2020. doi: 10.1038/s41578-019-0142-z.
- [386] M. S. Javed et al., “An ultra-high energy density flexible asymmetric supercapacitor based on hierarchical fabric decorated with 2D bimetallic oxide nanosheets and MOF-derived porous carbon polyhedra,” *J Mater Chem A Mater*, vol. 7, no. 3, pp. 946–957, Jan. 2019, doi: 10.1039/C8TA08816K.

- [387] S. Mahala, K. Khosravinia, and A. Kiani, “Unwanted degradation in pseudocapacitors: Challenges and opportunities,” *J Energy Storage*, vol. 67, p. 107558, 2023, doi: 10.1016/j.est.2023.107558.
- [388] H. Peng et al., “Pore and Heteroatom Engineered Carbon Foams for Supercapacitors,” *Adv Energy Mater*, vol. 9, no. 19, p. 1803665, May 2019, doi: 10.1002/AENM.201803665.
- [389] Y. Ma, L. Zhang, Z. Yan, B. Cheng, J. Yu, and T. Liu, “Sandwich-Shell Structured CoMn₂O₄/C Hollow Nanospheres for Performance-Enhanced Sodium-Ion Hybrid Supercapacitor,” *Adv Energy Mater*, vol. 12, no. 11, Mar. 2022, doi: 10.1002/AENM.202103820.
- [390] J. Yin, W. Zhang, N. A. Alhebshi, N. Salah, and H. N. Alshareef, “Synthesis Strategies of Porous Carbon for Supercapacitor Applications,” *Small Methods*, vol. 4, no. 3, Mar. 2020, doi: 10.1002/SMTD.201900853.
- [391] M. Khot and A. Kiani, “A review on the advances in electrochemical capacitive charge storage in transition metal oxide electrodes for pseudocapacitors,” *Int J Energy Res*, Sep. 2022, doi: 10.1002/er.8763.
- [392] M. Khot and A. Kiani, “Synthesis of self-grown nanostructured NiO via pulse ionization for binderless pseudocapacitor electrode,” *J Energy Storage*, vol. 55, p. 105779, Nov. 2022, doi: 10.1016/J.EST.2022.105779.
- [393] K. Khosravinia and A. Kiani, “Unlocking pseudocapacitors prolonged electrode fabrication via ultra-short laser pulses and machine learning,” *iScience*, vol. 26, no. 4, p. 106438, Apr. 2023, doi: 10.1016/J.ISCI.2023.106438.
- [394] H. Liu, Z. Sun, Y. Chen, W. Zhang, X. Chen, and C. P. Wong, “Laser Processing of Flexible In-Plane Micro-supercapacitors: Progresses in Advanced Manufacturing of Nanostructured Electrodes,” *ACS Nano*, vol. 16, no. 7. American Chemical Society, pp. 10088–10129, Jul. 26, 2022. doi: 10.1021/acsnano.2c02812.
- [395] P. G. Jamkhande, N. W. Ghule, A. H. Bamer, and M. G. Kalaskar, “Metal nanoparticles synthesis: An overview on methods of preparation, advantages and

- disadvantages, and applications,” *J Drug Deliv Sci Technol*, vol. 53, p. 101174, Oct. 2019, doi: 10.1016/J.JDDST.2019.101174.
- [396] H. J. Fan, “Pseudocapacitor Electrodes: Regular Pores Matter,” *Joule*, vol. 3, no. 2. Cell Press, pp. 317–319, Feb. 20, 2019. doi: 10.1016/j.joule.2019.01.014.
- [397] B. Niu, W. Jiang, B. Jiang, M. Lv, S. Wang, and W. Wang, “Determining the depth of surface charging layer of single Prussian blue nanoparticles with pseudocapacitive behaviors,” *Nat Commun*, vol. 13, no. 1, Dec. 2022, doi: 10.1038/s41467-022-30058-4.
- [398] S. Fleischmann et al., “Pseudocapacitance: From Fundamental Understanding to High Power Energy Storage Materials,” *Chem Rev*, vol. 120, no. 14, pp. 6738–6782, Jul. 2020, doi: 10.1021/ACS.CHEMREV.0C00170.
- [399] M. S. Javed et al., “Achieving high-energy density and superior cyclic stability in flexible and lightweight pseudocapacitor through synergic effects of binder-free CoGa₂O₄ 2D-hexagonal nanoplates,” *Nano Energy*, vol. 77, p. 105276, Nov. 2020, doi: 10.1016/J.NANOEN.2020.105276.
- [400] A. Gholami and A. Kiani, “Laser-induced nanofibrous titania film electrode: A new approach for energy storage materials,” *J Energy Storage*, vol. 31, p. 101654, Oct. 2020, doi: 10.1016/J.EST.2020.101654.
- [401] A. Gholami et al., “Electrochemical Performance of Titania 3D Nanonetwork Electrodes Induced by Pulse Ionization at Varied Pulse Repetitions,” *Nanomaterials* 2021, Vol. 11, Page 1062, vol. 11, no. 5, p. 1062, Apr. 2021, doi: 10.3390/NANO11051062.
- [402] M. Z. Iqbal, M. M. Faisal, and S. R. Ali, “Integration of supercapacitors and batteries towards high-performance hybrid energy storage devices,” *Int J Energy Res*, vol. 45, no. 2, pp. 1449–1479, Feb. 2021, doi: 10.1002/ER.5954.
- [403] F. Luan et al., “High energy density asymmetric supercapacitors with a nickel oxide nanoflake cathode and a 3D reduced graphene oxide anode,” *Nanoscale*, vol. 5, no. 17, pp. 7984–7990, Aug. 2013, doi: 10.1039/C3NR02710D.

- [404] M. Pathak and C. S. Rout, “Hierarchical NiCo₂S₄ nanostructures anchored on nanocarbons and Ti₃C₂T_x MXene for high-performance flexible solid-state asymmetric supercapacitors,” *Adv Compos Hybrid Mater*, vol. 5, no. 2, pp. 1404–1422, Jun. 2022, doi: 10.1007/S42114-022-00466-7.
- [405] C. A. Schneider, W. S. Rasband, and K. W. Eliceiri, “NIH Image to ImageJ: 25 years of image analysis,” *Nature Methods* 2012 9:7, vol. 9, no. 7, pp. 671–675, Jun. 2012, doi: 10.1038/nmeth.2089.
- [406] S. B. Kotsiantis and D. Kanellopoulos, “Data preprocessing for supervised leaning,” *Int J Comp Sci*, vol. 1, no. 2, pp. 1–7, 2006, doi: 10.1080/02331931003692557.
- [407] M. Frye, J. Mohren, and R. H. Schmitt, “Benchmarking of Data Preprocessing Methods for Machine Learning-Applications in Production,” *Procedia CIRP*, vol. 104, pp. 50–55, 2021, doi: 10.1016/J.PROCIR.2021.11.009.
- [408] R. R. Wilcox, *Introduction to Robust Estimation and Hypothesis Testing*. Elsevier, 2021. doi: 10.1016/C2019-0-01225-3.
- [409] M. Hall and L. Smith, “Feature subset selection: a correlation based filter approach,” in *Proceedings of International Conference on Neural Information Processing and Intelligent Information Systems*, 1998, pp. 855–858. doi: <https://hdl.handle.net/10289/1515>.
- [410] P. Schober, C. Boer, and L. A. Schwarte, “Correlation Coefficients,” *Anesth Analg*, vol. 126, no. 5, pp. 1763–1768, May 2018, doi: 10.1213/ANE.0000000000002864.
- [411] K. P. Murphy, *Probabilistic machine learning : an introduction*. MIT Press, 2022.
- [412] Aurélien Géron, *Hands-on machine learning with Scikit-Learn, Keras and TensorFlow: concepts, tools, and techniques to build intelligent systems*, 2nd ed. O’Reilly Media, Inc, 2019. Accessed: Mar. 05, 2023. [Online]. Available: <https://www.oreilly.com/library/view/hands-on-machine-learning/9781492032632/>
- [413] L. Breiman, J. H. Friedman, R. A. Olshen, and C. J. Stone, “Classification and regression trees,” *Classification and Regression Trees*, pp. 1–358, Jan. 2017, doi: 10.1201/9781315139470/.

- [414] A. Liaw and M. Wiener, "Classification and Regression by randomForest," R News, vol. 2, no. 3, pp. 18–22, 2002, doi: <http://cran.r-project.org/doc/Rnews/>.
- [415] L. Breiman, "Bagging predictors," Mach Learn, vol. 24, no. 2, pp. 123–140, 1996, doi: 10.1007/BF00058655.
- [416] S. Jha et al., "Data-Driven Predictive Electrochemical Behavior of Lignin-Based Supercapacitors via Machine Learning," Energy and Fuels, vol. 36, no. 2, pp. 1052–1062, Jan. 2022, doi: 10.1021/acs.energyfuels.1c03270.
- [417] H. I. Witten, E. Frank, A. H. Hall, and J. C. Pal, Data Mining: Practical Machine Learning Tools and Techniques. Todd Green-Elsevier, 2017.
- [418] R. A. Rutenbar, "Simulated annealing algorithms: An overview," IEEE Circuits and Devices Magazine, vol. 5, no. 1, pp. 19–26, Jan. 1989, doi: 10.1109/101.17235.
- [419] S. Kirkpatrick, C. D. Gelatt, and M. P. Vecchi, "Optimization by Simulated Annealing," Science (1979), vol. 220, no. 4598, pp. 671–680, May 1983, doi: 10.1126/SCIENCE.220.4598.671.
- [420] H. R. Najafabadi, T. G. Goto, T. C. Martins, A. Barari, and M. S. G. Tsuzuki, "Multi-objective Topology Optimization Using Simulated Annealing Method," Advances in Intelligent Systems and Computing, vol. 1296, pp. 343–353, 2021, doi: 10.1007/978-3-030-63403-2_31/COVER.
- [421] S. Zhou, X. Liu, Y. Hua, X. Zhou, and S. Yang, "Adaptive model parameter identification for lithium-ion batteries based on improved coupling hybrid adaptive particle swarm optimization- simulated annealing method," J Power Sources, vol. 482, p. 228951, Jan. 2021, doi: 10.1016/J.JPOWSOUR.2020.228951.
- [422] T. G. Goto et al., "Versatility of Simulated Annealing with Crystallization Heuristic: Its Application to a Great Assortment of Problems," Engineering Problems - Uncertainties, Constraints and Optimization Techniques, Jul. 2021, doi: 10.5772/INTECHOPEN.98562.
- [423] H. R. Najafabadi, T. G. Goto, M. S. Falheiro, T. C. Martins, A. Barari, and M. S. G. Tsuzuki, "Smart Topology Optimization Using Adaptive Neighborhood Simulated

- Annealing,” *Applied Sciences* 2021, Vol. 11, Page 5257, vol. 11, no. 11, p. 5257, Jun. 2021, doi: 10.3390/APP11115257.
- [424] H. R. Najafabadi, T. G. Goto, T. C. Martins, A. Barari, and M. de S. G. Tsuzuki, “Topology Optimization of Capacitive MEMS Accelerometers for Seismic Applications,” *Lecture Notes on Data Engineering and Communications Technologies*, vol. 146, pp. 760–772, 2023, doi: 10.1007/978-3-031-13588-0_66/COVER.
- [425] J. Li, Z. Wang, and S. Ma, “Estimation of health status of lithium-ion battery based on PF-SA,” *J Phys Conf Ser*, vol. 2079, no. 1, p. 012008, Nov. 2021, doi: 10.1088/1742-6596/2079/1/012008.
- [426] P. R. Chinnam, T. R. Tanim, E. J. Dufek, C. C. Dickerson, and M. Li, “Sensitivity and reliability of key electrochemical markers for detecting lithium plating during extreme fast charging,” *J Energy Storage*, vol. 46, p. 103782, Feb. 2022, doi: 10.1016/J.EST.2021.103782.
- [427] H. Tu, H. Feng, S. Srdic, and S. Lukic, “Extreme Fast Charging of Electric Vehicles: A Technology Overview,” *IEEE Transactions on Transportation Electrification*, vol. 5, no. 4, pp. 861–878, Dec. 2019, doi: 10.1109/TTE.2019.2958709.
- [428] Y. Liu, Y. Zhu, and Y. Cui, “Challenges and opportunities towards fast-charging battery materials,” *Nat Energy*, vol. 4, no. 7, pp. 540–550, 2019, doi: 10.1038/s41560-019-0405-3.
- [429] X. Lin, K. Khosravinia, X. Hu, J. Li, and W. Lu, “Lithium Plating Mechanism, Detection, and Mitigation in Lithium-Ion Batteries,” *Prog Energy Combust Sci*, vol. 87, no. September 2020, 2021, doi: 10.1016/j.pecs.2021.100953.
- [430] E. C. Cengiz, J. Rizell, M. Sadd, A. Matic, and N. Mozhzhukhina, “Review—Reference Electrodes in Li-Ion and Next Generation Batteries: Correct Potential Assessment, Applications and Practices,” *J Electrochem Soc*, vol. 168, no. 12, p. 120539, Dec. 2021, doi: 10.1149/1945-7111/AC429B.

- [431] S. P. Rangarajan, S. Sarkar, Y. Barsukov, and P. P. Mukherjee, “3e-A Versatile Operando Analytics Toolbox in Energy Storage,” *ACS Omega*, vol. 6, no. 49, pp. 33284–33292, Dec. 2021, doi: 10.1021/ACSOMEGA.1C05494/ASSET/IMAGES/LARGE/AO1C05494_0004.JPEG.
- [432] A. Bohinsky, S. P. Rangarajan, Y. Barsukov, and P. Mukherjee, “Preventing lithium plating under extremes: An untold tale of two electrodes,” *J Mater Chem A Mater*, vol. 9, no. 32, pp. 17249–17260, Aug. 2021, doi: 10.1039/d1ta05290j.
- [433] J. C. Hamar, S. V. Erhard, C. Zoerr, and A. Jossen, “Anode Potential Estimation in Lithium-Ion Batteries Using Data-Driven Models for Online Applications,” *J Electrochem Soc*, vol. 168, no. 3, p. 030535, 2021, doi: 10.1149/1945-7111/abe721.
- [434] T. Waldmann, M. Kasper, and M. Wohlfahrt-Mehrens, “Optimization of Charging Strategy by Prevention of Lithium Deposition on Anodes in high-energy Lithium-ion Batteries - Electrochemical Experiments,” *Electrochim Acta*, vol. 178, pp. 525–532, 2015, doi: 10.1016/j.electacta.2015.08.056.
- [435] X. Lin, J. Park, L. Liu, Y. Lee, W. Lu, and A. M. Sastry, “A Comprehensive Capacity Fade Model and Analysis for Li-Ion Batteries,” *J Electrochem Soc*, vol. 160, no. 10, pp. A1701–A1710, 2013, doi: 10.1149/2.040310jes.
- [436] R. Kohavi and G. John, “Wrappers for feature subset selection,” *Lecture Notes in Computer Science (including subseries Lecture Notes in Artificial Intelligence and Lecture Notes in Bioinformatics)*, vol. 7920 LNCS, no. 97, pp. 654–678, 2013, doi: 10.1007/978-3-642-39038-8_27.
- [437] T. Dietterich, C. Bishop, D. Heckerman, M. Jordan, and M. Kearns, “Adaptive Computation and Machine Learning,” 2021.
- [438] J. Mendes-Moreira, C. Soares, A. M. Jorge, and J. F. De Sousa, “Ensemble approaches for regression: A survey,” *ACM Comput Surv*, vol. 45, no. 1, 2012, doi: 10.1145/2379776.2379786.

- [439] R. Caruana, A. Niculescu-Mizil, G. Crew, and A. Ksikes, "Ensemble selection from libraries of models," *Proceedings, Twenty-First International Conference on Machine Learning, ICML 2004*, no. 1996, pp. 137–144, 2004, doi: 10.1145/1015330.1015432.
- [440] C. Paladiya and A. Kiani, "Nano structured sensing surface: Significance in sensor fabrication," *Sens Actuators B Chem*, vol. 268, pp. 494–511, Sep. 2018, doi: 10.1016/J.SNB.2018.04.085.
- [441] M. Moghareh Abed and A. Kiani, "Optical reflectivity of heat-treated nanofibrous silicon thin-films induced by high energy picosecond laser pulses," *Sens Biosensing Res*, vol. 30, p. 100385, Dec. 2020, doi: 10.1016/J.SBSR.2020.100385.
- [442] C. Paladiya and A. Kiani, "Synthesis of Silicon Nano-fibrous (SiNf) thin film with controlled thickness and electrical resistivity," *Results Phys*, vol. 12, pp. 1319–1328, Mar. 2019, doi: 10.1016/J.RINP.2018.12.093.
- [443] C. Paladiya, B. Kennedy, and A. Kiani, "Pulsed ionized mesh-like assembly of hybrid silica nanostructures with controlled resistivity," *Appl Surf Sci*, vol. 453, pp. 405–415, Sep. 2018, doi: 10.1016/J.APSUSC.2018.05.107.
- [444] S. J. Kwon et al., "Preparation and Characterization of Rutile-anatase Hybrid TiO₂ Thin Film by Hydrothermal Synthesis," *Clean Technology*, vol. 20, no. 3, pp. 306–313, Sep. 2014, doi: 10.7464/KSCT.2014.20.3.306.
- [445] J. He et al., "Facile Formation of Anatase/Rutile TiO₂ Nanocomposites with Enhanced Photocatalytic Activity," *Molecules* 2019, Vol. 24, Page 2996, vol. 24, no. 16, p. 2996, Aug. 2019, doi: 10.3390/MOLECULES24162996.
- [446] F. Scarpelli, T. F. Mastropietro, T. P. and N. Godbert, F. Scarpelli, T. F. Mastropietro, and T. P. and N. Godbert, "Mesoporous TiO₂ Thin Films: State of the Art," *Titanium Dioxide - Material for a Sustainable Environment*, Jun. 2018, doi: 10.5772/INTECHOPEN.74244.

- [447] M. C. Biesinger et al., “Quantitative Chemical State XPS Analysis of First Row Transition Metals, Oxides and Hydroxides”, doi: 10.1088/1742-6596/100/1/012025.
- [448] M. C. Biesinger, L. W. M. Lau, A. R. Gerson, and R. S. C. Smart, “Resolving surface chemical states in XPS analysis of first row transition metals, oxides and hydroxides: Sc, Ti, V, Cu and Zn,” *Appl Surf Sci*, vol. 257, no. 3, pp. 887–898, Nov. 2010, doi: 10.1016/J.APSUSC.2010.07.086.
- [449] M. E. Dufond et al., “Quantifying the Extent of Ligand Incorporation and the Effect on Properties of TiO₂ Thin Films Grown by Atomic Layer Deposition Using an Alkoxide or an Alkylamide,” *Chemistry of Materials*, vol. 32, no. 4, pp. 1393–1407, Feb. 2020, doi: 10.1021/ACS.CHEMMATER.9B03621/SUPPL_FILE/CM9B03621_SI_001.PDF.
- [450] T. Zheng and J. Dahn, “Effect of turbostratic disorder on the staging phase diagram of lithium-intercalated graphitic carbon hosts,” *Phys Rev B Condens Matter Mater Phys*, vol. 53, no. 6, pp. 3061–3071, 1996, doi: 10.1103/PhysRevB.53.3061.

Appendix A

The MATLAB and Python code produced for a portion of this thesis is shared in this section.

Specific Areal Capacitance and Discharge Time Calculation MATLAB Code based on GCD Curve.

```
>clc, clear all, close all, warning off
%%Specific Capacitance Calculation
>disp('Dchg/Chg_Time');
>disp('Dchg/Chg_Time');

% % Load cycle file
>cycle = readmatrix('test1.xlsx', 'Sheet','test1');
>cycle1 = readtable('test1.xlsx', 'Sheet','test1');
>TCyc = cycle(:, 1);
>vCyc = cycle(:, 2);
>stepNum = cycle(:, 3);
>xArr_Dch = [];
>xArr_Chag = [];
>numStep = max(stepNum);

    for i = 1 : numStep
        >disp(['Cycle number is ', num2str(i)]);
        >indices = find(stepNum == i);
        >startIndex0 = min(indices);
        >endIndex0 = max(indices);
        >tAll = cycle1(:, 1);
        >t0 = tAll{startIndex0, :};
        >t1 = tAll{endIndex0, :};
        >T_chg_dch=t1-t0;
        >disp(['T_chg_dch=', num2str(T_chg_dch)]);

        >if i ==4
            >xArr_Dch = [xArr_Dch; [T_chg_dch]];
            >dch_time=(xArr_Dch);
            >v1=0.8;
            >v2=-0.8;
            >S_Cap= (4*0.000141)/((v2-v1)/dch_time); %% Equation 1
            >S_Cap=S_Cap*(-1000); %% Unit Conversion (mF/cm2)
        End

        if i ==3
            >xArr_Chag = [xArr_Chag; [T_chg_dch]];
        end

        >plot (vCyc, 'r'); hold on;
    end
# The End. Run & Enjoy.
```

MLP Construction Python-Code for Impedance and Specific Capacitance Prediction.

```
# Data Wrangling
import pandas as pd
import numpy as np
from google.colab import drive
import sys
# Preprocessing
from sklearn.preprocessing import StandardScaler, PowerTransformer
# VIF
from statsmodels.stats.outliers_influence import variance_inflation_factor
from statsmodels.tools.tools import add_constant
# Data Visualization
import matplotlib.pyplot as plt
from matplotlib import rcParams
import seaborn as sns
# SKLEARN
from sklearn.model_selection import train_test_split
from sklearn import metrics
from sklearn.model_selection import RepeatedKFold
# TENSORFLOW
import os
import logging
from keras.models import Sequential
from keras.layers import Dense
from keras.layers import Dropout
from tensorflow.keras.optimizers import Adam
from keras.metrics import MeanSquaredError, RootMeanSquaredError
import tensorflow
import tensorflow_addons as tfa
# Set TensorFlow logging level to error
tensorflow.get_logger().setLevel(logging.ERROR)
# Set random seeds for reproducibility
RANDOM_SEED = 35
np.random.seed(RANDOM_SEED)
tensorflow.random.set_seed(RANDOM_SEED)
os.environ['TF_CPP_MIN_LOG_LEVEL'] = '2'
# Mount Google Drive
drive.mount('/content/gdrive', force_remount=True)
sys.path.append("/content/gdrive/My Drive")
ROOT = "/content/gdrive/My Drive"
# Data Loading and Preprocessing
# Get data
def get_data(path='Test1.xlsx'):
    data_path = os.path.join(ROOT, path)
    data = pd.read_excel(data_path, index_col=None, dtype={'Name': str, 'Value': float})
    return data
# Find numerical columns
def get_numeric_cols(data):
    num_types = ['int64', 'float64']
    return list(data.select_dtypes(include=num_types))
# Targets: |Z|max, Dch_Time
TARGET = 'Dch_Time'
# Drop extra columns
drop_it(data, ['Start-Freq', 'End_Frequenc', 'Chg_Time', 'Spe_Capa'])

Continued>>>>>>>
```

```

# Find upper and lower boundaries for outlier removal
col = TARGET
upper_boundary, lower_boundary = find_boundaries(data, col, 1.5)
upper_boundary, lower_boundary
# Identify and remove outliers
outliers = np.where(data[col] > upper_boundary, True,
                    np.where(data[col] < lower_boundary, True, False))
outliers_df = data.loc[outliers, col]
data = data.loc[~outliers, :]
# Power Transformation
data = power_transform(data)
# Standardize
cols = data.columns
st = StandardScaler()
data = st.fit_transform(data)
data = pd.DataFrame(data, columns=cols)

# Multilayer Perceptron (MLP)
parameters = {
    'optimizer__learning_rate': 0.001,
    'model__neurons': 64,
    'model__dropout_rate': 0.5,
    'model__activation': 'tanh',
    'epochs': 400,
    'batch_size': 16
}
X, y = separate_it(data, TARGET)
X_train, X_test, y_train, y_test = train_test_split(X, y, test_size=0.2,
                                                    random_state=35)
optimizer1 = Adam(learning_rate=parameters['optimizer__learning_rate'])
n_inputs = X_train.shape[1]
model = Sequential()
model.add(Dense(parameters['model__neurons'],                    input_dim=n_inputs,
                activation=parameters['model__activation']))
model.add(Dropout(parameters['model__dropout_rate']))
model.add(Dense(1, activation='linear'))
model.compile(optimizer=optimizer1, loss='mse', metrics=[MeanSquaredError()])
history = model.fit(X_train, y_train,
                    validation_data=(X_test, y_test),
                    epochs=parameters['epochs'],
                    batch_size=parameters['batch_size'],
                    verbose=0)

y_pred = model.predict(X_test)

# The End. Run & Enjoy.

```

Random Forest Regression Construction Python-Code for Impedance and Specific Capacitance Prediction.

```
%Data Wrangling and Preprocessing
%Import necessary libraries

import pandas as pd
import numpy as np
from google.colab import drive
import sys
from sklearn.preprocessing import StandardScaler
from statsmodels.stats.outliers_influence import variance_inflation_factor
from statsmodels.tools.tools import add_constant
import matplotlib.pyplot as plt
from matplotlib import rcParams
import seaborn as sns
from sklearn.model_selection import train_test_split
from sklearn.model_selection import KFold
from sklearn.model_selection import cross_val_score
from sklearn import metrics
from sklearn.model_selection import RandomizedSearchCV
from sklearn.ensemble import RandomForestRegressor

% Set up environment

%matplotlib inline
plt.style.use("seaborn")
rcParams['figure.figsize'] = (24, 12)
drive.mount('/content/gdrive', force_remount=True)
sys.path.append("/content/gdrive/My Drive")
ROOT = "/content/gdrive/My Drive"

% Load and preprocess data
def get_data(path='FINAL_DATASE888.xlsx'):
    data_path = os.path.join(ROOT, path)
    data = pd.read_excel(data_path, index_col=None, dtype={'Name': str,
'Value': float})
    return data

def get_numeric_cols(data):
    num_types = ['int64', 'float64']
    return list(data.select_dtypes(include=num_types))

def drop_it(data, indexs, axis=1, inplace=True):
    data.drop(indexs, axis=axis, inplace=True)
    print(f'{indexs} dropped!')

Continued>>>>>>
```

```

% ... (more functions for data manipulation)

TARGET = 'Dch_Time'
data = get_data()
cols = get_numeric_cols(data)
data = data[cols]
drop_it(data, ['Start-Freq', 'End_Frequenc', 'Chg_Time', 'Spe_Capa'])
cols = data.columns
st = StandardScaler()
data = st.fit_transform(data)
data = pd.DataFrame(data, columns=cols)
col = TARGET
upper_boundary, lower_boundary = find_boundaries(data, col, 1.5)
outliers = np.where(data[col] > upper_boundary, True, np.where(data[col] <
lower_boundary, True, False))
data = data.loc[~outliers, :]
col = TARGET
distance_factor = 1.5
upper_boundary, lower_boundary = find_boundaries(data, col, distance_factor)
outliers = np.where(data[col] > upper_boundary, True, np.where(data[col] <
lower_boundary, True, False))
outliers_df = data.loc[outliers, col]
outlier_rate = len(outliers_df) / len(data)
indp_vars = get_indp_vars(data, [TARGET])
cols, vif = get_vif(indp_vars, 5)
drop_it(data, ['Scan_Speed_Base_Elec', 'Scan_Speed_Change_Elec',
'Oxidation_Base', 'Ti/Ox_Base', 'Re(Z)MAX', 'LM(ZMAX)', 'Re(Z)MIN',
'LM(ZMIN)', '|Z|Min'])

% Model Building and Evaluation
X, y = separate_it(data, TARGET)
X_train, X_test, y_train, y_test = train_test_split(X, y, test_size=0.4,
random_state=35)
reg_random_forest = RandomForestRegressor(**parameters, random_state=35)
reg_random_forest.fit(X_train, y_train)
y_pred = reg_random_forest.predict(X_test)
score = metrics.mean_squared_error(y_test, y_pred)


%Print model evaluation metrics
print(f'R^2: {metrics.r2_score(y_test, y_pred)}')
print(f'RMSE: {np.sqrt(metrics.mean_squared_error(y_test, y_pred))}')
print(f'RMSE (absolute value): {np.sqrt(np.abs(score))}')
%Save and visualize results
df_res = pd.DataFrame({'Actual': y_test, 'Predicted': y_pred.flatten()})
df_res.to_csv('result_RFR_DCH.csv', index=False)
sns.lmplot(x='Actual', y='Predicted', data=df_res, fit_reg=False)
d_line = np.arange(df_res.min().min(), df_res.max().max())
plt.plot(d_line, d_line, color='red', linestyle='--')
plt.show()
plot_pred_actl(y_pred, y_test, '', '')


# The End. Run & Enjoy.

```

Appendix B – Copyright Permission

Chapter 2-Section 2.1

Home Help Live Chat kavian khosravinia



Unwanted degradation in pseudocapacitors: Challenges and opportunities
Author: Siddharth Mahala, Kavian Khosravinia, Amirkianoosh Kiani
Publication: Journal of Energy Storage
Publisher: Elsevier
Date: 1 September 2023
© 2023 Elsevier Ltd. All rights reserved.


Journal Author Rights


Please note that, as the author of this Elsevier article, you retain the right to include it in a thesis or dissertation, provided it is not published commercially. Permission is not required, but please ensure that you reference the journal as the original source. For more information on this and on your other retained rights, please visit: <https://www.elsevier.com/about/our-business/policies/copyright#Author-rights>

[BACK](#) [CLOSE WINDOW](#)

© 2023 Copyright - All Rights Reserved | Copyright Clearance Center, Inc. | Privacy statement | Data Security and Privacy | For California Residents | Terms and Conditions
Comments? We would like to hear from you. E-mail us at customercare@copyright.com

Chapter 2-Section 2.2

Home Help Live Chat Sign in Create Account



Lithium Plating Mechanism, Detection, and Mitigation in Lithium-Ion Batteries
Author: Xianke Lin, Kavian Khosravinia, Xiaosong Hu, Ju Li, Wei Lu
Publication: Progress in Energy and Combustion Science
Publisher: Elsevier
Date: November 2021
© 2021 Elsevier Ltd. All rights reserved.

Journal Author Rights

Please note that, as the author of this Elsevier article, you retain the right to include it in a thesis or dissertation, provided it is not published commercially. Permission is not required, but please ensure that you reference the journal as the original source. For more information on this and on your other retained rights, please visit: <https://www.elsevier.com/about/our-business/policies/copyright#Author-rights>

[BACK](#) [CLOSE WINDOW](#)

Chapter 3 and 4- Section 3.1.4 and Section 4.1

Home Help Live Chat kavian khosravinia



Unlocking pseudocapacitors prolonged electrode fabrication via ultra-short laser pulses and machine learning

Author: Kavian Khosravinia, Amirkianoosh Kiani
Publication: IScience
Publisher: Elsevier
Date: 21 April 2023
© 2023 The Author(s).


Journal Author Rights


Please note that, as the author of this Elsevier article, you retain the right to include it in a thesis or dissertation, provided it is not published commercially. Permission is not required, but please ensure that you reference the journal as the original source. For more information on this and on your other retained rights, please visit: <https://www.elsevier.com/about/our-business/policies/copyright#Author-rights>

[BACK](#) [CLOSE WINDOW](#)

© 2023 Copyright - All Rights Reserved | Copyright Clearance Center, Inc. | Privacy statement | Data Security and Privacy | For California Residents | Terms and Conditions
Comments? We would like to hear from you. E-mail us at customer-care@copyright.com

Chapter 3 -Section 3.1

Home Help Live Chat kavian khosravinia



Protocol for fabricating pseudocapacitor electrodes using ultra-short laser pulses for in situ nanostructure generation

Author: Kavian Khosravinia, Amirkianoosh Kiani
Publication: STAR Protocols
Publisher: Elsevier
Date: 15 September 2023
© 2023 The Author(s).

Journal Author Rights

Please note that, as the author of this Elsevier article, you retain the right to include it in a thesis or dissertation, provided it is not published commercially. Permission is not required, but please ensure that you reference the journal as the original source. For more information on this and on your other retained rights, please visit: <https://www.elsevier.com/about/our-business/policies/copyright#Author-rights>

[BACK](#) [CLOSE WINDOW](#)

© 2023 Copyright - All Rights Reserved | Copyright Clearance Center, Inc. | Privacy statement | Data Security and Privacy | For California Residents | Terms and Conditions
Comments? We would like to hear from you. E-mail us at customer-care@copyright.com



Attribution-NonCommercial- NoDerivatives 4.0 International (CC BY-NC-ND 4.0)

This is a human-readable summary of (and not a substitute for) the [license](#). [Disclaimer](#).

You are free to:

Share — copy and redistribute the material in any medium or format

The licensor cannot revoke these freedoms as long as you follow the license terms.